DOCTORAL THESIS

Mechanical characteristics and damage mechanisms of stitched carbon/epoxy composites under static and fatigue loads

ARIEF YUDHANTO

DIVISION OF AEROSPACE ENGINEERING
GRADUATE SCHOOL OF SYSTEM DESIGN
TOKYO METROPOLITAN UNIVERSITY

MARCH 2013

Doctoral Thesis

Mechanical characteristics and damage mechanisms of stitched carbon/epoxy composites under static and fatigue loads

Arief Yudhanto

Division of Aerospace Engineering
Graduate School of System Design
Tokyo Metropolitan University
March 2013

Mechanical Characteristics and Damage Mechanisms of Stitched Carbon/Epoxy Composites under Static and Fatigue Loads

静的および疲労荷重下での炭素繊維／エポキシ縫合複合材の力学特性と損傷メカニズム

by

Arief Yudhanto
Student ID 09991571
B.Eng, Aeronautics and Astronautics, Bandung Institute of Technology (2002)
M.Eng, Mechanical Engineering, National University of Singapore (2006)

Submitted to the Division of Aerospace Engineering, Graduate School of System Design,
in partial fulfillment of the requirements for the degree of
Doctor of Engineering in Aerospace Engineering
at the
TOKYO METROPOLITAN UNIVERSITY
March 2013

Certified by advisor

Professor Naoyuki Watanabe
Division of Aerospace Engineering
Graduate School of System Design
Tokyo Metropolitan University

PhD thesis committee:

Professor Naoyuki Watanabe	Tokyo Metropolitan University (Chairman)
Professor Masahito Asai	Tokyo Metropolitan University
Professor Hiroshi Suemasu	Sophia University
Associate Professor Koichi Kitazono	Tokyo Metropolitan University
Associate Professor Satoshi Kobayashi	Tokyo Metropolitan University

The research reported in this thesis was carried out at the Division of Aerospace Engineering, Graduate School of System Design, Tokyo Metropolitan University (TMU), 6-6 Asahigaoka, Hino-shi, Tokyo 191-0065, Japan, between October 1, 2009 and March 31, 2013.

Some experimental works reported in this thesis were also carried out at the Advanced Composites Technology Center, Japan Aerospace Exploration Agency (JAXA), 6-13-1 Ohsawa, Mitaka-shi, Tokyo 181-0015, Japan, between April 1, 2010 and March 31, 2013.

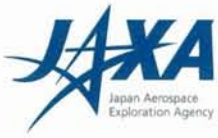

The research is part of a joint-collaboration between TMU and JAXA with the financial support from Tokyo Metropolitan Government under the project of Asian Network of Major Cities 21 (ANMC-21).

This thesis is typeset using LaTeX.

This work is dedicated to my late father
saṅ lwir tirtha kitêṅ mahardhika
(who is like nectar to wise souls)

Abstract

Objective of this thesis is to understand the effect of stitch parameters (stitch density, stitch thread thickness, stitch pattern, stitch orientation) on the in-plane mechanical properties and damage mechanisms of Vectran-stitched and Kevlar-stitched carbon/epoxy composites under static and fatigue loads. Experimental test series comprising static tension, static compression, open hole tension, open hole compression, tension-tension and compression-compression fatigue tests are performed. Characterization of architectural changes induced by stitching process, e.g. fiber breakage, fiber waviness, resin-rich region, stitch debonding, and their correlation with mechanical performance and damage mechanisms is discussed in details. Two analytical works are also described in this thesis: first, a multi-scale modeling scheme to predict 3-D thermo-elastic constants of stitched composites by employing asymptotic expansion homogenization method; second, application of Average Stress Criterion to predict open hole tension strength of stitched composites. Investigation of Vectran-stitched composites shows that moderately stitched composites (stitched 6×6; moderate stitch density) under static tension experience a slight strength reduction, while densely stitched composites (stitched 3×3; high stitch density) exhibit a modest improvement of strength in comparison with unstitched composites. Stitching with either stitch density is found to promote a vast number of cracks, but densely stitched composites are sufficiently effective in impeding the growth of delamination, which translates into higher tensile strength. Accordingly, under fatigue loads, densely stitched composites exhibit better fatigue life due to similar mechanism: delamination impediment provided by the stitches. Tensile modulus of stitched composites is slightly reduced mainly due to fiber waviness. Compression tests on Vectran-stitched composites show that regardless stitch density or thread thickness stitched composites generally exhibit lower compressive strength than unstitched composites. Stitching induces a formation of resin-rich region, which triggers early cracking, fiber splitting and fiber kinking at relatively lower compression load. Analytical work dealing with the predictions of 3-D thermo-elastic constants of Vectran-stitched composites shows that homogenization results are in a good agreement with the experiments. Investigation of Kevlar-stitched composites shows that stitched composites with hole are sensitive to stitch orientation, in which transverse stitching (perpendicular to loading direction) significantly reduces tensile strength due to stitch debonding and ensuing interaction amongst debondings. On the other hand, stitched composites with holes are independent of stitch orientation because the failure is greatly controlled by the stress concentration at the hole rims that surpasses the criticality of stitch debonding. Thus, normal stress distribution in Kevlar-stitched composites with holes can be estimated by Lekhnitskii theory, and open hole tensile strength can be estimated by Average Stress Criterion. Investigation of Kevlar-stitched composites under fatigue loads reveals that stitch pattern of round stitching (stitches encircling the holes) reduces fatigue life due to damage acceleration around the hole rim, whilst parallel stitching does not pose any significant effect on fatigue life. Finally, recommendation on how to improve the mechanical performance of stitched composites is given. This thesis endorses that stitching is an effective through-thickness reinforcement method for composites in the next generation aircraft.

Keywords: Stitched composites, tension, compression, fatigue, damage, open hole

Contents

List of Figures

List of Tables

Nomenclature

Symbols	Definition
a	Delamination length
a_0	Characteristic length
a_{com}	Combined waviness amplitude
a_{in}	In-plane waviness amplitude
a_{out}	Out-of-plane waviness amplitude
A_0	Gage area
A_1, A_2, A_i	Delamination area
A_d	Total delamination area
A_n	Normalized delamination area
A_s	Cross-sectional area of stitch thread
CD_o	Crack density of oblique crack
CD_t	Crack density of transverse crack
d_f	Fiber diameter
d_{max}	Maximum displacement
E_{dyn}	Dynamic stiffness
E_{dyn-i}	Dynamic stiffness at N_1 (first cycle)
E_i	Instantaneous tensile stiffness or secant modulus
E_{ijkl}	Elastic tensor
E_L	Longitudinal modulus of composite constituent, e.g. fiber, matrix
E_T	Transverse modulus of composite constituent
E_{un}	Tensile modulus of unstitched composites
E_x	Longitudinal modulus of composites
E_x^n	Normalized longitudinal modulus of composites
E_y	Transverse modulus of composites
f	Body force
$g(x,y)$	Periodic vector function
G_{LT}	Shear modulus (in-plane) of composite constituent
G_{TT}	Shear modulus (out-of-plane) of composite constituent
G_{xy}	Shear modulus of composite
t	Thickness of composite laminate
K_T	Stress concentration factor
L, l	Length
l_g	Gage length
m	Mass
m_f	Gradient of S-N curve
n_{oi}	Number of oblique crack per section
n_{ti}	Number of transverse crack per section
N	Number of cycle during fatigue test
N_f	Number of cycle required to fail the specimen (cycle-to-failure)
N_i	Number of i_{th} cycle
N_p	Stiffness degradation onset; cycle at which stiffness starts to rapidly drop

p	Stitch pitch
P_{max}	Maximum load
r	Hole radius
R	Load ratio ($\sigma_{min}/\sigma_{max}$)
R^2	Coefficient of variation (C.O.V)
s	Stitch spacing
S	Stress in S-N curve; surface of void in homogenization theory
SD	Stitch density
u	Displacement component
v	Virtual displacement component
V	Volume
V_f	Fiber volume fraction
V_{fl}	Local fiber volume fraction
V_{pr}	Volume of fiber preforms
V_{rl}	Local resin volume fraction
V_s	Stitch content
V_{vl}	Local void volume fraction
w	Weight
w_a	Weight of composite plate in open air
w_g	Width in gage area
w_p	Weight of preform
w_w	Weight of composite plate in the water
Y	Base cell volume
¥	Solid part

α_L, α_T	Coefficient of thermal expansion (longitudinal and transverse direction) for composite constituent
α_x, α_y, α_z	Coefficient of thermal expansion in x-, y-, z-directions
χ^{kl}	Characteristic displacement vector
ΔT	Temperature difference
ε	Strain
ε_f	Failure strain of composite
ε_{max}	Strain level corresponds to σ_{max}
ε_{min}	Strain level corresponds to σ_{min}
ε_T	Failure strain of composite constituent
ϵ	Ratio between microscopic and macroscopic domain
Γ_d	Prescribed displacement
Γ_t	Surface at which the traction acts
μ	Linear density of stitch thread
ν_{LT}	Poissons ratio (in-plane) of composite constituent
ν_{TT}	Poissons ratio (out-of-plane) of composite constituent
ν_{xy}	Poissons ratio of composite
Ω	Elastic body
ϕ_0	Fiber waviness angle generally used for UD composites
ϕ_{com}	Combined waviness angle

ϕ_{in}	In-plane waviness angle
ϕ_{out}	Out-of-plane waviness angle
Ψ_i	Characteristic displacement vector
ρ	Density
ρ_c	Density of composite
ρ_f	Density of fiber
ρ_r	Density of resin
ρ_w	Density of water
σ	Stress
σ_∞	Remote stress
σ_{amp}	Stress amplitude
σ_d	Stress at delamination onset
σ_{max}	Maximum stress
σ_{mean}	Mean stress
σ_{min}	Minimum stress
σ_{oc}	Stress at oblique crack onset
σ_{OHC}	Open hole compression strength
σ_{OHT}	Open hole tension strength
σ_{tc}	Stress at transverse crack onset
σ_{uc}	Compressive strength
σ_{ut}	Tensile strength
σ_{ut}^n	Normalized tensile strength
σ_y	Normal stress distribution
σ_z	Interlaminar normal stress
τ_{xz}	Interlaminar shear stress
τ_y	Yield stress of composites under axial shear
θ	Void part

Chapter 1

Introduction

1.1 Background

1.1.1 Composites in aircraft and delamination problems

Advanced composite materials have been used in aerospace industry since 1960s. In the early years, aircraft manufacturers used composites to develop stabilizer, flap and wing skin for military aircrafts, e.g. F-15 [45]. In 1965, McDonnell Douglas implemented composites in commercial airplane, e.g. nacelle cowl door of DC-9. The application of composites in commercial airplanes was then growing in a modest rate [16] (see Fig. 1.1). The reason for the limited use of composite in commercial airplane is high cost of composite fabrication and certification for composite components [22]. Amid cost issue, in the second millennium, a tremendous increase of composite usage in commercial airplane was witnessed when Airbus 380, which comprises up to 22% of composites, made its maiden flight in April 2005. Afterwards, the use of composites went beyond 50%, and it was commemorated by the release of Boeing 787 in 2007. The forthcoming Airbus 350-XWB that is anticipated to be flying in 2014 would be using 52% of composites [25]. In aerospace industry, composite material has been a preferred choice over metallic material because of its high strength-to-weight ratio, high stiffness-to-weight ratio, excellent durability and non-corrosive characteristics. For airliners, these aspects translate into higher payload-range and lower direct operating cost (fuel, maintenance, etc.).

Albeit their growing use in commercial airplanes, composite materials employed to fabricate airframes are mainly based on pre-impregnated laminate (pre-preg). Although the quality of pre-preg is considered excellent, e.g. fiber volume fraction (V_f) can be consistently maintained around 60%, pre-preg is merely two-dimensional (2-D) in nature. In addition to the relatively high cost of pre-preg production using autoclave, 2-D composites are notoriously weak in the through-thickness direction [79]. As a result, 2-D composites exhibit poor interlaminar fracture toughness, and thus, they are very susceptible to delamination, i.e. separation between plies, especially when impact loading such as bird strike, debris impact or tooling drop is involved [99]. Delamination is a critical damage because it resides in the interior of composites, and severely reduces load-bearing capability of composite structures. Therefore,

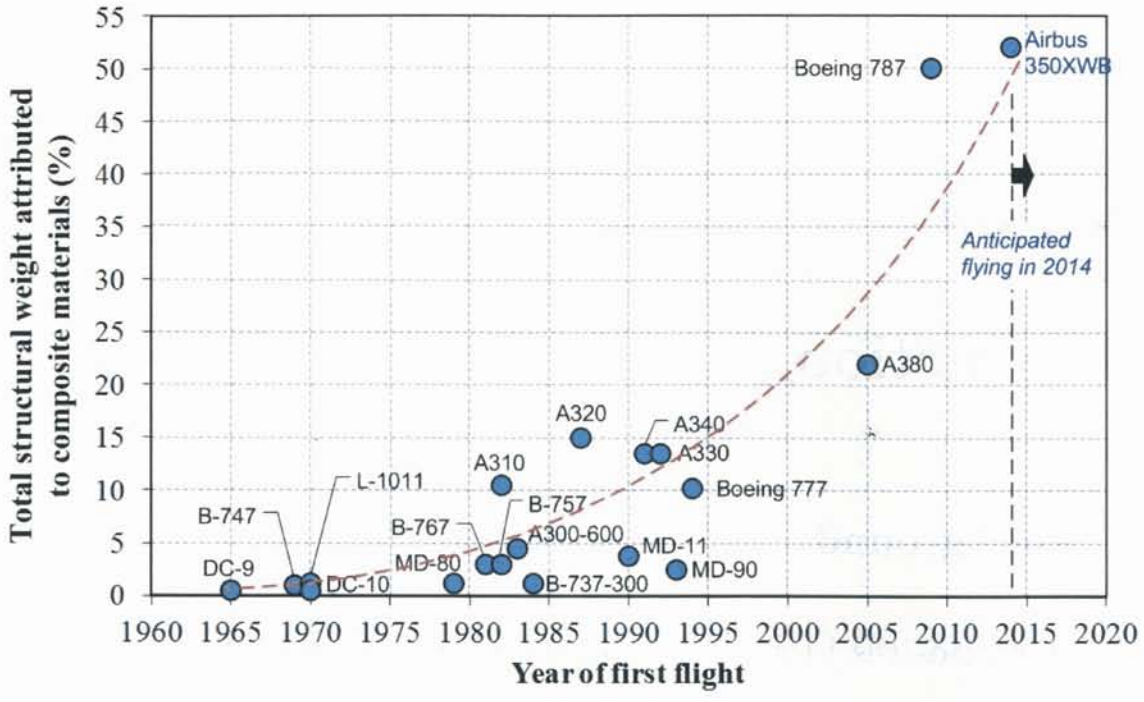

Figure 1.1: Weight percentage of composite materials in commercial airplanes [16]

a method to alleviate delamination in composites, or at least to reduce delamination size, is highly desirable because damage tolerance can be enhanced.

1.1.2 Delamination suppression method: stitching

Methods to suppress delamination in composites are of various types, and they have been developed throughout the years. The methods include the application of toughened resin [28], interleaving concepts [32, 62], Z-pinning and stitching [107]. All methods aim at improving delamination resistance, but each comes with its own shortcomings. Toughened resin, for instance, is effective in increasing interlaminar fracture toughness, but it is more costly than ordinary epoxy, which is generally used to produce composites. Interleaving, i.e. laying films between plies, is also expensive in terms of manufacturing cost because of its slow and arduous process; its cost is even more expensive than toughened resin. Z-pinning is also effective in improving delamination resistance, yet it is simple in terms of implementation. However, Z-pins may induce fiber waviness that significantly reduces compressive strength [107]. Furthermore, if Z-pins could not be maintained to be vertically straight, through-thickness (out-of-plane) properties of composites may also be reduced. A method to improve delamination resistance that receives high interest is stitching. Stitching process is carried out by simply inserting relatively thin threads into dry fabrics so that the stitch threads become an integral part of composites. Fig. 1.2a illustrates the stitching process of a stack of fabrics, and Fig. 1.2b shows the cross-sectional view of stitch composites. In a way, the presence of stitch thread in composites transforms the originally 2-D composites into three-dimensional (3-D) composites. Stitching significantly improves out-of-plane properties of composites and,

importantly, their damage tolerance. Over the other techniques (toughened resin, interleaving concepts, Z-pinning), stitching could be a preferred method because of following reasons: (i) insertion of stitch yarns can be done by employing techniques commonly available in textile industry, (ii) compared to other techniques such as weaving, knitting and braiding, stitching offers the simplest process [107], (iii) stitching is applicable to reinforce local region, e.g. circular cut-out, to potentially reduce the delamination growth and to join the components [19, 50], (iv) stitching can be employed to bind complex reforms.

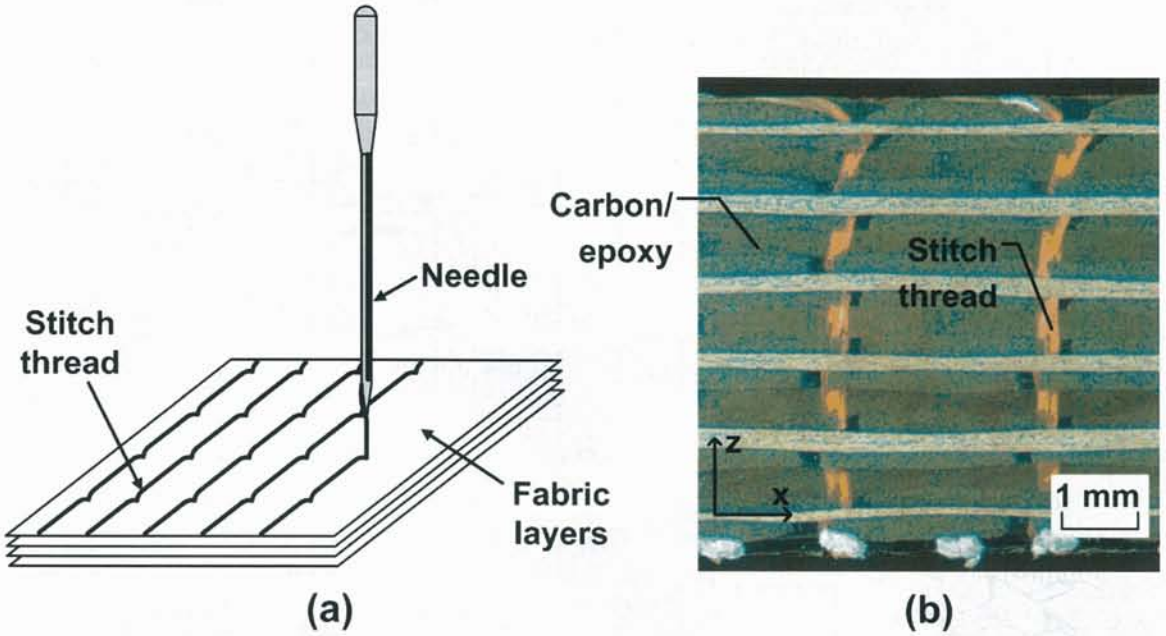

Figure 1.2: (a) Stitching process of fabric layers, (b) cross-section of stitched carbon/epoxy composites as observed from optical microscope

Early development of stitching technique for advanced composites was due to a joint venture between NASA and Boeing [13]. NASA Advanced Composites Technology (ACT) program was set up in 1989, and Advanced Stitching Machine (ASM) was built to produce large composite wing structure by incorporating stitched/RFI (resin film infusion) technique. Since then, research on the so-called *stitched composites* was spreading to other regions including Europe, Australia and Japan. Techniques and materials to produce higher quality stitched composites are also evolving. Incorporating high-strength threads, such as Kevlar®, carbon, Dyneema®, into composite systems is now common. To avoid breaking the fibers in composites, stitching process is usually carried out on the dry preforms prior to resin infiltration process. Stitched composite can then be finally fabricated using resin transfer molding (RTM), vacuum assisted resin transfer molding (VaRTM) or other cost-effective methods. Despite the encouraging development of stitched composites, however, the application of stitched composites has been very limited. To the best of author's knowledge, there may be two manufactures that have implemented stitched composites in aircraft structures. Airbus applied stitched composites to fabricate rear-pressure bulkhead of A380 [26], whilst Gulfstream Aerospace applied stitched composites for belly fairing of Gulfstream G150 [97]. In the future, under ACT program, NASA and Boeing are going to implement stitched composites to build a blended-wing-body vehicle X-48B (see Fig. 1.3a). A concept called PRSEUS or

Pultruded Rod Stitched Efficient Unitized Structure shown Fig. 1.3b is initiated, and aiming to build skin-stringer assembly whereby the joining process is carried out by several runs of stitch threads [66, 113]. However, many aircraft manufacturers today are still reluctant to use stitched composites. Their reluctance could stem from the fact that stitched composites are costly. Stitching also creates initial defect so-called stitch debonding when adhesion between stitch thread and resin is poor. The enhancement of out-of-plane mechanical properties, e.g. impact performance, is often traded-off with the reduction of in-plane mechanical properties, e.g. compression strength. Next two sections shall briefly discuss the mechanical performance of stitched composites under out-of-plane and in-plane loadings.

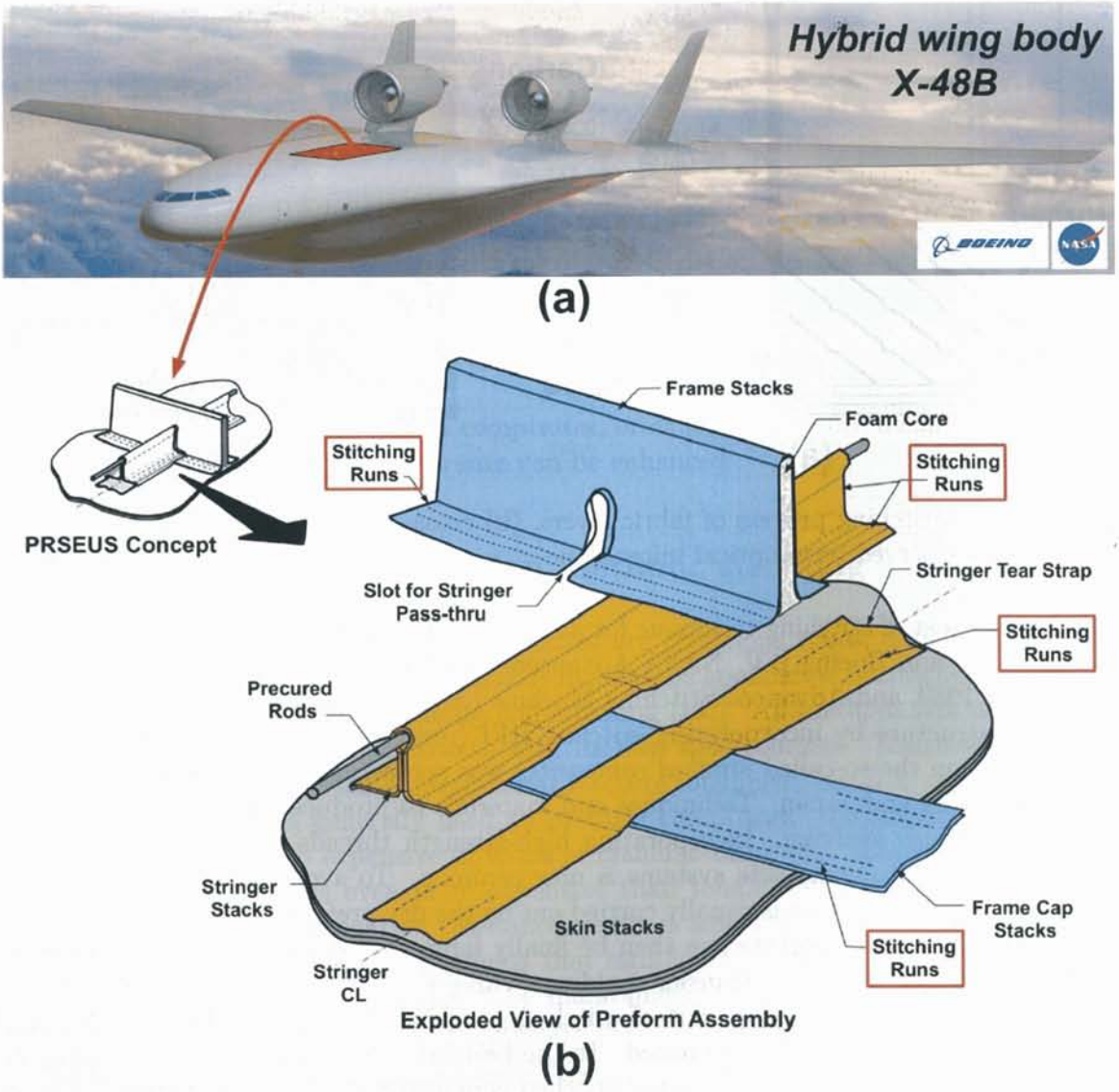

Figure 1.3: (a) X-48B blended-wing-body flight demonstrator developed by NASA and Boeing, (b) PRSEUS concept potentially applied for X-48B [113]

1.2 Review of Stitched Composites under Out-of-Plane Loading

Under out-of-plane mechanical loading (e.g. mode I, impact loadings), stitched composites generally perform better than unstitched composites. The reason is that the stitch threads are able to provide bridging traction that impedes the delamination. Thus, damage tolerance of composites can be enhanced. This positive aspect paves a way for many researchers to embark on the investigation of out-of-plane mechanical performance of stitched composites because the apparent benefit of stitching can be readily demonstrated. Several researchers found that stitched composites exhibit an improved mode I interlaminar fracture toughness because delamination growth can be inhibited by the through-thickness stitches [38, 65, 104, 107]. In that regard, stitching is able to provide better delamination resistance by giving closure traction forces that reduce the tensile strain acting on the delamination tip. Similarly, stitching is also effective in improving mode II delamination resistance of carbon/epoxy composites [64]. While unstitched carbon/epoxy exhibits unstable crack growth during end-notch flexure (ENF) test, carbon/epoxy stitched with Kevlar thread could provide traction forces to stabilize the crack growth that eventually creates an increase of mode II delamination toughness up to 3.2 times. Advantage of stitching in enhancing delamination resistance of composites is also apparent when impact loading is involved, e.g. low-velocity and high-velocity impacts [20, 61, 72, 80, 103, 106, 121]. As illustrated in Fig. 1.4a, when a thin composite is subjected to a drop of metallic ball in low-velocity impact case, delamination appears at the bottom part of composite. If stitch threads are employed to reinforce the composite, post-impact delamination area could be significantly reduced. Fig. 1.4b illustrates the comparison of C-scan images between unstitched and stitched composites in which delamination area in stitched composites is smaller than that in unstitched composites [103]. In high-velocity impact case, stitched composites experience smaller size of bullet perforation damage as compared to unstitched composites. In both cases, because post-impact damage area in stitched composites is smaller than that in unstitched composites, the residual strength (e.g. compression after impact strength) can therefore be improved.

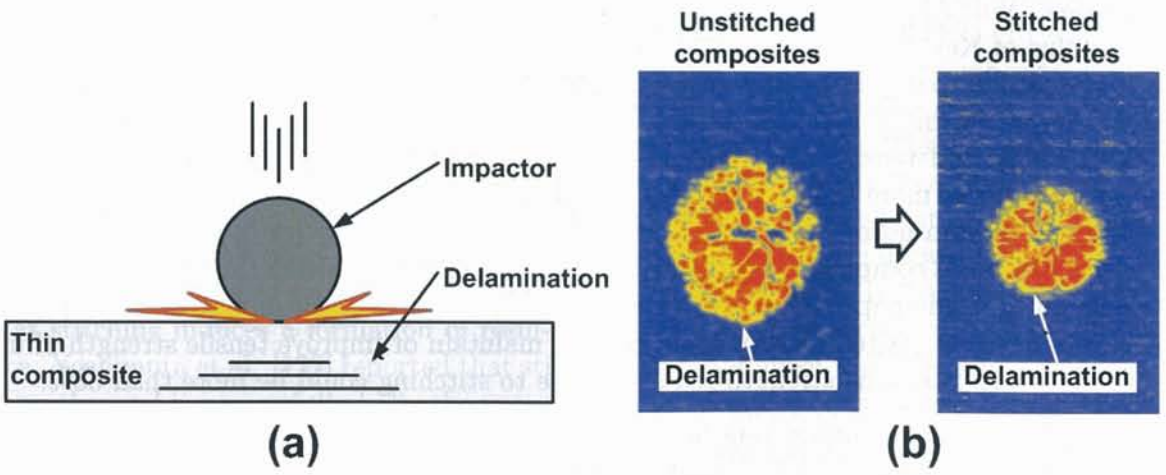

Figure 1.4: (a) Thin composite under low-velocity impact, (b) comparison of C-scan images between unstitched and stitched composites after low-velocity impact [103]

1.3 Review of Stitched Composites under In-Plane Loading

Investigation of in-plane mechanical properties of stitched composites has been carried out by many researchers for more than 20 years. The investigation, regrettably, yields dubious conclusion of whether stitching reduces, maintains or improves in-plane mechanical performance of composites. Reasons for such uncertainty have been correlated with the distortion experienced by composites during stitching process. For instance, in-plane fibers may be broken due to puncture of needle and friction of stitch thread during stitch insertion; in-plane fiber tows may be misaligned from their principal axis; fibers may be compacted during stitch insertion. To give a more thorough review, this part provides research findings of in-plane mechanical properties of stitched composites pertaining to tensile, compression and fatigue, as well as their corresponding damage mechanisms. Published reports of stitched composites containing geometrical changes, i.e. holes, are also reviewed. Published works on the prediction of in-plane mechanical properties for stitched composites are also discussed. In each section, research gaps are identified.

1.3.1 Tensile characteristics and damage mechanisms

Dickinson found that tensile strength of carbon/epoxy composites is reduced by 19% due to stitching [35]. Thuis and Bron [106] also revealed that carbon/epoxy suffers 39.7% strength reduction when the adopted stitch density (SD) is as high as 0.10/mm^2. It should be mentioned here that SD is defined as a number of stitch per unit area (unit for SD used throughout this thesis is 1/mm^2; more terminologies used in stitched composites shall be given in Chapter 2). Yoshimura et al. [122] showed that tensile strength of cross-ply carbon/epoxy laminates is reduced by approximately 16.5% when high stitch density of 0.11/mm^2 is used. Kamiya and Chou [67] found that stitching reduces tensile strength and tensile stiffness of carbon/epoxy by 10.4% and 7.5%, respectively. By incorporating Kevlar stitches into glass/epoxy, Wu and Wang [117] found that tensile modulus is reduced by 5.4%. Tensile modulus of Kevlar-stitched glass/epoxy is reduced of up to 9.4% in comparison to the unstitched counterparts [33]. In contrast, only a few researchers have actually reported a strength improvement of composites due to stitching [21, 85]. Nevertheless, correlation between stitching and tensile performance is made by Mouritz et al. [82, 83, 84] utilizing published results of more than a decade. Fig. 1.5 is taken from Ref. [82], and it displays the relationship between normalized tensile strength and stitch density (or 'z-binder content' in the chart) of various composite systems utilizing different kinds of stitch thread thickness and stitch material. This paper concludes that there is no clear relationship between stitching and tensile strength. Stitch density could reduce, maintain or improve tensile strength of up to 20%. In some cases, the strength reduction due to stitching could be more than 30%.

Although effect of stitching on tensile strength is unclear, several mechanisms responsible for the change of strength were proposed. Those who found that stitching improves tensile strength propose at least two reasons: (i) stitching effectively suppresses delamination during tensile loading, (ii) stitching increases local fiber volume through compaction effect. On the other hand, those who found that stitching reduces tensile strength or stiffness generally

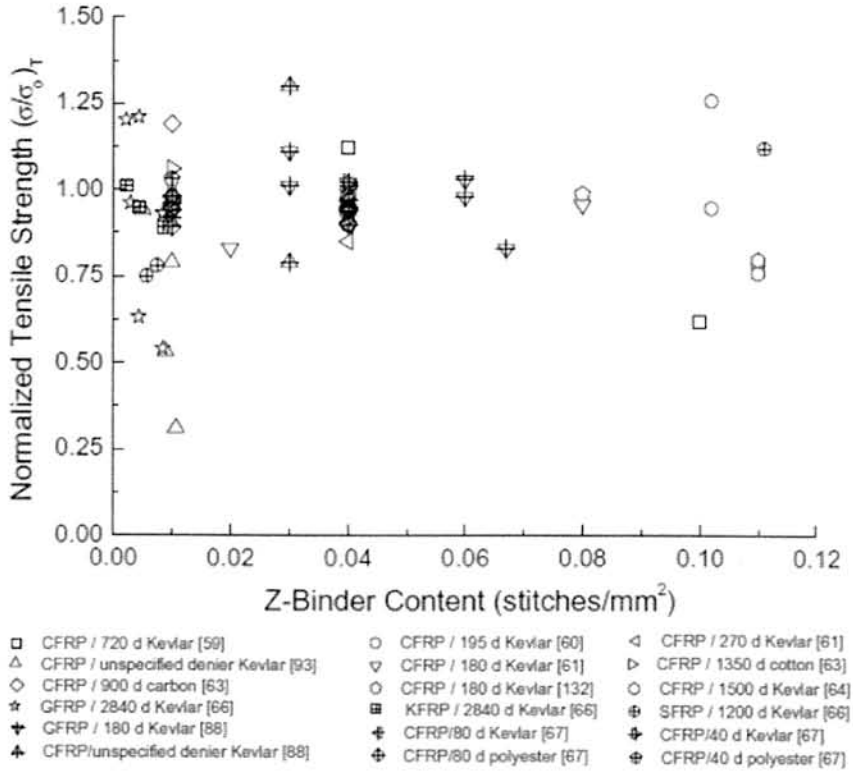

Figure 1.5: Effect of z-binder content (stitch density) on tensile strength of various composites [82]

pinpoint fiber waviness, fiber misalignment, breakage of in-plane fiber, resin-rich region or their complex combination as the plausible cause [107]. Because of these conflicting results, it is difficult to conclude under which mechanism or stitch parameters (stitch density, stitch thread thickness, stitch configuration, stitch orientation, etc.) that the tensile properties can be improved or reduced by stitching.

Nonetheless, above findings suggests that the change of tensile properties due to stitching is generally related with damage mechanisms and architectural changes in composites induced by stitching process. In this regard, characterization of both damage and architecture of stitched composites is of great importance. Characterization of damage in general fashion has been attempted by several researchers. Edgren et al. [41] investigated the effect of crack density on the tensile properties of non-crimp fabrics (NCF) stitched with polyester thread. They found that the effect of damage on longitudinal modulus is small, while Poisson's ratio is significantly reduced by the damage developed in stitched NCF. Truong et al. [108] found that stitching induces a formation of resin-rich region, which is acting as damage initiation site. Yoshimura et al. [122] reported that stitching does not affect the onset and accumulation of cracks, and it successfully halts the progress of edge-delamination. Koissin and co-workers [69] found that stitching induces local increase of fiber volume fraction by 16%, promotes earlier crack formation in off-axis tows and impedes the delamination growth.

However, beyond the aforementioned findings, several key questions related to the tensile behavior, damage mechanism and architectural changes of stitched composites have not been

addressed: (i) what is the effect of stitch density on tensile properties and the corresponding damage mechanisms?, (ii) what is the qualitative and quantitative description of damage in stitched composites?, (iii) under which condition that the tensile properties in composites can be improved or reduced by stitching; (iv) how to possibly improve the tensile performance of stitched composites?, (v) what is the detailed description of compaction mechanism proposed by Mouritz and Cox [82], and how it may be responsible for the change of properties or damage mechanisms?.

1.3.2 Compressive characteristics and damage mechanisms

Failure of composites under compression is often catastrophic, and the corresponding compressive strength is usually lower than the tensile strength. Because of these reasons, compressive properties are frequently used as criteria in aircraft structural design. When stitching is implemented in composites, understanding of compressive properties as well as damage mechanisms of stitched composites is certainly essential.

Similar to the tensile case, effect of stitching on compressive properties is uncertain whether it improves, reduces or maintains the properties. Several researchers found that stitching does not alter compressive properties of composites. Dow and Smith [37] employed Kevlar and S-2 glass to reinforce carbon/epoxy composites, and found that the compressive strength of stitched composites is similar with that of unstitched ones. Du et al. [39], Harris et al. [52] and Herszberg and Bannister [54] also found that Kevlar does not significantly change the compressive strength of carbon/epoxy composites. While stitching was reported not to significantly affect the compressive properties of composites, some other researchers found that stitching could improve the compressive properties. Stitching could increase compressive strength of composites when bi-axial stitching is employed [2]. The reason for the compressive strength improvement was not explained in this case. In most cases, however, stitching reduces compressive strength of composites. Review of compressive behavior of stitched composites reveals that stitching degrades compressive strength by 15% [82]. Reduction of compressive strength in stitched NCF is reported by Hesz and Himmel [56]. Reduction of compressive strength may reach 55% depending on the type of composite system, stitching parameters and fixtures [84]. In terms of fixture, as reported by Reeder [95], when compression test is carried out by specimens with longer gage length, no appreciable change of compressive strength is noted. On the other hand, when compression test is carried out by short-block compression test method, the reduction of strength is apparent. This behavior is related with the change of failure mode, whereby specimen with longer gage length would fail in Euler buckling behavior, while the latter would fail by fiber kinking. Reeder postulated that the failure of stitched composites under compression is greatly determined by fiber waviness. Fiber waviness and its correlation compressive strength have been widely assessed for unidirectional or cross-ply composites [1] and 3-D woven composites [76], but not for stitched composites (especially when stitch density or stitch thread thickness is varied).

Failure mechanisms in stitched composites under compression were investigated by several researchers [31, 42, 95]. Three failure mechanisms were proposed:

- First mechanism: stitching suppresses the delamination, and causes composites to fail by a combination of matrix cracking and fiber buckling;

- Second mechanism: stitched composites failed by diagonal, shear-mode type of fracture, while unstitched composites failed by delamination;

- Third mechanism: kinking of outer ply fibers is responsible for the strength degradation. Kinking of outer ply fibers is due to the surface loop yarn as well as the spreading and breakage of fibers during stitching process. This mechanism indicates that yarn tension during stitching may cause wavy outer tows, which eventually causes premature failure by kinking.

Three failure mechanisms above are graphically illustrated by Mouritz and Cox in Fig. 1.6 stating that fiber waviness angle (ϕ_0) is a dominant factor determining the compressive failure types [82]. Mouritz and Cox proposed that if ϕ_0 is higher than the criterion given in Eq. (1.1) any stitch densities applied to the composite system would result in fiber kinking mechanism.

$$\phi_0 \approx \frac{12a^2\tau_y}{\pi^2 t^2 E_1'} \tag{1.1}$$

where a is delamination length, τ_y is yield stress under axial shear, t is thickness of laminate, and $E_1'=E_1/(1\text{-}\nu_{12}^2)$. However, failure mechanisms and their corresponding approximation described in Fig. 1.6 are somewhat conservative, and may be valid only for composite with initial and measurable delamination. Initial delamination, however, may not be detected nor exist in composites prior to compression testing. Beyond the proposed failure mechanisms above, to the best of author's knowledge, no work has been done to describe the actual sequence of compressive failure in stitched composites. A clear correlation between stitch density, stitch thread thickness, stitch content or fiber waviness with compressive properties of stitched composites has not been addressed. Possible improvement of compressive performance of stitched composites has not been proposed.

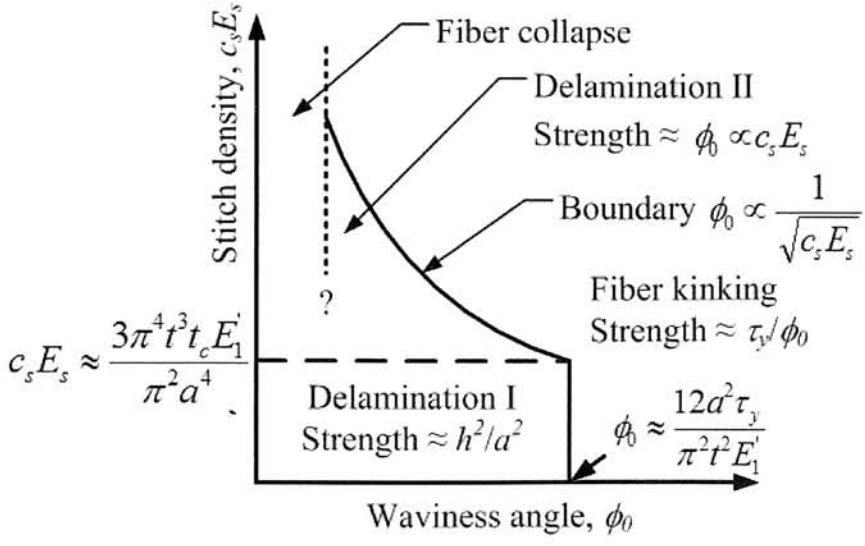

Figure 1.6: A failure map for stitched composites under compression [82]

1.3.3 Fatigue characteristics and damage mechanisms

The behavior whereby composites fail due to repeated or cyclic stresses applied below ultimate strength is defined as fatigue. Fatigue behavior of composites could be more complex than static behavior. The complexity may increase with the presence of stitching in the composites. Published reports on fatigue of stitched composites are fairly limited and diverse to suggest a general conclusion on the efficacy of stitching in composites. A few exploratory papers on fatigue properties of stitched composites can be reviewed in Refs. [82, 83, 84, 107]. It is noted that one of the earliest fatigue investigations was performed by Portanova et al. [93]. They found that stitching carbon/epoxy composites using Kevlar does not change the compression-compression fatigue life and failure mode of carbon/epoxy. Stitching only decelerates the progression of delamination without showing other significant advantage. The other investigation on fatigue of stitched composites was reported by Vandermey et al. [111]. They found that stitching induces some damage in composites, but at the same time, it is able to reduce the delamination growth. After those early investigations, a number of researchers also investigated fatigue performance of stitched composites. Herszberg et al. [55] revealed that Dyneema-stitched composites have better fatigue resistance than Kevlar-stitched composites, or the unstitched ones. Experimental study by Shah Khan and Mouritz [98] suggests that stitching significantly reduces tensile fatigue life of glass-reinforced polymer laminates when they are subjected to tension-zero load cycle (load ratio $R = 0$). Aymerich et al. [21] reported that fatigue life of matrix-dominated laminates of $[\pm 30/90]_S$ is improved by stitching, whilst that of fiber-dominated laminates of $[\pm 45/0/90]_S$ is reduced. Aymerich et al. [19] also found that fatigue life of stitched joints is improved up to five times when stitch pitch (distance between stitch penetration holes, p) of 2 mm is employed. Mouritz [81] found that fatigue performance of stitched laminates is reduced by nearly ten times (i.e. one order) although the stitch content used is only 0.8%. Beier et al. [24] found that stitching shortens fatigue life of carbon/epoxy laminates at high stresses. Damage caused by stitching in carbon/epoxy under fatigue loading was investigated by Aono and co-workers [18, 17]. Some recent investigations on fatigue of stitched composites were reported on stitched NCF [3, 29, 110, 109]. Adden et al. [3] focused on the fatigue behavior of NCF made of glass fibers. Damage development was captured, and stiffness degradation due to fatigue loading in stitched NCF was numerically modeled. They found that the stiffness degradation and fatigue crack growth in stitched NCF is dependent on stitching direction. Likewise, Vallons et al. [109, 110] and Carvelli et al. [29] concluded that fatigue life of stitched NCF made of carbon fibers is also highly dependent on the direction of stitching. When the direction of stitching is in-line with the direction of fatigue loading, fatigue life of NCF can be improved, vice versa. However, literatures of fatigue behavior of stitched composites spanning for more than two decades indicate that the effect of stitch density on fatigue characteristics of carbon/epoxy has not been studied, especially when it includes fatigue life, stiffness degradation and fatigue damage mechanisms.

1.3.4 Stitched composites with holes and damage mechanisms

In aircraft structures, holes are commonly created to reduce structural weight or to facilitate joining. However, holes generally induce high stress concentration during loading, and

consequently, damage is often initiated from the holes. Studies of mechanical properties of stitched laminates with holes exist although they are very limited in number. Portanova et al. [93] performed studies on stitched composites containing circular hole. They performed open hole fatigue on stitched and unstitched carbon/epoxy laminates, and found that during fatigue tests, stitching does not alter the failure mode. Thuis and Bron [106] studied open hole strength of Kevlar-stitched carbon/epoxy laminates, and revealed that 6 mm diameter hole degrades tensile strength by 43% and 54% for laminates with SD of $0.04/\text{mm}^2$ and $0.10/\text{mm}^2$, respectively. Herszberg et al. [55] conducted open hole fatigue, and revealed that Dyneema-stitched composites has better fatigue performance than Kevlar-stitched composites. Yoshimura [120] analyzed the effect of hole on crack and delamination progression in stitched laminates under static tension using finite element method, and validated the analytical results with the experiments. His numerical results are in a good agreement with experiments. Chen et al. [30] found that stitching reduces stress concentration around the hole in quasi-isotropic T300/QY9512 laminates, and open hole tensile strength remains to be unaffected with the direction of stitching. Han et al. [50] found that round stitching (stitch lines around circular hole) increases strain concentration factor.

Investigation of stitched composites with holes generally overlooks one of the important stitch parameters, namely stitch orientation. Effect of stitch orientation has been commonly performed for stitched composites *without* holes instead. For example, Larsson [72] reported that tensile modulus and tensile strength of stitched carbon/epoxy are insensitive to the stitch orientation. Experimental studies by Pang et al. [90] suggested that creep resistance of laminates could be improved if stitching direction is aligned with the loading direction. Experimental and analytical investigation on Kevlar-stitched T300/QY9512 performed by Zhang and Wei [123] showed that tensile strength is not affected by stitch orientation for any stitch densities. Comparing the results of machine-direction and cross-direction static tensile tests of chain stitched biaxial (± 45) carbon/epoxy NCF, Vallons et al. [109] found that effect of stitch orientation is insignificant in terms of tensile stiffness and strength. It is evident that the study of mechanical performance and failure mechanism of stitched composites containing circular hole is still called for. Prediction of open hole tensile (OHT) strength for stitched composites by utilizing a popular approach in industry, for instance, Average Stress Criterion (ASC), has not been available. In fact, the prediction of OHT using ASC is useful to validate the efficacy of that criterion for stitched composites. In addition, effect of stitch pattern on stitched composites with holes under fatigue has not been investigated. Thus, several key research questions in this part are summarized as follows: (i) what is the effect of stitch orientation on tensile properties and damage mechanisms of stitched composites?, (ii) how to predict open hole tension strength of stitched composites?, (iii) what is the effect of stitch pattern, for example round stitching and parallel stitching, on the mechanical performance and damage mechanisms of stitched composites with holes under fatigue?.

1.3.5 Predictions of thermo-elastic constants of stitched composites

During material selection process, knowledge of basic thermo-elastic constants of composites is very important. Thermo-elastic constants would often be obtained by extensive experimental testings. Albeit important, such testings are costly and time consuming. To complement

the tests, it is useful to use analytical models so that the effect of certain parameter or constituent on the thermo-elastic constants of composites can be assessed.

Analytical models to fully predict thermo-elastic constants for stitched composites are very few. Most models deal with mechanical properties. Dickinson et al. [36] proposed a 3-D unit cell model with star pattern to evaluate the elastic properties of stitched composites. Grassi et al. [47] proposed two models: the first model was used to evaluate the elastic constants and local stress distribution, and the second model was used to study the interlaminar shear stresses. Hesz et al. [57] proposed a unit cell model built in *ANSYS* to predict elastic constants of stitched NCF. A unit cell model for predicting 3-D mechanical properties of laminates containing through-thickness reinforcement is built using voxel mesh approach [49]. A unit cell model for Z-fiber is proposed by Krueger, in which finite element code based on a 2-D general Cosserat couple stress theory was developed [70]. Finite element code *FLASH* was used to predict compressive strength of fiber composites [100]. Prediction of elastic properties of stitched composites by representative volume element was proposed by Riccio et al. [96]. Fiber tow properties were calculated using micromechanics-based rule of mixture. Three finite element models were developed for NCF: one lamina model, two cross-ply laminates model of $[0/90]_2$ and $[0/90]_S$. FE commercial code ANSYS was used throughout the modeling [46]. However, the existing models only produce mechanical properties. Often, the models are not robust enough in the sense that it is time consuming (for example, voxel mesh [49]) and connectivity between plies may not be compatible in evaluating stress distribution and interaction of damages between plies. Prediction of thermal expansion coefficients of stitched composites is often disregarded. Thus, models to fully predict 3-D thermo-elastic constants of stitched composites are still needed in this respect.

1.4 Problem Statements and Objectives

Apart from the existing propositions to explain the in-plane mechanical behavior of stitched composites under static and fatigue loads, many aspects in stitched composite are not clearly understood. This is due to the fact that systematic and detailed studies have not been carried out, and clear justification has not been made. The need to construct a deeper understanding of basic in-plane mechanical characteristics of stitched composites is what motivates this thesis.

This thesis generally aims to understand the effect of stitch parameters on in-plane mechanical characteristics and damage mechanisms of stitched carbon/epoxy composites under static and fatigue loads. Effects of various stitch parameters, namely stitch density (moderately stitched, densely stitched), stitch orientation (longitudinal stitch, transverse stitch), stitch pattern (round stitch, parallel stitch) on the properties are discussed. Two stitch materials are studied, namely Kevlar-29 and Vectran® (Kuraray). Vectran is relatively new material, which is employed to produce airbag landing for NASA's Mars Pathfinder. The strength of Vectran is comparable to that of Kevlar, which is a popular choice among through-thickness reinforcement yarns. Another advantage of Vectran is that it has very low moisture absorption that is beneficial for composites applied in wet environment. Vectran-stitched composites are studied because their basic in-plane mechanical characteristics under static and fatigue are not available in the literature. Complete characterization of Vectran-stitched composites

subjected to interlaminar tension tests (so-called ITT and DCB tests), low-velocity impact and compression-after-impact was performed by Tan [102].

In conjunction with the investigation of mechanical properties, damage mechanisms related to stitch parameters are also elucidated. Practical aspect dealing with holes in stitched composites is described in details. Analytical works in this thesis are (i) to propose robust models to predict 3-D thermo-elastic constants of stitched composites by employing asymptotic expansion homogenization method, (ii) to clarify a criterion to predict open hole tension (OHT) strength of composites, namely Average Stress Criterion (ASC). Experimental and numerical investigations pertaining to the general objective are listed below:

- Effect of stitch density on the tensile characteristics and damage mechanisms of Vectran-stitched carbon/epoxy composites
- Analytical models to predict 3-D thermo-elastic constants of stitched composites
- Effect of stitch density and stitch thread thickness on compressive characteristics and damage mechanisms of Vectran-stitched carbon/epoxy composites
- Effect of stitch density on fatigue life, stiffness reduction and fatigue damage mechanisms of Vectran-stitched carbon/epoxy composites
- Tensile characteristics and damage mechanism of Kevlar-stitched carbon/epoxy composites with and without holes by considering stitch orientation, and applicability of ASC on stitched composites
- Fatigue characteristics and damage mechanisms of Kevlar-stitched carbon/epoxy composites with holes by considering stitch pattern of round stitch and parallel stitch

1.5 Overview of the Thesis

The thesis is divided into seven chapters as follows.

Chapter 1 discusses the background and objectives of the research. Literature survey of in-plane mechanical properties of stitched composites, particularly under static tension, static compression, fatigue, spanning for more than two decades is provided. Studies on stitched composites with holes are discussed. Existing analytical methods to predict mechanical properties of stitched composites are also discussed. Objectives and overview of the thesis are also given.

Chapter 2 discusses Vectran-stitched carbon/epoxy composites under tension. Effect of stitch density on the in-plane mechanical properties as well as underlying damage mechanisms under static load is discussed. Two types of stitched composites are assessed: moderately stitched composites and densely stitched composites. Characterization of architectural changes induced by stitching process, namely fiber waviness and fiber compaction, is given. Models to predict thermo-elastic constants of stitched composites using homogenization method are given. Predicted properties of stitched composites obtained by homogenization method are compared with tensile test result.

Chapter 3 discusses Vectran-stitched carbon/epoxy composites under compression. Compressive characteristics of moderately and densely stitched composites as well as their damage mechanisms. In addition, effect of stitch thread thickness on compressive properties is also discussed. Correlation between measured fiber waviness and compressive properties is established. Damage characterization is also performed to study the detailed damage sequence in stitched composites under compression.

Chapter 4 discusses Vectran-stitched carbon/epoxy composites under fatigue. Effect of stitch density on the tension-tension (T-T) fatigue characteristics and damage mechanisms is discussed. In conjunction with Chapter 2, moderately and densely stitched composites are studied. Effect of stitch density on fatigue life, stiffness degradation and fatigue damage development is assessed.

Chapter 5 discusses Kevlar-stitched carbon/epoxy composites with and without holes under tension. Effect of stitch orientation on tensile properties and failure mechanisms is assessed. Stitch orientations are of longitudinal (parallel to loading direction) and transverse (perpendicular to loading direction) stitching. Effect of stitch debonding on failure characteristics is discussed. Normal stress distribution at the hole rim of Kevlar-stitched composites with hole is predicted using Lekhnitskii theory, and experimentally validated. The applicability of Average Stress Criterion to predict open hole tension strength of stitched composites with holes is investigated.

Chapter 6 discusses Kevlar-stitched carbon/epoxy composites with holes under fatigue. Three cases are experimentally studied in this chapter: (i) tension-tension (T-T) fatigue life and damage mechanism of stitched composites with round stitch (encircling the hole), (ii) T-T fatigue life and damage mechanism of stitched composites with parallel stitch, (iii) C-C fatigue life and damage mechanism of stitched composites with parallel stitch.

Chapter 7 compiles all concluding remarks from the investigation discussed from Chapter 2 to Chapter 6. Chapter 7 also gives overall conclusions on the viability of stitching as reinforcement method, and recommendations to improve the mechanical properties and damage characteristics of stitched composites.

Chapter 2

Vectran-stitched carbon/epoxy composites under tension

2.1 Overview

First part of this chapter discusses the experimental investigation of tensile characteristics and damage mechanisms of Vectran-stitched carbon/epoxy composites. Effect of stitch density on the tensile properties (tensile strength, tensile modulus, Poisson's ratio, failure strain) is evaluated. Composite specimens are unstitched, moderately stitched and densely stitched composites. Fiber waviness in composite is measured with the aid of optical microscope, and the correlation between fiber waviness and tensile properties is established. Measurement of local fiber volume fraction is performed to investigate the fiber compaction mechanism. Damage mechanisms in unstitched and stitched composites are described qualitatively and quantitatively based on acoustic emission test and X-ray radiography results. Effectiveness of stitching in composites is discussed. Second part deals with analytical models to predict 3-D thermo-elastic constants for Vectran-stitched composites utilizing asymptotic expansion homogenization method. Tensile modulus and Poisson's ratio obtained from homogenization method are compared with experimental results.

2.2 Experimental Details

2.2.1 Materials

Composite system used in present investigation is Vectran-stitched carbon/epoxy composites. Carbon is T800SC-24kf (Toray Industries), while the epoxy is XNR/H6813 Denatite (Nagase ChemteX). Stitch material used as through-thickness reinforcement is Vectran HT (Kuraray), which is a thermotropic liquid crystal polymer. A liquid crystal is categorized as 'thermotropic' if its phase transforms into either isotropic or conventional crystal at a certain range of temperature [53]. Mechanical and thermal properties of T800SC [7], XNR/H6813 [4] and Vectran [8, 78, 92] are provided in Table 2.1.

Table 2.1: Mechanical and thermal properties of carbon fiber, epoxy resin and Vectran stitch

Properties	Unit	Carbon fiber T800SC-24kf	Epoxy resin XNR/H6813	Stitch thread Vectran HT
E_L	GPa	294	8.96	75
E_T	GPa	6.50	8.96	3.00
G_{LT}	GPa	18.20	3.45	5.00
G_{TT}	GPa	6.50	3.45	5.00
ν_{LT}	-	0.32	0.35	0.30
ν_{TT}	-	0.41	0.35	0.30
σ_{ut}	MPa	5880	50	3200
ε_T	%	2.0	5.7	3.8
d_f	μm	5	-	24
ρ	g/cm^3	1.81	1.23	1.41
α_L	10^{-6}/K	-0.56	65	-4.80
α_T	10^{-6}/K	5.60	65	5.00

Fabrication of composite system is performed by Toyota Engineering Corporation using specialized method derived from the one in Ref. [119]. The fabrication is carried out by at least two processes: (i) preparation of carbon preforms (stitched and unstitched preforms), (ii) curing process. It is important to note that in between the processes measurement of fiber volume fraction of both preform and cured plate is carried out. In the first fabrication process (preparation of preforms), a base-plate with a number of surrounding pins is employed to arrange twenty layers of dry T800SC fibers. Layer or tow orientation of the preforms is $[+45/90/\text{-}45/0_2/+45/90_2/\text{-}45/0]_S$. This tow orientation is not quasi-isotropic because its in-plane layers do not have the same number of fibers in certain direction. In this case, the composite system contains 30% of 0 °, 30% of 90 °, 20% +45 ° and 20% of −45 ° tows.

To produce stitched preforms, the distance between two stitch lines (spacing, s) and the distance between two stitch knots (pitch, p) are prescribed in order to determine the stitch density (SD). SD denotes a number of stitch per unit area (unit is 1/mm^2), and can be calculated using following expression

$$SD = \frac{1}{s \times p} \tag{2.1}$$

After defining the stitch density, stitching process is performed by inserting twisted Vectran threads into the dry preforms. Linear density (μ) of Vectran thread is 200 denier (22.2 tex; 40 filaments per yarn). Vectran is selected due to its high strength and stiffness comparable to Kevlar-29, yet it has much lower moisture regain as compared to Kevlar. For instance, at 293 K (20 °C) and relative humidity of 90% , moisture regain of Kevlar is 5.4, while that of Vectran is less than 0.1. Insertion of stitch threads adopts modified-lock stitch type. The illustration of modified-lock stitch and terminologies used in stitching process can be seen in Fig. 2.1. In modified-lock stitch type, needle and bobbin threads are parallel with x-axis and y-axis, respectively. This stitch type provides orthogonal binding to the preforms that restricts a possible movement in x-, y- or both directions.

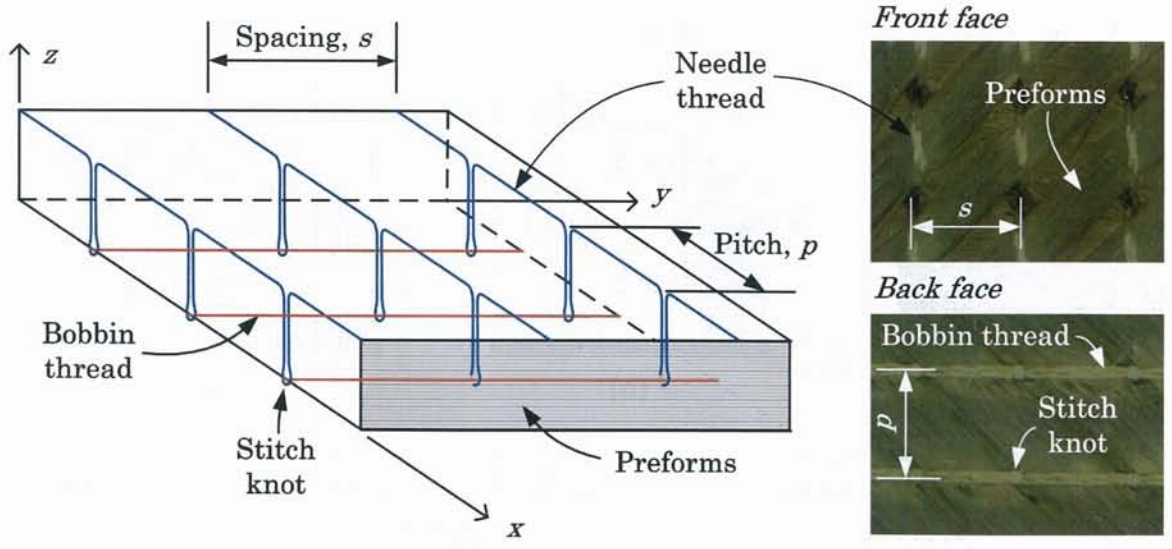

Figure 2.1: Modified-lock stitch pattern and terminologies used in stitching process

To produce unstitched preforms, similar process with the one used to fabricate stitched preforms is employed, except that some tooling adjustments are made in such a way that specified areas in the preforms are not penetrated by the stitch needles. The specified area in this regard is the dimension of unstitched test samples. Thus, the rest of the areas in the preforms contains several runs of stitch thread forming a frame-like pattern.

In the second process (curing process), epoxy resin (XNR/H6813) is infused into the carbon preforms by means of Resin Transfer Moulding (RTM) process. Epoxy is cured at 393 K (120 °C) for 2 hr and, subsequently, at 453 K (180 °C) for 4 hr. Nominal dimension of composite plate is 310 mm long and 205 mm wide with the target thickness of 4 mm.

In present experiment, three composite types are prepared based on the prescribed stitch densities, namely (i) 'unstitched' ($s = 0$, $p = 0$, $SD = 0.0$, volume fraction of stitch yarn $V_s = 0.0\%$), (ii) moderately stitched composite so-called 'stitched 6×6' ($s = 6$ mm, $p = 6$ mm, $SD = 0.028/\text{mm}^2$, $V_s = 0.088\%$), (iii) densely stitched composites so-called 'stitched 3×3' ($s = 3$ mm, $p = 3$ mm, $SD = 0.111/\text{mm}^2$, $V_s = 0.350\%$). V_s can be calculated using following formula

$$V_s = \frac{2A_s}{s \times p} \tag{2.2}$$

where A_s is a cross-sectional area of the stitch thread. A_s is determined from the area measurement of stitch cross-section obtained from optical microscopy. Composite specimens used in this experiment can be seen in Fig. 2.2, where it displays unstitched, stitched 6×6 and stitched 3×3 specimens.

2.2.2 Fiber volume fraction measurement

As mentioned in Section 2.2.1, fiber volume fraction was measured for preforms and cured plates of three specimen types. The measurement was performed by Toyota Engineering

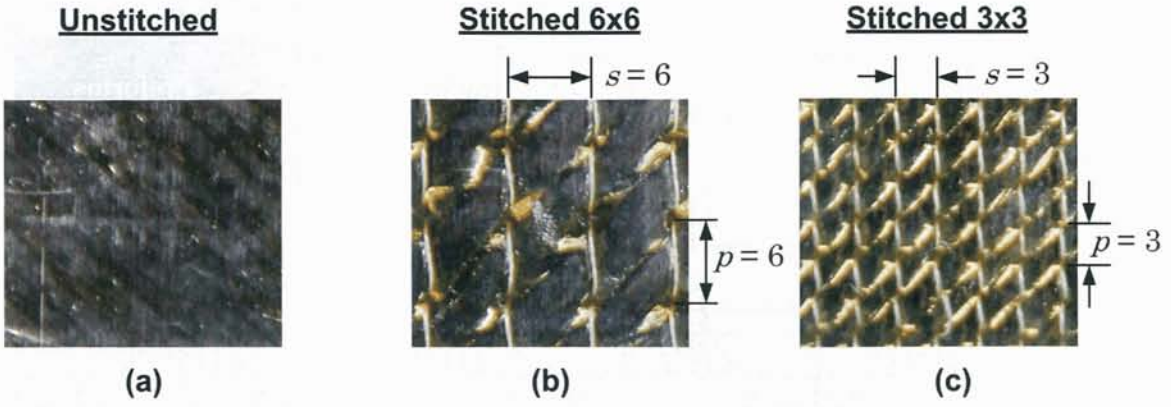

Figure 2.2: Composite types used in static tension tests: (a) unstitched, (b) stitched 6×6 (moderately stitched composites), (c) stitched 3×3 (densely stitched composites) (dimension in mm)

Corporation as well. Preform is called 'pre-RTM specimen', while cured plate is called 'post-RTM specimen'. Fiber volume fraction of pre-RTM specimens (V_{fp}) is calculated using following expression

$$V_{fp} = \frac{w_p}{\rho_f lwt} \tag{2.3}$$

where w_p and ρ_f are the measured weight of the preform and the density of fiber, respectively. w_p is given in Table 2.2, while ρ_f is already given Table 2.1. Length (l), width (w) and thickness (t) were obtained by measuring the dimension of the pre-RTM specimen. Thickness was measured on nine measurement points described in Fig. 2.3. These points are denoted as A1, A2, A3, B1, B2, B3, C1, C2 and C3. V_{fp} can then be calculated using Eq. (2.3), and the result is shown in Table 2.2. V_{fp} for unstitched, stitched 6×6 and stitched 3×3 is $50.2 \pm 0.6\%$, $49.2 \pm 0.4\%$ and $52.2 \pm 0.3\%$, respectively.

Measurement of fiber volume fraction for post-RTM specimens (V_f) was carried out using density method. Dimension of composite plate, including length, width and thickness, was first measured. Thickness of post-RTM specimen was obtained by averaging the thicknesses measured from the nine points described above. In addition, weight of the specimen in open air (W_a) and under the water (W_w) was measured. V_f is calculated using following expression

$$V_f = \frac{\rho_c - \rho_r}{\rho_f - \rho_r} \tag{2.4}$$

where ρ_c and ρ_r are density of composite plate and density of resin, respectively. ρ_r is density of epoxy, and can be obtained from Table 2.1. ρ_c is estimated by dividing weight of composite plate in the water (W_w) with its volume, and it is obtained by following equation

$$\rho_c = \frac{W_a \rho_w}{W_a - W_w} \tag{2.5}$$

V_{fp} for post-RTM specimen can be seen in Table 2.3. V_{fp} for unstitched, stitched 6×6 and

stitched 3×3 is 53.3 ± 0.3%, 53.8 ± 0.4% and 54.3 ± 0.2%, respectively.

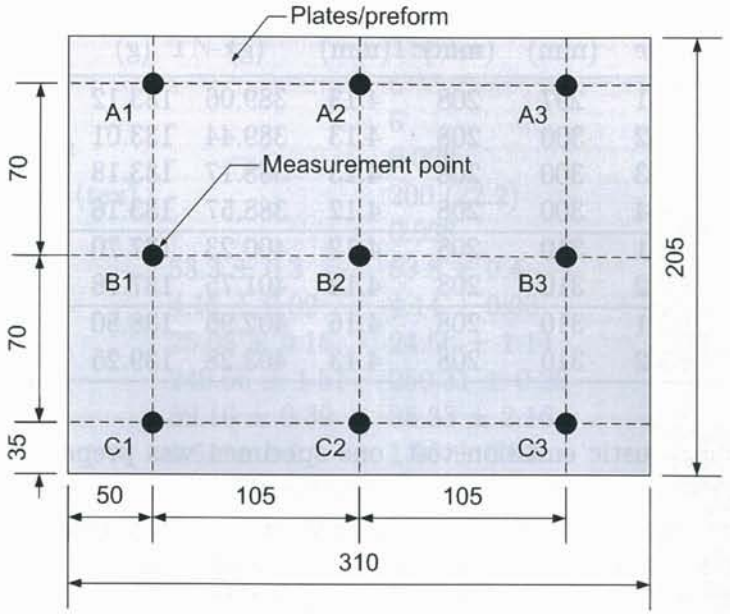

Figure 2.3: Location of thickness measurement points for pre- and post-RTM specimens (dimension in mm)

Table 2.2: Fiber volume fraction of preforms (pre-RTM specimen)

Type	Plate code	l (mm)	w (mm)	t (mm)	w_p (g)	V_{fp} (%)	V_{fp} (Avg.) (%)
Unstitched	F1-1	305	210	4.43 ± 0.20	260	50.6	50.2 ± 0.6
	F1-2	305	210	4.47 ± 0.23	260	50.1	
	F1-3	305	210	4.52 ± 0.23	260	49.5	
	F1-4	305	210	4.42 ± 0.19	260	50.7	
Stitched 6×6	F2-1	321	215	4.38 ± 0.07	271	49.5	49.2 ± 0.4
	F2-2	320	216	4.44 ± 0.04	272	48.9	
Stitched 3×3	F3-1	320	217	4.18 ± 0.07	276	52.4	52.2 ± 0.3
	F3-2	320	218	4.21 ± 0.04	277	52.0	

2.2.3 Tensile test specimens

Test specimens were prepared by cutting post-RTM specimen using water-cooled cutting machine AC-400CF (Maruto). Cutting direction is in-line with the direction of stitch needle threads, which is the loading direction as well. Nominal dimension of test specimen is 250 mm long and 25 mm wide, which adopts the standard test specimen recommended by SACMA SRM 4R-94 [12] (see Fig. 2.4). After the cutting process, edges of test specimen were polished three sequential times using rough (grit #500), moderately smooth (grit #1000), and very smooth (grit #1200) rotating abrasive papers. At least three test specimens were prepared

Table 2.3: Fiber volume fraction of cured plates (post-RTM specimen)

Type	Plate code	l (mm)	w (mm)	t (mm)	w_a (g)	w_w (g)	V_f (%)	V_f (Avg.) (%)
Unstitched	F1-1	297	208	4.13	389.06	133.12	53.2	53.3 ± 0.3
	F1-2	300	208	4.13	389.44	133.01	53.3	
	F1-3	300	208	4.13	388.17	133.18	53.6	
	F1-4	300	208	4.12	388.57	133.16	53.4	
Stitched 6×6	F2-1	310	208	4.12	400.23	137.70	54.0	53.8 ± 0.4
	F2-2	310	208	4.14	401.75	137.78	53.5	
Stitched 3×3	F3-1	310	208	4.16	402.95	138.80	54.1	54.3 ± 0.2
	F3-2	310	208	4.13	403.28	139.25	54.4	

for tensile test. For acoustic emission test, one specimen was prepared, while for damage characterization, three test specimens were prepared for each specimen type. Table 2.4 shows the detail specification of test specimens including code, dimension, physical property and quantity of samples for each test. Specimen codes for unstitched, stitched 6×6 200d and stitched 3×3 200d are TN-x, TS62-x and TS32-x, respectively, whereby x denotes sample numbering.

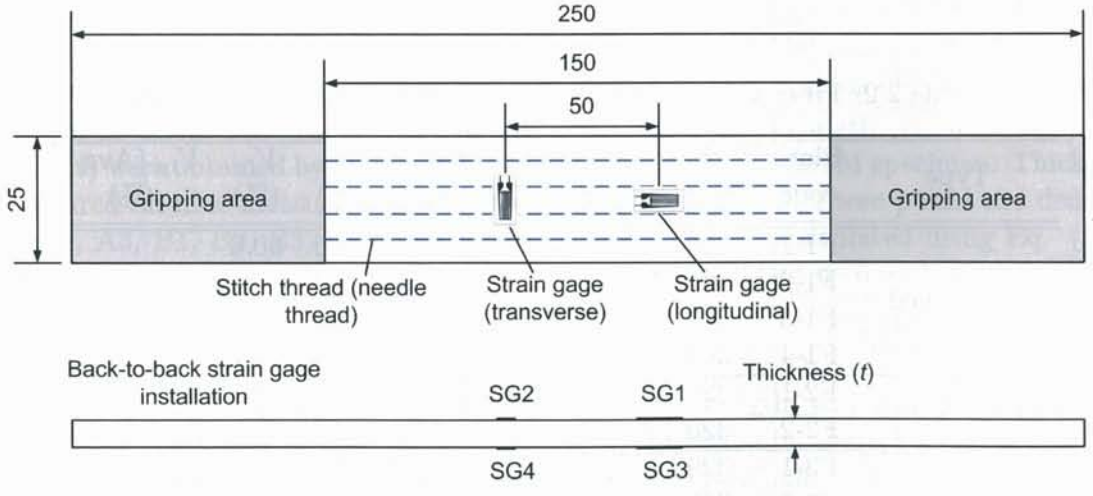

Figure 2.4: Tensile test specimen (dimension in mm)

2.2.4 Tensile test procedures

Tensile test was carried out using servo-hydraulic machine *Instron 8802* that has load cell capacity of 100 kN (maximum tension). Loading rate applied during tensile test was 1 mm/min. The test specimens used no tabs during the test. Instead, wedge grips, which are capable of preventing the specimen slippage during the test, were employed. Environment setting was set at room temperature of 293 K (20 °C). Personal computer containing *Wave Logger* software (Keyence) was used to register load and displacement data. Stress is evaluated by dividing the load with gross area (width × thickness) of the test specimen, while strain is

Table 2.4: Specification of test specimens for tension test

Parameter	Unit	Unstitched	Stitched 6×6 200d	Stitched 3×3 200d
Code	-	TN-x	TS62-x	TS32-x
s	mm	-	6	3
p	mm	-	6	3
SD	$1/mm^2$	-	0.028	0.111
μ	denier (tex)	-	200 (22.2)	200 (22.2)
V_s	%	-	0.088	0.350
V_f	%	53.3 ± 0.3	53.8 ± 0.4	54.3 ± 0.2
t	mm	4.15 ± 0.02	4.14 ± 0.03	4.17 ± 0.03
w	mm	25.05 ± 0.15	24.56 ± 1.14	24.76 ± 0.17
l	mm	249.56 ± 1.51	250.31 ± 0.26	250.0 ± 0.0
W	g	39.16 ± 0.39	38.33 ± 2.16	38.90 ± 0.47
ρ	g/cm^3	1.51 ± 0.0	1.50 ± 0.01	1.51 ± 0.01
		3 (tensile test)	3 (tensile test)	4 (tensile test)
Quantity	pcs.	1 (AE test)	1 (AE test)	1 (AE test)
		3 (X-ray)	3 (X-ray)	3 (X-ray)

measured using four strain gages (Kyowa) in back-to-back configuration (see Fig. 2.4). Distance between two strain gages is 50 mm. This distance provides sufficient clearance between two strain gages, and easy guidance across all samples. Two strain gages (SG1 and SG3) are used to record longitudinal strains, whilst the others (SG2 and SG4) are used to record transverse strains. Strain values displayed in the stress-strain curve were the averaged values of two strain gages.

From the tensile test, stress-strain curves as illustrated in Fig. 2.5a were obtained. Mechanical properties obtained from stress-strain curves are static tensile strength (σ_{ut}), failure strain (ε_f), tensile modulus (E_x) and Poisson's ratio (ν_{xy}). Data reduction process to evaluate those properties can be reviewed in Ref. [12]. Maximum point of the stress-strain curve is σ_{ut} that is obtained by dividing the maximum load with gross area of specimen. The corresponding strain with respect to σ_{ut} is ε_f. E_x, also known as initial modulus, is calculated by following equation

$$E_x = \frac{\sigma_2 - \sigma_1}{\varepsilon_{L2} - \varepsilon_{L1}} \tag{2.6}$$

where ε_{L1} and ε_{L2} are 0.1% and 0.3%, respectively, while σ_1 and σ_2 are their corresponding stresses. ε_L is an average value of two longitudinal strain gages attached back-to-back in the specimen. To obtain Poisson's ratio ν_{xy}, Fig 2.5b can be referred to, and following equation can be employed

$$\nu_{xy} = \frac{-\varepsilon_{T2} - \varepsilon_{T1}}{\varepsilon_{L2} - \varepsilon_{L1}} \tag{2.7}$$

where, ε_{L1} and ε_{L2} are 0.1% and 0.3%, respectively. ε_{T1} and ε_{T2} are the corresponding strains obtained from transverse strain gages.

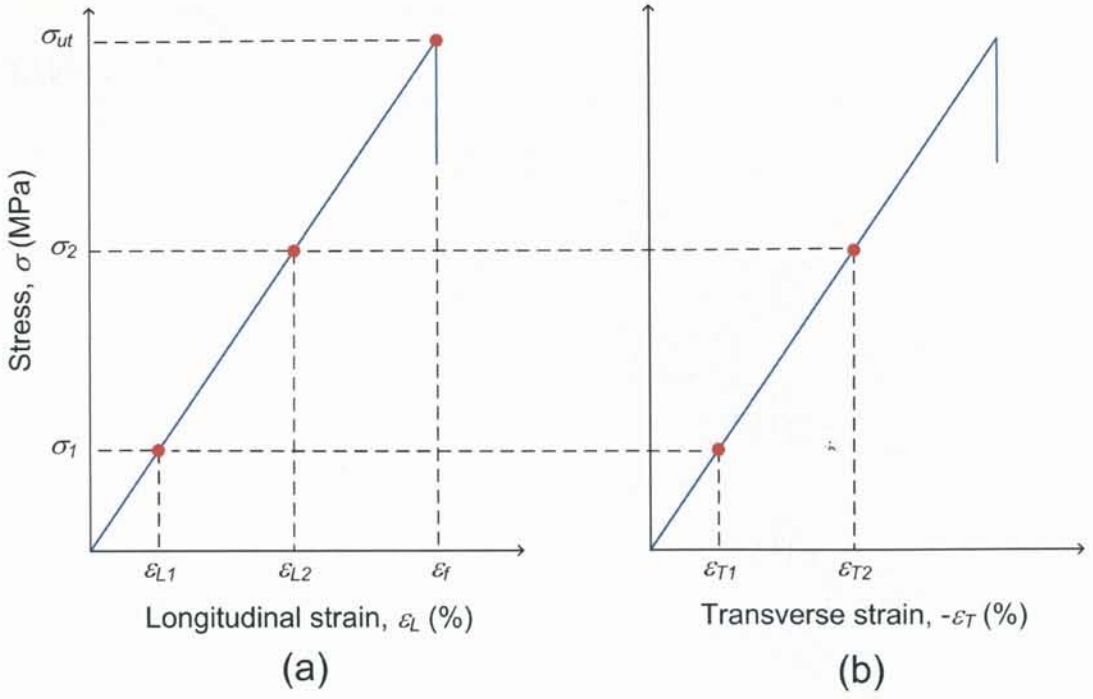

Figure 2.5: Schematic of (a) stress and longitudinal strain, (b) stress and transverse strain

2.2.5 Damage characterization procedures

Acoustic emission test

Damage characterization for unstitched and stitched composites under static tension is firstly carried out by acoustic emission (AE) test. AE test is performed to specifically monitor the damage accumulation by capturing transient waves emitted by rapid strain energy release generated by the development of damage modes in composites, namely delamination, matrix cracking, fiber breakage, etc. The particular objective in present AE test is to understand the effect of stitch density on the damage activity within composites. It seeks to answer the following question: how stitch density may affect the damage stages and accumulation in composites during static tensile test. AE test is formally proposed by Lomov et al. [75] to be included in the study of damage initiation and development in textile composites. As shown in Fig. 2.6, AE test was done by mounting two AE sensors (Channel 1 and Channel 2) onto the surface of the specimen in a linear configuration. Resonant frequency of the sensor is 150 kHz (PAC R15I). The distance between two sensors is 80 mm. To improve sound energy transmission between sensors and the specimen, a couplant material, i.e. vacuum sealing compound (Shin-Etsu Silicone), is also applied to the interface between sensors and the specimen [105]. AE hit threshold is 60 dB, a limit where transverse crack or delamination is commonly detected by AE sensors [99]. The specimen is then tensioned until it fails, while AE data (AE hit, AE count, AE energy, duration, frequency, amplitude, etc.) recorded by two AE sensors is registered and processed using Samos AE System (Physical Acoustic Corp.).

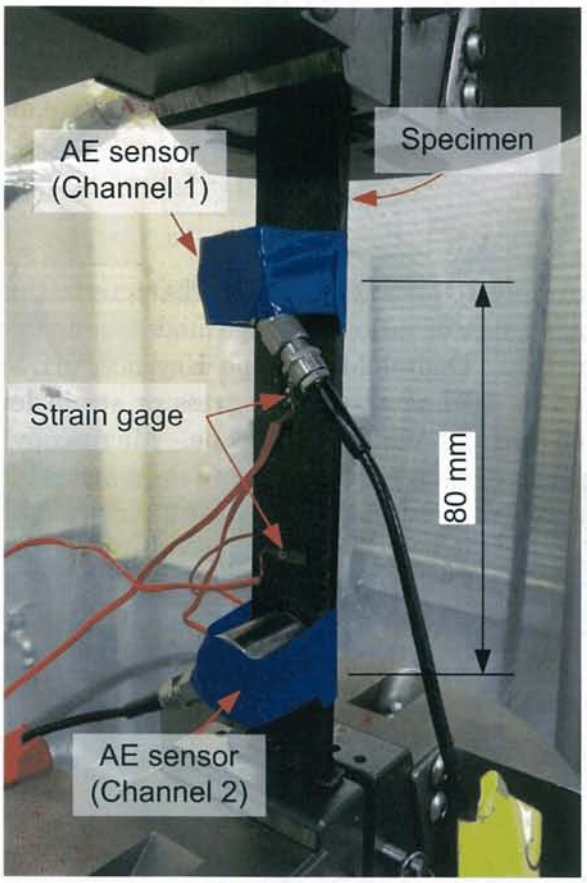

Figure 2.6: AE test setup: positioning of AE sensors on the specimen

Interrupted test and X-ray radiography

Damage characterization was also performed by conducting interrupted test and X-ray radiography. This damage characterization aims at identifying the damage modes as observed from X-ray images, and analyzing the growth of damage modes in qualitative and quantitative manners. Interrupted test was carried out by testing the specimen under static tension with a loading rate of 0.5 mm/min. The test was halted at several strain levels of 0.5%, 0.6%, 0.7%, 0.8%, 1.0% and 1.2%. Test specimen was removed from the testing machine. Zinc Iodide (ZnI) penetrant was then applied to the edges, front and back faces of the specimen in order to enhance the contrast of the damage. To obtain X-ray image, the specimen was subsequently exposed to the soft X-rays by employing Softex SV-100AW machine. The setting for X-ray radiography process was 17.5 kVp (maximum voltage applied across an X-ray tube), 1.5 mA (current used to generate X-rays) and 8 min (exposure time). The trace of damages in the specimen was then printed on negative film (Envelopak IX, Fujifilm Industry). Analog-to-digital image conversion was done by using Epson GT-X970 dual-lens scanner with a resolution of 2400 dots per inch. After digital image of X-ray had been obtained, qualitative assessment of damage was performed by identifying the damage modes, categorizing the damage modes, monitoring the growth of each damage mode. Monitoring the growth of damage stage-by-stage aims at giving general insight on how the damage may

initiate, how the stitches may affect the damage mechanisms in composites and how the damage mode may interact one another. Quantitative damage assessment is subsequently performed by measuring/counting and evaluating the growth rate of each damage mode.

Optical microscopy

Optical microscopy is performed to assist the damage characterization by X-ray radiography. It aims to provide a magnified view of various damage modes found in composites. The optical microscopy is carried out using Digital Microscope Keyence VHX-900. After a specimen had been subjected to tensile loading at certain stress or strain level, and prior to X-ray radiography, the specimen was put under microscope. Microscopy images of the surfaces and edges of the specimen were obtained using digital data acquisition system. The type of damage, for instance transverse crack, and its corresponding growth was noted.

2.2.6 Local fiber volume fraction measurement

Overview of fiber compaction mechanism

One of the drawbacks of stitching process is that the fiber tows of the preforms are locally compacted. The so-called compaction mechanism due to stitching results in a local increase of fiber volume fraction. Compaction mechanism and its possible relation with mechanical properties of stitched composites is first coined by Mouritz and Cox [82]. To give a better understanding of the compaction mechanism during stitching process Fig.2.7a can be reviewed. It illustrates the schematic of $(0\,°/90\,°/0\,°)$ tows before and after stitch insertion. Before the insertion of stitch thread, fiber tows are assumed straight and possess 'lower V_f'. After the insertion of stitch thread, the tows are halved, and each one-half move sideways due to, primarily, tensioning force applied during stitching process. The tow region adjacent to the stitch thread is the most compacted region, in which the gap among fibers becomes narrow ('higher V_f'). Compaction of fibers due to stitching process is further enhanced by curing process, e.g. RTM. During RTM process, stitched preforms are permeated by resin, and compressed (pressurized) to ensure proper resin infiltration and dimensional similarity, i.e. similar thickness, across all batches of stitched composite plates. Thus, the tow region adjacent to the stitch thread, which is already compacted, is even more compacted after RTM process. Fig.2.7b shows the cross-sectional view of $0\,°$ tows in stitched composites after RTM process. It shows that in the region adjacent to the stitch threads (or between two stitch lines), fiber compaction is apparent. Within this region, the gap among fibers becomes extremely narrow. Due to this reason, the fiber volume fraction in this vicinity is locally increased. Based on this observation, local fiber volume fraction (V_{fl}) of stitched composite would therefore be slightly higher than that of unstitched composites. In present study, it is proposed that V_{fl} between two stitch lines could be used as an indicator for the existence of fiber compaction mechanism in stitched composites.

When fiber compaction is experienced by off-axis tows, e.g. $90\,°$, early crack initiation may occur. Thus, in this thesis, it is also proposed that fiber compaction is considered the plausible reason for early initiation and rapid development of cracks in stitched composites. The

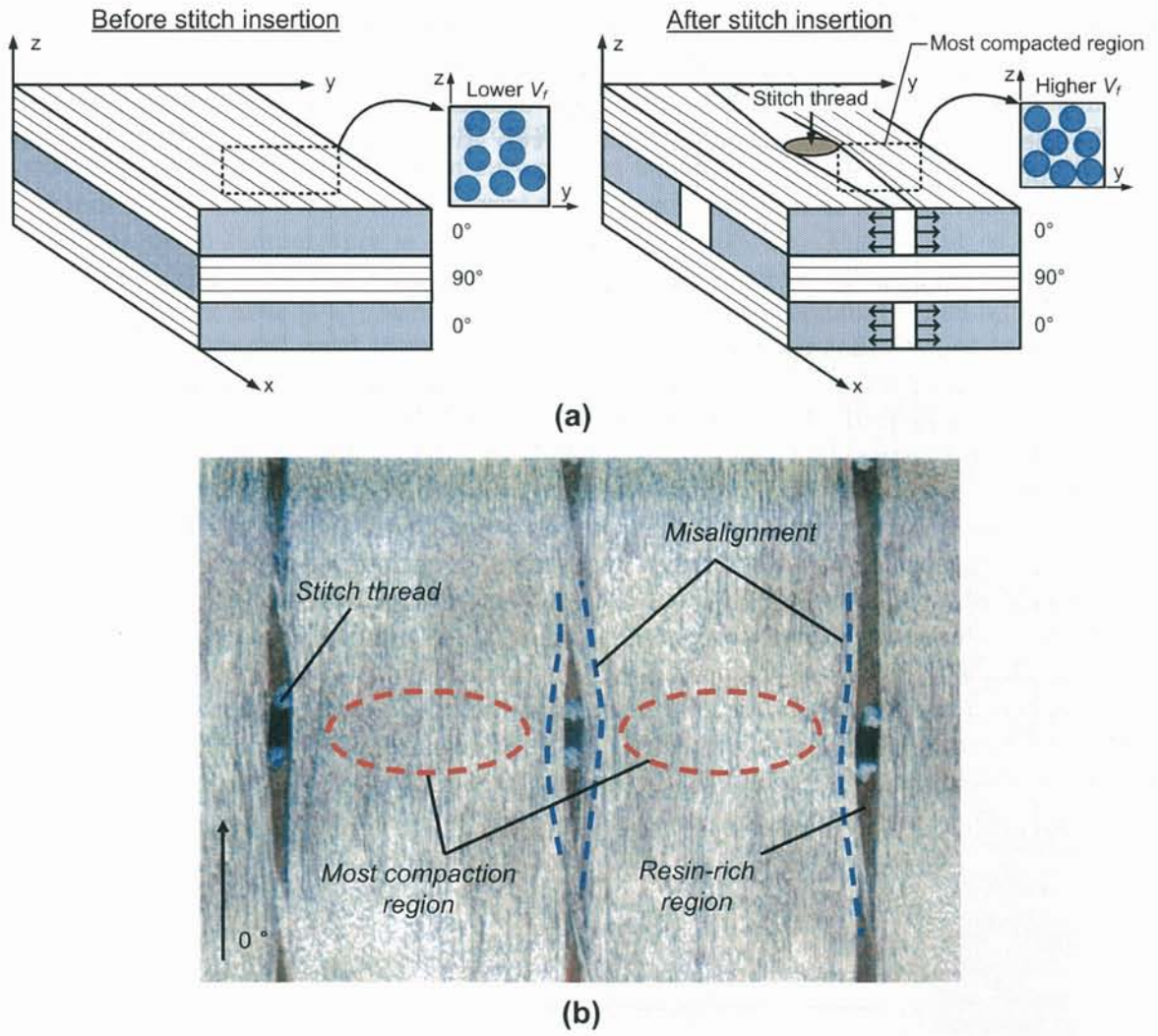

Figure 2.7: (a) Schematic of fiber compaction process before and after stitch insertion, (b) cross-sectional view of compaction between stitch threads

mechanism follows this process: when a fiber tow is compacted, the gap between fibers within the tow is reduced. As such, stress concentration in the matrix phase among fibers is high, and fiber/matrix debonding easily occurs. The coalescence of a number of fiber/matrix debondings may induce interfiber breakage, and causes rapid development of off-axis cracks. The failure process at fiber/matrix interface has actually been investigated by Hobbiebrunken et al. [58], and they suggested that the microscopic stresses in fiber/matrix interface are influenced by the distance between fibers, difference of CTE between fiber and matrix, fiber diameter, fiber shape, relative position between fibers and matrix yield stress. In present case, distance between fibers is a parameter that is greatly influenced by the stitching process through compaction mechanism. Nonetheless, report of the quantification of V_{fl} in stitched composites is very limited. The earliest V_{fl} measurement is probably conducted by Weimer and Mitschang [115]. They measured V_{fl} around stitch holes, and found that V_{fl} is relatively low. Their results did not, however, reflect the compaction mechanism due to following reason: the V_{fl} measurement was only performed on the samples containing higher

amount of resin, which are obtained from a region around stitch penetration holes (resin-rich region). Beyond the measurement done by Weimer and Mitschang, V_{fl} measurement, especially between two stitch lines, has not been available in literature. Following sections describe the detail of V_{fl} measurement between two stitch lines by two methods: burn-off test and optical microscopy.

Burn-off test

It is important to note that the measurement of V_{fl} is different from the measurement of V_f described in Section 2.2.2. V_{fl} in this part is obtained by conducting burn-off test that adopts JIS Standard K 7079-1991 (Testing Methods for Fibre Content and Void Content of Carbon Fiber Reinforced Plastics) [9]. The method consists of weight measurement of sample, burn-off of the sample using fire flame, re-measurement of the remaining sample and calculation of volume fraction. However, the sample size does not comply with the one specified in Ref. [9]. The sample size, especially for the stitched composites, is customized to facilitate the present V_{fl} measurement. As shown in Fig. 2.8, sample was cut between two stitch lines, and it only includes volumetric section where compaction effect would likely to occur. Width of the sample is smaller than the stitch spacing (s). It should be mentioned here that the sample does not include needle and bobbin threads. For unstitched and stitched 6×6 specimens, length of the sample is 10 mm, width is 4.4 mm and thickness is 4 mm. For stitched 3×3, because the spacing is only 3 mm, width of sample is 2.1 mm.

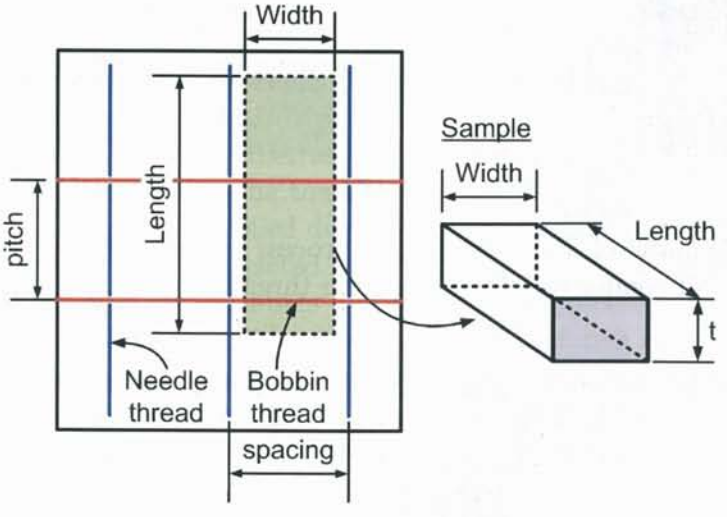

Figure 2.8: Sample for V_{fl} measurement by burn-off test

Three to five small samples were prepared from two batches of each specimen type. The samples were weighed in open-air condition and under the water using specific gravity measurement kit (Shimadzu SMK-01). The temperature of the water was 297 K (24 °C) and density of water (ρ_w) was determined from the look-up table ($\rho_w = 0.997296$ g/cm^3). The sample was subsequently wrapped using Nickel Chromium (NiCr) wire with melting temperature of 1673 K (1400 °C) to ensure that it was still intact during burning process. The diameter of NiCr wire is 0.23 mm. The wrapped sample was weighed again in open-air condition. After the weight measurement process, the wrapped sample was tied to an additional

100 mm-long NiCr string. Metal tweezer was used to hold the NiCr string, and the sample was then burned using Piezo gas torch lighter (GT Prinee 8000) under fume hood. It is noteworthy that the fire flame coming out of the gas torch usually consists of two parts: outer flame and inner flame. The sample is burned by the tip of inner flame. After the burning process, the remains, which consist of only carbon fibers, were put on the ceramic plate. It is important to note that carbon fibers were not decomposed during burn-off process because its decomposition temperature is as high as 3773 K (3500 °C). The weight of the remains including the NiCr wire was measured. After the measurement and burning process, local volume fraction of fiber (V_{fl}), resin (V_{rl}) and void (V_{vl}) were evaluated based on the formula given in Ref. [9].

Optical microscopy

Second measurement of V_{fl} is performed with the aid of digital microscope (Nikon Eclipse MA200). Two samples with dimension of 18 mm long and 18 mm wide are cut from each specimen type (unstitched, stitched 6×6 and stitched 3×3). The edges of sample are polished using rotating abrasive papers. The sample edges, specifically in 90 ° tow, are then observed under optical microscope with the magnification of up to 2000×. Several images of fiber arrangement in 90 ° tows are obtained. The measurement of V_{fl} is done by measuring the area of the fibers occupying a selected region, and dividing the total fiber area with the area of the region. The result of V_{fl} measurement obtained by optical microscopy is compared with that obtained by burn-off test.

2.2.7 Fiber waviness measurement

Description of fiber waviness

Fiber waviness is defined as a local deviation of fibers with respect to their predetermined axis. Fibers appear wavy, and the waviness is often approximated by sinusoidal function. Fiber waviness differs from fiber misalignment. In the latter, fibers deviate from proper alignment of the whole laminates. Fiber waviness is a processing defect that affects the mechanical performance of composites, especially under compression, and the magnitude of thermal expansion coefficients. Fiber waviness is mainly caused by dimension of specimen, cooling rate and tool plate materials during curing process [71]. In present study, wavy fiber tows are also found in both unstitched and stitched composites. The direction of waviness can be in-plane and out-of-plane. Photomicrographs of out-of-plane waviness and in-plane waviness of on-axis fiber tows (0 ° tows) can be seen in Figs. 2.9a and 2.9b, respectively. Fig. 2.9a is a cross-sectional view of composite in $x - z$ plane with pre-determined observation length (l) and thickness (t), while Fig. 2.9b is cross-sectional view of 0 ° tow of stitched composite in $x - y$ plane.

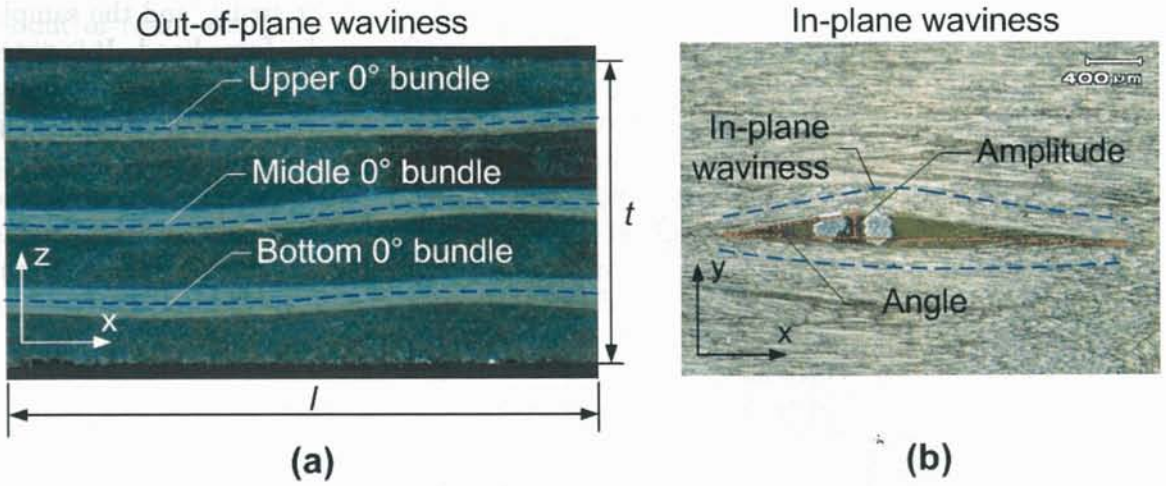

Figure 2.9: (a) Out-of-plane waviness, (b) in-plane waviness

Measurement of out-of-plane and in-plane waviness

In present study, observation of waviness in both directions is carried out using optical microscope. Based on the optical microscopy images, two parameters are introduced to represent the waviness, namely waviness amplitude and waviness angle. Four parameters are measured, namely out-of-plane waviness amplitude (a_{out}), out-of-plane waviness angle (ϕ_{out}), in-plane waviness amplitude (a_{in}) and in-plane waviness angle (ϕ_{in}).

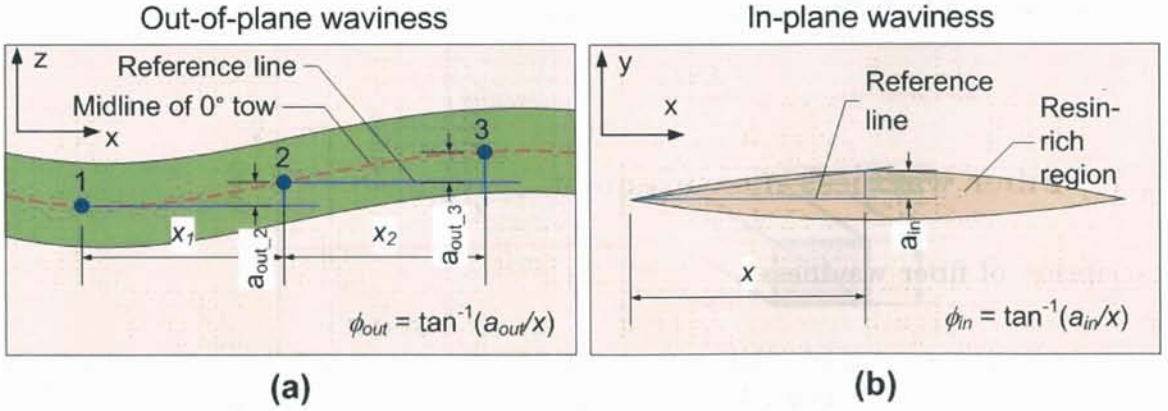

Figure 2.10: Measurement method for (a) out-of-plane waviness, (b) in-plane waviness

As illustrated in Fig. 2.10a, a_{out} is measured by discretizing 0 ° tow image using points made in the centerline of the tow. It is important to note that the measurement of waviness was performed on 0 ° tow only because the mechanical properties of composites under tension are mainly controlled by the degree of waviness in this on-axis tow. In each specimen there are six 0 ° tows (three tows seen on the right edge and three tows seen on the left edge). Observation length (l) is approximately 10 mm. Each fiber tow is then divided into ten segments. Thus, there are eleven points in each tow, and the distance between two points is 1 mm. As an illustration, three points are shown in Fig. 2.10a. The first point, indicated as '1', is a reference point which defines $x = 0$ and $z = 0$. The waviness amplitude in out-of-plane

direction (a_{out_2}) is calculated as a vertical distance between point-2 and point-1 (y_2 - y_1). It should be noted that a_{out_1} is zero. ϕ_{out_2} is calculated from the tangent of waviness amplitude with respect to the distance between point-1 and point-2. Formula to calculate ϕ_{out} is given in Fig. 2.10a. For out-of-plane waviness parameters, there are 66 waviness amplitudes and 60 waviness angles obtained from each specimen. Waviness amplitude and angle are measured in two samples for each specimen types, which means that 252 data are available for the assessment of out-of-plane waviness for each specimen type.

Nomenclatures for the measurement of in-plane waviness amplitude and angle are shown in Fig. 2.10b. At least two samples are cross-sectioned in $x - y$ plane, specifically in $0°$ tow. In each sample, there are at least six resin-rich regions in stitched 6×6 samples and 15 resin-rich regions in stitched 3×3 samples. This resin-rich region contains two stitch threads. a_{in} is obtained by measuring the distance between the waviness peak and the reference line. Correspondingly, ϕ_{in} is defined as a tangent between amplitude and the distance between projected point and the starting point in reference line. In every resin-rich region, only maximum values of amplitude and angle waviness are measured. There are approximately 96 data points comprising amplitude and angle that are available for the assessment of in-plane waviness.

Calculation of combined waviness

As described above, four parameters are obtained from the waviness measurement, namely a_{out}, ϕ_{out}, a_{in} and ϕ_{in}. In this thesis, two new parameters representing combined effect of waviness are proposed, namely combined waviness amplitude (a_{com}) and combined waviness angle (ϕ_{com}). a_{com} is obtained by following equation

$$a_{com} = \sqrt{(a_{out})^2 + (a_{in})^2} \tag{2.8}$$

ϕ_{com} is obtained by following equation

$$\phi_{com} = \sqrt{(\phi_{out})^2 + (\phi_{in})^2} \tag{2.9}$$

Based on formulae above, correlation between combined waviness and mechanical properties (tensile modulus in this chapter, and compressive strength in Chapter 3) will be made.

2.3 Experimental Results and Discussion

2.3.1 Stress-strain curves

Stress-strain curves of unstitched, stitched 6×6 and stitched 3×3 carbon/epoxy composites subjected to static tensile loading are shown in Fig. 2.11. In general, stress-strain curves of three composites exhibit linearity prior to peak stress, except that at higher strain values, the curves are slightly inflected due to several reasons: (i) crack growth in off-axis tows, (ii) initiation of delamination at the specimen edges, (iii) detachment of strain gages from

the specimen. Unstitched specimens (TN-1, TN-2, TN-3) show similar stress-strain curves despite the fact that, for example, TN-1 and TN-2 exhibit a softening at $\varepsilon = 1\%$. Stitched 6×6 and stitched 3×3 specimens exhibit more diverse curves amongst specimens. For example, TS62-4 curve exhibits higher gradient, i.e. stiffer, than that of TS6-1, TS62-2 or TS62-3. In stitched 3×3 cases, as the stress reaching maximum level, TS32-3 seems to be softer than TS32-1 or TS32-3. This behavior is probably influenced by the characteristic location where the strain gage is attached. Stitched specimens exhibit different surface characteristic. In stitched specimens, the strain gages are usually attached on thick resin-rich layer or resin-rich region. These regions are inevitable effect of stitching process. In this region, the strain values tend to be higher than the ones obtained in unstitched specimens. Furthermore, when the cracks appear in thick resin layer of stitched specimens, the strain gages happen to be above the cracks are easily detached, especially at higher stress level. Unstitched specimens, on the other hand, display no resin-rich region, and thin resin layer. Thus, the strain values in unstitched specimens are relatively more consistent than the ones obtained in stitched specimens.

2.3.2 Secant modulus

From the stress-strain curves shown in Fig. 2.11, secant modulus is obtained in order to show the trend of instantaneous tensile stiffness E_i during the test. E_i can be calculated by following equation

$$E_i = \frac{\Delta\sigma}{\Delta\sigma} = \frac{(\sigma_{i+1} - \sigma_i)}{(\varepsilon_{i+1} - \varepsilon_i)} \tag{2.10}$$

The strain interval of 0.1% is defined between ε_i and ε_{i+1}, and the corresponding stresses of σ_i and σ_{i+1} are obtained accordingly. E_i of all specimens is obtained, and normalized with average E_i of unstitched composites (E_{un}). E_{un} is 52.2 GPa. Normalized secant modulus E_i/E_{un} is averaged for each specimen type, and the average E_i/E_{un} of respective material type can be seen in Fig. 2.12. It is evident that in the beginning the secant modulus of stitched 6×6 and stitched 3×3 is already lower than that of unstitched composites. This indicates that stitching reduces tensile modulus of composites. The inflection point in normalized secant modulus is also identified. Inflection point is the onset of stiffness drop, which can be followed by an abrupt drop as in unstitched and stitched 6×6, or gradual decline as in stitched 3×3. The stiffness drop may be related with the interaction between saturation of off-axis cracks and rapid increase of delamination. Onset of stiffness drop for unstitched, stitched 6×6 and stitched 3×3 is marked with A, B and C, respectively. As shown in Fig. 2.12, the onset of stiffness drop is identified: point A of unstitched is at σ = 585 MPa; point B of stitched stitched 6×6 point B is at σ = 500 MPa; point C of stitched 3×3 is at σ = 410 MPa.

2.3.3 Failure mode

Failure of carbon/epoxy for both unstitched and stitched composites is signified by an explosive sound due to a complete fracture of on-axis fibers. Fig. 2.13 shows the typical failure of unstitched, stitched 6×6 and stitched 3×3 under static tension. Failure mode of all specimens is characterized by an extensive amount of delamination, matrix crackings in off-axis tows,

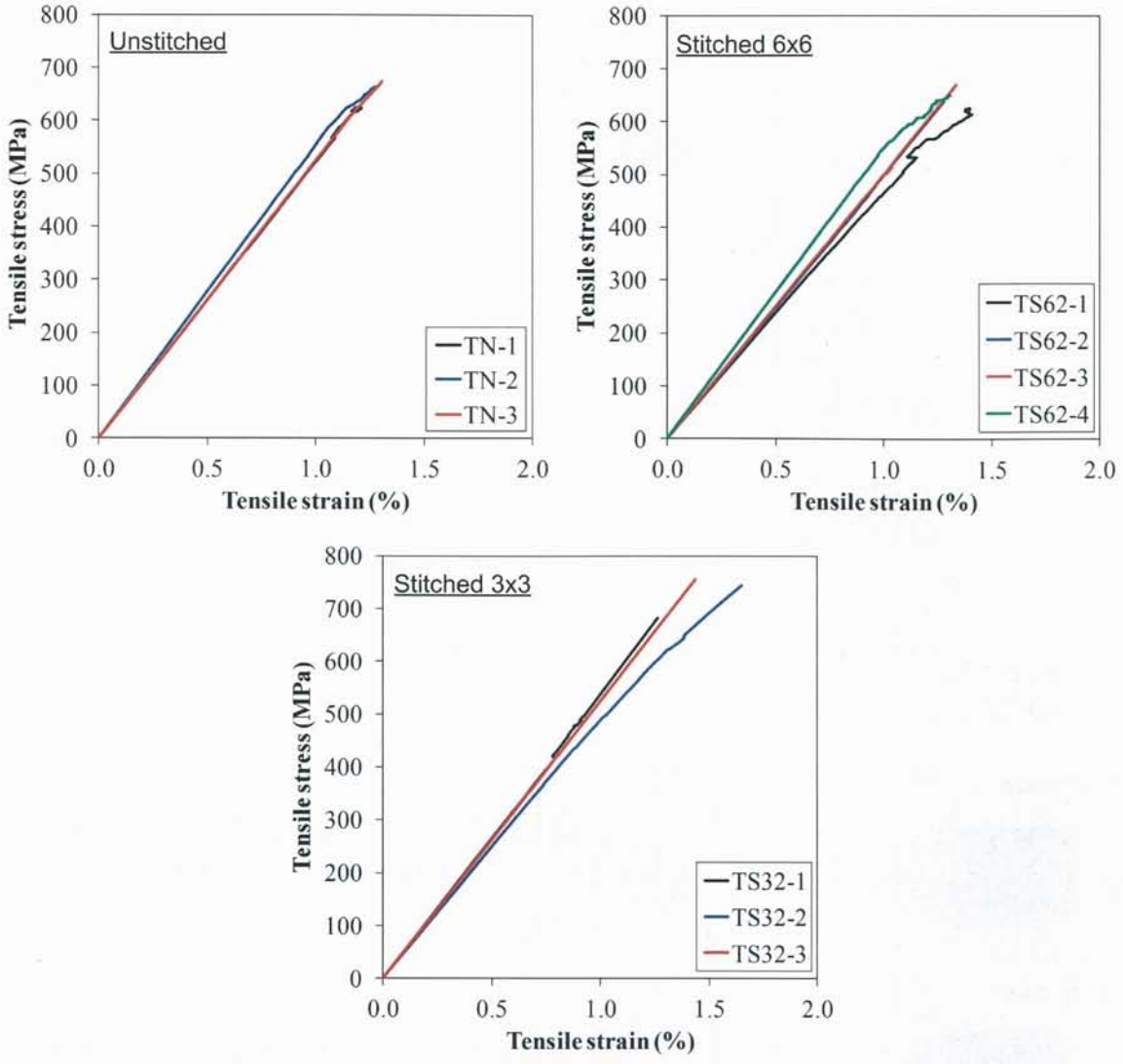

Figure 2.11: Stress-strain curves of unstitched, stitched 6×6 and stitched 3×3

fiber splitting and fiber fracture in on-axis tows. In stitched 6×6 and stitched 3×3 composites, particularly, partitioning of fiber bundles and breakage of stitch thread are evident. It is also noticed that much of the fiber tows in stitched composites, e.g. stitched 3×3, are still intact due to the binding effect provided by modified-lock stitch. This binding effect creates local 'brooming' in stitched composites. In constrast, unstitched composites fractured into two or three parts after tension.

2.3.4 Tensile properties

Tensile properties of unstitched, stitched 6×6 and stitched 3×3 are given in Table 2.5. Ultimate tensile strength σ_{ut} of unstitched, stitched 6×6 and stitched 3×3 is 654 ± 26 MPa, 645 ± 19 MPa and 722 ± 34 MPa, respectively. σ_{ut} of stitched 6×6 is 1.4% lower than that of

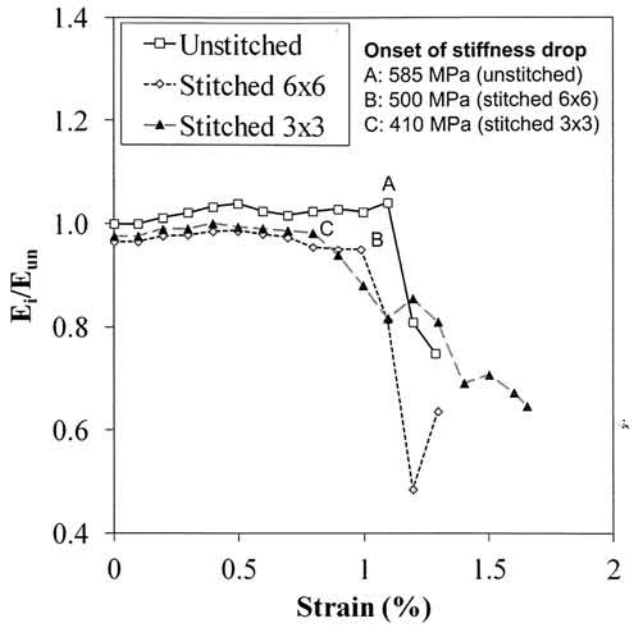

Figure 2.12: Average secant modulus of unstitched, stitched 6×6 and stitched 3×3 carbon/epoxy composites under static tension

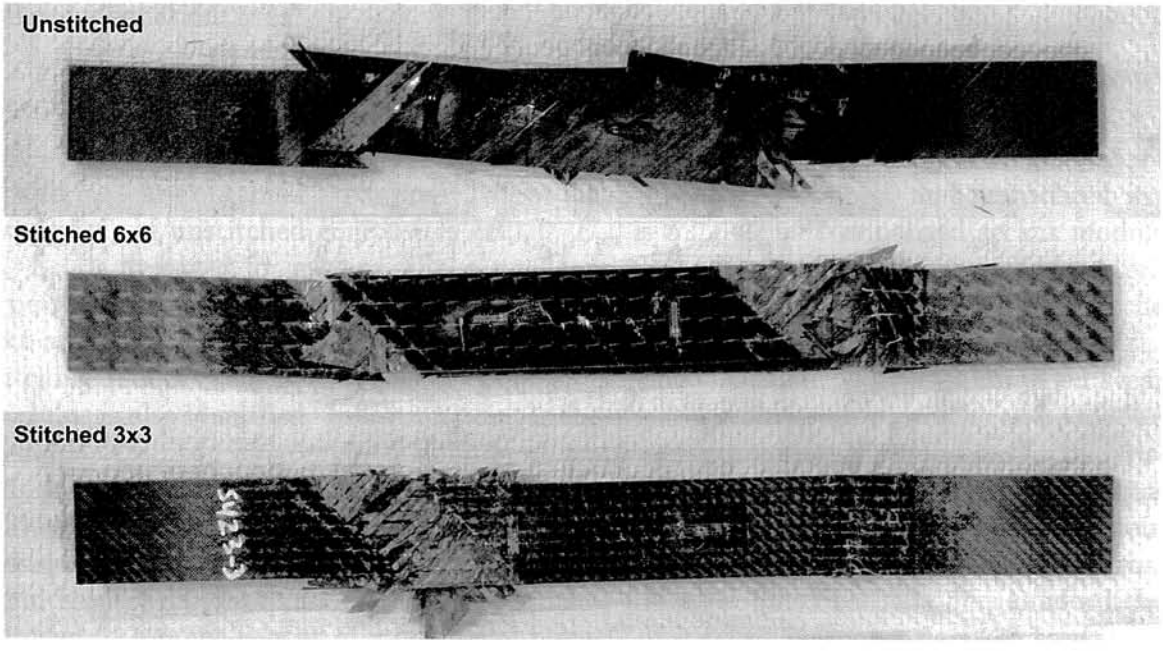

Figure 2.13: Failure of unstitched, stitched 6×6 and stitched 3×3 under static tension

unstitched composites, while stitched 3×3 exhibits 10.4% higher σ_{ut} than that of unstitched composites. Failure strain ε_f of stitched 6×6 and stitched 3×3 is 1.33% and 1.45%, respectively, and both values are higher than that of unstitched composites ($\varepsilon_f = 1.26\%$). Table 2.5 also shows that initial tensile modulus E_x of unstitched composites is 53.1 ± 1.9 GPa, while that of stitched 6×6 and stitched 3×3 is 51.1 ± 3.1 GPa and 51.7 ± 2.1 GPa, respectively. E_x

of stitched 6×6 and stitched 3×3 is 3.7% and 2.5%, respectively, lower than that of unstitched composites. The reduction of tensile modulus in stitched composites is common [67, 82, 117]. Modulus reduction is generally related to fiber waviness and change of fiber volume fraction induced by stitching process. Poisson's ratio ν_{xy} is found to be slightly affected by stitching. The largest reduction of Poisson's ratio of 5.7% in comparison to unstitched composites is experienced by stitched 6×6.

Table 2.5: Mechanical properties of unstitched, stitched 6×6 and stitched 3×3

Properties	Unit	Unstitched	Stitched 6×6	Stitched 3×3
P_{max}	kN	68.3 ± 2.0	66.8 ± 2.1	76.6 ± 2.2
d_{max}	mm	4.60 ± 0.11	4.90 ± 0.66	5.29 ± 0.59
σ_{ut}	MPa	654 ± 26	645 ± 19	722 ± 34
σ_{ut}^{n}	MPa	654 ± 26	651 ± 19	736 ± 35
ε_f	%	1.26 ± 0.06	1.33 ± 0.06	1.45 ± 0.19
E_x	GPa	53.1 ± 1.9	51.1 ± 3.1	51.7 ± 2.1
E_x^n	GPa	53.1 ± 1.9	51.6 ± 3.1	52.7 ± 2.2
ν_{xy}	-	0.333 ± 0.007	0.314 ± 0.013	0.324 ± 0.005

2.3.5 Effect of stitch density on tensile properties

Tensile strength

Table 2.5 shows that σ_{ut} of stitched 6×6 is 1.3% lower than that of unstitched, while σ_{ut} of stitched 3×3 is 10.5% higher than that of unstitched. In order to understand the real effect of stitch density on tensile strength, firstly, effect of fiber volume fraction V_f should be removed. It is because σ_{ut} of composites is greatly controlled by the content of fibers, and stitching indeed causes some variation of V_f (see again Table 2.3. Normalizing σ_{ut} with V_f is therefore necessary for several reasons: (i) to understand how much V_f affects the strength, (ii) to allow a fair comparison between stitched and unstitched composites due to the variation of V_f. Normalized tensile strength (σ_{ut}^{n}) can be calculated by multiplying σ_{ut} of respective composite with normalized volume fraction, which is defined as a ratio between V_f of respective composite and V_f of unstitched composite (for example, $V_{f-stitched6\times6}/V_{f-unstitched}$). V_f for each composite can be reviewed in Table 2.3.

Table 2.5 also shows σ_{ut}^{n} of unstitched, stitched 6×6 and stitched 3×3. σ_{ut}^{n} of unstitched composites is 654 MPa, whilst that of stitched 6×6 and stitched 3×3 is 651 MPa and 736 MPa, respectively. σ_{ut}^{n} of stitched 6×6 becomes 0.5% lower than that of unstitched composites. σ_{ut}^{n} of stitched 3×3 is 12.5% higher than that of unstitched composites. This finding suggests that V_f also contributes to the change of tensile strength of stitched composites although the contribution is considered minor. Other factors may seem to govern the reduction of strength in stitched 6×6, and increase of strength in stitched 3×3. As later shown, characterization of damage would reveal the main reason for strength reduction or improvement in stitched composites.

Failure strain

Stitched 6×6 and stitched 3×3 exhibit failure strain of 1.33% and 1.45%, respectively, while the failure strain of unstitched composites is 1.26%. An increase of failure strain in composites is generally caused by the behavior of the resin. Composite systems that contain higher amount of resin would naturally absorbs energy in order to deform plastically [23]. The energy absorption reduces the stress concentration of intact fibers adjacent to the broken ones, which in turn, lower the possibility of intact fibers to break. As a result, failure strain can be prolonged. In stitched composites, resin-rich region may assist the increase of energy absorption during tensile loading that eventually prolong the strain to failure. Thus, failure strain of both stitched 6×6 and stitched 3×3 is relatively higher than that of unstitched composites.

Tensile modulus

Tensile modulus is greatly determined by V_f and waviness of on-axis fibers, i.e. 0° tows. Apparent result of low V_f and large waviness in 0° tows would be the reduction of tensile modulus. Normalization of tensile modulus is therefore necessary for the same reasons with that for tensile strength. Normalized tensile modulus (E_x^n) for unstitched, stitched 6×6 and stitched 3×3 is shown in Table 2.5. After normalization, tensile modulus of unstitched composite is 53.1 GPa, while that of stitched 6×6 and stitched 3×3 is 51.6 GPa and 52.7 GPa, respectively. The declining trend of tensile modulus, however, still prevails even after the effect of fiber volume fraction has been removed. E_x^n of stitched 6×6 and stitched 3×3 is 2.8% and 0.8%, respectively, lower than that of unstitched composites. The tensile modulus differences of 2.8% and 0.8% for stitched 6×6 and stitched 3×3, respectively, are smaller than the differences of tensile modulus when normalization is not performed (3.8% for stitched 6×6, 2.6% for stitched 3×3). The difference of modulus, before and after normalization, indicates that reduction of stiffness for both stitched 6×6 and stitched 3×3 is partly influenced by V_f. As later shown, fiber waviness has more profound effect on the reduction of tensile modulus in stitched composites. In addition, it is also observed that the tensile modulus of stitched 6×6 is slightly lower than that of stitched 3×3. The main reason is that the waviness in stitched 6×6 is larger than that in stitched 3×3. The smaller waviness in stitched 3×3 is due to the fact that pitch of 3 mm makes the fiber tows in stitched 3×3 relatively straight in comparison to that in stitched 6×6. Hence, fiber waviness is smaller in stitched 3×3, and therefore tensile modulus is relatively maintained.

Poisson's ratio

As already shown in Table 2.5, ν_{xy} for unstitched is 0.333, while that of stitched 6×6 and stitched 3×3 is 0.314 and 0.324, respectively. There is a declining trend of Poisson's ratio when stitching is introduced to carbon/epoxy. The reduction may reach 5.7% for stitched 6×6 and 2.7% for stitched 3×3. The reduction of Poisson's ratio in stitched composites is also reported by Kamiya and Chou [67]. Reasons for the reduction of Poisson's ratio is postulated herein:

- Stitching and its tensioning force may slightly misalign the orientation of fiber tows
- Stitching may also change the thickness distribution of each fiber tows
- Modified-lock stitch type affects the ratio of deformation between transverse contraction and longitudinal expansion of stitched composites. The orthogonal binding induced by needle and bobbin threads in modified-lock stitch pattern (see again Fig. 2.1) may restrict the movement of in-plane fibers in longitudinal and transverse directions. This orthogonal binding may reduce the magnitude of deformation, which in turn, change the ratio between transverse and longitudinal strains used to obtain Poisson's ratio.

2.3.6 Correlation between fiber waviness and tensile modulus

Table 2.6 shows the result of fiber waviness measurement of 0 ° unstitched, stitched 6×6 and stitched 3×3. Four waviness parameters a_{in}, ϕ_{in}, a_{out} and ϕ_{out} are displayed. In addition, combined waviness of a_{com} and ϕ_{com} are also included in Table 2.6. a_{out} of out-of-plane waviness in unstitched, stitched 6×6 and stitched 3×3 is 112 ± 56 μm, 134 ± 34 μm and 121 ± 51 μm, respectively. ϕ_{out} of unstitched, stitched 6×6 and stitched 3×3 is 4.21 ± 1.82 °, 5.71±1.14 ° and 3.77±1.11 °, respectively. Slightly higher waviness exhibited by stitched 6×6 and 3×3 indicates that stitching may seem to have minor effect on out-of-plane waviness. Table 2.6 also shows that a_{in} and ϕ_{in} of stitched 6×6 are 113±17 μm and 4.68±1.85 °, which are slightly higher than those of stitched 3×3 (110±21 μm, 4.24±0.76 °). In-plane waviness is obviously larger than that of unstitched composites (a_{in} = 19±7 μm, ϕ_{in} = 0.11±0.04 °).

Table 2.6: Amplitude and angle of waviness in 0 ° tows in unstitched, stitched 6×6 200d and stitched 3×3 200d

Specimen	Out-of-plane waviness		In-plane waviness		Combined waviness	
	a_{out} (μm)	ϕ_{out} (°)	a_{in} (μm)	ϕ_{in} (°)	a_{com} (μm)	ϕ_{com} (°)
Unstitched	112 ± 56	4.21 ± 1.82	19 ± 7	0.11 ± 0.04	114 ± 56	4.21 ± 1.82
Stitched 6×6	134 ± 34	5.71 ± 1.14	113 ± 17	4.68 ± 1.85	175 ± 38	7.38 ± 2.17
Stitched 3×3	121 ± 51	3.77 ± 1.11	110 ± 21	4.24 ± 0.76	164 ± 55	5.67 ± 1.35

From the measurement of waviness above, graphs that correlate combined waviness with tensile modulus are made, and they are depicted in Fig. 2.14. It is evident that both in-plane and out-of-plane waviness greatly affects the tensile modulus. If the waviness amplitude and angle are high, the tensile modulus will be relatively low, vice versa. It is concluded herein that the reduction of tensile modulus experienced by stitched composites is strongly correlated with waviness of 0 ° tows in both in-plane and out-of-plane directions.

2.3.7 AE test results

Fig. 2.15 shows cumulative AE hit of three specimens plotted against applied stress. Cumulative AE hit is used to distinguish the damage accumulation process among specimens. The curves are divided into three stages representing three stress ranges that indicate damage processes: Stage I (0-400 MPa), Stage II (400-500 MPa) and Stage III (above 500 MPa).

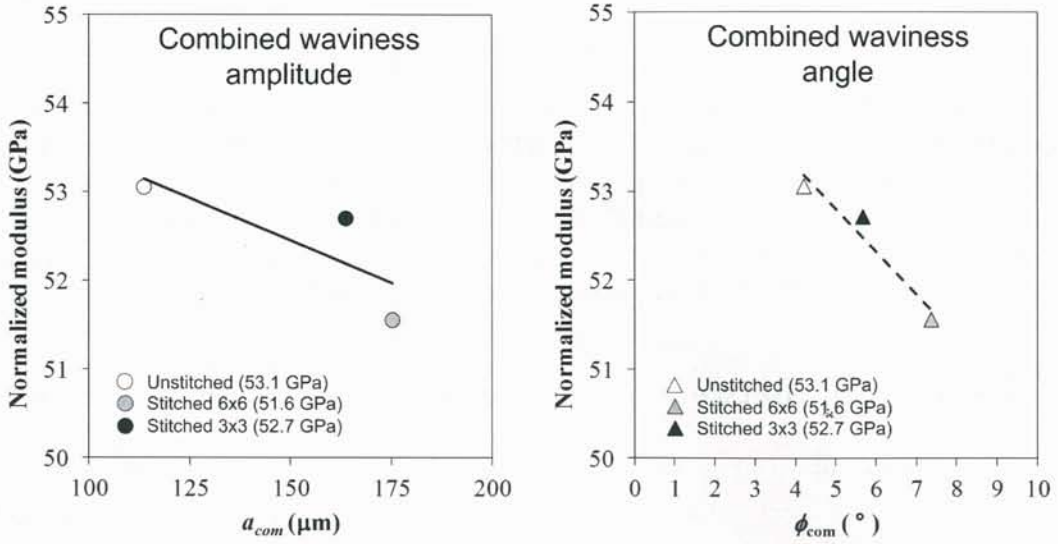

Figure 2.14: Correlation between normalized tensile modulus and combined waviness (amplitude a_{com} and angle ϕ_{com})

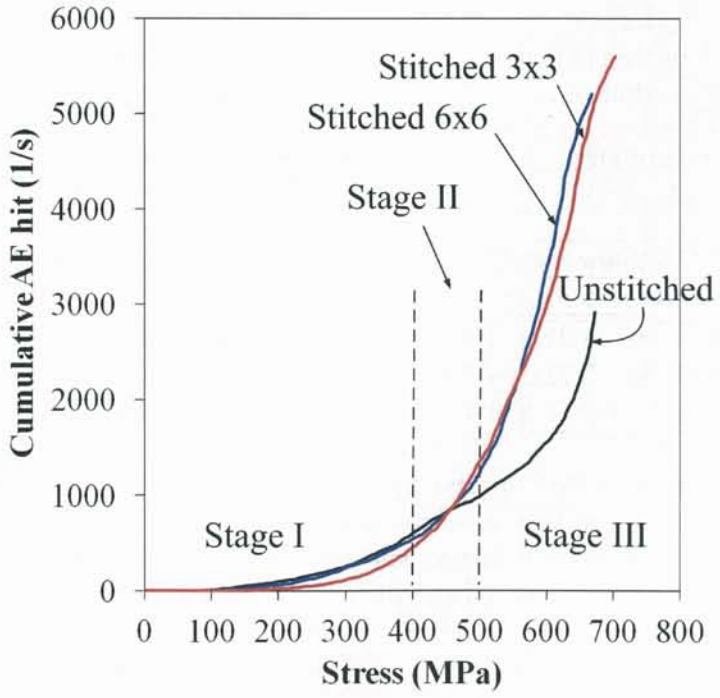

Figure 2.15: Cumulative AE hit of unstitched and stitched carbon/epoxy composites

Stage I

Stage I is characterized by damage initiation and gradual damage accumulation. In this initial stage, damage accumulation rate in unstitched and stitched 6×6 is higher than that in stitched 3×3. However, AE hit corresponds to stress level below 200 MPa is strongly

correlated with the cracking in resin layer at the corner of specimen edges (see Fig. 2.16). This type of damage is triggered by relatively thick resin layer at the upper part of specimen, and due to initial cracking after cutting process, which may not be perfectly polished. At approximately 200 MPa, the damage mode appears to be transverse cracks.

Stage II

In Stage II, stitched 6×6 and stitched 3×3 display rapid increase of AE hit. Stage II is considered as the onset of rapid damage accumulation for stitched composites. On the other hand, damage accumulation in unstitched composites seems to be more gradual than that in stitched composites. Stage II can be considered as a transitional zone of the damage accumulation process.

Stage III

In Stage III, unstitched composites exhibits lower AE hit as compared to stitched composites. Rapid development of damage after 500 MPa is greatly dependent on the density of transverse cracks, oblique cracks and delamination. AE hit rate in stitched composites is also influenced by the development of damage around stitches and resin-rich region. In other words, the overall AE hit registered in stitched composites is not merely the result of mixed activities of transverse cracks, oblique cracks and delamination, but also defects around the stitches and resin-rich region.

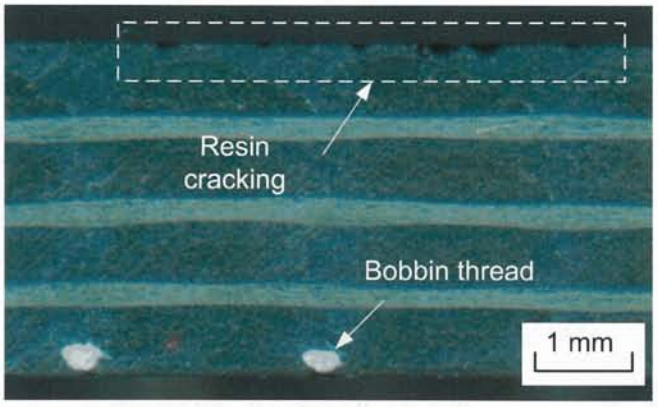

Figure 2.16: Cracking in resin layer at the corner of specimen edges

2.3.8 X-ray radiography results

X-ray radiography images for unstitched, stitched 6×6 and stitched 3×3 are shown in Fig. 2.17. X-ray images are obtained from interrupting the tensile test at various strain levels: 0.5%, 0.6%, 0.7%, 0.8%, 1.0% and 1.2%. X-ray images on the left, middle and right columns correspond to unstitched, stitched 6×6 and stitched 3×3, respectively. The associated stress levels are given below the images. It is shown that at $\varepsilon = 0.5\%$ transverse cracks emanating from the edges of the specimen are captured. It is noteworthy that the transverse crack in stitched composites appears before the crack around stitch thread. It indicates that the bonding between Vectran and surrounding epoxy and fibers is relatively strong. When the load is gradually increased, the length of transverse cracks is also increased. When some

of the transverse cracks reach the other edges, oblique cracks oriented in +45°, −45° or both directions appear. When the transverse cracks begin to saturate, oblique cracks are markedly growing exponentially. After the oblique cracks initiate, delamination in the interface of 90°/+45° and 90°/−45° appears from the specimen edges. At $\varepsilon = 1.2\%$, stitched 3×3 experiences smaller delamination area as compared to unstitched and stitched 6×6. It shows that the delamination seems to be arrested by the stitches. It is also observed that the delamination develops early in stitched 3×3 and stitched 6×6 specimens as compared to that in unstitched specimen. However, in stitched 6×6, the stitches are unable to slow down the growth of delamination, while the transverse and oblique crack densities are higher than those in unstitched composites. As a result, stitched 6×6 in average failed at around 645 MPa, which is lower than that of unstitched and stitched 3×3.

2.3.9 Qualitative damage assessment

Progress of damage in composites is admittedly complex, but possible mechanisms based on the X-ray radiographs could be attained. Fig. 2.18 displays the schematics of damage mechanisms in unstitched composites (top) and stitched composites (bottom). This qualitative damage assessment is made herein to facilitate the distinction of damage mechanisms between unstitched and stitched composites. Stage A to Stage F indicates the damage sequence in composites. The corresponding strain level is given below the letters. It is important to note that the same letter in the damage sequence of unstitched and stitched composites may not referes to the same stress level. Readers may refer to Fig. 2.17 for the respective stress level. As illustrated in Fig. 2.18, transverse cracks initiates at the edges of specimen (Stage A). In unstitched composites, they are followed by the multiplication of transverse cracks, whilst in stitched composites, they are followed by both multiplication and extension of cracks (Stage B). While the transverse cracks begin to grow in unstitched composites, they already reach the other edge in stitched composites (Stage C). Stage D shows that oblique cracks begin to appear at the edges. In Stage D, transverse cracks of unstitched composites reach the other edge. Stage E of unstitched composites is signified by the initiation of delamination, and the growth of oblique cracks. Likewise, Stage E of stitched composites is marked by delamination and growth of oblique cracks. In addition, damages around stitch area in the form of resin cracking at the specimen surface, specifically near the stitch holes, also appear in stitched composites (Stages E and F; filled holes). This resin cracking may grow and coalesce with the neighboring cracks. Delamination in both unstitched and stitched composites is growing, except that in stitched composites, the growth of delamination can be impeded by the stitches. It is also important to note that stitch damage appear in nearly all of stitch regions. After Stage F, fiber splitting begins to appear and the failure is characterized by the breakage of 0° tows.

2.3.10 Quantitative damage assessment

Five damage modes have been identified from X-ray images, namely transverse matrix cracks (oriented in 90° direction), oblique matrix cracks (oriented in both +45° and −45° directions), delamination, defects around stitches and fiber splitting. To give a better visualiza-

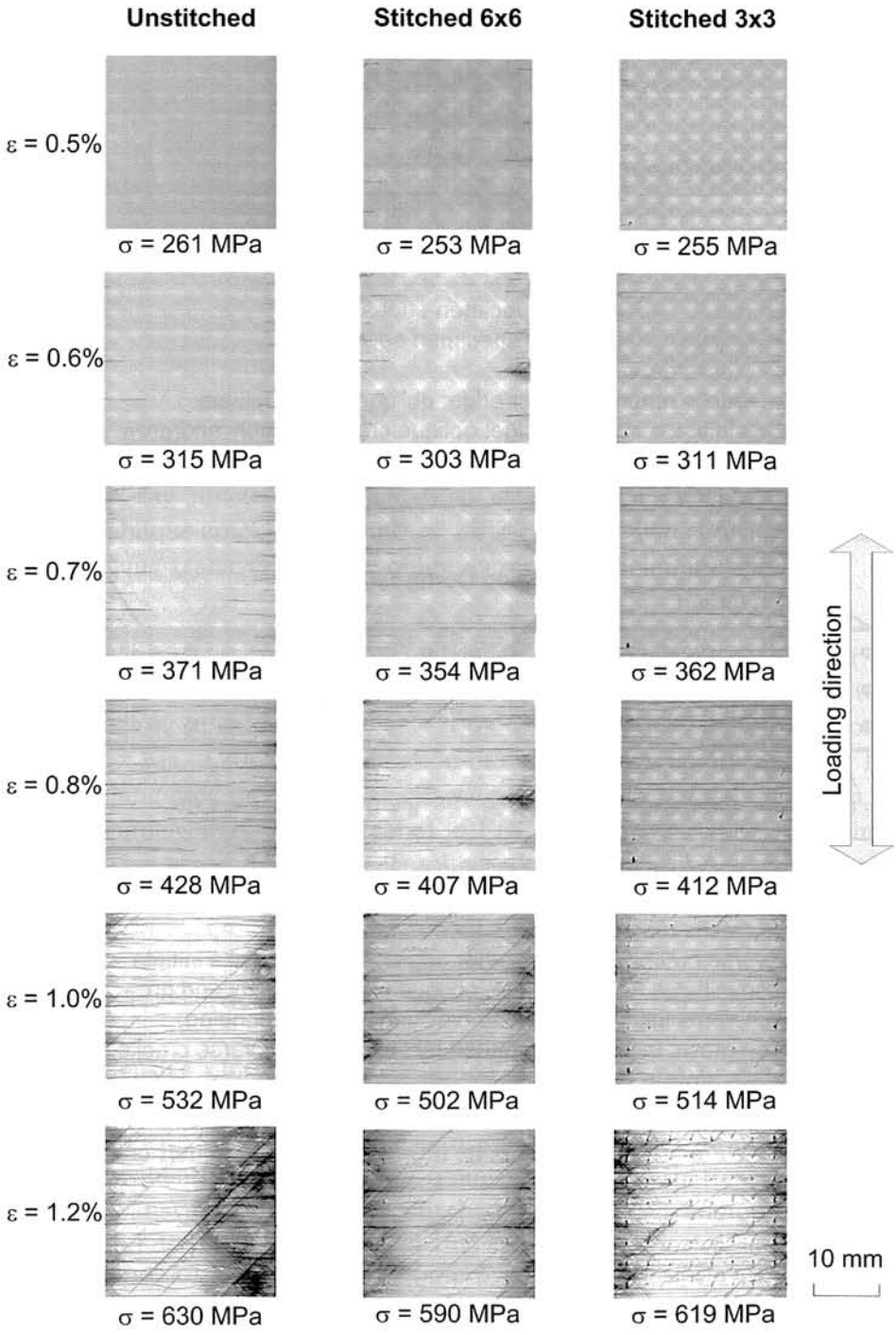

Figure 2.17: X-ray radiographs of damage progression in unstitched, stitched 6×6 and stitched 3×3 under static tension

tion of the damage modes, optical microscopy images of those damage modes are provided in Fig. 2.19. In Fig. 2.19a, transverse crack, oblique crack, delamination, defect around stitch and fiber splitting are indicated. In Fig. 2.19b, transverse crack, oblique crack and delamination observed from optical microscope are noted.

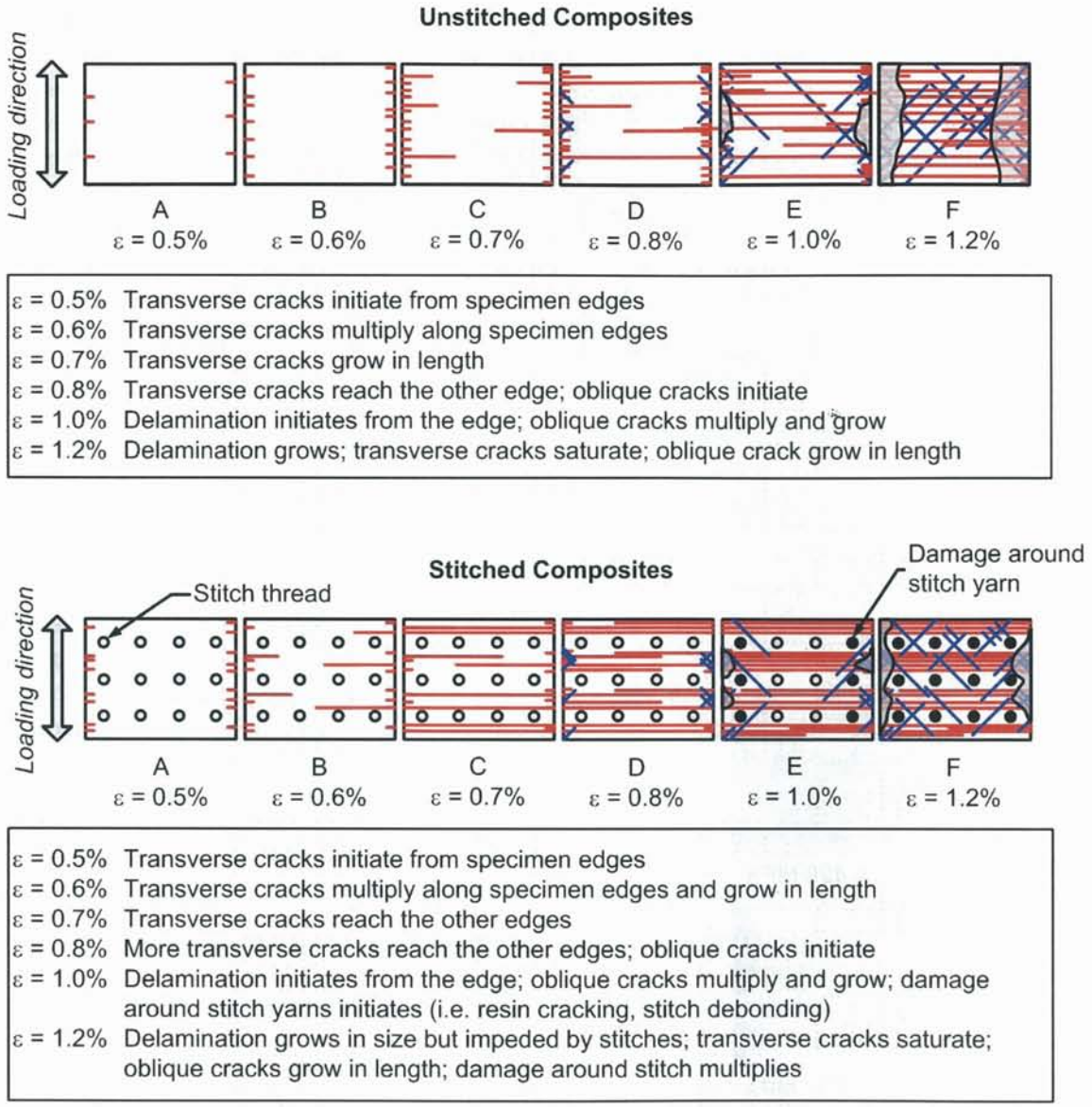

Figure 2.18: Damage mechanisms in unstitched and stitched composites

In this section, quantification of the damage modes is given. Due to complexity of damage modes, only three damage modes are quantified, namely transverse crack, oblique crack and delamination. Crack density, and hence the crack spacing, is measured and calculated for transverse and oblique cracks. As for the delamination, projected delamination area appearing from the specimen edges is measured. In order to count the damage, damage observation area (gage area, A_0) of X-ray image is firstly determined. A_0 is approximately 3750 mm^2 (gage length l_g = 150 mm, gage width w_g = 25 mm). To count the number of transverse crack, as illustrated in Figs. 2.20 (dimension is not to scale), A_0 is subdivided into five sections (section 1-5). Number of transverse crack in each section (n_{ti}) is then counted and divided by the gage length (l_g). Transverse crack density (CD_t) is calculated as a total number of transverse crack density in each section (n_{ti}/l_g) divided by 5. The

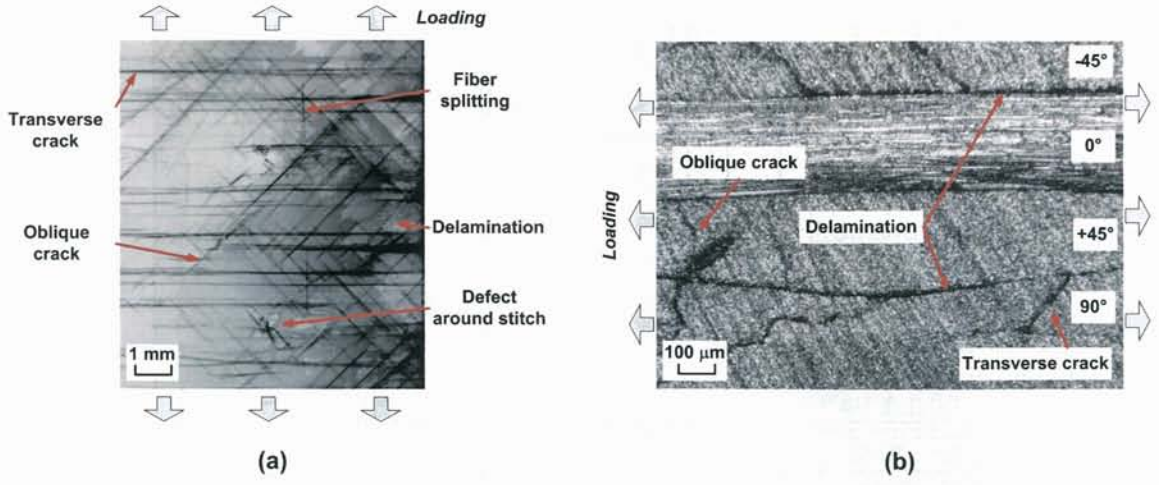

Figure 2.19: (a) X-ray image of stitched 6×6 at $\varepsilon = 1.2\%$ showing five damage modes (transverse crack, oblique crack, delamination, fiber splitting, defect around stitch), (b) cross-sectional view showing transverse crack, oblique crack and delamination

formula for calculating CD_t can be seen below Fig. 2.20a. Likewise, in order to calculate oblique crack density (CD_o), same counting technique is applied, whereby a total number of oblique crack density in each section (n_{oi}/l_g) is divided by 5. The formula for calculating CD_o is shown below Fig. 2.20b. Quantification of delamination is, on the other hand, rather straightforward. Using area measurement software, total projected delamination area (A_d) in the X-ray images is measured. As illustrated in Fig. 2.20c, for instance, a specimen exhibits two edge delamination areas A_1 and A_2. Total area is A_d. The normalized delamination area ($A_n = A_d/A_0$) can then be calculated using formula given below Fig. 2.20c.

Growth of transverse cracks

Transverse crack density plotted against applied stress is given in Fig. 2.21. It is shown that stitching promotes earlier transverse crack, and subsequently higher crack density in carbon/epoxy composites. Stitching seems to affect the initial number of crack per unit length, which subsequently determines its quantity and growth throughout the specimen at later stages. Transverse cracks in unstitched and stitched composites grow until the stress reaches around 400 MPa, and beyond this stress level, transverse cracks tend to reach saturation level. Present results also show that stitches do not alter to the crack multiplication rate.

Early initiation and rapid growth of transverse cracks in 90° tows of stitched composites is postulated as a result of fiber compaction mechanism. Readers may consult Section 2.2.6 for the compaction mechanism. Fig. 2.22 illustrates *lower* V_f that refers to the fiber packing arrangement in 90° of unstitched composites, while *higher* V_f refers to that of stitched composites. When fibers almost touch one another (as in the case of higher V_f), stress concentration between fibers is considerably high, and crack may easily occur. As described by Chou [32], the stress concentration factor between these fibers may reach the ratio between fiber stiffness and matrix stiffness. In addition, when fiber compaction occurs, transverse

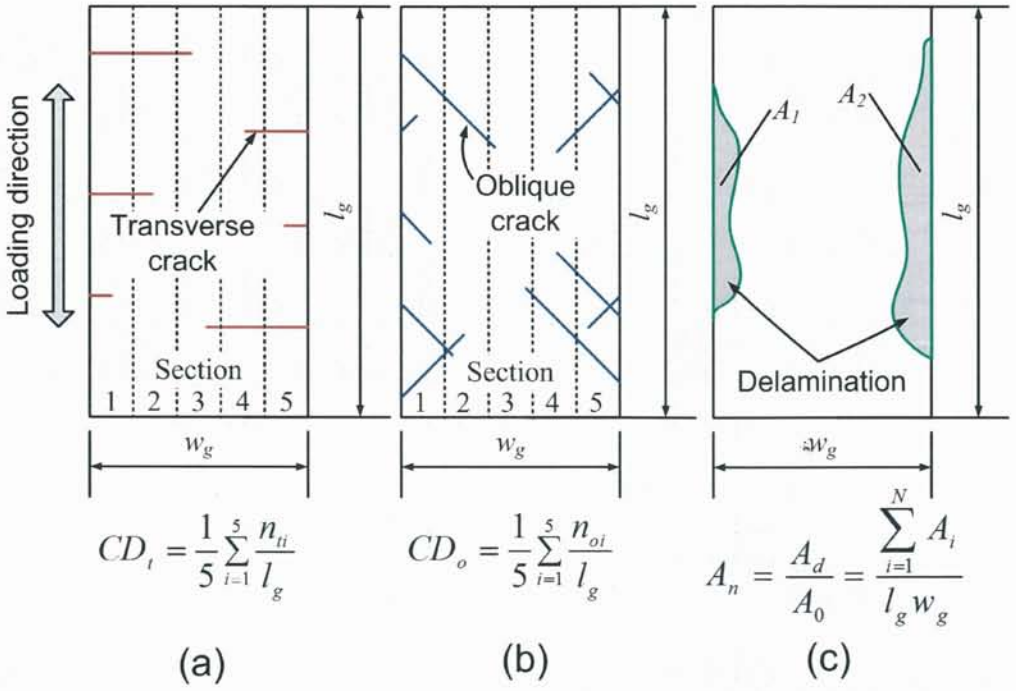

Figure 2.20: Methods to calculate (a) transverse crack density (CD_t), (b) oblique crack density (CD_o), (c) normalized delamination area (A_n)

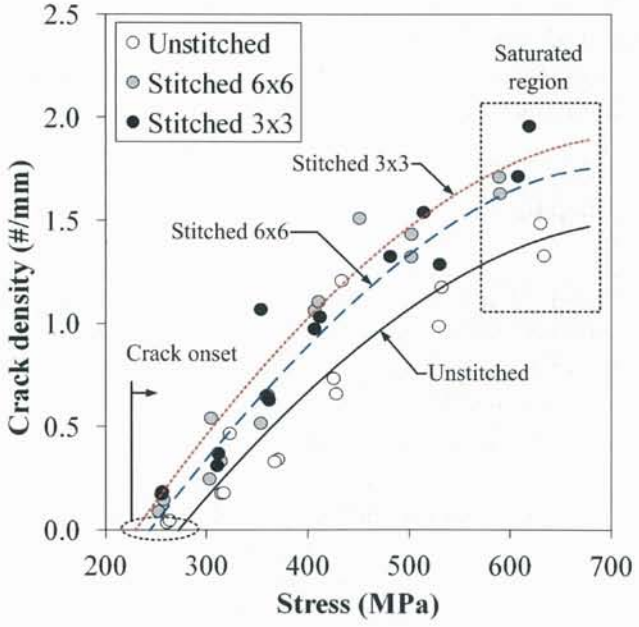

Figure 2.21: Transverse crack density plotted against tensile stress

modulus of fiber tow is locally increased. Higher transverse modulus results in earlier stress recovery between transverse cracks, and thus, it is expected that transverse crack density is also increased. The mechanism for the early formation of cracking in 90° tow is described here to accompany Fig. 2.22:

Fiber tow is compacted ⇒ gap between fibers is reduced ⇒ stress concentration in the matrix phase between fibers is high ⇒ fiber/matrix debonding occurs ⇒ coalescence of fiber/matrix debonding ⇒ early crack initiation

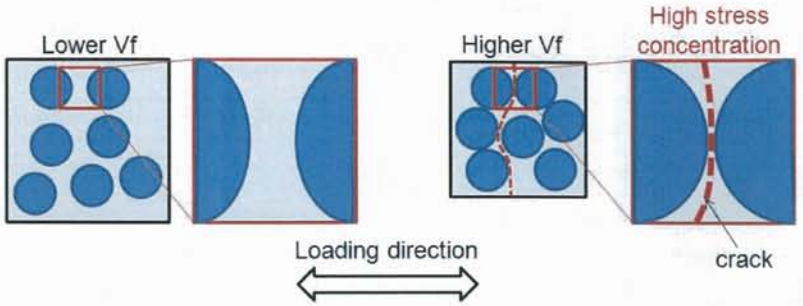

Figure 2.22: Schematic of fiber packing in off-axis tow: comparison between lower V_f (existing in unstitched composites) and higher V_f (existing in stitched composites) in terms of early crack initiation

To prove the existence of fiber compaction mechanism in stitched composites, local fiber volume fraction V_{fl} is measured by two methods already described in Section 2.2.6, namely burn-off test and optical microscopy. These are considered indirect technique to show the existence of V_{fl}. Table 2.7 shows the results of burn-off test and optical microscopy whereby V_{fl}, V_{rl} and V_{vl} for each specimen type are given. Based on burn-off test results, it is shown that stitched 6×6 and stitched 3×3 exhibit slightly higher local fiber volume fraction as compared to unstitched composites. Average V_{fl} of unstitched composites is 53.4%, while that of stitched 6×6 and stitched 3×3 is 56.2% and 56.9%, respectively. Meanwhile, average V_{fl} of unstitched composites obtained based on optical microscopy images is 47.7%, while that of stitched 6×6 and stitched 3×3 is 53.4% and 55.4%, respectively. It is clear that measurement of local volume fraction of fiber based on two methods shows similar tendency, and fiber volume fraction between two stitch threads is increased.

Table 2.7: Local volume fraction of carbon/epoxy samples

Method	Volume fraction	Unit	Unstitched	Stitched 6×6	Stitched 3×3
Burn-off test	V_{fl}	%	53.4 ± 1.1	56.2 ± 1.4	56.9 ± 0.6
	V_{rl}	%	44.9 ± 1.3	42.9 ± 1.0	42.1 ± 0.7
	V_{vl}	%	1.8 ± 0.2	0.9 ± 0.6	1.0 ± 0.6
Optical microscopy	V_{fl}	%	47.7 ± 4.9	53.4 ± 3.7	55.4 ± 3.2
	V_{rl}	%	52.3 ± 4.9	46.6 ± 3.7	44.6 ± 3.2
	V_{vl}	%	n/a	n/a	n/a

To corroborate the measurement results, samples of fiber arrangement in 90° tow taken from optical microscopy are shown in Fig. 2.23. These samples are obtained from area between two stitch lines. It is shown that the gap among fibers in stitched 6×6 and stitched 3×3 is relatively smaller than that in unstitched samples. The smaller gap among fibers indicates that the compaction is apparent. Thus, it can be concluded based on burn-off test and optical

microscopy observation that stitching induces compaction effect, which increases both local fiber volume fraction. This factor is he plausible reason for early initiation of transverse crack in stitched composites.

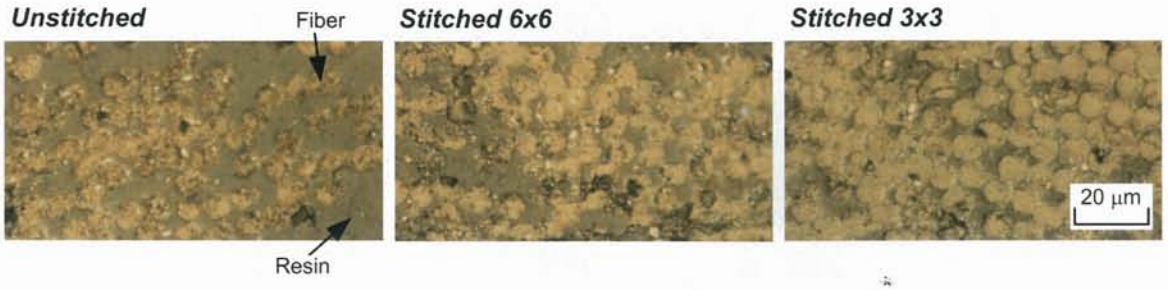

Figure 2.23: Fiber arrangement in 90° tow of unstitched, stitched 6×6 and stitched 3×3

Growth of oblique cracks

Fig. 2.24 shows the growth of oblique crack plotted against applied tensile stress. Oblique crack begins to appear when transverse crack density reaches approximately 0.3-0.7/mm. The growth rate of oblique crack in stitched composite is considered higher than that in unstitched composite, specifically after 500 MPa, when the transverse crack begins to saturate. The reason behind this behavior is that oblique cracks does not only appear as independent cracks in 45 or −45° tows, but also appear as contiguous cracks due to their interaction with transverse cracks in 90° tows and delamination.

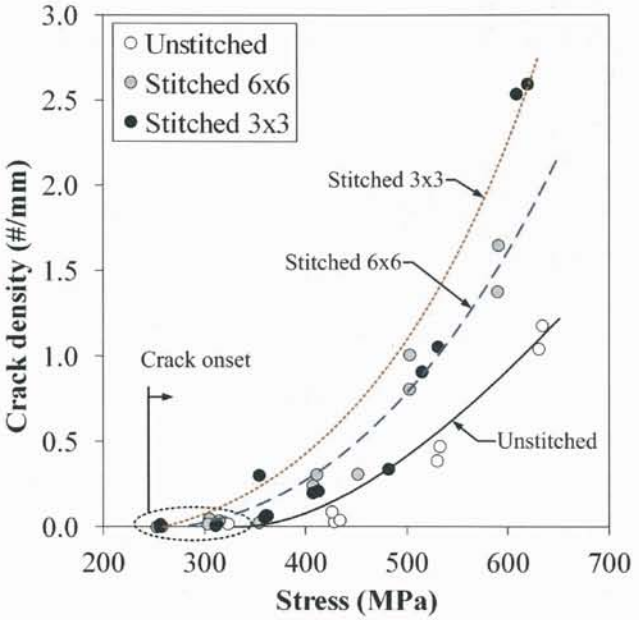

Figure 2.24: Oblique crack density plotted against tensile stress

Growth of delamination

Delamination is found to emanate from the free-edges of specimen; similar behavior with transverse and oblique cracks. The delamination does not originate from the stitch threads. Delamination is considered as the primary damage in composites, and in this case, the eminent ability of stitches to impede the delamination emanating from the edges is demonstrated. In present experiment, delamination is found at the interfaces between between $+45°$ (or $-45°$) and $90°$ tows. Delamination area (A_d) is then measured and normalized with the gage area (A_0). The normalized delamination (A_d/A_0) of stitched and unstitched composites plotted against tensile stress can be seen in Fig. 2.25. Delamination appears in the range between 330 MPa and 490 MPa, and it is growing rapidly as the applied stress is gradually increased. It is noted that the delamination in stitched 6×6 developed earlier than that in unstitched and stitched 3×3. Such behavior is triggered by the interaction between transverse cracks and oblique cracks. Between 550 and 600 MPa (70%-85% of σ_{ut}), effect of stitching is somewhat evident. At the same stress level (for example 580 MPa), stitched 3×3 delaminated of around 13%, whilst unstitched and stitched 6×6 composites delaminated of around 15% and 21%, respectively. In this case, the effectiveness of stitch threads in stitched 3×3 composites in impeding delamination translates into modest improvement of tensile strength.

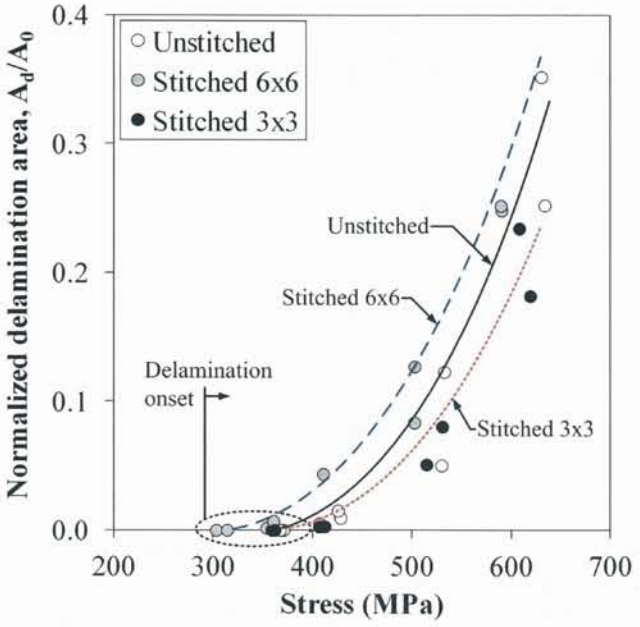

Figure 2.25: Delamination growth plotted against tensile stress

Onset of damage

Estimated stress levels at the onset of damage modes (transverse crack, oblique crack, delamination) are given herein. The stress levels are estimated from the initiation of damage modes shown in Figs. 2.21, 2.24 and 2.25. Table 2.8 shows that stitched 3×3 experiences the earliest transverse cracks, which is at 210 MPa. The transverse cracks are followed by

oblique cracks that occur at 321 MPa. The earliest onset of delamination is exhibited by stitched 6×6 that experiences delamination initiation at 361 MPa.

Table 2.8: Estimated stress level at the onset of damage modes

Specimen	Transverse crack onset σ_{tc} (MPa)	Oblique crack onset σ_{oc} (MPa)	Delamination onset σ_d (MPa)
Unstitched	245	368	412
Stitched 6×6	223	317	361
Stitched 3×3	210	321	402

2.3.11 Effectiveness of stitching: some remarks on damage mechanisms

Effectiveness of stitching is discussed in the framework of its ability in inhibiting delamination. Delamination, in this respect, is one of the principal damage modes in composites. Other principal damage mode inducing final failure is fiber breakage. Initiation of delamination at the interface between plies is influenced by

- relatively high interlaminar stresses due to a mismatch in thermal expansion coefficient between plies [94]
- flaws (or void) in the matrix
- property of the matrix
- thickness of matrix between two adjacent plies
- constraints provided by the adjacent plies
- stacking sequence (when the angle difference between two adjacent plies is high, e.g. between 0 ° ply and 90 ° ply, delamination may easily occur)

Delamination commonly initiates at the free-edges of specimen or structures because interlaminar normal stress (σ_z) and interlaminar shear stress (τ_{xz}) are extremely high in this region exceeding the threshold of interlaminar strength. Effect of delamination on the characteristics of composites is noted as follows (i) delamination can promote early failure, (ii) delamination can prompt other damage modes, (iii) delamination may reduce the local stiffness of a structure. In other words, delamination deteriorates the overall performance of composites although it may not be the cause of failure. When stitching is introduced in composites, specifically when through-thickness reinforcement is performed, the interlaminar stresses between plies are reduced. Thus, delamination can be delayed. The reduction of interlaminar stresses is related to the role of stitches in providing closing traction between plies. However, present investigation shows that stitched 6×6 composites exhibit lower strength in comparison to unstitched and stitched 3×3, and this is because of two reasons: (i) stitching induces early formation of cracks, (ii) stitched 6×6 pattern is considered too sparse to suppress the

growth of delamination that ensues the crack. As for the latter reason, the distance of 6 mm in stitched 6×6 specimens is insufficient to provide closing traction for the aggressive growth of edge delamination. Hence, larger delamination area in stitched 6×6 specimens inevitably occurs, and along with the cracks, they cause some loss of overall integrity of the laminates. Therefore, stitched 6×6 failed earlier than unstitched and stitched composites. On the other hand, stitched 3×3 is considered effective in inhibiting the delamination growth despite the fact that there is a higher crack density in stitched 3×3 as compared to unstitched and stitched 6×6. Stitching by 3×3 pattern provides better bridging traction between plies as compared to stitched 6×6. Shear stresses occurred between plies are partly sustained by 3×3 pattern. Because interlaminar stresses between plies in stitched 3×3 composites can be reduced, the overall integrity of composite can be maintained. Thus, failure in stitched 3×3 composite can be deferred. This translates into a modest increase of tensile strength in stitched 3×3 in comparison to unstitched and stitched 6×6.

2.4 Analytical Study

The analytical study deals with the prediction of 3-D thermo-elastic constants for unstitched and stitched composites. The prediction is carried out using homogenization method employing asymptotic expansion series. This section is divided into four parts. First part deals with the review of homogenization method. Second part discusses the development of finite element (FE) unit cell models (*micromechanics models*) to represent fiber tow, and thermo-elastic constants of fiber tow obtained by homogenization method. Third part discusses the development of FE unit cell models (*mesomechanics models*) to represent unstitched, stitched 6×6 and stitched 3×3, and thermo-elastic constants of obtained from each model. In the last part, comparison between predictions and experimental results is made, and recommendation for future work is outlined.

2.4.1 Homogenization method

Homogenization method is a rigorous analytical method to solve a system composed of a large amount of heterogeneous and periodic microstructure that can be regarded as macroscopically homogeneous macrostructure. Despite its mathematical rigor, homogenization method is an efficient and accurate method, whereby the periodicity of the model is guaranteed. This method is developed from partial differential equations with varying coefficients [48], and the underlying theory assumes two conditions:

- the field variables vary on multiple scales due to the existence of microstructure
- the microstructure is spatially periodic

A 3-D elastic body consisting of periodic microstructure is illustrated in Fig. 2.26. The elastic body denoted as Ω region lies in the macroscopic Cartesian coordinate system (x_1-x_2-x_3). The body Ω is subjected to body force f, while the boundaries Γ_t and Γ_d represent surface traction and prescribed displacement, respectively. The periodic microstructure, which consists of

a number of identical unit cells, can be viewed at macroscopic and microscopic levels. To simplify the description, 2-D coordinate systems in both macroscopic (x_1-x_2) and microscopic (y_1-y_2) levels are now considered. At macroscopic level, a 2-D unit cell shown in Fig. 2.27 with the dimension of $L_1 \times L_2$ resides in x_1-x_2 macroscopic coordinate, and exists among other cells. At microscopic level, the unit cell with the dimension of l_1 and l_2 exists independently in y_1-y_2 microscopic coordinate. This microscopic domain is called Y-domain, in which ¥ is a solid part, whilst θ is a void part. S denotes the surface of void part.

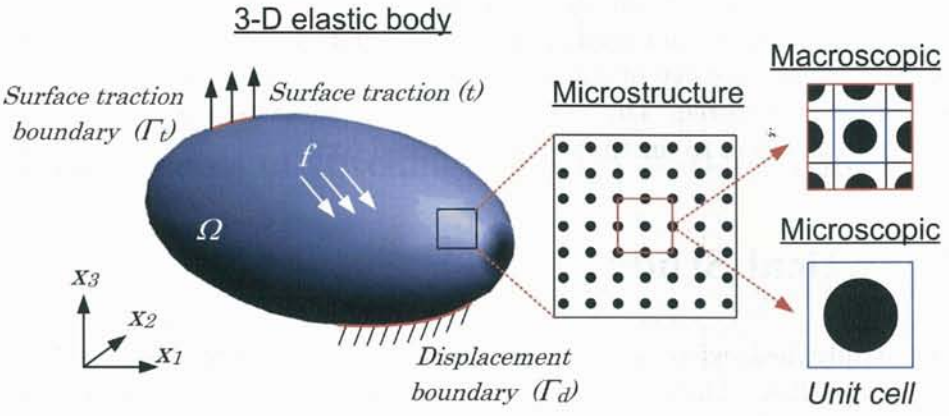

Figure 2.26: Elastic body and periodic microstructure

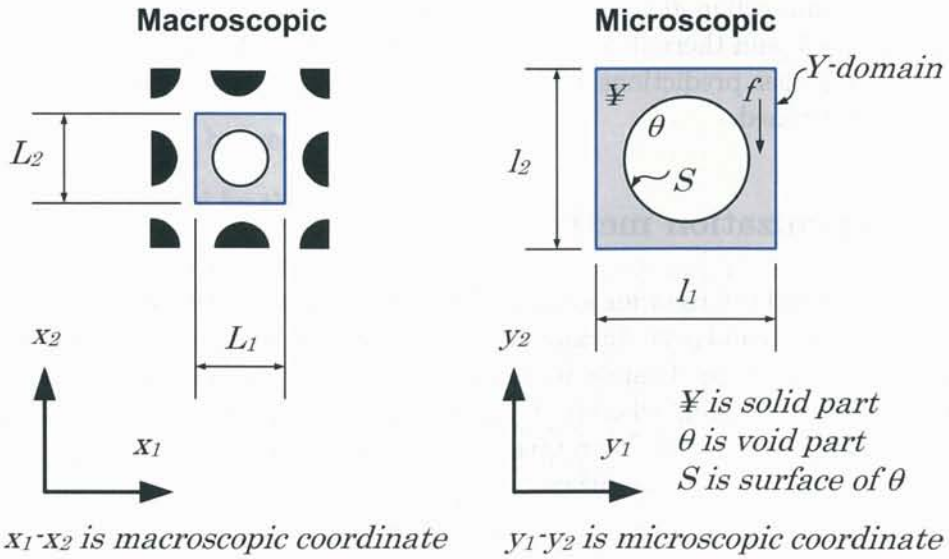

Figure 2.27: Unit cell at macroscopic and microscopic levels

A function that represents both macroscopic and microscopic coordinate systems called periodic vector function $g^\epsilon(x)$ is introduced. The reason is because Ω^ϵ would essentially exhibit a large variation due to the co-existence of microscopic and macroscopic structures. $g^\epsilon(x)$ can be expanded into

$$g^\epsilon(x) = g(x, y) = g(x_1, x_2, x_3, y_1, y_2, y_3) \tag{2.11}$$

where superscript ϵ is a ratio between macroscopic and microscopic, i.e. $\epsilon = x/y = L_1/l_1 = L_2/l_2 = L_3/l_3$. The infinite periodicity is described three-dimensionally by Y-periodicity in microscopic coordinate, in which Eq. (2.11) becomes

$$g^\epsilon(x,y) = g(x,y+Y) = g(x_1,x_2,x_3,y_1+Y_1,y_2+Y_2,y_3+Y_3) \tag{2.12}$$

Differentiation of $g^\epsilon(x)$ with respect to macroscopic coordinate x yields

$$\frac{\partial}{\partial x_i}[g(x,y)] = \frac{\partial}{\partial x_i}\left[g\left(x, y=\frac{x}{\epsilon}\right)\right] = \frac{\partial g}{\partial x_i} + \frac{1}{\epsilon}\frac{\partial g}{\partial y_i} \tag{2.13}$$

Limit of the periodic function $\Psi(x,y)$ is defined as follows

$$\lim_{\epsilon\to 0^+} \int_{\Omega^\epsilon} \Phi(x,y)\, d\Omega \to \frac{1}{|Y|}\int_{\Omega}\int_{¥} \Phi(x,y)\, dY\, d\Omega \tag{2.14}$$

$$\lim_{\epsilon\to 0^+} \int_{S^\epsilon} \Phi(x,y)\, d\Omega \to \frac{1}{|Y|}\int_{\Omega}\int_{S} \Phi(x,y)\, dS d\Omega \tag{2.15}$$

where $|Y|$ represents volume of the unit cell.

Thermo-elastic problem can generally be solved using the weak form of boundary value problem so-called *the principle of virtual work* as follows

$$\int_{\Omega^\epsilon} E^\epsilon_{ijkl}\left(\frac{\partial u^\epsilon_k}{\partial x_l} - \alpha^\epsilon_{kl}\Delta T\right)\frac{\partial v_i}{\partial x_j}\, d\Omega = \int_{\Omega^\epsilon} f^\epsilon_i\, d\Omega + \int_{\Gamma^\epsilon} t_i v_i\, d\Gamma + \int_{S^\epsilon} p^\epsilon_i v_i\, dS \tag{2.16}$$

where $u^\epsilon_k(x)$ and $v_i(x,y)$ are displacement components (including the microstructure) and virtual displacement, respectively. E^ϵ_{ijkl} and α^ϵ_{kl} are elastic tensor and coefficient of thermal expansion, respectively. ΔT is temperature difference between a reference temperature and current temperature. The first until third terms in the right-hand-side is body force f, traction force t and force p on surface S, respectively.

It may be useful to recall that in linear elasticity case stress-strain relationship that includes thermal effect can be expressed as follows

$$\sigma^\epsilon_{ij} = E^\epsilon_{ijkl}\left(\frac{\partial u^\epsilon_k}{\partial x_l} - \alpha^\epsilon_{kl}\Delta T\right) \tag{2.17}$$

And, in small deformation theory strain-strain relationship can be expressed as follows

$$\varepsilon^\epsilon_{ij} = \frac{1}{2}\left(\frac{\partial u^\epsilon_i}{\partial x_j} + \frac{\partial u^\epsilon_j}{\partial x_i}\right) \tag{2.18}$$

Displacement and stress can be approximated by asymptotic expansion series

$$u_i^\epsilon(x) = u_i^0(x,y) + \epsilon u_i^1(x,y) + \epsilon^2 u_i^2(x,y) + ... \tag{2.19}$$

$$\sigma_i^\epsilon(x) = \sigma_i^0(x,y) + \epsilon \sigma_i^1(x,y) + \epsilon^2 \sigma_i^2(x,y) + ... \tag{2.20}$$

By substituting Eq. (2.19) into Eq. (2.16), and arranging the terms with the same power of ϵ, a governing equation can be obtained

$$\begin{aligned}\int_{\Omega^\epsilon} E_{ijkl}^\epsilon \Bigg\{ &\frac{1}{\epsilon^2}\frac{\partial u_k^0}{\partial y_l}\frac{\partial v_i}{\partial y_j} + \frac{1}{\epsilon}\left[\left(\frac{\partial u_k^0}{\partial x_l} + \frac{\partial u_k^1}{\partial y_l} + \alpha_{kl}^\epsilon \Delta T\right)\frac{\partial v_i}{\partial y_j} + \frac{\partial u_k^0}{\partial y_l}\frac{\partial v_i}{\partial x_j}\right] \\ &+ \left[\left(\frac{\partial u_k^0}{\partial x_l} + \frac{\partial u_k^1}{\partial y_l} + \alpha_{kl}^\epsilon \Delta T\right)\frac{\partial v_i}{\partial x_j} + \left(\frac{\partial u_k^1}{\partial x_l} + \frac{\partial u_k^2}{\partial y_l}\right)\frac{\partial v_i}{\partial x_j}\right] + \epsilon(...)\Bigg\} d\Omega \\ &= \int_{\Omega^\epsilon} f_i^\epsilon v_i d\Omega + \int_{\Gamma_\epsilon} t_i v_i d\Gamma + \int_{S^\epsilon} p_i^\epsilon v_i \, dS \end{aligned} \tag{2.21}$$

Eq. (2.21) holds if the terms with the same order of ϵ are equal to zero. They are described order-wise in the following sub-sections.

Order of ε^{-2}

$$\lim_{\epsilon \to 0^+} \int_\Omega E_{ijkl}^\epsilon \frac{\partial u_k^0}{\partial y_l}\frac{\partial v_i}{\partial y_j} \, d\Omega = \frac{1}{|Y|}\int_\Omega \int_{¥} E_{ijkl}^\epsilon \frac{\partial u_k^0}{\partial y_l}\frac{\partial v_i}{\partial y_j} \, dY d\Omega = 0 \tag{2.22}$$

By choosing virtual displacement $v = v(y)$ and applying integration by parts, Eq. (2.22) can then be expressed as follows

$$\frac{1}{|Y|}\int_\Omega \int_{¥} \left\{\frac{\partial}{\partial y_j}\left(E_{ijkl}^\epsilon \frac{\partial u_k^0}{\partial y_l} v_i(y)\right)\right\} dY d\Omega - \frac{1}{|Y|}\int_\Omega \int_{¥} \left\{\frac{\partial}{\partial y_j}\left(E_{ijkl}^\epsilon \frac{\partial u_k^0}{\partial y_l}\right) v_i(y)\right\} dY d\Omega = 0 \tag{2.23}$$

Application of Gauss' divergence theorem to Eq. (2.23) yields

$$\frac{1}{|Y|}\int_\Omega \left\{ \int_{¥} \left[-\frac{\partial}{\partial y_j}\left(E_{ijkl}^\epsilon \frac{\partial u_k^0}{\partial y_l}\right) v_i(y)\right] dY + \int_S E_{ijkl}^\epsilon \frac{\partial u_k^0}{\partial y_l} n_j v_i(y) \, dS \right\} d\Omega = 0 \tag{2.24}$$

For any arbitrary value of v_i, displacement u^0 can be expressed as

$$u^0 = u^0(x) \tag{2.25}$$

where u^0 is macroscopic displacement. In this regard, the first term in Eq. (2.24) is only dependent on macroscopic coordinate x.

Order of ε^{-1}

$$\lim_{\epsilon\to 0^+}\int_\Omega E^\epsilon_{ijkl}\left[\left(\frac{\partial u^0_k}{\partial x_l}+\frac{\partial u^1_k}{\partial y_l}-\alpha^\epsilon_{kl}\Delta T\right)\frac{\partial v_i}{\partial y_j}+\frac{\partial u^0_k}{\partial y_l}\frac{\partial v_i}{\partial x_j}\right]d\Omega$$

$$=\int_\Omega\left[\frac{1}{|Y|}\int_{¥}E^\epsilon_{ijkl}\left(\frac{\partial u^0_k}{\partial x_l}+\frac{\partial u^1_k}{\partial y_l}-\alpha^\epsilon_{kl}\Delta T\right)\frac{\partial v_i}{\partial y_j}\,dY\right]d\Omega$$

$$=\frac{1}{|Y|}\int_\Omega\int_S p_i v_i\,dS d\Omega \quad (2.26)$$

By applying virtual displacement $v = v(x)$ into Eq. (2.26), following equilibrium equation can be obtained

$$\int_{¥}E^\epsilon_{ijkl}\left(\frac{\partial u^0_k}{\partial x_l}+\frac{\partial u^1_k}{\partial y_l}-\alpha^\epsilon_{kl}\Delta T\right)\frac{\partial v_i}{\partial y_j}\,dY=0 \quad (2.27)$$

Order of ε^0

$$\lim_{\epsilon\to 0^+}\int_\Omega E^\epsilon_{ijkl}\left[\left(\frac{\partial u^0_k}{\partial x_l}+\frac{\partial u^1_k}{\partial y_l}-\alpha^\epsilon_{kl}\Delta T\right)\frac{\partial v_i}{\partial x_j}+\left(\frac{\partial u^1_k}{\partial x_l}+\frac{\partial u^2_k}{\partial y_j}\right)\frac{\partial v_i}{\partial y_j}\right]d\Omega$$

$$=\int_\Omega\frac{1}{|Y|}E^\epsilon_{ijkl}\left[\left(\frac{\partial u^0_k}{\partial x_l}+\frac{\partial u^1_k}{\partial y_l}-\alpha^\epsilon_{kl}\Delta T\right)\frac{\partial v_i}{\partial x_j}+\left(\frac{\partial u^1_k}{\partial x_l}+\frac{\partial u^2_k}{\partial y_j}\right)\frac{\partial v_i}{\partial y_j}\right]d\Omega$$

$$=\int_\Omega\left(\frac{1}{|Y|}\int_{¥}f_i v_i\,dY\right)d\Omega+\int_{\Gamma_\epsilon}t_i v_i\,d\Gamma \quad (2.28)$$

By substituting virtual displacement of $v = v_i(x)$ into Eq. (2.28), an equilibrium equation can be obtained as follows

$$\int_\Omega\left[\frac{1}{|Y|}\int_{¥}E^\epsilon_{ijkl}\left(\frac{\partial u^0_k}{\partial x_l}+\frac{\partial u^1_k}{\partial y_l}-\alpha^\epsilon_{kl}\Delta T\right)d\Omega\right]\frac{\partial v_i(x)}{\partial x_j}\,d\Omega$$

$$=\int_\Omega\left(\frac{1}{|Y|}\int_{¥}f_i\,dY\right)v_i(x)\,dY+\int_{\Gamma_\epsilon}t_i v_i(x)\,d\Gamma \quad (2.29)$$

If the virtual displacement v_i is defined as $v_i(y)$, following expression can be obtained

$$\int_{¥}E^\epsilon_{ijkl}\left(\frac{\partial u^1_k}{\partial x_l}+\frac{\partial u^2_k}{\partial y_j}\right)\frac{\partial v_i(y)}{\partial y_j}\,dY=\int_{¥}f_i v_i(y)\,dY \quad (2.30)$$

Displacement field shown in Eq. (2.19) can be defined as

$$u_i^{\epsilon}(x) = u_i^0(x,y) + \epsilon u_i^1(x,y) \tag{2.31}$$

where $u_i^1(x,y)$ is assumed as

$$u_i^1(x,y) = -\chi_i^{pq}(y)\frac{\partial u_p^0(x)}{\partial x_q} - \Psi_k(x,y) \tag{2.32}$$

where χ^{pq} are *characteristic displacement vector* relevant to the deformation mode 'kl' of the unit cell. Hence, following equation can be obtained

$$\int_{¥} \left(E_{ijkl}^{\epsilon} - E_{ijpq}^{\epsilon}\frac{\partial \chi_p^{kl}(y)}{\partial y_q} \right) \frac{\partial v_i(y)}{\partial y_j}\, dY = 0 \tag{2.33}$$

$$\frac{1}{|Y|}\int_{¥} \chi_i^{kl}\, dY = 0 \tag{2.34}$$

From the thermal deformation, characteristic displacement vector of Ψ_i is also obtained from the following

$$-\int_{¥} E_{ijkl}^{\epsilon}\frac{\partial \Psi_k}{\partial y_l}\frac{\partial v_i}{\partial y_j}\, dY = \int_{¥} E_{ijkl}^{\epsilon}\alpha_{kl}^{\epsilon}\Delta T\frac{\partial v_i}{\partial y_j}\, dY \tag{2.35}$$

$$\frac{1}{|Y|}\int_{¥} \Psi_i\, dY = 0 \tag{2.36}$$

Eq. (2.20) can also be expressed as follows

$$\sigma_{ij}^{\epsilon}(x) = \sigma_{ij}^0(x,y) \tag{2.37}$$

where $\sigma_{ij}^0(x,y)$ can be obtained by following expression

$$\sigma_{ij}^0(x,y) = \left(E_{ijkl}^{\epsilon}(x,y) - E_{ijpq}^{\epsilon}(x,y)\frac{\partial \chi_p^{kl}(x,y)}{\partial y_q} \right) \frac{\partial u_k^0(x)}{\partial x_l} - E_{ijkl}^{\epsilon}(x,y)\frac{\partial \Psi_k(x,y)}{\partial y_l} - E_{ijkl}^{\epsilon}\alpha_k\Delta T \tag{2.38}$$

where in 3-D formulation, six sets of relevant problem to χ^{kl} $(k,l = 1,2,3)$ must be solved by considering its symmetry.

Macroscopic equilibrium equation can be expressed as follows:

$$\int_{\Omega} E^0_{ijkl} \frac{\partial u^0_k}{\partial x_l} \frac{\partial v_i(x)}{\partial x_j} \, d\Omega = \int_{\Omega} \tau_{ij}(x) \frac{\partial v_i(x)}{\partial x_j} \, d\Omega + \int_{\Omega} \sigma^t_{ij}(x) \frac{\partial v_i(x)}{\partial x_j} \, d\Omega + \int_{\Omega} b_i(x) v_i(x) \, d\Omega + \int_{\Gamma_\epsilon} t_i(x) v_i(x) \, d\Gamma \quad (2.39)$$

Macroscopic homogenized elastic constants E^0_{ijkl} can be obtained as follows:

$$E^0_{ijkl} = \frac{1}{|Y|} \int_{¥} E^{\epsilon}_{ijkl} - E^{\epsilon}_{ijpq} \frac{\partial \chi^{kl}_p}{\partial y_q} \, dY \quad (2.40)$$

And, the terms used to express microscopic thermal effects and thermal strains can be obtained from following equations

$$\tau_{ij}(x) = \frac{1}{|Y|} \int_{¥} E^{\epsilon}_{ijkl} \frac{\partial \Psi_k}{\partial y_l} \, dY \quad (2.41)$$

$$\sigma^t_{ij}(x) = \frac{1}{|Y|} \int_{¥} E^{\epsilon}_{ijkl} \alpha^{\epsilon}_{kl} \Delta T \, dY \quad (2.42)$$

$$b_i(x) = \frac{1}{|Y|} \int_{¥} f_i \, dY \quad (2.43)$$

Points identified in microscopic coordinate system shown Fig. 2.28 helps to define the periodic boundary condition in homogenization method. Periodic boundary conditions are

$$y_1 \in \lfloor 0, y^0_1 \rfloor, y_2 \in \lfloor 0, y^0_2 \rfloor, y_3 \in \lfloor 0, y^0_3 \rfloor \quad (2.44)$$

And, χ^{kl} should satisfy

$$\chi^{kl}_1(0, y_2, y_3) = \chi^{kl}_1(y^0_1, y_2, y_3) \quad (2.45)$$

$$\chi^{kl}_1(y_1, 0, y_3) = \chi^{kl}_1(y_1, y^0_2, y_3) \quad (2.46)$$

$$\chi^{kl}_1(y_1, y_2, 0) = \chi^{kl}_1(y_1, y_2, y^0_3) \quad (2.47)$$

which means that two opposite faces of the unit cell should deform in an identical manner.

By incorporating finite element procedures, homogenization method described above is implemented in *Fortran 90*. Output of the program is homogenized thermo-elastic constants of the finite element model prescribed in pre-processing steps. Pre-processing steps include unit

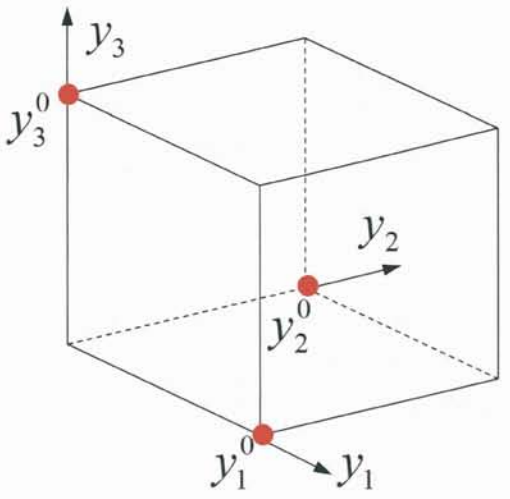

Figure 2.28: Microscopic model defining periodic boundary condition

cell geometrical modeling of fiber tow or stitched composite, defining element types, defining material properties, meshing, merging all nodes and renumbering.

2.4.2 Prediction of thermo-elastic constants of fiber tow

A finite element model is developed using *MSC.Patran* 2008, and used to obtained thermo-elastic constants of fiber tow. The process to build the model is illustrated in Fig. 2.29. It is shown that the cross-sectional shape of fiber tow is usually almost elliptical. Within this tow, arrangement of the fiber is naturally random. The arrangement of fiber can be idealized as hexagonal packing. A unit cell of hexagonal packing is identified, and the 3-D unit cell is geometrically built using MSC.Patran, whereby elements type is also defined. Element type used in this so-called micromechanics model is hexahedron 20 nodes. As shown, micromechanics model contains 1792 elements and 8689 nodes. Three micromechanics models with fiber volume fraction of 45%, 47% and 49% are built. Different V_f is assigned for each specimen type because stitch density affects the local fiber fraction in fiber tows. Higher stitch density would result in higher fiber volume fraction of tow. Results of the models are used in mesomechanics models, whereby V_f = 45% for unstitched model, V_f = 47% for stitched 6×6 model and V_f = 49% for stitched 3×3 model. Fiber is T800SC-24kf, and the thermo-mechanical properties are E_L = 294 GPa, E_T = 6.50 GPa, G_{LT} = 18.20 GPa, G_{TT} = 6.50 GPa, ν_{LT} = 0.32, ν_{TT} = 0.41, α_L = -0.56×10^{-6}/K, α_T = 8.10×10^{-6}/K. Resin is XNR/H6813, and it is assumed isotropic. The thermo-mechanical properties of XNR/H6813 are as follow E = 8.96 GPa, G = 3.45 GPa, ν = 0.35, α = 65×10^{-6}/K. The thermo-elastic properties of T800SC and XNR/H6813 can also be reviewed in Table 2.1. Thermo-mechanical properties of fiber tow obtained by homogenization method can be seen in Table 2.9. These thermo-mechanical properties are used in FE models of stitched composites described in Section 2.4.3.

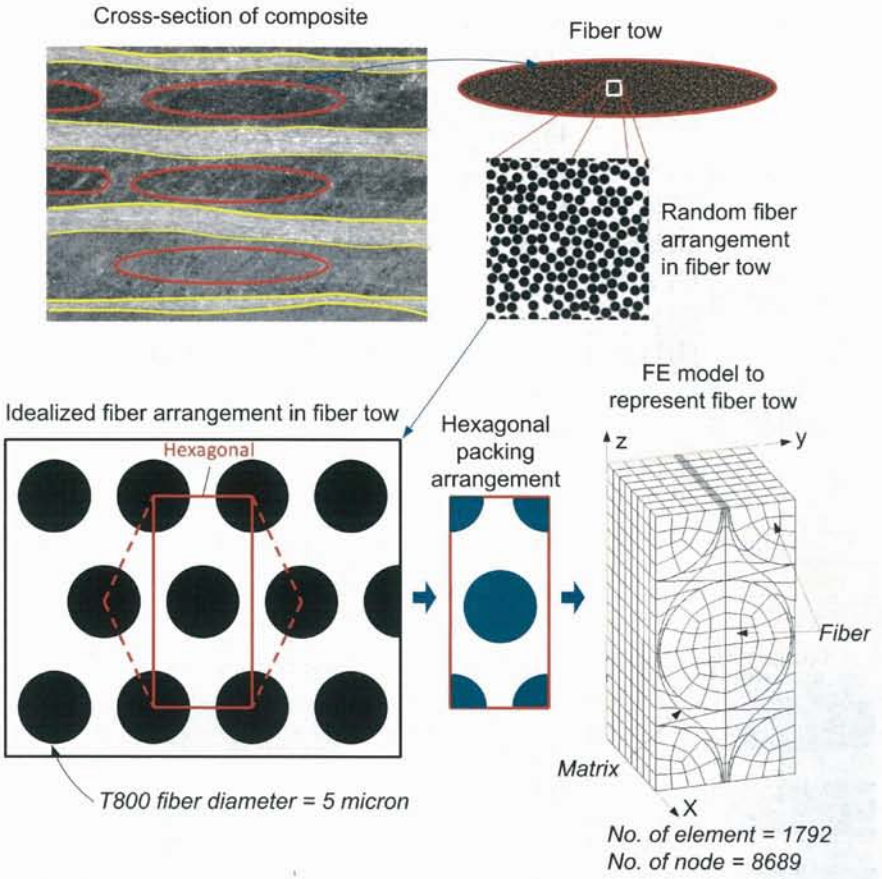

Figure 2.29: Development of micromechanics model to evaluate thermo-elastic constants of fiber tow

2.4.3 Prediction of thermo-elastic constants of composites

Mesomechanics models used to obtained thermo-elastic constants of unstitched, stitched 6×6 and stitched 3×3 are developed using MSC.Patran 2008. The models are developed based on several assumptions pertaining to geometrical characteristic of unstitched, stitched 6×6 and stitched 3×3 composites. Several assumptions are made:

- To reduce the complexity of the modeling of present composite system, which is $[+45/90/-45/0_2/+45/90_2/-45/0]_S$, only four tows are modeled with following composition: 0° tows (30%), 90° tows (30%), $+45^\circ$ tows (20%) and -45° tows (20%)
- For all models, cross-section of fiber tow is assumed rectangular (see Fig. 2.30a)
- To simplify the modeling of stitched composites, resin-rich region is assumed resin channel (see Fig. 2.30b)
- In stitched composite models, cross-section of stitch thread is assumed octagonal (see Fig. 2.30c), and the width is 0.25 mm.

Table 2.9: Thermo-elastic constants of fiber tow obtained from micromechanics models

Properties	Unit	Unstitched	Stitched 6×6	Stitched 3×3
V_f	%	45	47	49
E_x	GPa	133.9	140.1	146.2
E_y	GPa	8.389	8.356	8.322
E_z	GPa	8.431	8.298	8.165
G_{xy}	GPa	9.879	9.935	9.991
G_{xz}	GPa	9.902	9.995	10.09
G_{yz}	GPa	4.790	4.852	4.913
ν_{xy}	-	0.347	0.348	0.348
ν_{xz}	-	0.329	0.338	0.348
ν_{yz}	-	0.472	0.464	0.455
α_x	10^{-6}/K	1.219	1.377	1.535
α_y	10^{-6}/K	31.53	41.78	52.03
α_z	10^{-6}/K	31.73	42.00	52.27

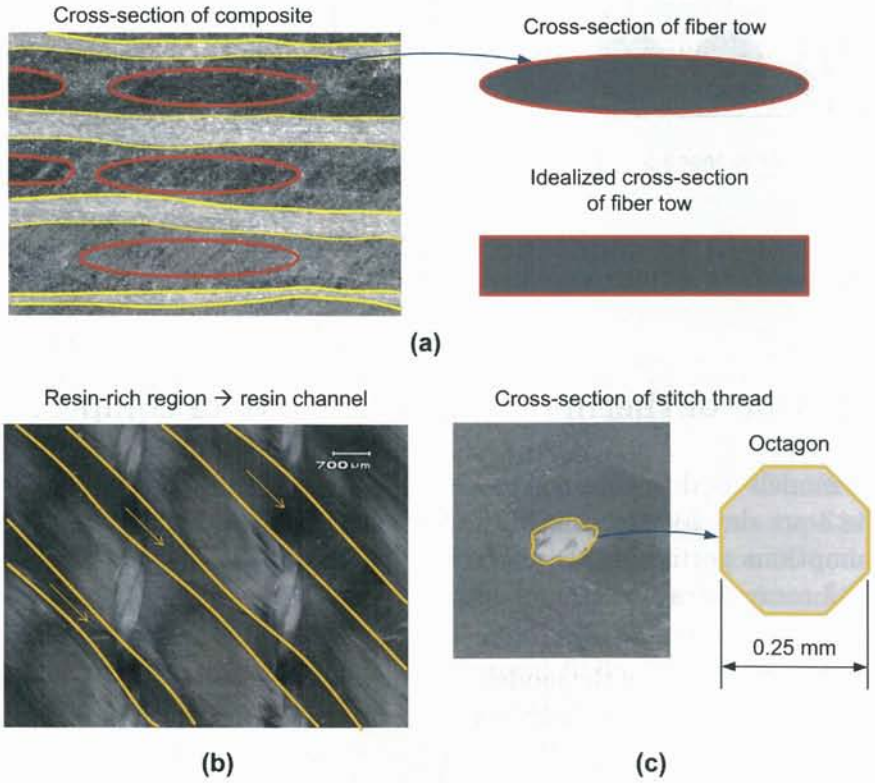

Figure 2.30: Assumptions for building mesomechanics models (a) idealized fiber tow, (b) resin-rich region, (c) cross-section of stitch thread

Geometry of mesomechanics model for unstitched composites can be seen in Fig. 2.31, while the idealization process in the modeling of stitched 6×6 and stitched 3×3 can be seen in Figs. 2.32 and 2.33, respectively. Element type used in the models is hexahedron 20-node. Number of element and nodes are as follows: unstitched (4608 elements, 21425 nodes),

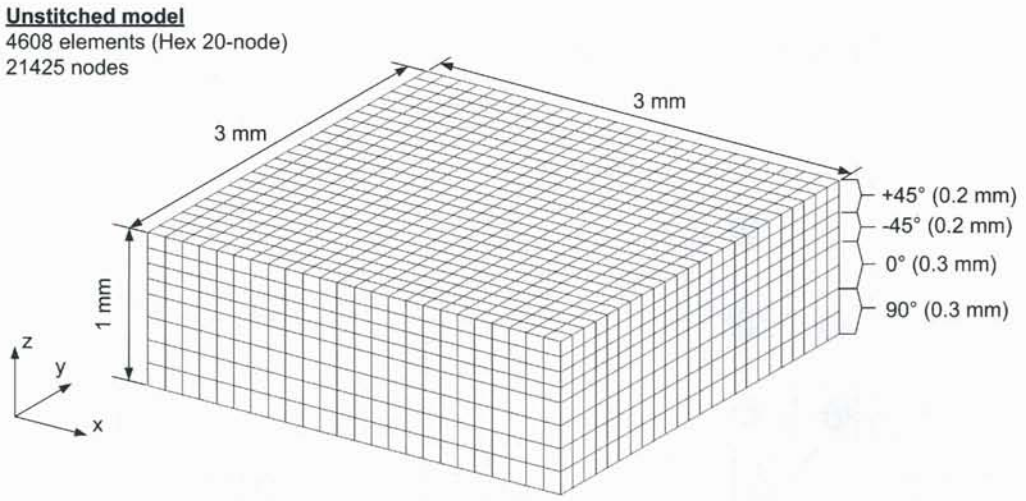

Figure 2.31: Mesomechanics model for unstitched composite

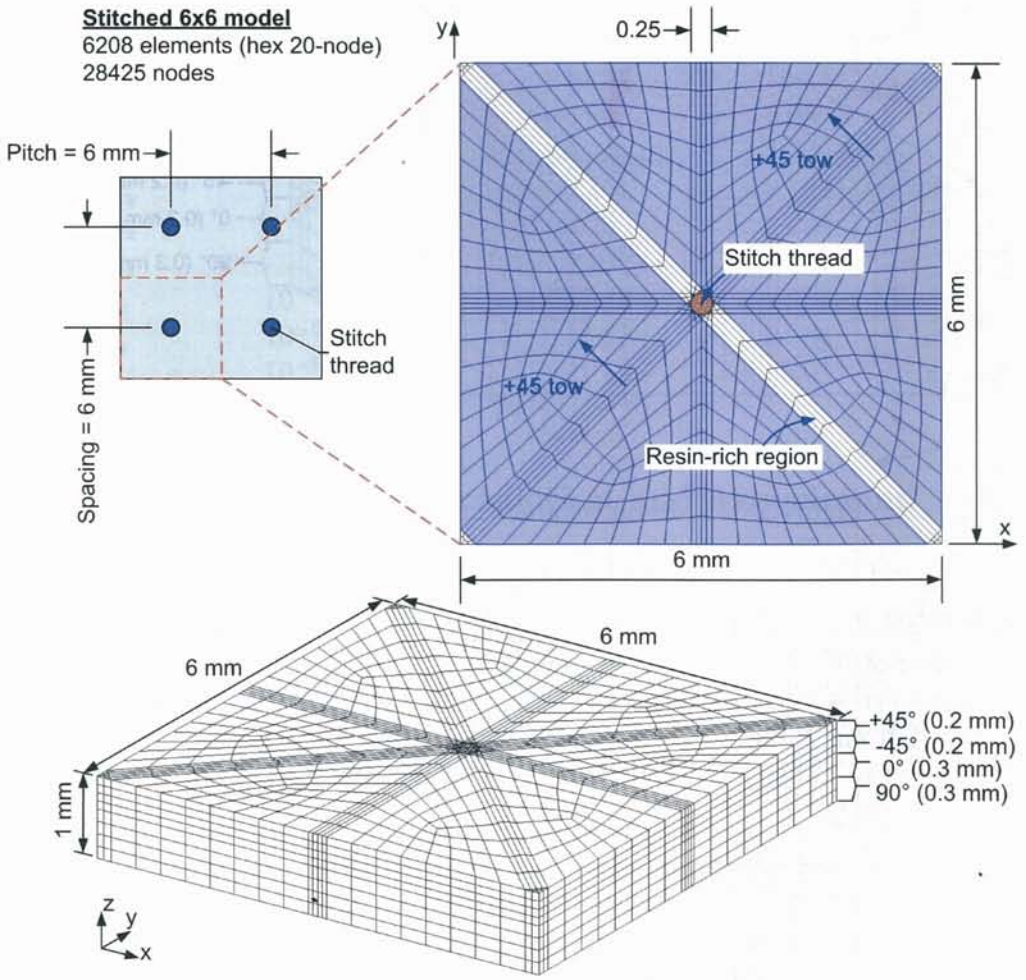

Figure 2.32: Mesomechanics model for stitched 6×6

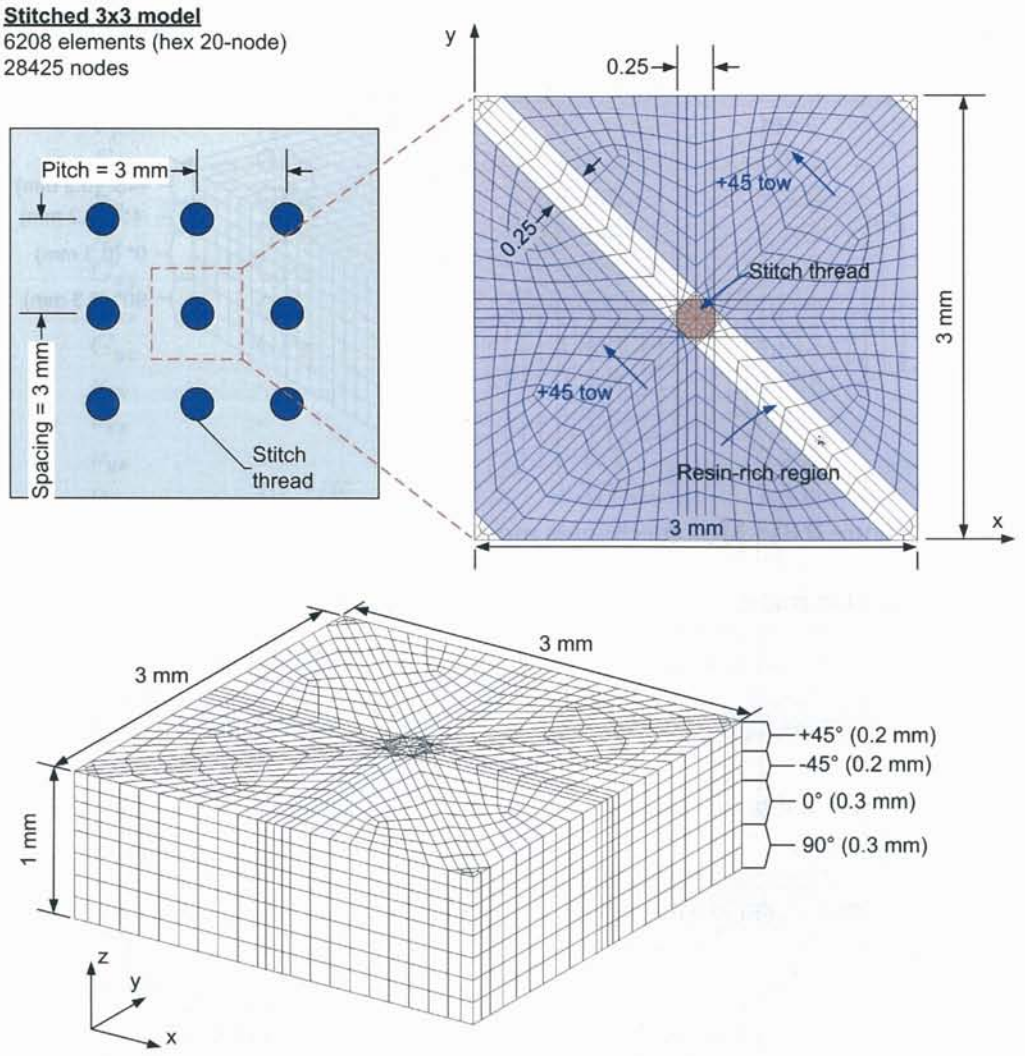

Figure 2.33: Mesomechanics model for stitched 3×3

stitched 6×6 (6208 elements, 28425 nodes), stitched 3×3 (6208 elements, 28425 nodes). Information of number of element and number of node is given in the respective figure. Mechanical and thermal properties of fiber tow used for unstitched, stitched 6×6 and stitched 3×3 models are obtained from Table 2.9. Resin-rich region uses thermo-mechanical properties of XNR/H6813 given in Table 2.1. Properties of Vectran stitch thread can also be reviewed in Table 2.1.

Table 2.10 shows the mechanical properties and coefficient of thermal expansion of unstitched, stitched 6×6 and stitched 3×3 evaluated by using homogenization method. In terms of E_x, unstitched composites clearly exhibit larger value than stitched 6×6 and stitched 3×3. E_x of unstitched composites is 59.29 GPa, while that of stitched 6×6 and stitched 3×3 are 53.46 GPa and 55.34 GPa, respectively. Similar tendency is also observed for E_y, in which unstitched composites show larger value. In this case, the lower values of E_x and E_y in stitched composites is due to resin-rich region in the form of resin channel. On the other hand, as observed in Table 2.10, E_z of stitched 6×6 and stitched 3×3 is 74% and 67%,

respectively, higher than that of unstitched composites. This indicates that stitch thread, that is oriented in z-direction, is effective in improving the through-thickness modulus of composites. This implies that further improvement of through-thickness modulus may be achieved by utilizing thicker and stiffer stitch thread. However, thicker stitch thread may further reduce in-plane properties of composites. In terms of shear moduli of G_{xy}, G_{xz} and G_{yz}, no significant difference is observed when comparison is made among unstitched, stitched 6×6 and stitched 3×3. This is originated from the fact that the shear moduli of fiber tow, resin and stitch thread are similar. Poisson's ratio of stitched 6×6 and stitched 3×3 is slightly smaller than that of unstitched composites indicating that lateral deformation in stitched composites may be restrained by the stitching.

Table 2.10: Thermo-elastic constants of unstitched, stitched 6×6 and stitched 3×3 obtained from mesomechanics models

Properties	Unit	Unstitched	Stitched 6×6	Stitched 3×3
E_x	GPa	59.29	53.46	55.34
E_y	GPa	59.28	53.46	55.11
E_z	GPa	10.35	18.01	17.25
G_{xy}	GPa	19.70	14.52	16.23
G_{xz}	GPa	6.46	6.94	6.99
G_{yz}	GPa	6.46	6.94	7.04
ν_{xy}	-	0.204	0.151	0.182
ν_{xz}	-	0.387	0.205	0.202
ν_{yz}	-	0.387	0.205	0.201
α_x	10^{-6}/K	14.73	17.82	24.97
α_y	10^{-6}/K	14.72	17.82	24.64
α_z	10^{-6}/K	39.20	21.12	30.03

2.4.4 Comparison between prediction and experiment

Results of homogenization method, specifically tensile modulus E_x and Poisson's ratio ν_{xy}, are compared with tensile test results. As shown in Fig. 2.34, E_x of unstitched composites obtained by homogenization method is 59.29 GPa, while that obtained by experiment is 53.1 GPa. Difference of 11.7% is found between homogenization method and experiment. For stitched composites, a better agreement is found between homogenization results and experiments. E_x of stitched 6×6 obtained from homogenization method is 53.46 GPa, while that obtained from experiment is 51.1 GPa. This results in a difference of 4.6%. When E_x obtained by homogenization and experiment for stitched 3×3 is compared, the difference is 7%. The reason for the lower value of E_x in the experiment is probably due to two reasons: lower actual fiber volume fraction in fiber tows, and the fiber waviness that may exist in the actual specimens. Nevertheless, homogenization method in general could capture the tendency of tensile modulus reduction due to the presence of stitch thread.

ν_{xy} of unstitched, stitched 6×6 and stitched 3×3 obtained by experiments is 38.7%, 51.4% and 43.8%, respectively, higher than that obtained by homogenization method (see Fig. 2.35). The large difference of Poisson's ratio between experiment and homogenization method could

be attributed to different method in acquiring the strain values used to evaluate Poisson's ratio. In experiments, strain values are obtained from the strain gages that are attached on the surface of the specimens. The surface of specimen is often resin-rich region that would exhibit larger deformation during loading. On the other hand, the strains used to evaluate Poisson's ratio in homogenization method is obtained from all elements in mesomechanics model, not only from the surface of the models, including elements of fiber tows, resin-rich region and stitch thread (in stitched composites cases). Another reason is that present mesomechanics models have some limitations that the waviness is not modeled, resin-rich region may be of eyelet shape and the composition of tows may have some variations.

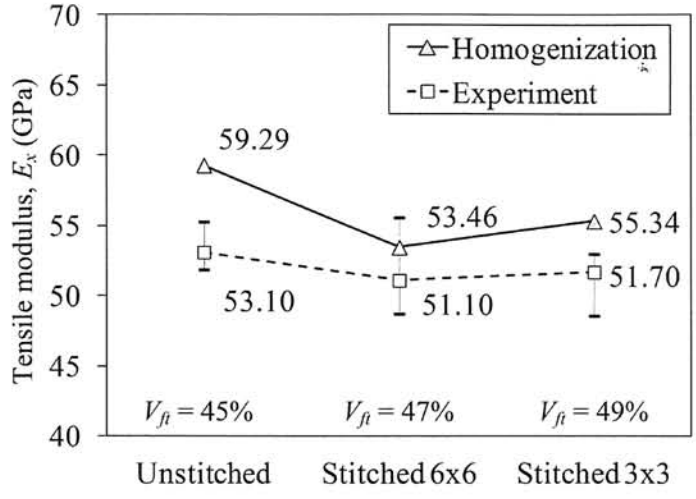

Figure 2.34: Tensile modulus: comparison between experiment and homogenization method

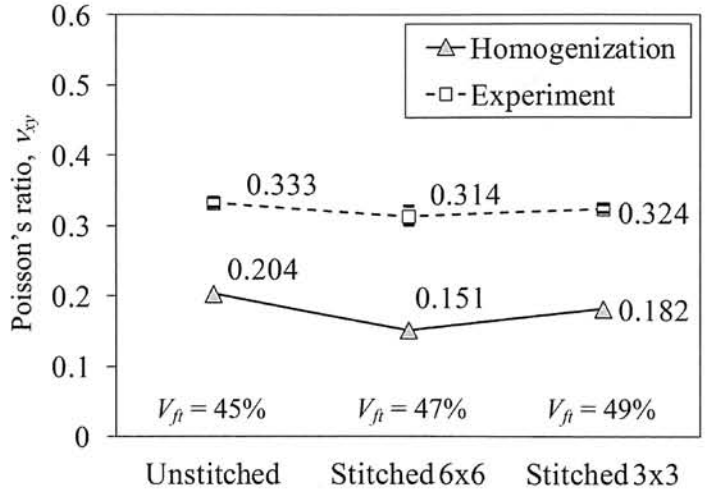

Figure 2.35: Poisson's ratio: comparison between experiment and homogenization method

In summary, despite some idealization and assumptions made in the modeling of fiber tow and composites, it is generally found that homogenization method can predict the tendency of adding stitches into carbon/epoxy that translates into some reduction of tensile modulus and

Poisson's ratio. Homogenization method will be able to predict thermo-elastic constants with better accuracy if the followings are carried out in the modeling processes: (i) adjustment of fiber tow volume fraction to better represents the actual tow; (ii) fiber waviness in in-plane and out-of-plane directions is modeled; (iii) full thickness of the composites is explicitly modeled.

2.5 Concluding Remarks

Tensile test and damage characterization of carbon/epoxy composites stitched with Vectran thread have been performed. Several findings are summarized herein:

- Densely stitched composites ($SD = 0.111/\text{mm}^2$) exhibits higher tensile strength in comparison to moderately stitched composites and unstitched due to an effective impediment of edge delamination. The improvement is around 10%.
- Stitching reduces tensile modulus of carbon/epoxy by approximately 4% due to both in-plane and out-of-plane waviness of 0° tows.
- Failure strain in stitched composites is higher than that of unstitched composites due to the presence of resin-rich region whose plastic deformation helps to reduce stress concentration in intact fibers so as to extend the strain-to-failure.
- Poisson's ratio in carbon/epoxy composites is reduced by around 6% with stitching, and this tendency could be caused by the misalignment of fiber tows due to tautness of stitching, change of tow thickness due to stitching, and modified-lock stitch pattern that restricts the deformation of composite in lateral directions.
- Damage characterization reveals that stitching induces higher density of transverse and oblique cracks. The reason for this behavior is mainly due to the fiber compaction mechanism that reduces the spacing between fibers in off-axis plies, and eventually triggers early fiber/matrix debonding.
- Compaction effect between two stitch lines is quantitatively confirmed by burn-off test and optical microscopy on volumetric section of stitched composites, specifically between two stitch lines. It is revealed that the fiber compaction indeed occurs as indicated by an increase of local fiber volume fraction. Optical microscopy also confirms that stitching reduces the gap between fibers, and thus, increases the fiber volume fraction.
- Homogenization method is found to be accurate in predicting thermo-mechanical properties of unstitched and stitched composites. Despite some simplifications, tensile modulus obtained by homogenization method is in a good agreement with experiments. However, comparison of Poisson's ratio between homogenization and experiments yields a difference of above 30%. This is due to the fact that during experiment the strain values (longitudinal and transverse strains) used to calculate Poisson's ratio are actually the values of specimen surface, which is resin-rich region. Other reasons include

the limitation of mesomechanics models that did not include waviness, adjustment of fiber volume fraction, and incorporation of finite thickness effect.

- As a general conclusion of this part, it is proposed that in order to improve the tensile properties of carbon/epoxy composites, following methods can be pursued: (i) to employ stitched 3×3 configuration so as to impede the delamination growth, (ii) to minimize in-plane and out-of-plane waviness in carbon/epoxy so as to maintain tensile modulus, (iii) to reduce the thickness of off-axis tows (90°, +45°, −45°) so as to increase the stress level for crack initiation (crack onset)

Chapter 3

Vectran-stitched carbon/epoxy composites under compression

3.1 Overview

This chapter discusses experimental investigation of compressive characteristics and damage mechanisms of Vectran-stitched carbon/epoxy composites. Composite specimens under investigation are the same as in Chapter 2, which are unstitched, stitched 6×6 200d and stitched 3×3 200d. Additionally, two more specimens having thicker stitch thread are prepared, namely stitched 6×6 400d and stitched 3×3 400d. In this chapter, effect of stitch density and stitch thread thickness on compressive properties of carbon/epoxy composites is assessed. Correlation between compressive properties and fiber waviness is also established. Damage mechanisms in unstitched and stitched composites under compression are discussed in details.

3.2 Experimental Details

3.2.1 Materials

Material system used in compression test is Vectran-stitched carbon/epoxy composites. Carbon fiber is T800SC-24kf, while the epoxy is XNR/H6813 Denatite. Stitch material is Vectran with linear density of 200 denier (200d) and 400 denier (400d). Thermo-mechanical properties of T800SC, XNR/H6813 and Vectran can be reviewed in Table 2.1. Tow orientation is $[+45/90/\text{-}45/0_2/+45/90_2/\text{-}45/0]_S$. Stitch pattern is modified-lock stitch (see again Fig. 2.1). Five composite specimens are prepared:

- unstitched ($SD = 0.0$, $V_s = 0.0\%$)
- stitched 6×6 200d ($SD = 0.028/\text{mm}^2$, $V_s = 0.088\%$)
- stitched 6×6 400d ($SD = 0.028/\text{mm}^2$, $V_s = 0.175\%$)

- stitched 3×3 200d ($SD = 0.111/\text{mm}^2$, $V_s = 0.350\%$)
- stitched 3×3 400d ($SD = 0.111/\text{mm}^2$, $V_s = 0.700\%$)

Specimen codes for unstitched, stitched 6×6 200d, stitched 6×6 400d, stitched 3×3 200d and stitched 3×3 400d are CN-x, CS62-x, CS64-x, CS32-x and CS34-x, respectively. x denotes specimen numbering. Specification of compression specimens including stitch parameters, V_f of specimens, dimension, sample quantity, is given in Table 3.1.

3.2.2 Compression test specimens

Dimension of compression test specimen is 80 mm long and 15 mm wide. Schematic of the test specimen can be seen in Fig. 3.1. This dimension conforms with compression test fixture used in present experiment, namely NAL-II. NAL-II is a metallic fixture for non-hole compressive (NHC) test proposed by Japan Aerospace Exploration Agency [88]. Test specimen is prepared by cutting the cured plate using water-cooled cutting machine AC-400CF. After cutting process, edges of the specimen are polished using abrasive rotating sandpapers with following roughness levels: rough (grit #500), moderately smooth (grit #1000) and very smooth (grit #1200). Gage area in compression test specimen is 10 mm long and 15 mm wide. Longitudinal and transverse strain gages (Kyowa) denoted as SG1 and SG2 are attached on front and back faces of specimen, respectively.

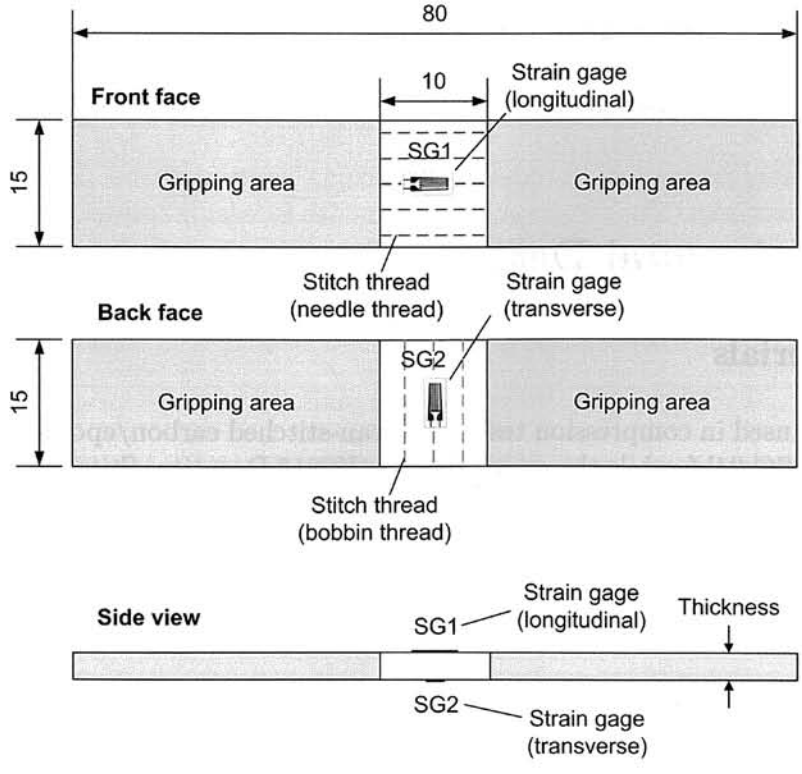

Figure 3.1: Compression test specimen of NAL-II (dimension in mm)

Table 3.1: Specification of test specimens for compression test

Parameter	Unit	Unstitched	Stitched 6×6 200d	Stitched 6×6 400d	Stitched 3×3 200d	Stitched 3×3 400d
Code	-	CN-x	CS62-x	CS64-x	CS32-x	CS34-x
s	mm	-	6	6	3	3
p	mm	-	6	6	3	3
SD	$1/mm^2$	-	0.028	0.028	0.111	0.111
μ	denier (tex)	-	200 (22.2)	400 (44.4)	200 (22.2)	400 (44.4)
V_s	%	-	0.088	0.175	0.350	0.700
V_f	%	53.3 ± 0.3	53.8 ± 0.4	52.6 ± 0.0	54.3 ± 0.2	54.1 ± 0.0
t	mm	4.158 ± 0.013	4.107 ± 0.015	4.142 ± 0.015	4.100 ± 0.014	4.095 ± 0.004
w	mm	14.90 ± 0.01	14.80 ± 0.09	4.095 ± 0.004	14.98 ± 0.03	15.00 ± 0.02
l	mm	79.81 ± 0.45	79.87 ± 0.05	79.95 ± 0.10	79.95 ± 0.10	79.99 ± 0.02
W	g	7.47 ± 0.06	7.40 ± 0.10	7.40 ± 0.0	7.43 ± 0.05	7.38 ± 0.05
ρ	g/cm^3	1.51 ± 0.0	1.52 ± 0.01	1.50 ± 0.01	1.51 ± 0.01	1.50 ± 0.01
Quantity	-	3	3	5	5	5

3.2.3 Compression test fixture

As mentioned, NAL-II fixture is used in compression test. It is selected because, as already demonstrated by Ogasawara and Ishikawa [87], experimental results obtained utilizing NAL-II are reliable, repeatable and similar to those obtained by well-known standards of SRM-1 (SACMA) and ASTM D6641 (CLC). The specimen size compatible with NAL-II is also relatively small that it reflects its efficiency. Another advantage is that the specimen does not require end-tabs since NAL-II fixture provides two metal supports that give sufficient clamping effect. Fig. 3.2a shows NAL-II fixture. The fixture consists of two main parts, namely the supports and alignment collar. The supports consisting of two components (Support-1, Support-2) are used to clamp the specimen at both ends, to provide base support, and to prevent brooming of specimen ends. In each support, four screws are used to clamp the specimen, specifically in gripping areas. After the specimen has been clamped, the alignment between Support-1 and Support-2 is checked. This alignment process is done by pre-test alignment apparatus shown in Fig. 3.2b. Before the pre-test alignment process the screws are not heavily tightened to allow a smooth entrance into the alignment apparatus. When both supports have been aligned, screws are tightened within the alignment apparatus. Afterwards, specimen and the supports are taken out from pre-test alignment apparatus, and inserted into the alignment collar. The collar contains two windows with rounded corners. These windows provide access for strain gage cables and for visual observation of specimen during compression test.

3.2.4 Compression test procedures

Compression test is carried out using *Instron 4505* and its renewed system of 5500 with maximum load cell capacity of 100 kN. Test setup utilizing NAL-II fixture on Instron 4505 is shown Fig. 3.2c. Loading rate applied during compression test is 1 mm/min. Environment setting is set at room temperature of 293 K (20 °C). Computer terminal with Bluehill software is used to register load and displacement data. Stress is obtained by dividing the load with gross area of specimen ($w \times t$). Strains are obtained from SG1 and SG2 strain gages positioned in the configuration shown in Fig. 3.1. For each specimen type, three to five test samples are tested to obtain compressive properties. Compressive properties obtained during the tests are compression strength (σ_{uc}), failure strain (ε_f), compression modulus (E_x) and Poisson's ratio (ν_{xy}).

3.2.5 Damage characterization procedures

Damage characterization is carried out by conducting interrupted test and optical microscopy on specially-designed test specimens. The objectives are to capture the damage process, and to have comparative damage mechanisms between unstitched and stitched composites under compression. Based on the observations reported by other researchers [40, 101, 114], one of the damage mechanisms in composites under compression is fiber kinking, which generally occurs in 0 ° fibers. Fiber kinking is generally triggered by initial fiber waviness and shear yield stress of matrix [27, 43, 82]. In order to capture the development of fiber kinking

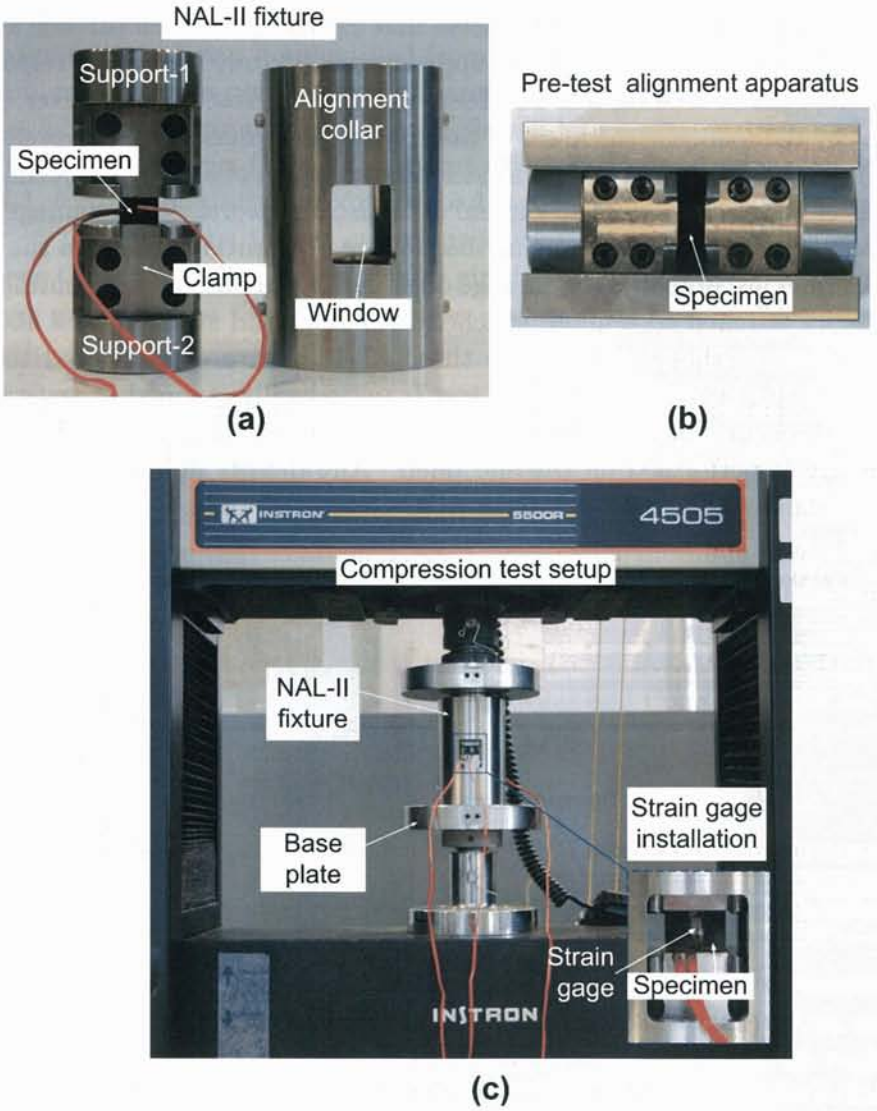

Figure 3.2: (a) NAL-II compression test fixture, (b) pre-test alignment apparatus, (c) compression test setup

and subsequent damage modes, a test specimen that clearly exhibits internal part of 0° tow is intentionally made to aid damage observation. This test specimen is called *damage observation specimen*, and the process to produce such specimen is shown in Fig. 3.3a. To produce damage observation specimen the upper part of original compression test specimen is firstly trimmed in in-plane direction (x-y plane) up to a level whereby upper 0° tow is approximately cut into half. The trimming process is carried out using water-jet cutting machine (Maruto). After trimming process, two edges and front face of gage region are polished three times using abrasive rotating sandpapers starting from rough (grit #500), moderately smooth (grit #1000), and finally, very smooth (grit #1200). After polishing process, thickness of specimen that is originally around 4.15 mm becomes thinner. Thickness among damage observation specimens varies depending on the position of 0° tow relative to the back face of specimen, that is between 3.1 to 3.4 mm. Fig. 3.3b shows an example of front

face of stitched specimen after trimming process that exhibits 0°, stitch threads and resin-rich region. Using such specimen, any damages appearing in 0° tows, resin-rich region and stitch thread upon compression loading can be observed using microscope. However, it should be mentioned that by reducing the thickness of the specimen the maximum compressive load will be reduced. Thus, the maximum compressive load of damage observation specimen would be lower than that of compression test specimen. It is also noteworthy that damage observation specimen is non-symmetrical, which means that failure may initially occur in the front face of 0° tow. Five samples are prepared for damage observation specimens representing unstitched, stitched 6×6 200d, stitched 6×6 400d, stitched 3×3 200d and stitched 3×3 400d. Damage observation specimen is then inserted into the NAL-II fixture. Interrupted test is carried out with loading rate of 0.5 mm/min. The test is periodically stopped at several load levels before final failure occurs. In each level, the specimen is taken out from the machine, and optical microscopy is performed on the specimen. Any defects appearing in the front face and edges of the damage observation specimen are captured and noted.

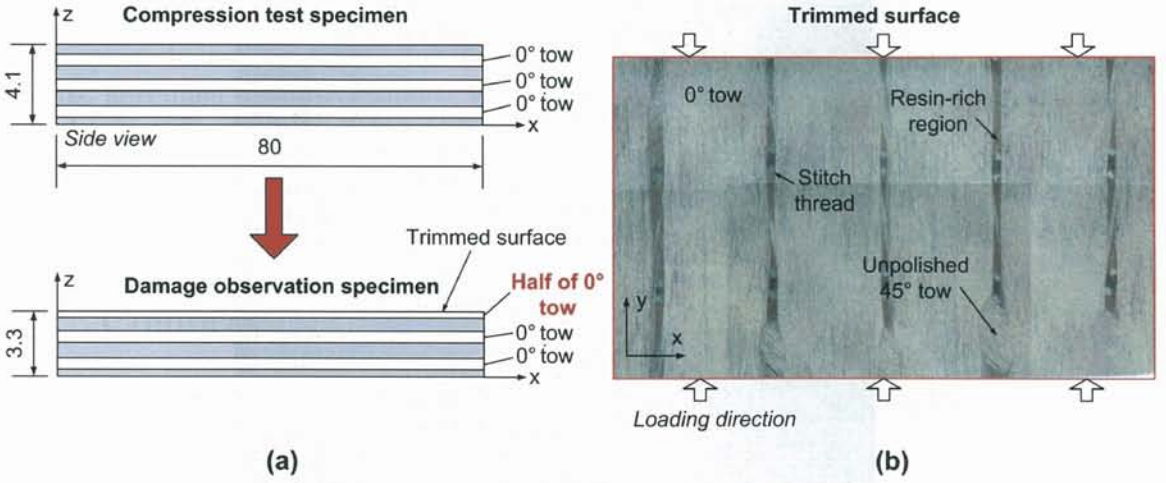

Figure 3.3: (a) Process to produce damage observation specimen, (b) trimmed surface of gage area in damage observation specimen

3.3 Experimental Results and Discussion

3.3.1 Load-displacement and stress-strain curves

Fig. 3.4 shows load-displacement and stress-strain curves for unstitched composites, stitched 6×6 200d, stitched 6×6 400d, stitched 3×3 200d and stitched 3×3 400d. The load, displacement, stress and strain actually lie on the negative axis, but for convenience, they are displayed in positive axis. In general, all load-displacement curves exhibit linearity before maximum load is reached regardless stitch density and stitch thread thickness. After maximum load is reached, almost all curves experience abrupt drop to a level whereby specimen could not sustain additional loads. This abrupt drop indicates that the compressive failure is a sudden event. The linearity suggests that there is a minimum amount of damage processes

that can be inferred from load-displacement curves. This is different from general tension case whereby damage initiation can be identified from a knee-point in load-displacement curves. In compression case, a knee-point is not apparent in load-displacement curves. However, there are cases whereby maximum load is not followed by an abrupt drop, and this is shown by CN-1 and CN-3 specimens (Unstitched) and CS62-2 specimen (Stitched 6x6 200d). In specimen CN-1, for instance, after maximum load is reached at 30.55 kN with corresponding displacement of 1.56 mm, the jagged curve ensues until the displacement is reaching 2.69 mm. Specimens CN-3 and CS62-2 also display similar jagged curves although the drops are not as many as in CN-1 case. The jagged curve is caused by fiber kinking occurred outside the gage length.

Stress-strain curves of all specimen types are given in Fig. 3.5. Maximum stress obtained from each curve is used to calculate compressive strength σ_{uc}. For the specimens exhibiting jagged curves (CN-1, CN-3, CS62-2), σ_{uc} is obtained by dividing the maximum load prior to the first drop prior to jagged pattern. Failure strain ε_f is obtained from the longitudinal strain data corresponded to the maximum load. Compressive modulus E_x is calculated based on the strains obtained from SG1 (longitudinal) and their corresponding stresses. Two stress values at $\sigma = 0.1\%$ and 0.3% are used to calculate compressive modulus. Poisson's ratio ν_{xy} are calculated based on longitudinal and transverse strain values. Procedure to calculate compressive strength, failure strain, compressive modulus and Poisson's ratio can be reviewed in Ref. [10].

3.3.2 Failure mode

Post-mortem observation utilizing optical microscope is performed on each specimen to observe the failure mode of composites under compression. The failure under compression is usually catastrophic regardless stitched or unstitched. Fig. 3.6 shows an example of edge condition in stitched specimens before and after compression loading. Two vertical lines indicate the limit of 10 mm gage length. Before the test, two locations of maximum waviness amplitude in 0° tows are indicated in Fig. 3.6a. After the test (see Fig. 3.6b), it is observed that 0° tows are fractured at several locations where the maximum waviness is residing. The fracture location in 0° tows is usually preceded by fiber kinking. Other failure modes also exist: delamination at the interfaces of $(0^\circ/-45^\circ)$ and $(-45^\circ/0^\circ)$; delamination adjacent to the fractured 0° tows at specimen edge; matrix crackings in 90°, $+45^\circ$, -45° tows.

Fiber kinking initiates at a location whereby maximum fiber waviness exists. Mechanism of fiber kinking in 3-D composite system has been described by Tong et al. [107]. Upon compressive loading, kinking will start to appear when the matrix around misaligned fibers is undergoing plastic yielding. This matrix yielding allows a portion of fibers within 0° tow to rotate in parallel, which eventually causes fiber fracture over two planes. Characteristics of fiber kinking found in present experiment is shown in Fig. 3.7a, whereby a band of 0° fibers is broken. Schematic of fiber kinking drawn based on Fig. 3.7a is shown in Fig. 3.7b. Parameters in fiber kinking are identified as kink band width and kink angle. In Fig. 3.7b, kink band width is approximately 40 μm, whilst kink angle is 25. The magnitude of kink band width may vary depending upon the thickness of fiber tow and the degree of waviness.

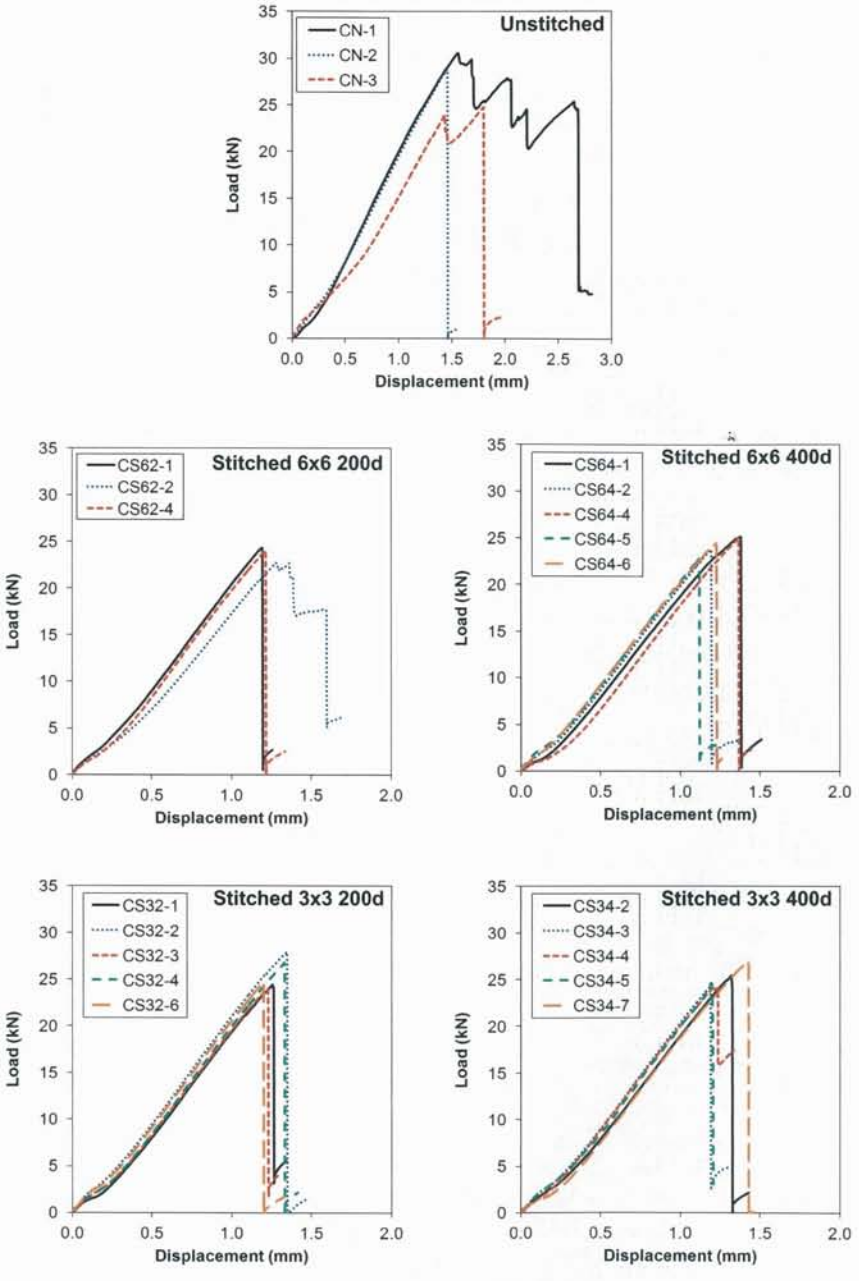

Figure 3.4: Load-displacement curves of unstitched composites, stitched 6×6 200d, stitched 6×6 400d, stitched 3×3 200d and stitched 3×3 400d

3.3.3 Compressive properties

Compressive properties, namely compressive strength, compressive modulus, Poisson's ratio and failure strain, for all specimen types are given in Table 3.2. Normalized compressive strength and normalized compressive modulus are also given Table 3.2 as well. Method to obtain normalized properties can be reviewed in Section 2.3.5.

Table 3.2: Compressive properties of unstitched and stitched composites (stitched 6×6 200d, stitched 6×6 400d, 3×3 200d and 3×3 400d

Parameter	Unit	Unstitched	Stitched 6×6 200d	Stitched 6×6 400d	Stitched 3×3 200d	Stitched 3×3 400d
Code	-	CN-x	CS62-x	CS64-x	CS32-x	CS34-x
P_{max}	kN	28 ± 3	24 ± 1	24 ± 1	26 ± 2	25 ± 1
d_{max}	mm	1.61 ± 0.17	1.23 ± 0.05	1.26 ± 0.11	1.27 ± 0.06	1.27 ± 0.10
σ_{uc}	MPa	453 ± 49	390 ± 15	395 ± 19	416 ± 27	408 ± 20
σ_{ut}^{n}	MPa	453 ± 49	394 ± 16	392 ± 19	427 ± 28	416 ± 20
ε_f	%	2.01 ± 0.22	1.57 ± 0.12	1.57 ± 0.14	1.59 ± 0.08	1.59 ± 0.13
E_x	GPa	49.2 ± 10.1	49.6 ± 9.1	52.8 ± 8.2	52.2 ± 6.1	49.4 ± 7.0
E_x^n	GPa	49.2 ± 10.1	50.1 ± 9.1	52.4 ± 8.1	53.6 ± 6.2	50.4 ± 7.2
ν_{xy}	-	0.346 ± 0.059	0.319 ± 0.089	0.332 ± 0.064	0.339 ± 0.059	0.308 ± 0.075

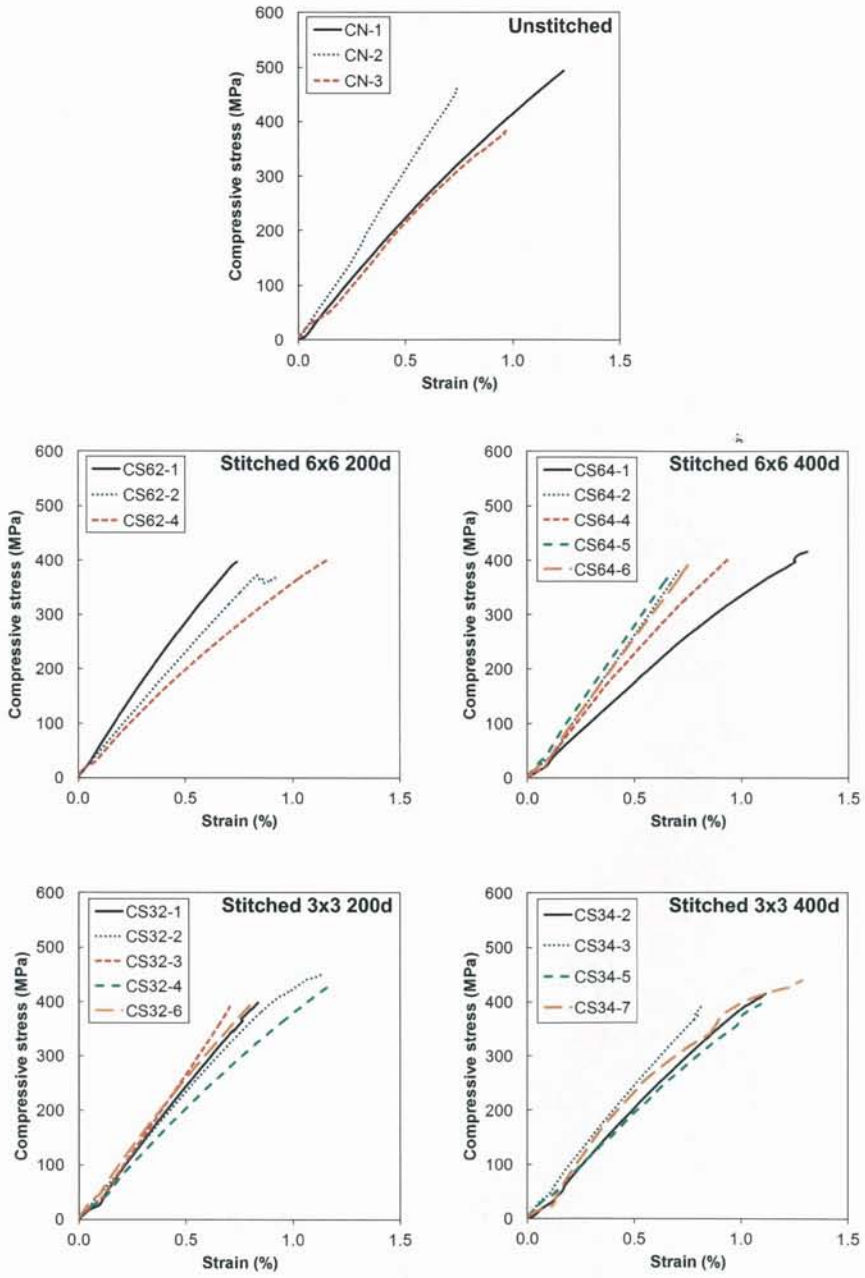

Figure 3.5: Stress-strain curves of unstitched composites, stitched 6×6 200d, stitched 6×6 400d, stitched 3×3 200d and stitched 3×3 400d

Compressive strength

Fig. 3.8 shows the comparison of compressive strength amongst specimens. Coefficient of variation (C.O.V.) across specimen types ranges between 4.0% and 10.8%, which indicates good dispersion amongst samples. Average compressive strength of unstitched composite is 453 MPa, while that of stitched 6×6 200d and stitched 3×3 200d is 390 MPa and 416 MPa, respectively. In comparison to unstitched composites, compressive strength of stitched

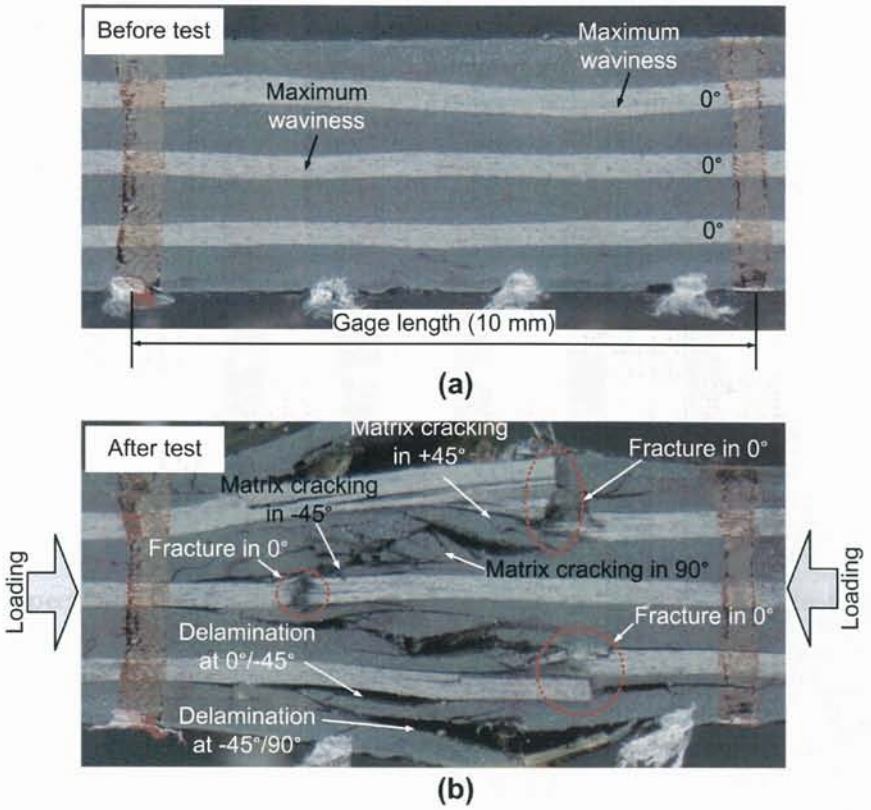

Figure 3.6: Edge of specimen (a) before compression test, (b) after compression test

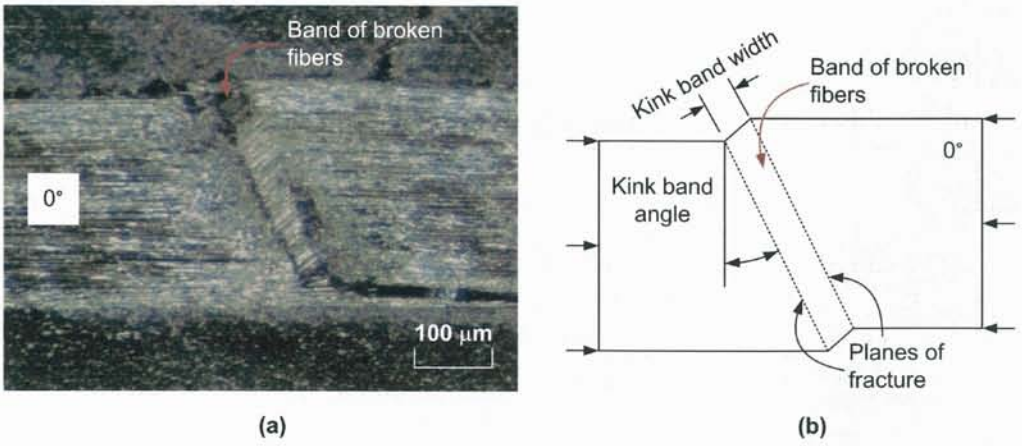

Figure 3.7: Fiber kinking in 0° tow of carbon/epoxy composites under compression (a) photomicrograph, (b) schematic

6×6 and stitched 3×3 is lower with difference of 13.9% and 8.2%, respectively. Compressive strength of stitched 6×6 400d and stitched 3×3 400d is 395 MPa and 408 MPa, respectively. The compressive strength of stitched 6×6 400d and stitched 3×3 400d is 12.8% and 9.9%, respectively, lower than that of unstitched composites. This indicates that stitched composites with 400 denier thread, similar to those having 200 denier thread, also experience lower compressive strength in comparison to unstitched composites. In other words, regardless

stitch density or stitch thread thickness, compressive strength of stitched composites is lower than that of unstitched composites. Even when the compression strength is normalized with fiber volume fraction, the compressive strength of stitched composites is still below that of unstitched one. This suggests that fiber volume fraction plays minimum effect, and that other factors may seem to govern the reduction of compression strength in stitched composites.

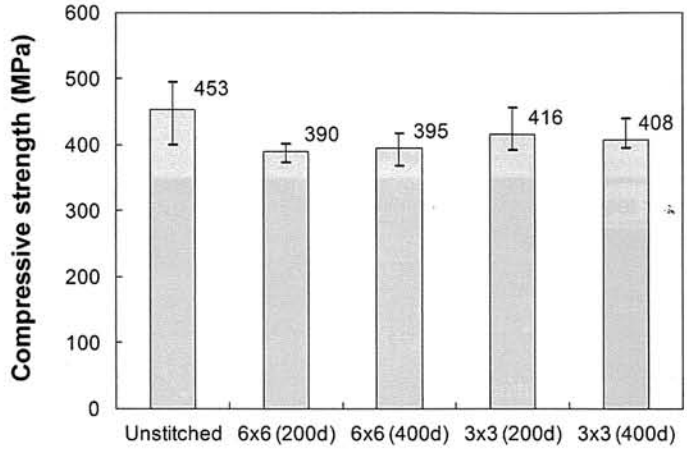

Figure 3.8: Compressive strength

Compressive modulus

Fig. 3.9 shows the comparison of compressive modulus (E_x) amongst specimens. In general, E_x of stitched composites is similar with that of unstitched composites regardless stitch density or thread thickness. Nonetheless, slight increase of E_x is also observed. Average E_x of unstitched is 49.2 GPa, while that of stitched 6×6 200d and stitched 3×3 200d is 49.6 GPa and 52.2 GPa, respectively. Stitched 6×6 200d and stitched 3×3 200d exhibit 0.89% and 6.10% higher modulus as compared to unstitched composites. With thicker thread, it is found that compressive modulus of stitched composites is also slightly higher. E_x of stitched 6×6 400d is 52.8 GPa, while that of stitched 3×3 400d is 49.3 GPa. Compressive modulus of stitched 6×6 400d and stitched 3×3 400d is 7.2% and 0.4%, respectively, higher than that of unstitched composites. After normalization with respect to V_f, normalized compressive strength of stitched 6×6 200d and stitched 3×3 400d is comparable with that of unstitched composites, which means that the modulus increase is partly related to the higher V_f. However, compressive strength of stitched 6×6 200d and stitched 3×3 200d is still higher than that of unstitched, although normalization has been performed. This slight increase seems to be related with the geometry, and in this case, it is the gage length. Longer gage length seems to produce slightly higher compressive modulus.

Failure strain

Failure strain (ε_f) of stitched 6×6 200d and stitched 3×3 200d under compression is lower than that of unstitched composites. ε_f of stitched 6×6 200d and stitched 3×3 200d is 1.57%

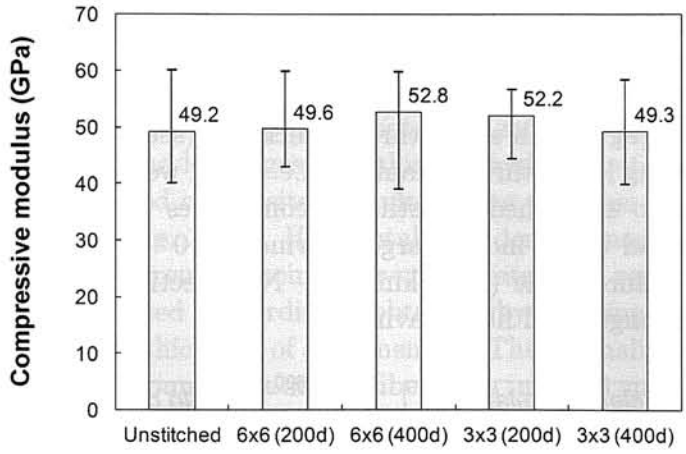

Figure 3.9: Compressive modulus

and 1.59%, respectively, while that of unstitched composites is 2.01%. On the other hand, ε_f of both stitched 6×6 400d and stitched 3×3 400d is 1.59%. In comparison to unstitched composites, ε_f of both stitched specimens having 400d thread thickness is 20.9% lower. The lower failure strain stitched composites may seem to follow the trend of compressive strength, in which the relatively lower strength exhibited by stitched composites is accompanied by lower failure strain. Hence, the reason causing the lower failure strain is also similar with that causing the lower compressive strength, i.e. fiber waviness.

Poisson's ratio

Table 3.2 shows that Poisson's ratio (ν_{xy}) of unstitched is 0.346, which is 7.7% and 2.0% higher than that of stitched 6×6 200d (0.319) and stitched 3×3 200d (0.339), respectively. ν_{xy} of stitched 6×6 400d is 0.332, whilst that of stitched 3×3 400d is 0.308. ν_{xy} of stitched 6×6 400d is lower that that of unstitched composites, which is 0.346. Reasons for the change of Poisson's ratio are fiber waviness due to stitching, and the change of thickness distribution of fiber tows.

3.3.4 Effect of stitch parameters on compressive properties

It is already shown that, in general, stitching degrades compressive strength of carbon/epoxy composites. However, it is not yet clear which stitch parameter that significantly affects the strength reduction. A correlation between compressive strength and stitch parameters is therefore made for all specimen types (unstitched, stitched 6×6 200d, stitched 6×6 400d, stitched 3×3 200d and stitched 3×3 400d). The stitch parameters are stitch density (SD), stitch content (V_s) and stitch thread thickness.

Fig. 3.10a shows the relationship between compressive strength and stitch density. $SD = 0.0$ for unstitched composites; $SD = 0.028/\text{mm}^2$ for stitched 6x6; $SD = 0.111/\text{mm}^2$ for stitched 3x3. It is shown that the correlation between compressive strength and stitch density is not clear. It indicates that higher stitch density does not always result in lower compressive

strength. When compressive strength is plotted against stitch content (see Fig. 3.10b), no clear correlation is found between them. Similar to stitch density, stitch content does not seem to control the compressive strength of carbon/epoxy. However, when the correlation is made between compressive strength with stitch thread thickness (see Fig. 3.10c) it is evident that stitched composites having larger thread diameter, i.e. 400d, would exhibit lower compressive strength in comparison to unstitched and stitched composites with 200d thread. The reason is that larger stitch thread would induce larger waviness of 0° tows, which are the principal tows that control the failure mode (fiber kinking). Next section deals with the correlation between compressive strength and fiber waviness.

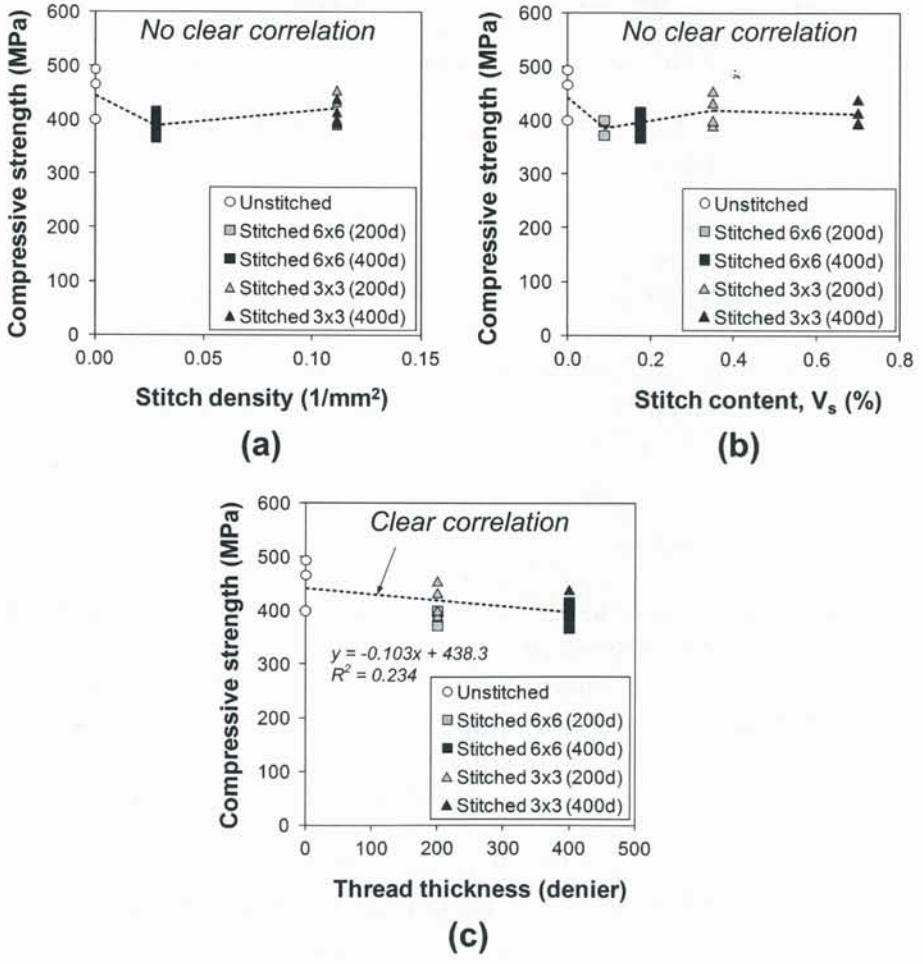

Figure 3.10: (a) Compressive strength vs. stitch density, (b) compressive strength vs. stitch content, (c) compressive strength vs. thread thickness

3.3.5 Effect of fiber waviness on compressive properties

Fiber waviness in all specimen types

Measurement of fiber waviness (out-of-plane and in-plane) is performed for 0° fiber tows of all specimen types under compression. Technique to measure waviness has been shown in Section

2.2.7, and same data is shared for tension and compression tests. Nevertheless, to provide a better visualization on how to extract the out-of-plane waviness, for instance, Fig. 3.11 can be observed. The measurement of out-of-plane waviness is done on the right and left edges of the gage length. In Fig. 3.11a, it is displayed that three misaligned 0 ° tows (upper, middle, lower) are apparent in right and left edges. For this particular set of data, the specimen code is CN-3, which is an unstitched composite. Results of the waviness measurement for totally six 0 ° tows can be seen in Fig. 3.11b. Horizontal axis denotes normalized x-coordinate or the relative position of measurement point in x-coordinate with respect to the gage length (l_g). Vertical axis is normalized z-coordinate obtained by dividing the relative position of centerline of 0 ° tow with the thickness of specimen (t). The normalization aims to provide a percentage of waviness. It is found that six 0 ° fiber tows in CN-3 specimen exhibit waviness of less than 10%.

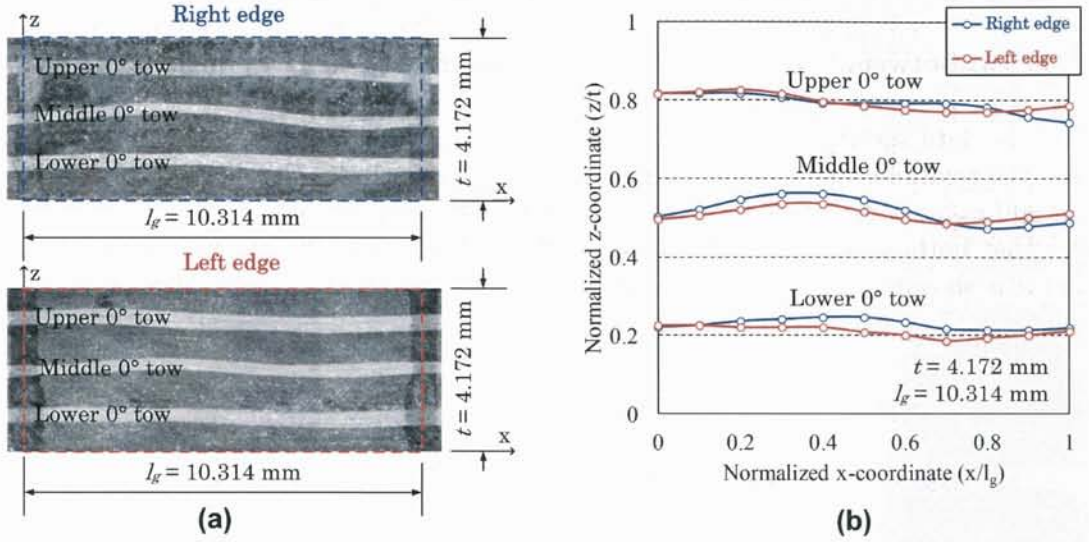

Figure 3.11: (a) Out-of-plane waviness of 0 ° tows on right and left edges (sample code: CN-3) (b) measurement result of out-of-plane waviness amplitude

Maximum amplitude of waviness (a_{out}) is then identified for six tows. Six values are then obtained and averaged. The average value is used as a representative a_{out} of each specimen. For example, 0 ° tows of the right edge of CN-3 specimen have maximum amplitudes of 308 μm (upper tow), 247 μm (middle tow) and 103 μm (lower tow). 0 ° tows of the left edge have maximum amplitudes of 166 μm (upper tow), 104 μm (middle tow) and 104 μm (lower tow). The average value of those amplitudes is 172 μm with standard deviation of 88 μm. In this case, the value of 172±88 μm is used to represent a_{out} of CN-3. Same procedure is carried out to obtained ϕ_{out} of each specimen tested under compression.

As for the in-plane waviness amplitude (a_{in}) and in-plane waviness angle (ϕ_{in}), the values used in this chapter are the same with those used in Chapter 2. Method to calculate a_{in} and ϕ_{in} can also be reviewed in Section 2.2.7. In addition, combined waviness of amplitude (a_{com}) and angle (ϕ_{com}) are also calculated for compression test specimens. A complete set of in-plane, out-of-plane and combined waviness of unstitched, stitched 6×6 200d, stitched 6×6 400d, stitched 3×3 200d and stitched 3×3 400d is given in Table 3.3

Table 3.3: Amplitude and angle of waviness in 0 ° tows for five specimen types

Specimen	Out-of-plane waviness		In-plane waviness		Combined waviness	
	a_{out} (μm)	ϕ_{out} (°)	a_{in} (μm)	ϕ_{in} (°)	a_{com} (μm)	ϕ_{com} (°)
Unstitched	112 ± 56	4.21 ± 1.82	19 ± 7	0.11 ± 0.04	114 ± 55	4.21 ± 1.82
Stitched 6×6 200d	134 ± 34	5.71 ± 1.14	117 ± 6	1.37 ± 0.03	179 ± 26	5.87 ± 1.10
Stitched 6×6 400d	154 ± 49	6.39 ± 1.09	199 ± 43	1.41 ± 0.06	254 ± 31	6.55 ± 1.06
Stitched 3×3 200d	121 ± 51	3.77 ± 1.11	80 ± 24	5.57 ± 0.45	147 ± 43	6.78 ± 0.61
Stitched 3×3 400d	127 ± 25	4.80 ± 0.51	83 ± 35	7.38 ± 1.42	152 ± 20	8.81 ± 0.29

Relationship between in-plane waviness and out-of-plane waviness

Based on the data shown in Table 3.3, relationship between a_{in} and a_{out} is made. Fig. 3.12a describes the relationship between a_{in} and a_{out}, which concludes that (i) stitching increases both a_{in} and a_{out}, (ii) the increase of a_{in} is strongly proportional to the increase of a_{out}. This indicates that both a_{in} and a_{out} are interdependent. A graph is also plotted between ϕ_{in} and ϕ_{out}, and it is shown in Fig. 3.12b. In contrast, no clear correlation between ϕ_{in} and ϕ_{out} can be made.

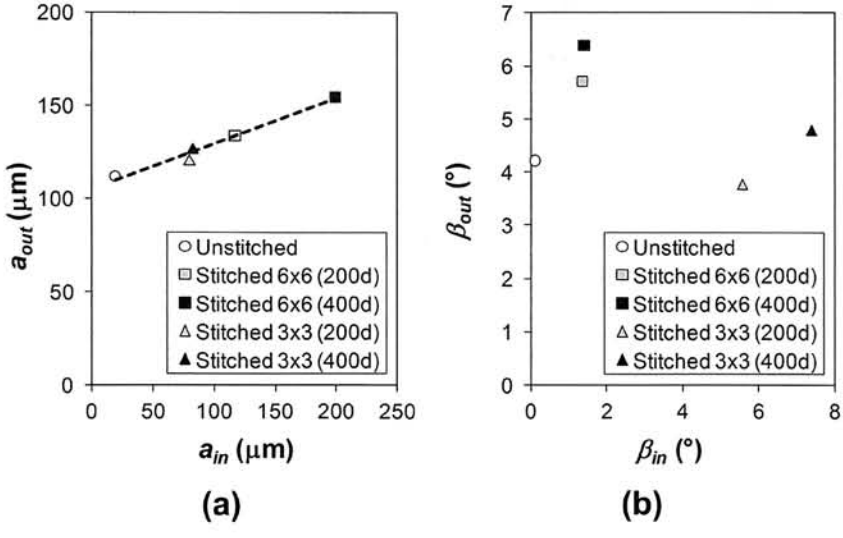

Figure 3.12: Relationship between in-plane and out-of-plane waviness (a) waviness amplitude, (b) waviness angle

Correlation between compressive strength and fiber waviness

Correlation between compressive strength and combined waviness is made for unstitched, stitched 6×6 200d, stitched 6×6 400d, stitched 3×3 200d and stitched 3×3 400d. Combined

waviness amplitude and angle are shown in Fig. 3.13a and Fig. 3.13b, respectively. Good correlation is found between compressive strength and both combined waviness amplitude and angle. This clearly shows that the reduction of compressive strength is strongly correlated with the increase of waviness in both in-plane and out-of-plane directions. Compressive failure is strongly determined by waviness of 0° tows, in which waviness triggers the formation of fiber splitting, which induces fiber kinking. Fiber splitting, which is essentially a matrix crack parallel to the 0° tows, is originated from the voids between fibers [43]. Therefore, minimizing both in-plane and out-of-plane waviness amplitudes in composites is beneficial in avoiding premature failure due to fiber splitting and fiber kinking.

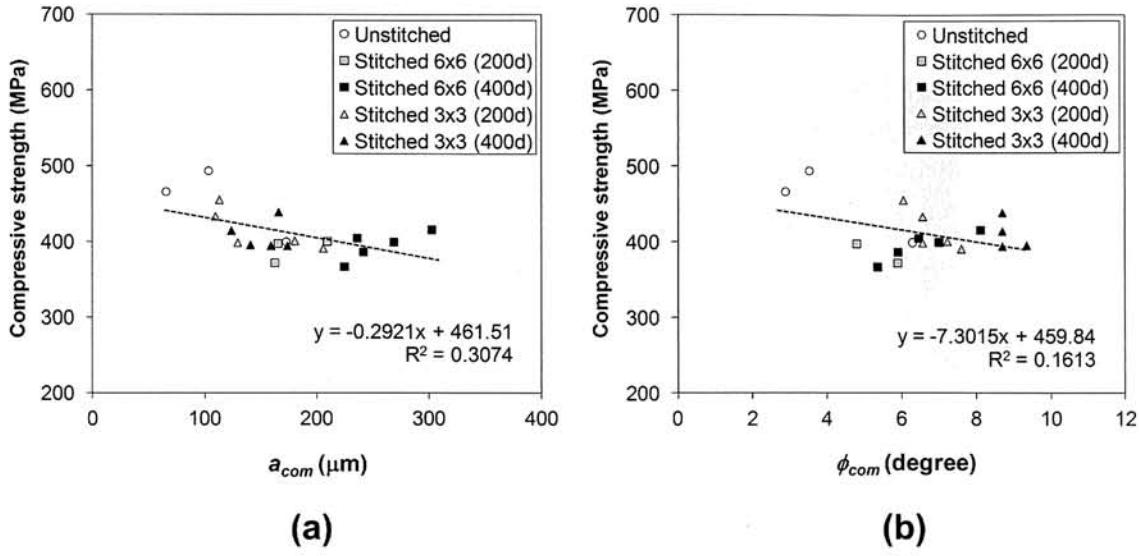

Figure 3.13: (a) Compressive strength vs. combined waviness amplitude, (b) compressive strength vs. combined waviness angle

3.3.6 Damage mechanisms in unstitched composites

Damage progression in unstitched composites, as observed from the edge and front face of the specimen, is described in this section. Unstitched specimen used for damage observation has a thickness of 3.303 mm and width of 14.85 mm. Before the test is started, images of specimen edges and front face are taken using optical microscope. The test is then carried out, and stopped at several load levels: 12.12 kN (249 MPa), 15.05 kN (309 MPa), 17.64 kN (363 MPa), 17.86 kN (367 MPa), 18.90 kN (388 MPa) and 17.90 kN (368 MPa; final failure). At each load level, images of edges and front face are again taken.

Fig. 3.14 shows the sequence of digital images of damage progression in unstitched composites, specifically in the front face, starting from 309 MPa up to 368 MPa (final failure). Fig. 3.14a shows that at 309 MPa, no damage is observed at the front face. When the load is increased to 363 MPa (Fig. 3.14b), several fiber splittings started to appear in 0° tow. No fiber kinking is visibly observed in the specimen at this stress level, implying that fiber splitting is the damage mode preceding fiber kinking. When the load is slightly increased to 367 MPa (Fig. 3.14c), the length of fiber splitting immediately increased reaching the boundary

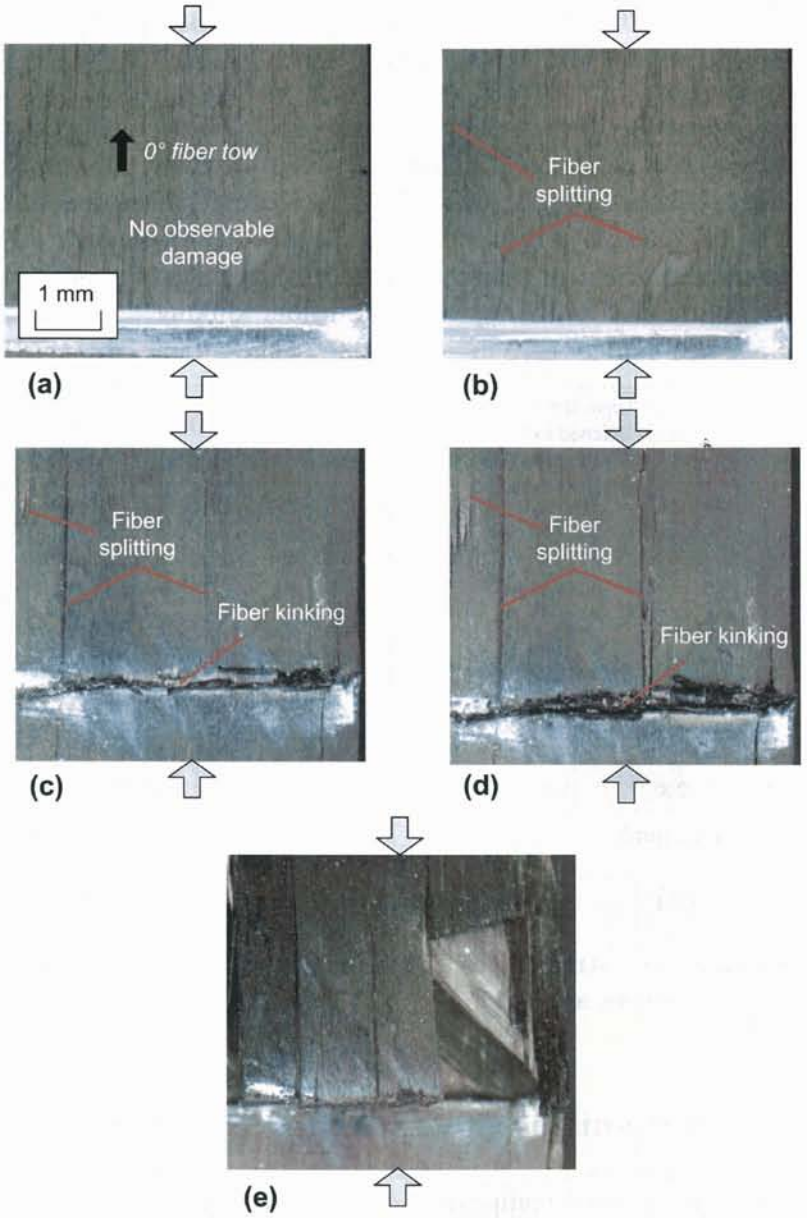

Figure 3.14: Damage progression at front face of unstitched composite under compression load: (a) 309 MPa, (b) 363 MPa, (c) 367 MPa, (d) 388 MPa, (e) 368 MPa (at failure)

of clamping region (indicated by horizontal white marker in Fig. 3.14c). At the same time, fiber kinking rapidly developed across the width of specimen. Fig. 3.14d shows that at 388 MPa the fiber splittings became more apparent, and kink band width is increased. The final failure is shown in Fig. 3.14e, and it occurred at 368 MPa. From the top surface, the final failure is characterized by extensive fiber splitting and delamination.

Fig. 3.15 shows the damage progression at the edge of unstitched composites. The images are of the same event with those shown in Fig. 3.14. Figs. 3.15a and 3.15b show that no damage is observed at the edge of specimen at 309 MPa and 363 MPa, respectively. When the load is increased to 367 MPa, fiber kinking occurred at upper 0° tow (Fig. 3.15c), and

the kinking immediately induced the initiation of delamination at the interfaces of 0°/+45° and +45°/90°. At 388 MPa, fiber kinking became more apparent, and delamination between +45° and 90° visibly grew towards the middle part of the specimen (Fig. 3.15d). At 368 MPa, final failure occurred and it is characterized by fracture of all 0° tows and delamination (Fig. 3.15e). Shear fracture is also evident that it connected two fiber ruptures.

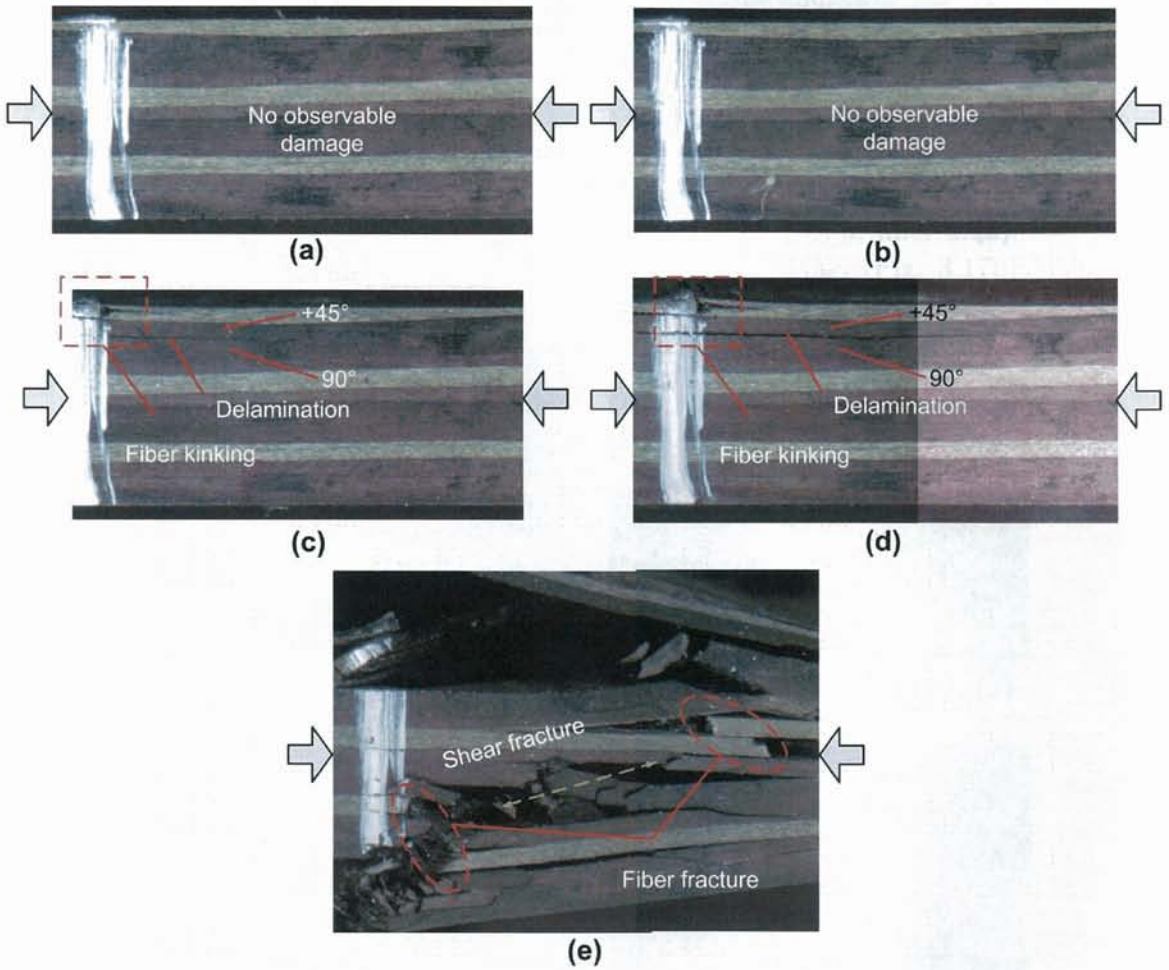

Figure 3.15: Damage progression at the edge of unstitched composite under compression load: (a) 309 MPa, (b) 363 MPa, (c) 367 MPa, (d) 388 MPa, (e) 368 MPa (at failure)

3.3.7 Damage mechanisms in stitched composites

Fig. 3.16 shows the sequence of damage in stitched composites under compression. It is noteworthy that the specimen used in this observation is stitched 3x3, which failed at maximum load of 15.08 kN (323 MPa). Thickness of specimen is 3.22 mm and width is 14.50 mm. For this specimen, the test is stopped six times at load level of 10.15 kN, 12.14 kN, 13.38 kN, 13.96 kN, 15.13 kN and 15.08 kN (final failure). The stresses equivalent to those load levels are 218 MPa, 260 MPa, 287 MPa, 299 MPa, 324 MPa and 323 MPa (final failure).

Fig. 3.16a shows the front face of pristine specimen (0 MPa) where no damage is observed.

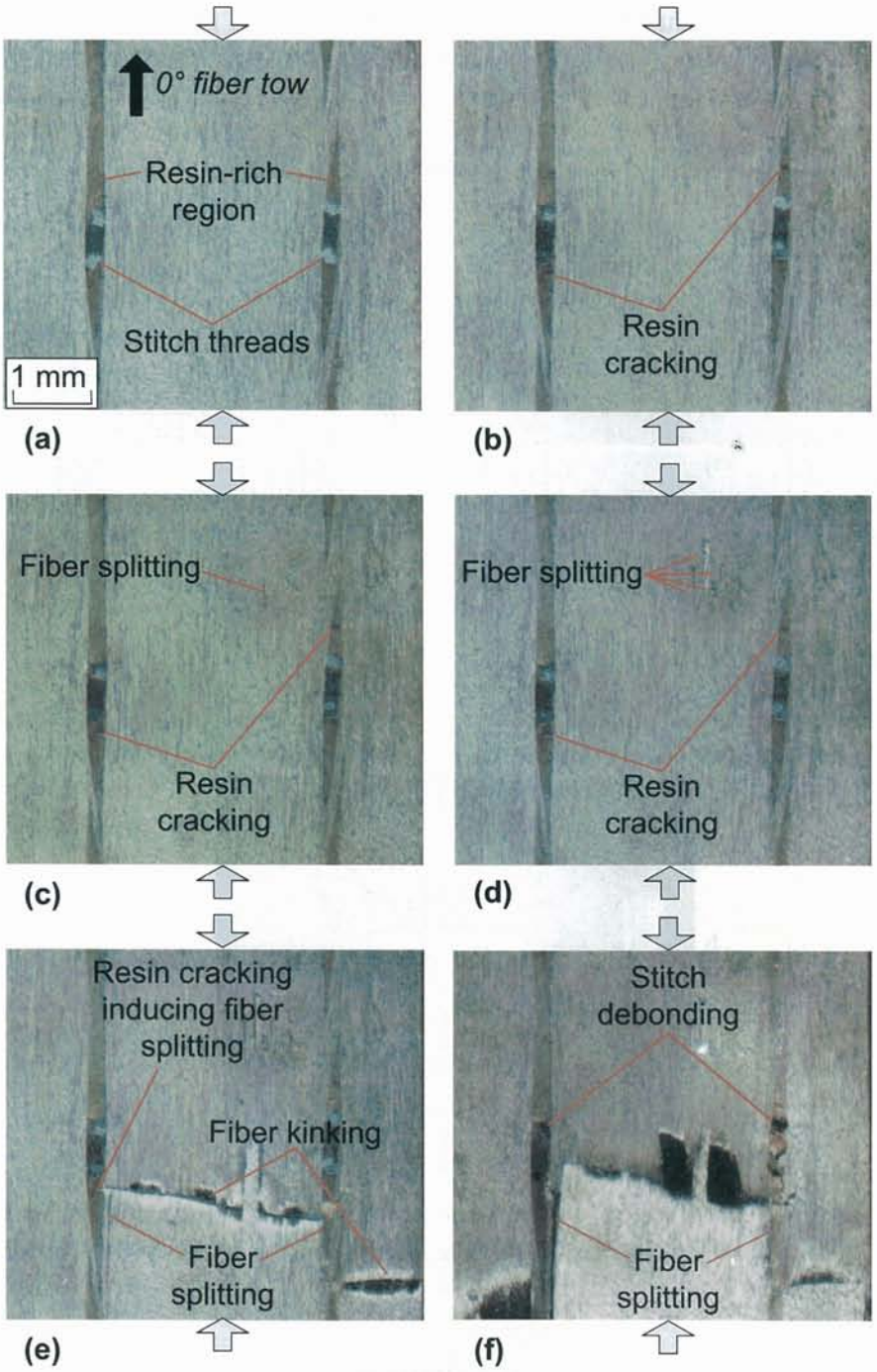

Figure 3.16: Damage progression in the front face of stitched composite under compression load: (a) pristine specimen (0 MPa), (b) 260 MPa, (c) 287 MPa, (d) 299 MPa, (e) 324 MPa, (f) 323 MPa (at failure)

When the stress level is increased to 218 MPa, damage is still not observed. Thus, the condition of test specimen is not shown here. When the stress is increased to 260 MPa, damage starts to appear in the form of resin cracking in the resin-rich regions (Fig. 3.16b). This resin cracking could be initiated by the voids in the resin-rich region. At 287 MPa,

in addition to the resin crackings, fiber splitting started to appear in 0° tow (Fig. 3.16c). Fiber splitting, as mentioned, may also be initiated by voids and waviness. When the stress reaches 299 MPa, fiber splittings multiply, but they do not seem to aggressively propagate in line with loading direction (Fig. 3.16d). When the stress is reaching 324 MPa, resin cracking residing in the resin-rich region induces a formation of fiber splitting at the edges of 0° tows (Fig. 3.16e). Resin cracking and fiber splitting would interact with fiber kinking that spans across the width of 0° tows. At 323 MPa, specimen fails, and final failure is characterized by debonding of stitch threads from the surrounding matrix (Fig. 3.16f). Fracture of 0° tows also becomes very apparent, and collapse of overall specimen is inevitable.

Accordingly, damage progression as observed from the edge of specimen is given in Fig. 3.17a shows the edge condition of stitched composites at 299 MPa, where there is no damage observed at this level. As the stress level is increased to 321 MPa, fiber kinking previously shown in Fig. 3.16d is clearly observed from the specimen edge (Fig. 3.17b). Similar to unstitched specimen, fiber kinking also induced the delamination at the interfaces of 0°/+45° and +45°/90°. Fig. 3.17c shows the final failure that is characterized by fracture of all 0° tows, extensive delamination, fiber splitting and shear fracture.

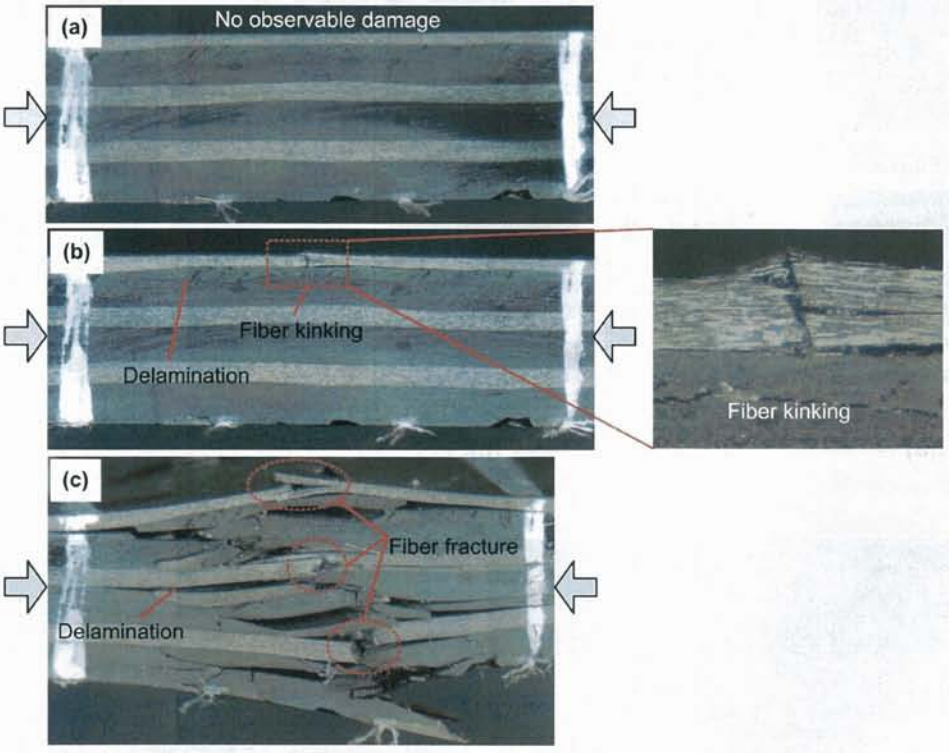

Figure 3.17: Damage progression at the edge of stitched composite under compression load: (a) 299 MPa, (b) 324 MPa, (c) 323 MPa (at failure)

3.3.8 Development of fiber kinking

Characteristic of fiber kinking is of interest because this failure mode, combined with fiber splitting and delamination, often determines the final failure of composites under compres-

sion. Fig. 3.18 shows the development of fiber kinking in 0° tow as observed from the edge and top surface of stitched composites. Figs. 3.18a and 3.18b are obtained when the specimen is not yet loaded (pristine specimen) and 249 MPa, respectively. Fig. 3.18c corresponds to the stress level of 278 MPa. At this stage, kink band is clearly observed. Location of fiber kinking is close to the resin-rich region, whereby fiber splitting is also found. Delamination is also observed between 0° and +45° tows. Increasing the stress to 299 MPa results in more apparent fiber kinking (see Fig. 3.18d). When the compression stress level is further increased, the specimen fully collapses at 289 MPa, which is slightly lower than the previous stress level. The final failure in stitched composites shown in Fig. 3.18e, and it is also characterized by fiber fracture, stitch debonding, fiber splitting and extensive delamination.

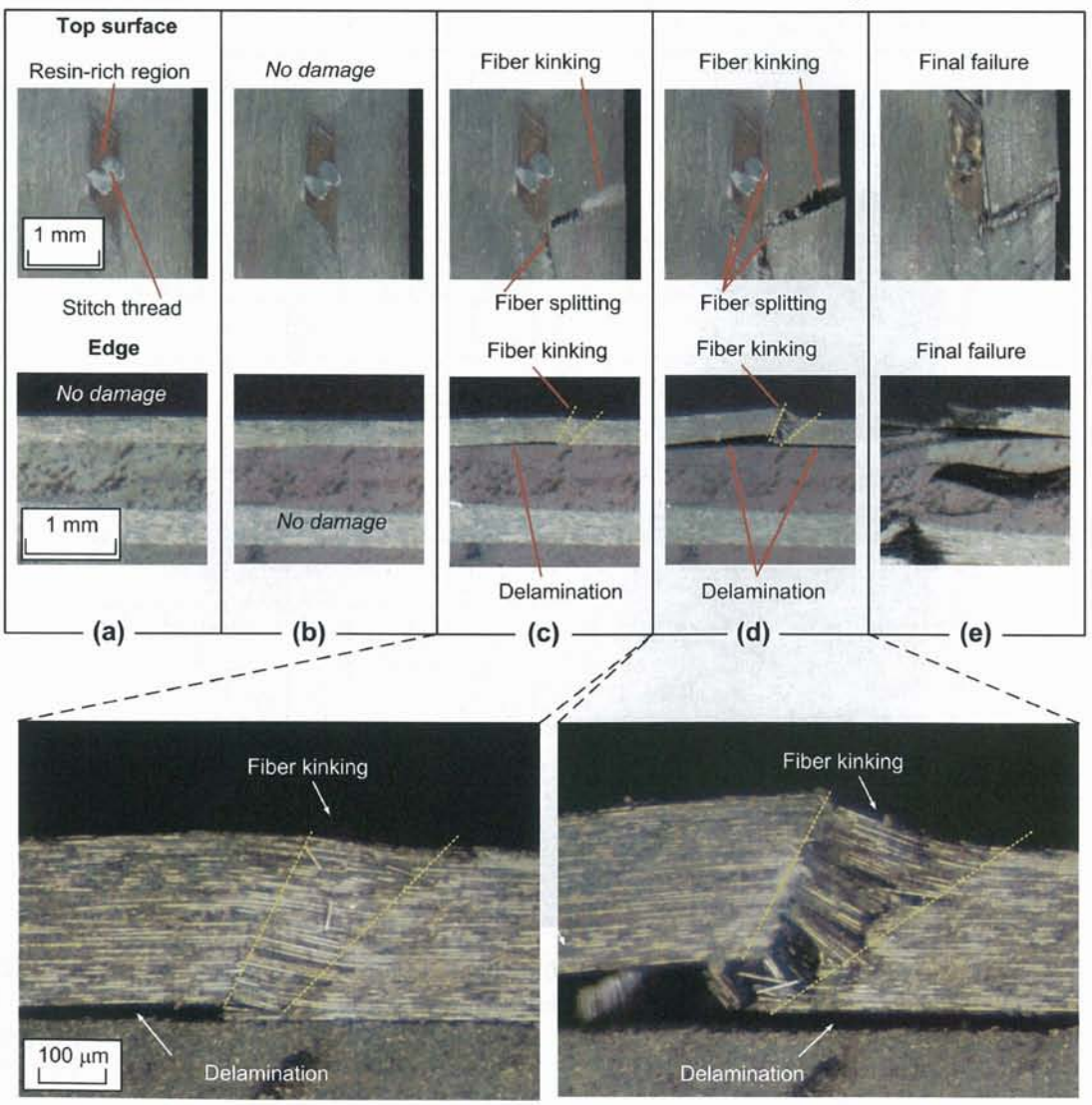

Figure 3.18: Initiation and development of fiber kinking in stitched composites: (a) Pristine specimen (no damage), (b) 249 MPa, (c) 278 MPa, (d) 299 MPa, (e) 289 MPa (at failure)

3.4 Concluding Remarks

Experimental investigation is performed to study the effect of stitch density and stitch thread thickness on compressive properties of carbon/epoxy composites. Several conclusions can be made as follows:

- Stitching generally reduces compressive strength of carbon/epoxy regardless the stitch density or stitch thread thickness. The reduction of compressive strength could reach approximately 14%, with the largest reduction is exhibited by stitched 6×6 200 denier. Reduction of compressive strength is strongly correlated with combined waviness of 0° tows, and early failure triggered by the cracking in resin-rich region.
- Compression modulus is modestly improved with stitching. The increase of compressive modulus could reach 16.5% by stitched 3×3 200 denier. The reason for modulus increment is influenced by fiber volume fraction and longer specimens used.
- Poisson's ratio of stitched composites is reduced up to around 11% in comparison with unstitched ones. In this case, it is experienced by stitched 3×3 400d. Stitching may restrain the lateral deformation of composites during compression, which eventually reduces the Poisson's ratio.
- Failure strain in stitched composites under compression is reduced by 22% indicating that the strain to failure is strongly dependent on the trend of compressive strength.
- Based on post-mortem analysis of failed specimens, failure of carbon/epoxy under compression is characterized by fracture of all tows, fiber kinking, delamination and matrix crackings.
- Investigation of damage mechanisms reveals the difference of damage sequence in unstitched and stitched composites:

  ***Unstitched composites**: fiber splitting ⇒ delamination ⇒ fiber kinking ⇒ final failure (rupture of all fibers, fiber kinking, extensive delamination, shear fracture)*

  ***Stitched composites**: cracking in resin-rich region near stitch thread ⇒ fiber splitting ⇒ delamination ⇒ fiber kinking ⇒ final failure (rupture of all fibers, fiber kinking, extensive delamination, shear fracture, stitch debonding)*

- Because compressive strength of stitched composites is lower than unstitched composites, regardless stitch density or thread thickness, stitching should not be employed in composite structures loaded under compression
- In order to improve compressive properties of stitched composites, several techniques are proposed here: (i) use of toughened resin to fabricate stitched composites; (ii) application of thin yet strong stitch thread to minimize resin-rich regions; (iii) minimizing fiber waviness by optimizing stitching forces applied to the fabrics.

Chapter 4

Vectran-stitched carbon/epoxy composites under fatigue

4.1 Overview

This chapter discusses experimental investigation of fatigue characteristics and damage mechanisms of Vectran-stitched carbon/epoxy composites. Effect of stitch density on three fatigue characteristics, namely fatigue life (S-N curve), stiffness degradation and fatigue damage growth, is discussed. Composite specimens are unstitched, stitched 6×6 200d and stitched 3×3 200d. Specification of cyclic loading applied during fatigue test is constant amplitude and tension-tension (T-T, $R = 0.1$) with sinusoidal waveform and frequency of 5 Hz. Maximum stress levels applied during fatigue test are defined between 50% and 80% relative to the static tensile strength of respective composite type. Fatigue damage growth is studied by conducting interrupted test at different cycles coupled with X-ray radiography. Quantification of damage is performed by measuring delamination growth, crack density of transverse and oblique cracks at various cycles and stress levels. Correlation between stiffness degradation and fatigue damage growth is described, and relationship between static and fatigue behavior is assessed.

4.2 Experimental Details

4.2.1 Materials

Material system used in fatigue test is the same as in Chapter 2, viz. Vectran-stitched carbon/epoxy composites. Carbon is T800SC-24kf, epoxy is XNR/H6813 Denatite, and the stitch material is Vectran 200 denier. Thermo-mechanical properties of T800SC, XNR/H6813 and Vectran can be reviewed in Table 2.1. Tow orientation is $[+45/90/-45/0_2/+45/90_2/-45/0]_S$. Stitch pattern is modified-lock stitch (see again Fig. 2.1). Three composite specimens prepared for fatigue test are (i) unstitched, (ii) stitched 6×6 200d, (iii) stitched 3×3 200d. Table 4.1 provides the specification of specimens used in fatigue test.

Table 4.1: Specification of test specimens for fatigue test

Parameter	Unit	Unstitched	Stitched 6×6 200d	Stitched 3×3 200d
Code	-	FN-x	FS62-x	FS32-x
s	mm	-	6	3
p	mm	-	6	3
SD	$1/mm^2$	-	0.028	0.111
μ	denier (tex)	-	200 (22.2)	200 (22.2)
V_s	%	-	0.088	0.350
V_f	%	53.3 ± 0.3	53.8 ± 0.4	54.3 ± 0.2
t	mm	4.18 ± 0.02	4.17 ± 0.02	4.18 ± 0.04
w	mm	25.93 ± 0.10	24.95 ± 0.05	25.01 ± 0.04
l	mm	250.50 ± 0.0	250.20 ± 0.27	251.10 ± 0.65
W	g	39.33 ± 0.21	39.28 ± 0.13	39.46 ± 0.15
ρ	g/cm^3	1.51 ± 0.0	1.51 ± 0.01	1.50 ± 0.01
Quantity	pcs.	4	5	5

4.2.2 Fatigue test specimens

Dimension of test specimen used in fatigue test is the same as in static case (Section 2.2.3): length is 250 mm and width is 25 mm. Schematic of test specimen used in fatigue test can be seen in Fig. 2.4. During fatigue test, the specimen is also untabbed in order to avoid premature failure around the tabs. Test specimens are obtained by cutting the mother plate using water-cooled cutting machine. After cutting process, edges of specimen are polished three times using abrasive rotating sandpaper (rough, grit #500; moderately smooth, grit #1000; very smooth, grit #1200). Polishing the edges of specimen is very important since any flaws remaining after cutting process are stress concentrators, which may cause premature failure. Specimen codes for unstitched, stitched 6×6 200d and stitched 3×3 200d are FN-x, FS62-x and FS32-x, respectively. x denotes sample numbering.

4.2.3 Fatigue test procedures

Fatigue test is carried out with constant-amplitude loading. Specimens are cyclically loaded between σ_{max} and σ_{min} until failure occurs, or pre-determined limit (for instance, 10^6 cycles) is achieved. Fig. 4.1 shows the nomenclatures used in constant-amplitude fatigue test. Note that the sinusoidal curve oscillates in the positive side of y-axis ($\sigma+$), which means 'tension-tension'. σ_{max} and σ_{min} represent the peak and the valley, respectively, in a full-sine wave (i.e. 1^{st} cycle). When both σ_{max} and σ_{min} lie in $\sigma+$, the loading cycle is tension-tension (T-T). The ratio between σ_{max} and σ_{min} is called load ratio ($R = \sigma_{min}/\sigma_{max}$). $R < 0$ corresponds to tension-compression (T-C), $0 < R < 1$ corresponds to tension-tension (T-T), and $R > 1$ corresponds to compression-compression (C-C). In present case, as mentioned, $R = 0.1$ is used, i.e. tension-tension.

Prior to conducting fatigue test, several parameters are defined in the testing machine, namely type of waveform, frequency (number of cycle per second), mean stress (σ_{mean}) and amplitude

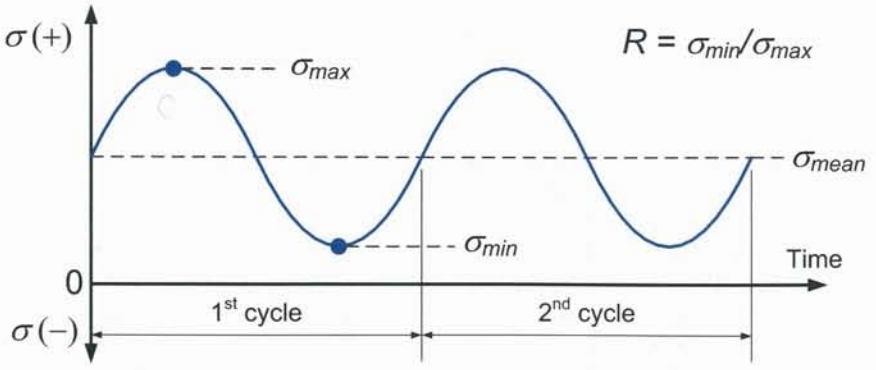

Figure 4.1: Nomenclatures used in fatigue testing

stress (σ_{amp}). In present case, waveform type is sinusoidal and frequency is 5 Hz. σ_{mean} and σ_{amp} can be calculated using following formulae

$$\sigma_{mean} = \frac{\sigma_{max} + \sigma_{min}}{2} \tag{4.1}$$

$$\sigma_{amp} = \frac{\sigma_{max} - \sigma_{min}}{2} \tag{4.2}$$

where σ_{max} and σ_{min} are determined based on the static tensile strength of composites.

Table 4.2 shows fatigue test setting used in present experiment. The test setting consists of applied maximum stress σ_{max}, σ_{min}, σ_{amp} and number of specimen. For each maximum stress level, at least one specimen is tested. Fatigue test is conducted under load control manner. σ_{max} is defined between 50% and 80% of σ_{ut} of respective material types. σ_{ut} in Table 4.2 is an average value of ultimate tensile strength (σ_{ut}) of respective specimen obtained from static test (see Table 2.5). Similar with static test, fatigue test is also carried out using servo-hydraulic Instron 8802. The temperature setting is maintained at 293 K (20 °C) .

4.2.4 Damage characterization procedures

Damage characterization is carried out by stopping the test at various cycles (N): 100, 200, 500, 1000, 1500, 2×10^3, 5×10^3, 10^4 and 10^6 cycles. Similar to damage characterization in Sub-Section 2.2.5, damage modes investigated in fatigue tests are transverse crack, oblique crack and delamination. Growth of each damage mode in a specimen is periodically monitored by performing X-ray radiography. Soft X-ray is also used to produce X-ray images of the specimen. To enhance the damage visualization during X-ray radiography, zinc-Iodide (ZnI) is applied onto the specimen. Upon proper drying process, the specimen is then exposed to soft X-ray. After converting the images to the digital ones, damage type that may exist in the specimen can be clearly observed. It should be mentioned that when a specimen is subjected to high σ_{max}, e.g. around 80% of σ_{ut}, the specimen could fail as early as 11,000 cycles. For such specimen, obviously, damage could only be assessed up to 11,000 cycles. In the case whereby a specimen can sustain fatigue loads exceeding 10^6 cycles, the test is

Table 4.2: Fatigue test setting

Specimen	Static	Fatigue					
	σ_{ut} (MPa)	σ_{max} (MPa)	σ_{max} (MPa)	σ_{min} (MPa)	σ_{mean} (MPa)	σ_{max}/σ_{ut}	Sample code
Unstitched	654	340	34	187	153	52%	FN-1
		408	41	225	184	62%	FN-2
		469	47	258	211	72%	FN-3
		542	54	298	244	83%	FN-4
Stitched 6×6	645	323	32	178	145	50%	FS62-1
		389	39	214	175	60%	FS62-2
		449	45	247	202	70%	FS62-3
		511	51	214	230	79%	FS62-4
		511	51	214	230	79%	FS62-5
Stitched 3×3	722	367	37	202	165	51%	FS32-1
		448	45	247	202	62%	FS32-2
		520	52	286	234	72%	FS32-3
		584	58	321	263	81%	FS32-4
		584	58	321	263	81%	FS32-5

automatically stopped at this cycle. The specimen that does not fail at 10^6 cycles is defined as 'Run-out', and marked with arrow ($\rightarrow$) in stress-cycle (S-N) curve. Run-out means that beyond 10^6 cycles, the specimen may display an infinite life. During the test, cycle-to-failure N corresponded to σ_{max} is noted, and SN curves are plotted based on this data. S-N curve is also known as fatigue life. y-Axis (or S) represents σ_{max} defined in linear scale, while x-axis is N defined in logarithmic scale.

4.2.5 Evaluation of stiffness degradation

Composite under fatigue loading generally exhibits progressive damage accumulation, and it is commonly shown by the reduction of stiffness [51, 112]. In present experiment, stiffness is obtained from the hysteresis loop in stress-strain diagram. The hysteresis loop is obtained by transforming load-time curves into stress-strain curves. Stress is calculated as instantaneous load divided by gross area of specimen. Strain is derived from the displacement of cross-head divided by specimen length. Once the hysteresis loop is obtained, gradient of stress-strain curves (stiffness) is calculated. This gradient is also called dynamic stiffness (E_{dyn}), which represents the response of composite under alternating stress [44]. E_{dyn} is a non-destructive means to measure residual stiffness. E_{dyn} is an efficient parameter since it can be measured continuously during fatigue test, unlike post-fatigue stiffness measurement, which is time-consuming, and yet only a handful of data could be obtained. By using E_{dyn}, the hassle of conducting static test during fatigue tests can be avoided, while the vast amount of data can be obtained.

In order to obtain E_{dyn}, load-time data obtained from fatigue test must be transformed into stress-strain curve. After transforming the load-time data into stress-strain, a number of

hysteresis loops could be obtained, and it is illustrated in Fig. 4.2a. Each hysteresis loop represents one cycle. The first loop is marked as N_1, second loop is N_2, and so on, up to a preferred N_{i-th}. E_{dyn} can be calculated by following expression

$$E_{dyn} = \frac{\sigma_{max} - \sigma_{min}}{\varepsilon_{max} - \varepsilon_{min}} \tag{4.3}$$

where σ_{max} is maximum stress, σ_{min} is minimum stress, ε_{max} is maximum strain and ε_{min} is minimum strain in hysteresis loop (see Fig. 4.2b).

It is noteworthy that in order to have a smooth hysteresis loop each fatigue cycle is constructed by at least ten data points. This process could be easily done in the dynamic testing software ($WaveMatrix$). Suppose that the frequency defined during fatigue test is 5 Hz then the number of data to be requested in the $WaveMatrix$ is 50 data/second.

E_{dyn} is plotted against number of cycle (N) expressed in logarithmic scale ($\log N$). The curve of E_{dyn} - $\log N$ represents residual stiffness curve. As illustrated in Fig. 4.3, stiffness degradation curve is characterized by the inflection point so-called stiffness degradation onset (N_p), stiffness decay and ultimate residual stiffness. Stiffness decay can be represented by the slope of stiffness degradation. In this experiment, effect of stitch density on the stiffness degradation characteristics is given.

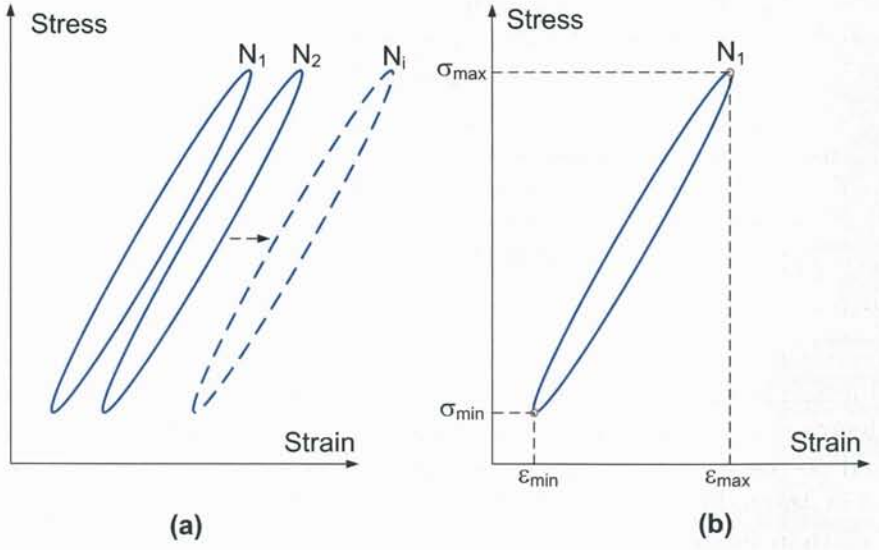

Figure 4.2: (a) Hysteresis loops, (b) parameters in hysteresis loop for calculation of E_{dyn}

4.3 Experimental Results and Discussion

4.3.1 Fatigue life

Table 4.3 shows fatigue test results of unstitched, stitched 6×6 200d and stitched 3×3 200d, in which specimen codes, σ_{max} and N_f are provided. In 'Remark' column, IT and CT denote

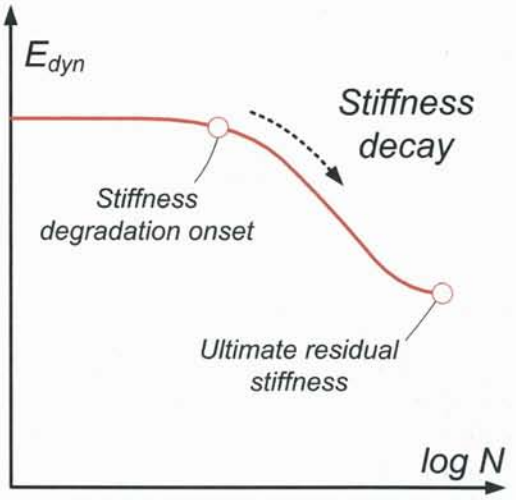

Figure 4.3: Illustration of stiffness degradation curve of E_{dyn} vs. log N

'interrupted test' and 'continuous test', respectively. Specimens marked with IT indicate that they are tested discontinuously in order to aid damage characterization process. Specimens marked with CT are tested continuously without being interrupted by the damage characterization process. It is shown that unstitched composite specimen (FN-1) survives fatigue loading up to 10^6 cycles without failure when σ_{max} is 340 MPa, while stitched specimens of FS62-2 and FS32-2 survive 10^6 cycles even the maximum stress applied to them is slightly higher (FS62-2 is subjected to σ_{max} = 389 MPa; FS32-2 is subjected to σ_{max} = 449 MPa). This indicates that stitched specimens seem to have modestly better fatigue life than unstitched specimens at certain range of maximum stress. When both stitched specimens are subjected to certain threshold below which they could survive 10^6 cycles (σ_{max} = 389 MPa for stitched 6×6; 449 MPa for stitched 3×3), specimens of FS62-1 and FS32-1, for instance, would certainly survive 10^6 cycles.

A graphical representation of how the specimens perform under fatigue loads is depicted by S-N curves. Fig. 4.4 shows S-N curves, in which the abscissa denotes cycle-to-failure N and the ordinate denotes σ_{max}. S-N curve of unstitched, stitched 6×6 200d and stitched 3×3 200d is plotted based on the data available in Table 4.3. Fatigue test data shown in Fig. 4.4 can be curve-fitted by the bi-linear curves. In Fig. 4.4, it is displayed that stitched 3×3 generally performs better than unstitched and stitched 6×6. For example, under σ_{max} of 448 MPa, stitched 3×3 can sustain cyclic loading up to 10^6 cycles, while stitched 6×6 composites, subjected to similar stress level (σ_{max} = 449 MPa), can only sustain cyclic loading up to 446368 cycles. Unstitched composites exhibit lower performance as compared to stitched 3×3: subjected to lower stress of 408 MPa, unstitched composites could only sustain 650370 cycles. The reason for the fatigue improvement in stitched 3×3 is strongly correlated with the ability of high stitch density in impeding the delamination growth. The mechanism shall be explained in the damage characterization part. S-N curve shown in Fig. 4.4 also implies that when carbon/epoxy exhibits good performance during static tension test, it will also perform well during T-T fatigue test, vice versa. Thus, poor fatigue behavior of stitched 6×6 could stem from its poor behavior during static test. As described in Chapter 2, under static tensile loading, stitched 6×6 200d failed at lower stress than stitched 3×3

200d and unstitched composites. Stitched 6×6 experiences higher density of transverse and oblique cracks as compared to unstitched composites, while the stitch density of 0.028/mm^2 is considered too sparse to impede the delamination growth, which is the principal damage in present carbon/epoxy. Consequently, stitched 6×6 fails at lower stress level, and exhibits lower ultimate tensile stress. It can be observed in Fig. 4.4 that the slope of fitted curves (m_f) of three specimens does not differ in an appreciable magnitude. This fact shows that possible change of damage mechanisms in carbon/epoxy due to stitching could not be captured by S-N curves. Therefore, S-N curve should not be used to postulate any damage mechanisms. S-N curves should rather be used to provide a general relationship between applied load and the fatigue limit of composites.

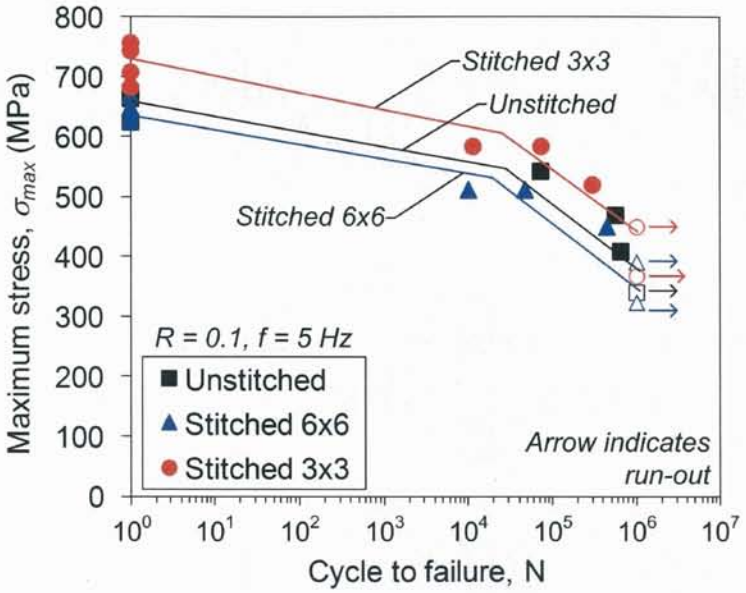

Figure 4.4: Fatigue life of unstitched, stitched 6×6 200d and stitched 3×3 200d

4.3.2 Failure mode

Fatigue failure in unstitched composites, as shown in Fig. 4.5, is characterized by extensive delamination, fiber breakage and matrix cracks in off-axis tows. The failure during fatigue, similar with static case, is also accompanied by an explosive sound. The failure in stitched composites, in addition to aforementioned failure modes, is also characterized by stitch breakage and separation of fiber tows. Prior to this failure, damage has been accumulated in the forms of matrix cracking and delamination. As in the case of stitched composites, some damages also appeared around the stitch threads during fatigue cycle. The characteristic of failure in carbon/epoxy during fatigue test is somewhat different from that during static test. Delamination occurred in specimens, especially in stitched composites, that failed under fatigue is more extensive than that in specimen under static loading.

Table 4.3: Fatigue test results of unstitched, stitched 6×6 and stitched 3×3

Specimen	Sample code	σ_{max} (MPa)	N_f	Remarks
Unstitched	FN-1	340	10^6	IT, run-out
	FN-2	408	650370	IT, failed
	FN-3	469	565317	IT, failed
	FN-4	542	72506	IT, failed
Stitched 6×6	FS62-1	323	10^6	IT, run-out
	FS62-2	389	10^6	IT, run-out
	FS62-3	449	446368	IT, failed
	FS62-4	511	10086	IT, failed
	FS62-5	511	47277	CT, failed
Stitched 3×3	FS32-1	367	10^6	IT, run-out
	FS32-2	448	10^6	IT, run-out
	FS32-3	520	298956	IT, failed
	FS32-4	584	11321	IT, failed
	FS32-5	584	73096	CT, failed

4.3.3 Stiffness degradation curves

Figs. 4.6 - 4.8 show stiffness degradation curves of unstitched, stitched 6×6 and stitched 3×3, respectively. Stiffness is expressed in a normalized value, i.e. actual dynamic stiffness is divided by initial dynamic stiffness (E_{dyn}/E_{dyn-i}). Initial dynamic stiffness is defined as a stiffness at N_1. The normalized stiffness is then plotted against N in logarithmic scale. It is shown that stiffness of composites, generally, tends to be initially constant up to an inflection point (stiffness degradation onset). Afterwards, stiffness is gradually reduced up to a certain value. It is apparent from the curves shown in Figs. 4.6 - 4.8 that stiffness degradation curves are greatly dependent on σ_{max}. The application of higher σ_{max} results in an earlier occurrence of stiffness degradation onset. Composites would have a tendency to exhibit larger slope when higher σ_{max} is applied. For example, subjected to $\sigma_{max} = 542$ MPa, unstitched composites would experience stiffness drop at 40 cycles, whilst subjected to lower σ_{max} of 340 MPa, the onset of stiffness drop occurs at 200 cycles. In terms of the slope of stiffness degradation curve, the specimen subjected to 542 MPa would exhibit slightly higher slope as compared to that subjected to 340 MPa. This tendency is also applicable to stitched 6×6 and stitched 3×3 specimens.

Table 4.4 provides stiffness degradation characteristics for unstitched, stitched 6×6 and stitched 3×3 composites. From Table 4.4, it can be seen that, with regard to ultimate residual stiffness, stiffness of unstitched composites is reduced between 12% and 24% at failure onset, or until 10^6 cycles, whichever earlier. For stitched 6×6, ultimate residual stiffness ranged between 13% and 29%, while the ultimate residual stiffness of stitched 3×3 specimens would range between 17% and 28%. From the observation of ultimate stiffness reduction characteristics, it is observed that the specimen which does not fail at 10^6 cycles tends to have stiffness reduction below 20% for unstitched composites, and 30% for stitched composites. The slope of stiffness degradation curve tends to be greater with higher σ_{max}.

Relationship between stiffness degradation onset (N_p) and σ_{max} is established based on the

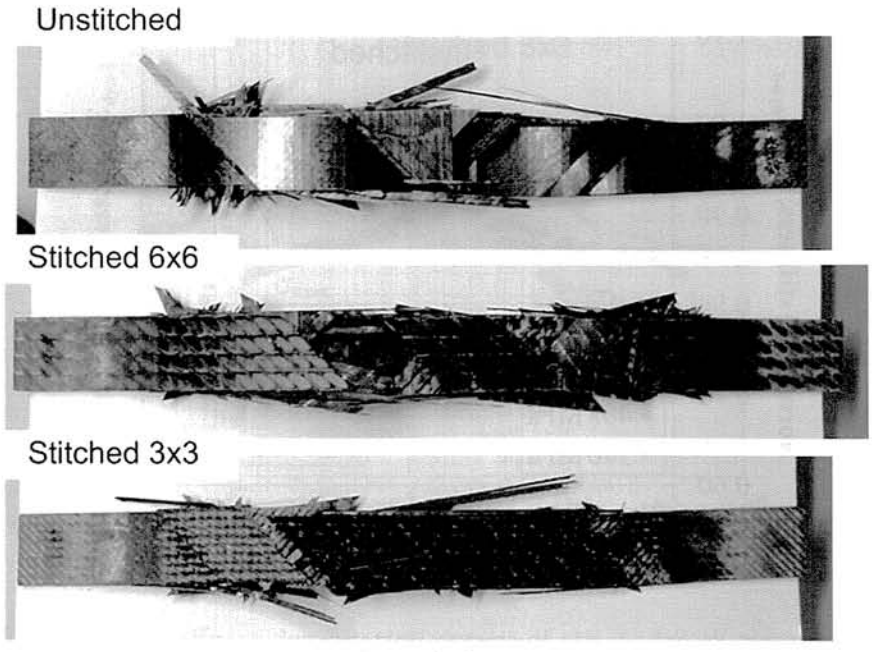

(a)

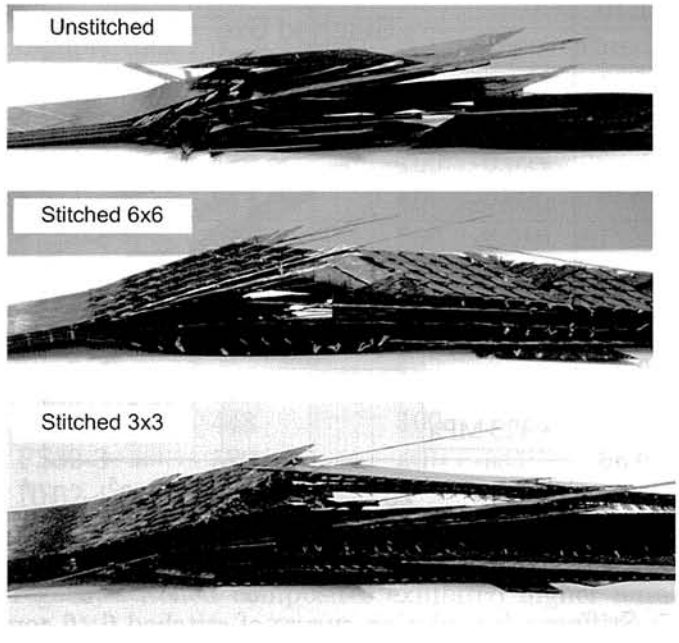

(b)

Figure 4.5: Fatigue failure of unstitched, stitched 6×6 and stitched 3×3: (a) top view, (b) side view

data given in Table 4.4, and it is shown in Fig. 4.9a. Fig. 4.9b shows the relationship between ultimate residual stiffness onset and σ_{max}. It is evident that stiffness degradation onset of unstitched and stitched composites is reduced with an increased of σ_{max}. Stitched

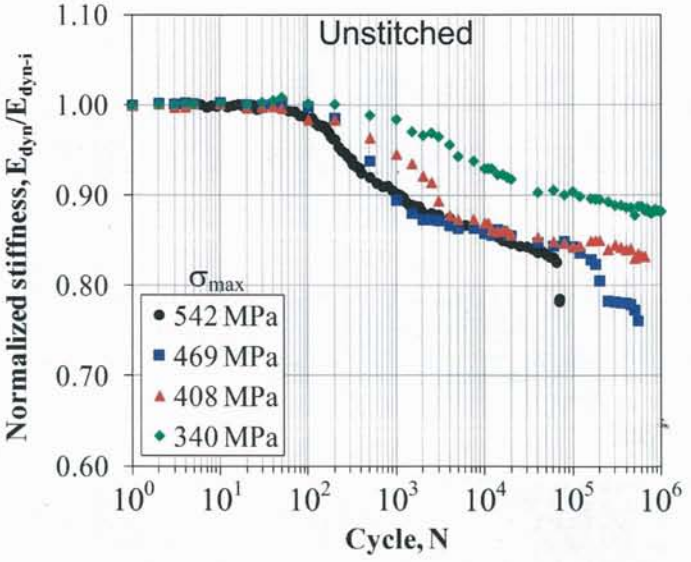

Figure 4.6: Stiffness degradation curves of unstitched composites

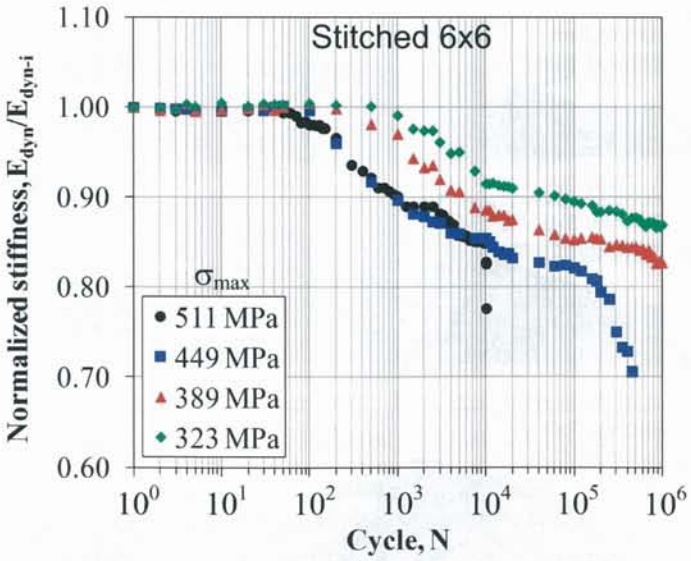

Figure 4.7: Stiffness degradation curves of stitched 6×6 composites

6×6 exhibited the earlier onset of stiffness degradation curve as compared to unstitched and stitched 3×3. The magnitude of stiffness reduction at final failure, or at 10^6 cycles (whichever earlier), can be seen in Fig. 4.9b. It is clear that specimens with higher stitch density would experience higher ultimate residual stiffness, and it is exhibited by stitched 3×3. The stiffness characteristics of composites under fatigue are strongly correlated with damage modes and their development. Early drop of dynamic stiffness is strongly correlated with early initiation of delamination in the specimen. Magnitude of stiffness reduced during ultimate failure of composites under fatigue could be related with the number of fiber splitting occurred in

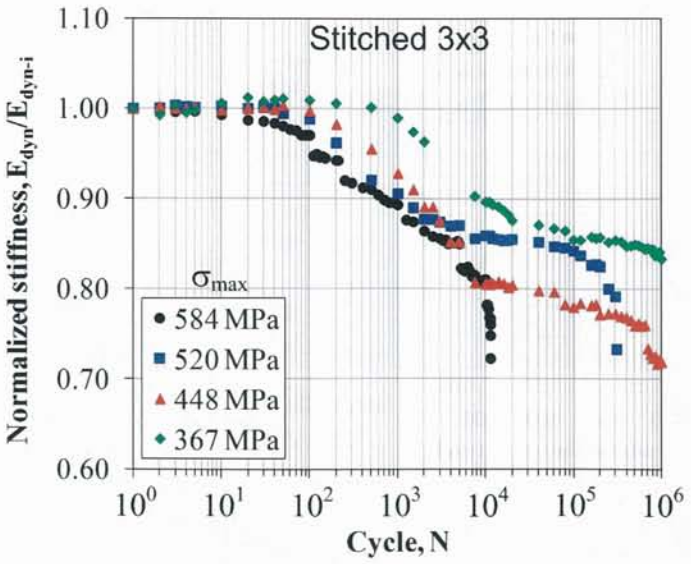

Figure 4.8: Stiffness degradation curves of stitched 3×3 composites

Table 4.4: Estimated stiffness degradation onset and ultimate stiffness reduction

Specimen	Sample code	σ_{max} (MPa)	N_p	Slope	Residual stiffness (%)
Unstitched	FN-1	340	200	-0.014	88*
	FN-2	408	50	-0.017	83
	FN-3	469	100	-0.021	76
	FN-4	542	40	-0.025	79
Stitched 6×6	FS62-1	323	500	-0.016	87*
	FS62-2	389	200	-0.017	83*
	FS62-3	449	50	-0.026	71
	FS62-4	511	30	-0.031	78
Stitched 3×3	FS32-1	367	500	-0.019	83*
	FS32-2	448	100	-0.026	72*
	FS32-3	520	40	-0.021	73
	FS32-4	584	5	-0.034	72

composites. In this regard, stitched composites exhibited higher number of fiber splitting as compared to unstitched composites. This formation of fiber splitting is triggered by the compaction of fibers in 0 ° tows.

4.3.4 Qualitative damage assessment

Damage analysis using X-ray radiography is performed at various cycles to observe the damage growth in unstitched and stitched composites during fatigue tests. Hosoi et al. [60] did similar damage analysis for the unstitched laminates. In present experiment, fatigue test is interrupted at various cycles of 100, 200, 500, 1000, 1500, 2×10^3, 5×10^3, 10^4, and

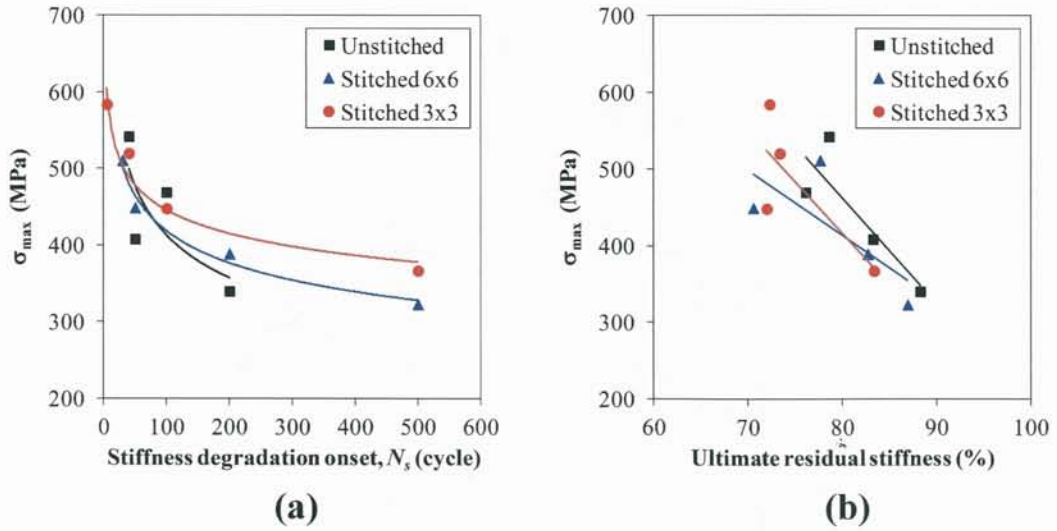

Figure 4.9: (a) Relationship between stiffness degradation onset (Np) and σ_{max}, (b) relationship between ultimate residual stiffness and σ_{max}

when the specimen is able to sustain the fatigue cycle up to 10^6 cycles, X-ray radiography is again performed to the specimen at that level. Several examples of X-ray images taken from unstitched and stitched 3×3 specimens at 10^2, 10^3 and 10^4 cycles can be seen in Fig. 4.10. X-ray images reveal that both unstitched and stitched 3×3 experience multiple types of damage, namely transverse crack, oblique crack, delamination, and cracking in resin-rich region. Qualitatively, damages developed in both stitched and unstitched composites under fatigue loads are very similar, except that in addition to aforementioned damage types, damage around stitches is also found in stitched composites. It is worth noted that σ_{max} applied to the unstitched specimen is 408 MPa, whilst σ_{max} applied to the stitched 3×3 specimen is 448 MPa. Under σ_{max} = 408 MPa, fatigue damage in unstitched composites at $N = 100$ is characterized by transverse and oblique cracks. As the cyclic loading is continued, at $N = 200$, delamination starts to appear from the edges. The delamination is growing rapidly as the cycling loading is ensued. When the fatigue cycle reached 10^4, unstitched composite is fully delaminated. Fig. 4.10 also shows fatigue damage development in stitched 3×3 composites subjected to σ_{max} = 448 MPa. Likewise, transverse and oblique cracks are developed at 100 cycles. In addition to transverse and oblique cracks, delamination is also found at 100 cycles. Delamination grew rapidly after 200 cycles, but its growth is arrested by the stitches when fatigue cycle reached 2000. Delamination developed in unstitched and stitched composites during fatigue test generally occurred at all interfaces between +45 ° and 90 ° tows regardless whether the composites are stitched or not. However, the characteristic of delamination found in stitched composites is different, whereby smaller delamination opening is observed in stitched composites. The opening of delamination and the delaminated interfaces can be seen in Fig. 4.11. It is noticed that stitching helped to provide bridging traction between plies so that the delamination opening is fairly reduced.

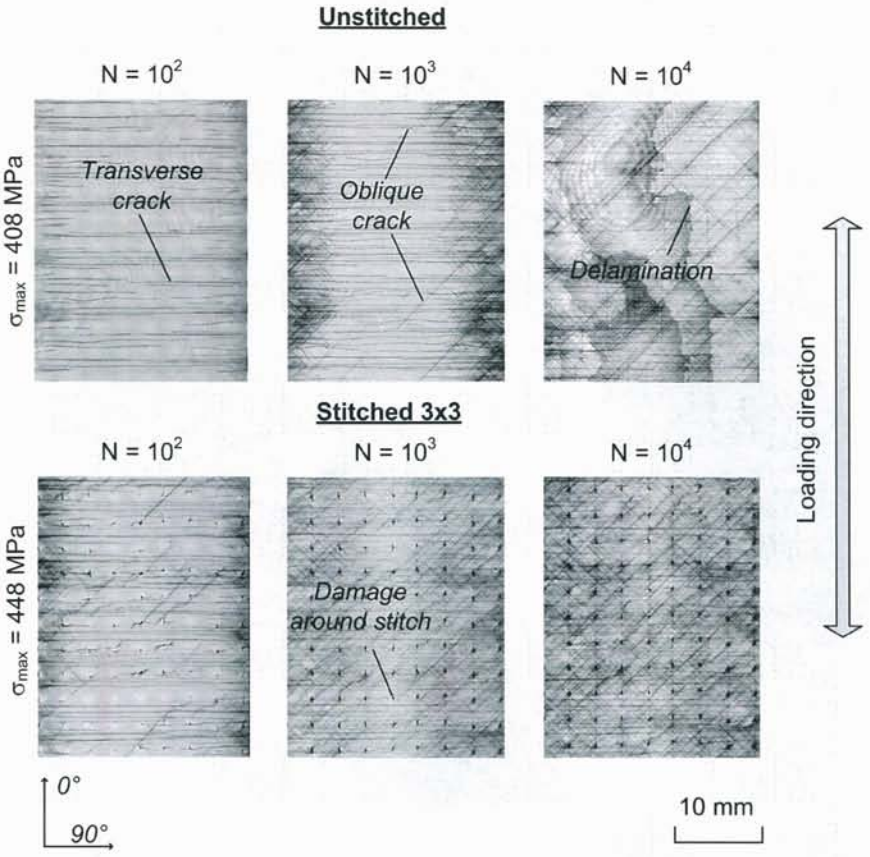

Figure 4.10: Damage development in unstitched and stitched 3×3 composites

4.3.5 Quantitative damage assessment

Quantification of fatigue damage growth is performed by evaluating the delamination area and crack density of transverse crack and oblique cracks. Methods to calculate crack density and delamination area can be reviewed in Chapter 2 (Sub-Section 2.2.5). As described in Sub-Section 2.2.5, for crack density calculation, X-ray image of the specimen, specifically the gage area, is divided into five sections. The number of cracks at each section is then counted. Crack density (number of crack per unit length) is an average value of number of cracks in five sections divided by the gage length.

Growth of transverse crack

Transverse crack density plotted against number of cycle for unstitched, stitched 6×6 and stitched 3×3 is given in Fig. 4.12. σ_{max} applied for unstitched, stitched 6×6 and stitched 3×3 is 340 MPa, 323 MPa and 367 MPa, respectively. The σ_{max} represents a proportion with respect to the ultimate tensile strength, in which approximately 50% is assigned. Crack density during static test shown in Fig. 4.12. This value is obtained by interpolating crack density data in Fig. 2.21. For example, σ_{max} applied for unstitched specimen is 340 MPa, and the corresponding crack density at 340 MPa obtained from Fig. 2.21 is 0.38/mm.

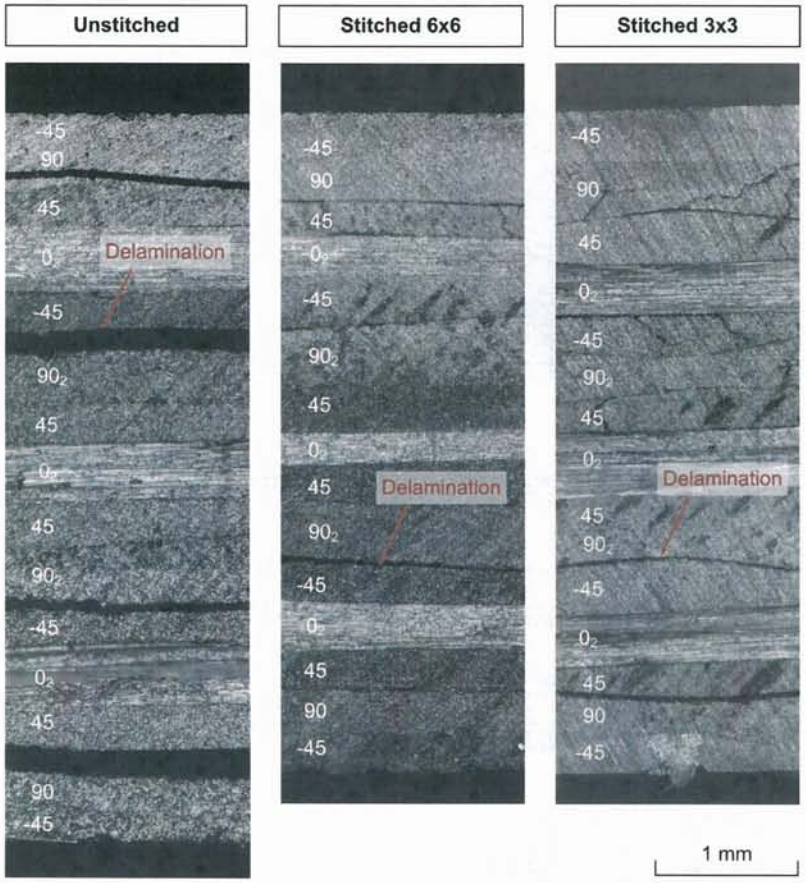

Figure 4.11: Delamination opening under cyclic loading for unstitched, stitched 6×6 and stitched 3×3

In general, as the specimens are subjected to fatigue loads, transverse crack density of stitched 3×3 is higher than that of unstitched and stitched 6×6. This tendency is similar with that obtained by static test, in which stitched composites exhibited more cracks as compared to unstitched composites. As shown, all specimens also show similar trend that the transverse crack gradually increases from 100 cycles and start to reach saturation level (commonly known as *characteristic damage state* or CDS) at 10^4 cycles. When CDS is reached, transverse crack density would not increase further as the cycle proceeds. This is because the spacing between cracks becomes significantly narrow, and other damage modes, e.g. delamination, initiate following the saturation of transverse and oblique cracks. As later shown, the saturation of transverse cracks would often be followed by the saturation of oblique cracks. At CDS, the number of transverse crack density for unstitched, stitched 6×6 and stitched 3×3 is approximately 3.3, 4.0 and 4.2 cracks/mm. It is noteworthy that although crack density has reached saturation level, the specimens are generally still able to sustain fatigue load. Thus, transverse crack does not seem to be the main damage mode that is responsible for the failure of stitched and unstitched composites.

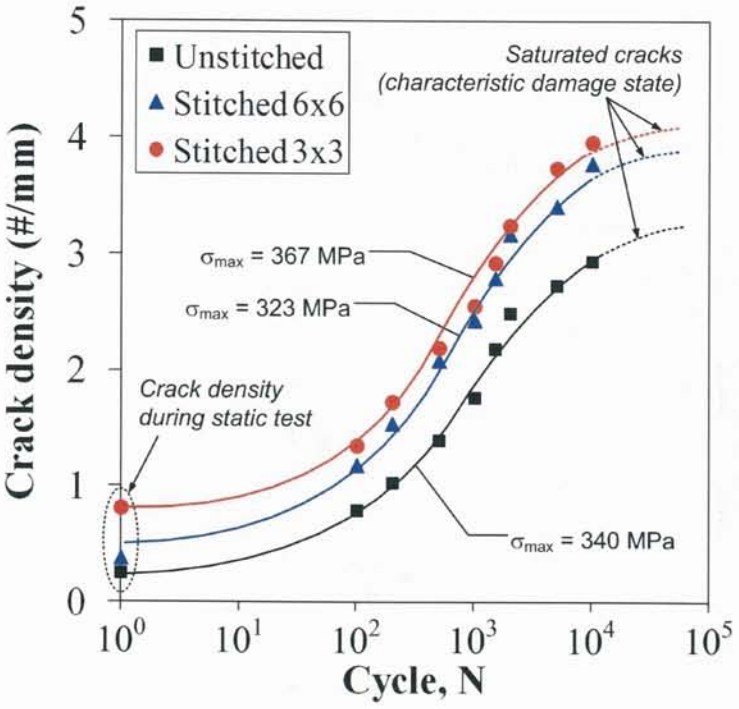

Figure 4.12: Transverse crack growth in unstitched, stitched 6×6 and stitched 3×3 under fatigue load

Growth of oblique crack

Fig. 4.13 shows the growth of oblique cracks in unstitched, stitched 6×6 and stitched 3×3 specimens subjected to fatigue loading with σ_{max} of 340 MPa, 323 MPa and 367 MPa, respectively. It is important to note that oblique crack is combination of two cracks growing in $+45^\circ$ and -45° directions. In general, oblique cracks grew later as compared to transverse crack. For instance, at 100 cycles, transverse crack density of unstitched specimen is 0.80/mm, whilst oblique crack density of the same specimen is still 0.05/mm. However, after approximately 500 cycles, the growth of oblique crack significantly increased surpassing the growth of transverse cracks. The reason for this behavior is that, in the earlier cycle (below 500 cycles), oblique crack occurred in composites is actually a contiguous crack. The contiguous crack is a short crack developed in $+45^\circ$ or -45° adjacent to 90° tows that already have transverse cracks. From X-ray images, contiguous cracks seem to be branching from the transverse cracks. After 500 cycles, the growth rate and crack density of oblique cracks is actually similar with transverse cracks.

Growth of delamination

As the transverse and oblique cracks grew in unstitched composites and reached certain cycle the delamination is also growing. The growth of delamination is greatly dependent on the applied maximum stress during fatigue test. Fig. 4.14 shows the growth of normalized

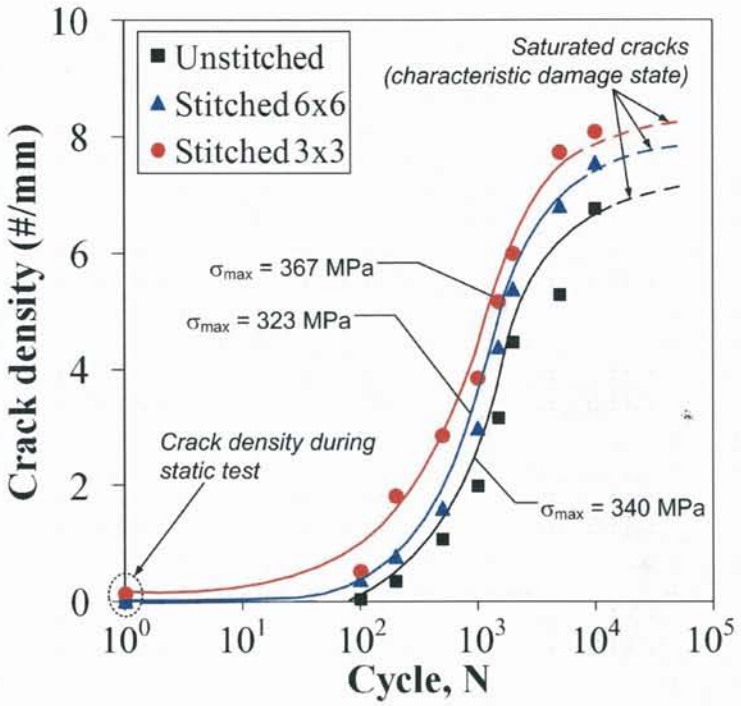

Figure 4.13: Oblique crack growth in unstitched, stitched 6×6 and stitched 3×3 under fatigue load

delamination area in unstitched composites subjected to four different maximum stresses. A threshold dash line at $A/A_0 = 1.0$ indicates that when the specimens reaching this line, based on X-ray images, the specimens have been fully delaminated.

The growth of delamination in unstitched specimens subjected to σ_{max} of 408 MPa and above show a rapid increase between 1000 and 5000 cycles. Below 408 MPa, for instance at 340 MPa, the growth of delamination is more gradual. It is also noticeable that under maximum stresses higher than 412 MPa, which is a delamination onset for unstitched composites, delamination has been developed in the first cycle. For instance, under $\sigma_{max} = 469$ MPa, delamination in the first cycle has been recorded at 12% of total gage area. As the fatigue cycle is increased, the delamination area rapidly increases, and results in a complete fatigue failure at 565317 cycles. When the delamination in unstitched composites has developed by 32% before fatigue test at $\sigma_{max} = 542$ MPa, it leads to a complete failure at much earlier cycle of 72,506. In contrast, when fatigue load is applied to unstitched composites at σ_{max} below which the delamination has not been initiated up to 200 cycles, such as in the case of $\sigma_{max} = 340$ MPa, unstitched specimen does not experience complete fatigue failure at 10^6 cycles. Under $\sigma_{max} = 340$ MPa, a very small delamination of 1.1% initiated at 500 cycles. A complete fatigue failure at 650370 cycles is also experienced by unstitched specimen subjected to $\sigma_{max} = 408$ MPa. Although this specimen is subjected to stress level slightly below the delamination onset, however, at very early cycle of 200, delamination has been developed by 3%.

Similar to unstitched composites, delamination growth in stitched 6×6 and stitched 3×3

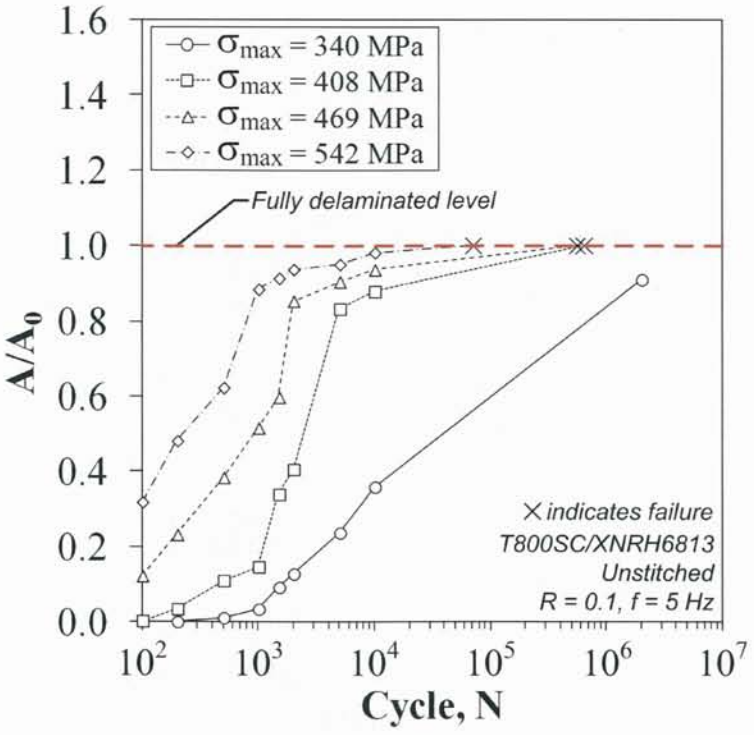

Figure 4.14: Delamination growth in unstitched composites under fatigue load

is greatly determined by the applied maximum stress during fatigue test. As shown in Fig. 4.15 (stitched 6×6) and Fig. 4.16 (stitched 3×3), when the applied maximum stress is below delamination onset for respective specimens, complete fatigue failure would occur. Delamination onset for stitched 6×6 and stitched 3×3 is 361 MPa and 402 MPa, respectively. These values are obtained from damage characterization in static tension case.

Fig. 4.15 shows that under $\sigma_{max} = 323$ MPa, stitched 6×6 specimen is able to survive 10^6 cycles without failure. This behavior is also true for stitched 3×3 specimen when it is subjected to $\sigma_{max} = 367$ MPa, under which stitched 3×3 specimen survived 10^6 cycles without failure. The effectiveness of stitch threads in impeding the fatigue delamination growth is demonstrated in this case. Subjected to slightly higher maximum stresses of 389 MPa (stitched 6×6) and 448 MPa (stitched 3×3), which are higher than delamination onset, both specimens could survive 10^6 cycles without failure. In both cases, the delamination area developed at 100 cycles is only 1% of total gage area. The delamination length growing from the specimen edges is smaller than the distance between stitch rows at the edges. Therefore, because the delamination area has not reached the stitch threads, the threads are still effective in inhibiting the growth of the delamination.

Comparison of delamination growth among unstitched, stitched 6×6 and stitched 3×3 can finally be made, and it is shown in Fig. 4.17. It is evident that stitched 3×3 provides better delamination impediment as compared to unstitched and stitched 6×6. The delamination growth in stitched 6×6 is larger than that in unstitched composites at similar σ_{max}. Delamination, in this regard, is considered the principal damage in both unstitched and stitched composites. This is due to the fact that after both transverse and oblique cracks reach charac-

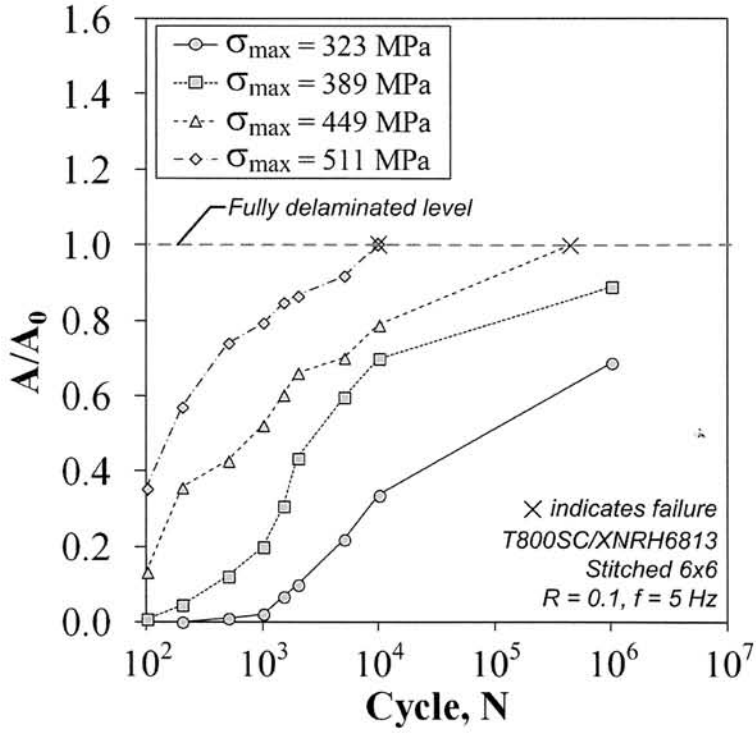

Figure 4.15: Delamination growth in stitched 6×6 composites under fatigue load

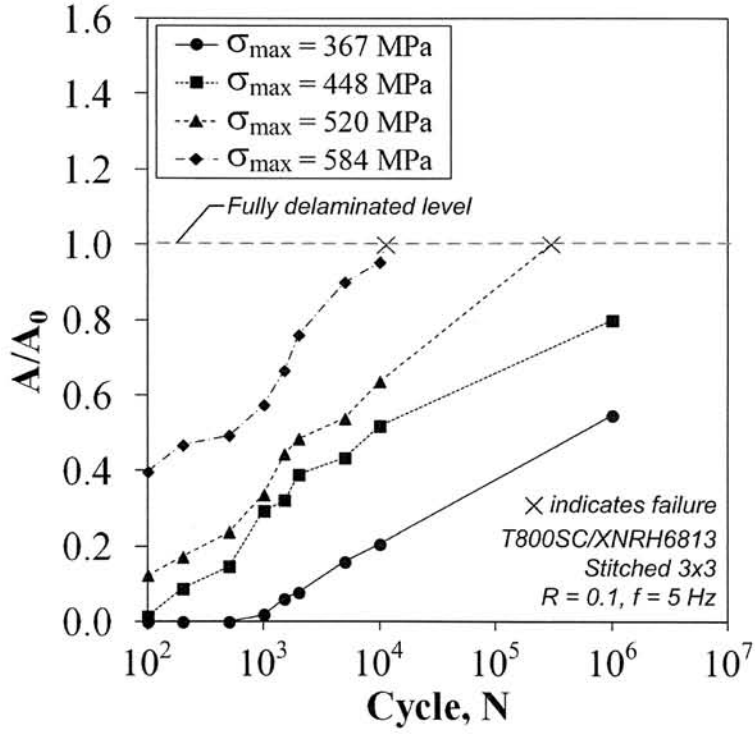

Figure 4.16: Delamination growth in stitched 3×3 composites under fatigue load

teristic damage state and they do not grow anymore, the major damage mode in composites remains to be delamination. The growth of delamination is considered stable under certain stress level. It is therefore important to re-iterate that, since delamination is known to be the principal damage, when the maximum stress applied to the composites is lower than the delamination onset, the specimen would likely to survive 10^6 cycles without complete failure.

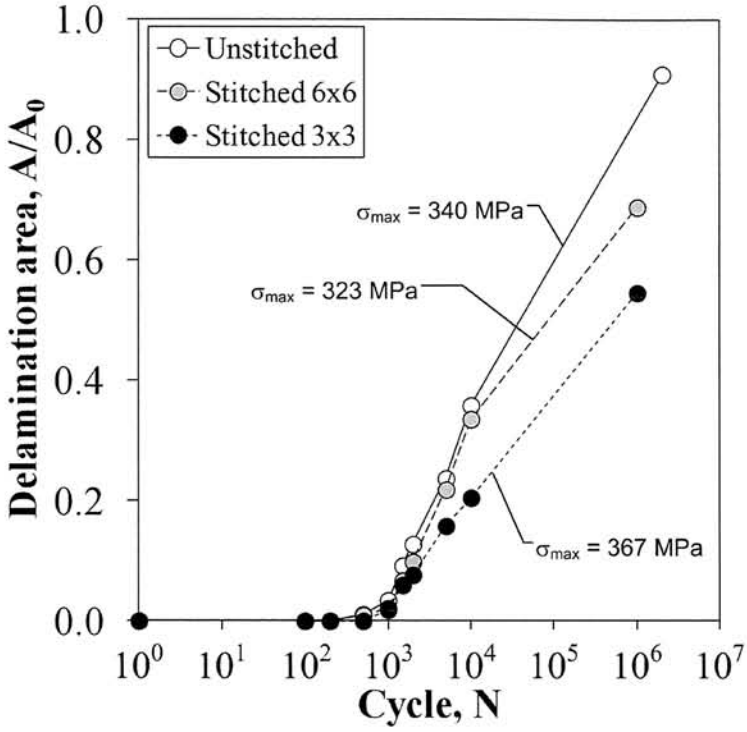

Figure 4.17: Comparison of delamination growth in unstitched, stitched 6×6 and stitched 3×3

4.3.6 Correlation between stiffness degradation and fatigue damage development

In this part, correlation between damage and stiffness degradation curve is established. This correlation is important to explain the underlying mechanisms that govern the stiffness degradation onset and the slope of stiffness degradation. Damage in composites under fatigue load is typically accumulated damage. Obvious effect of damage accumulation could not be inferred from *S-N* curve as it only describes the onset of failure corresponded to a certain applied stress. Stiffness degradation curves, on the other, could give a better understanding of the damage mechanisms when it is correlated with damage observation.

Fig. 4.18 shows stiffness degradation curve of unstitched composites under $\sigma_{max} = 408$ MPa. It is shown that between 1 and 100 cycles, residual stiffness of unstitched composite under fatigue is relatively constant. At 100 cycles, fatigue test is immediately stopped, and X-ray radiography is performed to the specimen. It is found that at 100 cycles, as indicated

in Fig. 4.18, transverse and oblique cracks have already been developed. Crack density of transverse crack and oblique crack in unstitched specimen at 100 cycles is 0.80 crack/mm and 0.05 crack/mm, respectively. Fatigue cycle is then continued up to 1000 cycles, and X-ray radiography is again performed to the specimen at that cycle. As displayed in Fig. 4.18, stiffness at 1000 cycles has been slightly reduced exceeding the stiffness degradation onset that is estimated at $N = 200$ (see Table 4.4). At $N = 1000$, delamination emanating from the edges of unstitched specimen has been developed. Based on this finding, it is postulated that the stiffness degradation onset between $N = 200$ and 1000 strongly corresponds to the initiation of delamination. As the cyclic loading is continued until $N = 10^4$, delamination has been occupying all gage area. After $N = 10^4$, cyclic loading is again continued, the specimen eventually failed at 650370 cycles with ultimate residual stiffness of 80%.

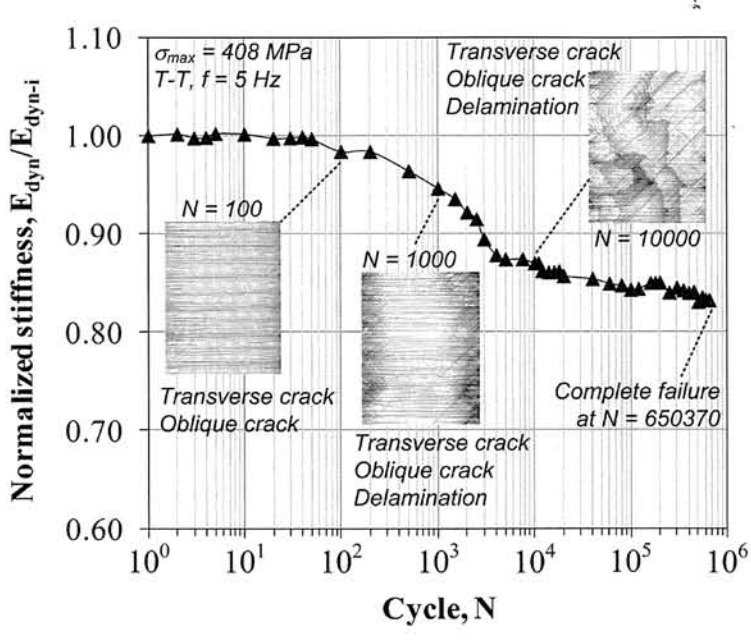

Figure 4.18: Relationship between stiffness degradation and damage mechanism in unstitched composites under $\sigma_{max} = 408$ MPa

Correlation between stiffness degradation and fatigue damage progression in stitched 6×6 and stitched 3×3 is similar. In this case, only the results of stitched 3×3 are shown. In the case of stitched 3×3 composite, particularly under $\sigma_{max} = 448$ MPa, Fig. 4.19 shows that several damage modes have been initiated at $N = 100$. The damage modes displayed by X-ray image in Fig. 4.19 (at $N = 100$) are transverse cracks, oblique cracks, defects around stitch thread ('stitch defect') and delamination. When the fatigue cycle is then continued, the stiffness is gradually reduced. X-ray observation is again performed at $N = 1000$, and more damages are found in stitched 3×3 composites. As the crack density for transverse and oblique cracks increased, stiffness is gradually reduced. Delamination has been extended, and defects are found in all stitch threads. At $N = 10^4$, X-ray radiography is again performed, and it is found that delamination is extended across the width of specimen. The specimen also shows a high crack density of both transverse and oblique cracks. Although the stiffness has been reduced by 20%, when the fatigue cycle is continued, the specimen could still sustain

fatigue cycle up to 10^6 cycles without a sign of failure.

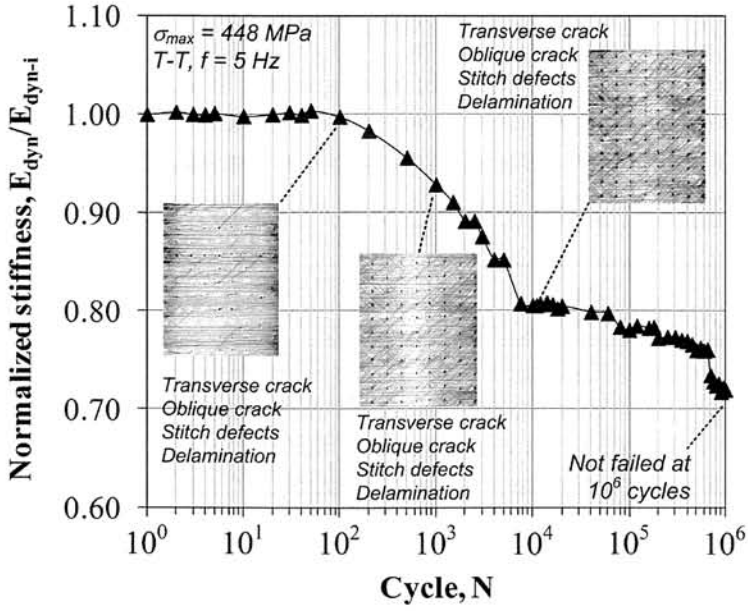

Figure 4.19: Relationship between stiffness degradation and damage mechanism in stitched 3×3 composites under σ_{max} = 448 MPa

Thus, from these two cases, it is evident that transverse and oblique cracks may not cause rapid reduction of stiffness in composites under fatigue. Rather, delamination is the main cause of rapid stiffness drop. For unstitched composites, when the delamination grows rapidly until occupying the whole gage area, fatigue failure may eventually occur. For stitched composites, although crack density is relatively higher than that for unstitched composites, they only induce the delamination growth rate. When delamination growth rate is fast, and it is eventually occupying all gage area, delamination opening can be bridged by the stitch threads. In other words, stitch threads provided closing traction for delamination. Therefore, it is revealed that if the delamination growth can be delayed then the onset of delamination can be extended, and fatigue life could eventually be extended as well. Below certain maximum stress, e.g. σ_{max} = 448 MPa, delamination growth still can be impeded resulting in an extended life up to 10^6 cycles.

4.3.7 Correlation between static and fatigue characteristics

Table 4.5 presents a correlation between delamination onset (σ_d) obtained during damage assessment in static test (Table 2.8), and fatigue test results. This correlation reveals the ability of stitch thread in delaying the fatigue failure in composites. For unstitched composites, when unstitched specimen is subjected to σ_{max} = 340 MPa, which is below σ_d of 412 MPa, specimen did not fail at 10^6 cycles. The reason is that the delamination has not been initiated. However, when σ_{max} applied to unstitched specimen is above 412 MPa, fatigue failure may follow. The behavior is different for stitched composites. For stitched 6×6, the

delamination onset during static is 361 MPa. When stitched 6×6 is subjected to σ_{max} = 389 MPa, which is above delamination onset, fatigue failure did not occur at 10^6 cycles. Likewise, when stitched 3×3 is subjected to σ_{max} = 448 MPa, which is above delamination onset of 402 MPa, specimen did not fail at 10^6 cycles. This indicates that stitched 6×6 and stitched 3×3 are actually able to restrain the delamination growth. However, the reason why stitched 6×6 has lower fatigue performance as compared to unstitched composites is that the crack density in stitched 6×6 is higher than that in unstitched composites.

Table 4.5: Correlation between delamination onset (σ_d) and fatigue test results

Specimen	σ_d (MPa)	σ_{max} (MPa)	σ_{max}/σ_d (MPa)	Remarks (MPa)	N_f (Cycles)
Unstitched	412	340	83%	No delamination	Not failed at 10^6
		408	99%	Delamination onset	650370
		469	114%	Delaminated by 14%	565317
		542	132%	Delaminated by 32%	72506
Stitched 6×6	361	323	89%	No delamination	Not failed at 10^6
		389	108%	Delaminated by 8%	Not failed at 10^6
		449	124%	Delaminated by 24%	446368
		511	142%	Delaminated by 42%	47277
Stitched 3×3	402	367	91%	No delamination	Not failed at 10^6
		448	111%	Delaminated by 11%	Not failed at 10^6
		520	129%	Delaminated by 29%	298956
		584	145%	Delaminated by 45%	73096

4.4 Concluding Remarks

Experimental investigation of fatigue behavior of Vectran-stitched carbon/epoxy composites has been performed. Particular attention is given to understanding the effect of stitch density on fatigue life, stiffness degradation and damage growth. Several conclusions can be made as follows:

- Fatigue life of densely stitched composites (stitched 3×3) is better than that of unstitched and moderately stitched composites (stitched 6×6). Improvement of fatigue life in densely stitched composites stems from the ability of stitch threads in impeding fatigue delamination growth.
- Failure mode of carbon/epoxy composites does not change significantly with the presence of stitch threads, except that in addition to extensive delamination, fiber breakage and matrix cracks in off-axis tows, stitched composites also experienced stitch breakage and separation of fiber tows. The difference between static and fatigue failure is that composites under fatigue exhibits a more extensive delamination than that under static.
- Densely stitched composites experience higher ultimate residual stiffness. However, stiffness degradation onset of both unstitched and stitched composites is reduced with

an increase of σ_{max}. Early drop of stiffness is strongly correlated with complex interaction of off-axis cracks and delamination.

- Magnitude of stiffness reduced during ultimate failure of composites under fatigue could be related with the number of fiber splitting, which is triggered by the compaction of fibers in 0 ° tows.

- Delamination found in stitched composites has smaller delamination opening than that in unstitched composites indicating that stitching provided bridging traction between plies so that the delamination opening is reduced.

- Subjected to fatigue loads, transverse crack density in stitched 3×3 is higher than that of unstitched and stitched 6×6. This tendency is similar with that obtained by static test. Although crack density has reached saturation level, the specimens are still able to sustain fatigue load. Thus, transverse crack does not seem to be the main damage mode that is responsible for the failure of stitched and unstitched composites. Oblique cracks generally grows later as compared to transverse crack, although at later stage their growth significantly increases, and surpasses the growth of transverse cracks.

- Delamination is considered the principal damage in both unstitched and stitched composites. Thus, when maximum stress applied to the composites is lower than the delamination onset, the specimen would likely to survive 10^6 cycles without complete failure.

- The growth of delamination is greatly dependent on the applied maximum stress during fatigue test. Delamination is the main cause of rapid stiffness drop. If delamination initiation can be delayed (i.e. onset of delamination is deferred) fatigue life of composites could be extended.

- It is found that when carbon/epoxy exhibit good performance during static tension test, it would also translate into good performance during T-T fatigue test, vice versa. In this case, stitched 3×3 performs better than unstitched and stitched 6×6.

- The improvement methods for stitched composites under fatigue loading may follow the ones described in Chapter 2: (i) to minimize fiber waviness (ii) to reduce the thickness of off-axis tows so as to increase the stress level for crack initiation (crack onset)

Chapter 5

Kevlar-stitched carbon/epoxy composites with and without holes under tension

5.1 Overview

First part of this chapter discusses experimental investigation of tensile characteristics and damage mechanisms of Kevlar-stitched carbon/epoxy composites with and without circular holes. Effect of stitch orientation on tensile properties, open hole tension (OHT) properties and damage mechanisms of Kevlar-stitched composites are evaluated. Stitch orientation investigated herein is longitudinal and transverse stitching. Second part is on the analytical study dealing with the calculation of normal stress distribution at the hole of stitched composites, and the prediction of OHT strength (σ_{OHT}) of stitched composites with different stitch orientations using Average Stress Criterion (ASC). The analytical results are then compared with experiments.

5.2 Experimental Details

5.2.1 Materials

Material system used is plain weave carbon/epoxy composites stitched with Kevlar thread. Schematic of plain weave fabric can be seen in Fig. 5.1. Plain weave is made by interlacing a number of fiber tows running in two different directions: 0° direction (warp tows) and 90° direction (weft tows). Plain wèave is selected because of its good drapability, i.e. ability to conform to complex shapes, and improved through-thickness properties in comparison with unidirectional or cross-ply composites. The width of warp and weft tows is 1.5 mm, while the thickness is 0.2 mm. Fiber type used is carbon T300-3K (Toray Industries, Inc.) [6].

Stitched plain weave is made by stacking twenty layers of plain weave fabric with tow orientation of $[(0/90)]_{20}$, and by stitching the layers with Kevlar-29 stitch thread. Kevlar is an

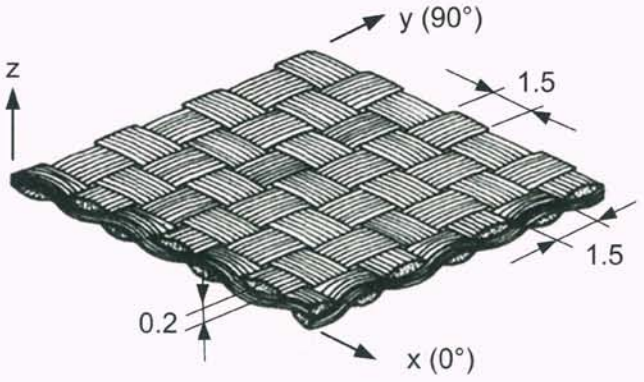

Figure 5.1: Schematic of plain weave fabric [34].

aramid fiber produced by DuPont [5, 118], and probably the most popular fiber employed to reinforce woven fabrics [77]. Its flexibility upon bending, owing to high nominal break strain (up to 100%), makes Kevlar very suitable for stitching material [86]. Kevlar is selected in this study due to its high strength and good resistance to abrasion and heat. Kevlar-29 thread with linear density of 1500 denier (167 tex) is inserted in through-thickness direction into fabric layers with spacing (s) of 12 mm and pitch (p) of 3 mm. Stitch density (SD) of 0.028/mm^2 is thus obtained. The stitch type used to integrate Kevlar-29 thread into the fabrics is lock-stitch type. Lock-stitch represents a simple, yet less susceptible to unraveling, and requires less tension as compared to chain-stitch [86]. To produce stitch composite plates, epoxy EP3631 (Loctite® 3631™ by Henkel) [15] is infused into stitched fabrics by employing resin transfer molding (RTM) process. Curing duration for EP3631 is 2 hr at temperature and pressure of 453 K (180 °C) and 0.588 MPa, respectively. The resulting cured plate has following dimension: 500 mm long, 500 mm wide and 4.2 mm thick. Fig. 5.2a shows top view of Kevlar-stitched plain weave composites whereby two lines running in x-direction are Kevlar-29 threads. The direction of stitch thread is parallel with the warp tows. Fig. 5.2b shows cross-sectional view of Kevlar-stitched composites whereby lock-stitch type can be observed. 'Wavy' bright lines are warp tows of the plain weave, which naturally exhibit out-of-plane waviness. Resin-rich region around stitch penetration hole is also indicated in Fig. 5.2b. Material and thermal properties of T300-3K, EP3631 and Kevlar-29 can be seen in Table 5.1.

5.2.2 Fiber volume fraction

Fiber volume fraction (V_f) of stitched carbon/epoxy is measured using density method using Eq. (2.4). Five small samples measuring approximately 25 mm long × 15 mm wide are cut from the specimens. Weight in air (W_a) and weight in water (W_w) of each sample are measured. Density of composite (ρ_c) can be calculated using Eq. (2.5). Average V_f of Kevlar-stitched carbon/epoxy is 59%.

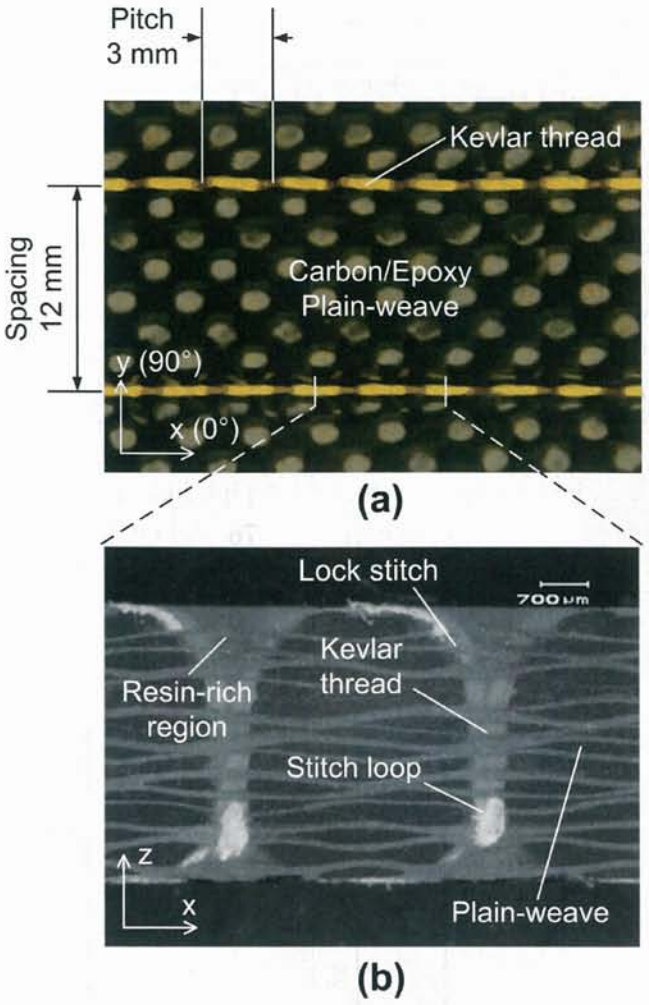

Figure 5.2: Kevlar-stitched carbon/epoxy composites (a) top view, (b) cross-sectional view

5.2.3 Test specimens

Four types of specimen are prepared by cutting the cured plate using water-jet cooled cutting machine AC400F (Maruto), namely (i) tension specimen with longitudinal stitch (code: LS); (ii) tension specimen with transverse stitch (code: TS); (iii) OHT specimen with longitudinal stitch (code: LSH); (iv) OHT specimen with transverse stitch (code: TSH). Nominal dimension of specimen is 250 mm long and 25 mm wide. Direction of stitch lines in LS and LSH specimens is parallel with loading direction and warp tows. Direction of stitch lines in TS and TSH specimens is normal to the loading direction and weft tows. Schematic of four types of specimen are given in Fig. 5.3.

Holes in LSH and TSH specimens are created at the center, specifically between two stitch lines. Location of holes represents a case whereby the position of the hole does not disrupt the continuity of stitch lines. The nominal diameter of hole is 6.35 mm. The hole is created by drilling the sample using a drill bit of 6.30 mm diameter, and followed by a reamer of 6.35 mm diameter. Before the drilling process, it is noteworthy that the specimen is 'sandwiched'

Table 5.1: Mechanical properties of fiber, resin and stitch yarn

Property	Unit	Fiber T300-3K	Resin EP3631	Stitch yarn Kevlar-29
E_L	GPa	234.6	0.106	70.5
E_T	GPa	6.03	0.106	2.59
G_{LT}	GPa	18.2	0.039	2.17
G_{TT}	GPa	6.6	0.039	n/a
ν_{TT}	-	0.2	0.35	0.36
ν_{LT}	-	0.4	0.35	n/a
σ_{ut}	MPa	3530	14.5	2920
ε_f	%	1.5	1150	3.6
d_f	μm	7	-	15.9
ρ	g/cm^3	1.76	1.1	1.44
α_L	10^{-6}/K	-0.41	76	-1.1
α_T	10^{-6}/K	5.60	76	5.00

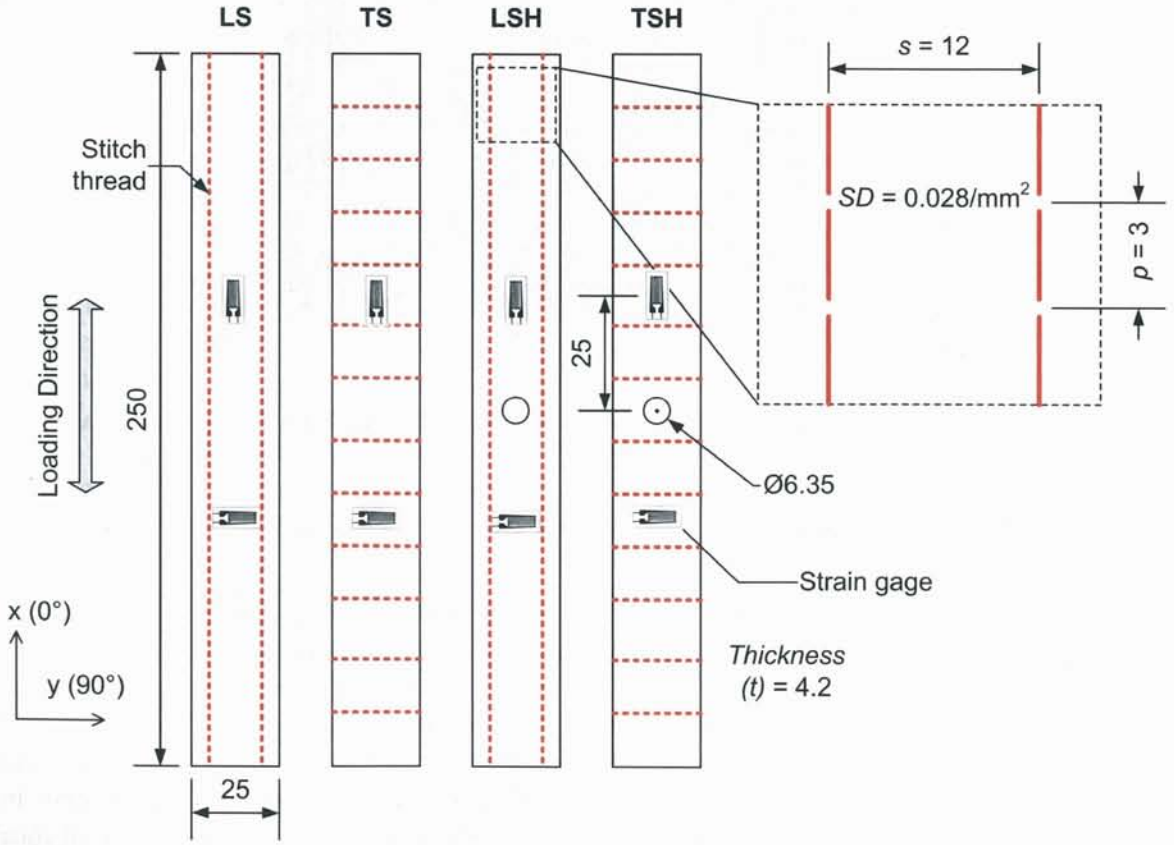

Figure 5.3: Tensile test specimens with longitudinal stitch (LS) and transverse stitch (TS); OHT specimens with longitudinal stitch (LSH) and transverse stitch (TSH) (dimension in mm)

between two small composite plates to provide clamping effect so that the defects around the hole, e.g. chip-out, splintering and delamination, can be minimized. At least three

Table 5.2: Specification of test specimens for tension and OHT tests

Parameter	Unit	Longitudinal stitch		Transverse stitch	
		Tension	OHT	Tension	OHT
Code	-	LS	LSH	TS	TSH
Hole diameter	mm	-	6.35	-	6.35
s	mm	12	12	12	12
p	mm	3	3	3	3
SD	$1/mm^2$	0.028	0.028	0.028	0.028
μ	denier (tex)	1500 (167)	1500 (167)	1500 (167)	1500 (167)
V_f	%	59	59	59	59
t	mm	4.18 ± 0.03	4.14 ± 0.04	4.14 ± 0.04	4.18 ± 0.01
w	mm	25.01 ± 0.01	23.79 ± 0.54	25.20 ± 0.03	25.09 ± 0.12
l	mm	249 ± 0.0	243.3 ± 0.4	249.3 ± 0.6	244 ± 0.0
Quantity	-	3	3	3	2

samples are prepared for each type of specimens, with the exception that only two samples are prepared for TSH specimen. Table 5.2 shows the specification of test specimens for tension and OHT tests.

5.2.4 Tensile and OHT tests procedures

Both tensile and OHT tests are carried out using *Instron 8802* with tensile capacity of 100 kN. Fig. 5.4 shows experimental setup consisting of test specimen, controller, data acquisition system, personal computer, and strain gage terminal box. Test procedures and data processing for fiber reinforced plastic composites are adopted from SRM 4R-94 of SACMA [12] for tension case, and ASTM D5766 [14] for OHT case. Constant displacement with cross-head speed of 1 mm/min is applied to the specimen. No tabs are used for the specimens. Instead, wedge grips referred to self-tightening grips are utilized to prevent the specimen from slipping throughout the test [59]. The test is performed at room temperature (RT) of 293 K (20 °C). Load data during the test is obtained from the load cell. For tension case, measured parameters from the tests are ultimate tensile strength σ_{ut}, failure strain ε_f, Poisson's ratio ν_{xy} and tensile modulus E_x. For OHT test, σ_{OHT} and ε_f are obtained. σ_{ut} and σ_{OHT} are calculated by dividing ultimate tensile load with gross area of specimen (width × thickness). Calculation of σ_{OHT} is in accordance with the calculation of ultimate strength outlined in ASTM D5766 [14]. E_x in tensile case is calculated as a gradient in the stress-strain curves between longitudinal strains of 0.1% and 0.3%. Transverse strains used to calculate Poisson's ratio are also obtained from the strain gages attached in the back-face of specimen. Figs. 5.5a and 5.5b show the installation of strain gage in open hole tension specimens of LSH and TSH, respectively. Five strain gages (abbreviated as SG) are used. SG1, SG2 and SG3 are used to obtain longitudinal strains along x-axis the specimen. In x-axis, SG1, SG2 and SG3 are located at $x_1 = 1$ mm, $x_2 = 5$ mm, and $x_3 = 8$ mm, respectively. SG4 and SG5 are used to measure longitudinal and transverse strains, respectively, in the far-field region. SG4 is located 25 mm above the hole, whilst SG5 is located 25 mm below the hole. The strain gage used is provided by Kyowa with specification of KFG uniaxial 120×, gage length of 5 mm,

gage factor of 2.09±1.0%.

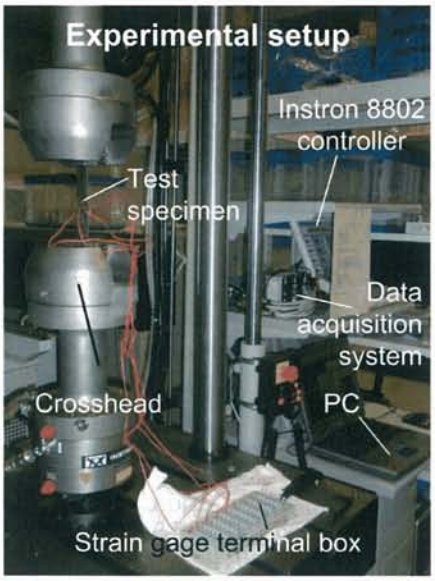

Figure 5.4: Experimental setup for tension and OHT tests

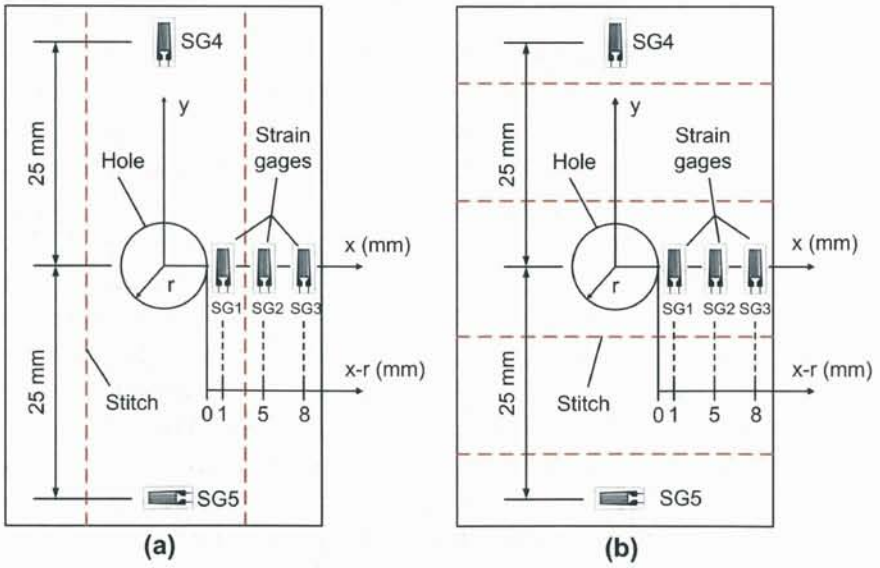

Figure 5.5: Location of strain gage in (a) LSH specimen (b) TSH specimen

5.2.5 Damage characterization procedures

Damage characterization aims to identify the effect of stitch orientation on the fracture morphology of stitched carbon/epoxy. The characterization is carried out by visual inspection (Canon digital camera), optical microscope (Mitutoyo) with magnification of up to 50×, image acquisition system (Olympus) and X-ray radiography (Softex). After the test, photograph of each specimen is taken. A magnified view of fractured region is then obtained

by optical microscope. Post-mortem investigation is also carried out by performing X-ray radiography utilizing Softex. Detailed procedure for X-ray radiography can be reviewed in Section 2.2.5. From these methods, damage mechanisms pertaining to the effect of stitch orientation on Kevlar-stitched composite with and without holes are described.

5.3 Experimental Results and Discussion

5.3.1 Stress-strain curves

Typical stress-strain curves of stitched carbon/epoxy plain weave composites for LS and TS specimens are shown in Figs. 5.6a and 5.6b, respectively. x-Axis denotes tensile strain obtained from the strain gage in longitudinal direction (SG4), while y-axis denotes tensile stress obtained by dividing applied load with gross area. LS and TS specimens exhibit linearity with no sign of a knee-point up to its final failure regardless the stitch orientation. This may suggest that progressive damage did not occur and the knee-point could not be captured using strain gage. Figs. 5.6c and 5.6d show the stress-strain curves of LSH and TSH specimens, respectively. No clear distinction can be made in terms of stress-strain curves amongst LS, TS, LSH and TSH specimens. All stress-strain curves exhibit similar linearity suggesting that stitching or presence of hole does not seem to alter the stress-strain response of carbon/epoxy plain weave, except that the ultimate stress of specimens with holes is considerably lower than those without holes.

5.3.2 Failure mode

Fig. 5.7 shows the photographs of typical static failure experienced by LS, TS, LSH and TSH specimens. As indicated by the ellipses, failure site of all specimens falls within the gage length, and the failure is characterized by brittle fracture. A more detailed observation is carried out using optical microscope. Failure of LS specimen, for instance, is characterized by a rupture of warp and weft tows. Fig. 5.8 visibly shows that the direction of brittle fracture is perpendicular to the loading direction making the rupture to be relatively straight across the width and through-thickness direction. The failure of TS, LSH and TSH specimens also shows similar characteristics with that of LS specimen. Such failure mode is akin to that of plain weave T300/EP2500 composites tested by Kawai and Taniguchi [68].

5.3.3 Tensile and OHT properties

Tensile and OHT properties of Kevlar-stitched plain weave are tabulated in Table 5.3. Average tensile strength of LS specimens is 616 MPa, while that of TS specimens is 465 MPa. In this case, reduction of 24.4% of tensile strength is observed when transverse stitching is introduced into carbon/epoxy composites. Correspondingly, average failure strain of TS specimens is lower than that of LS specimens (ε_f of LS specimen is 0.93%; ε_f of TS specimen is 0.72%). Failure strain of TS specimens is 29.7% lower than that of LS specimens. The reduction of strength as well as failure strain experienced by TS specimen is mainly related

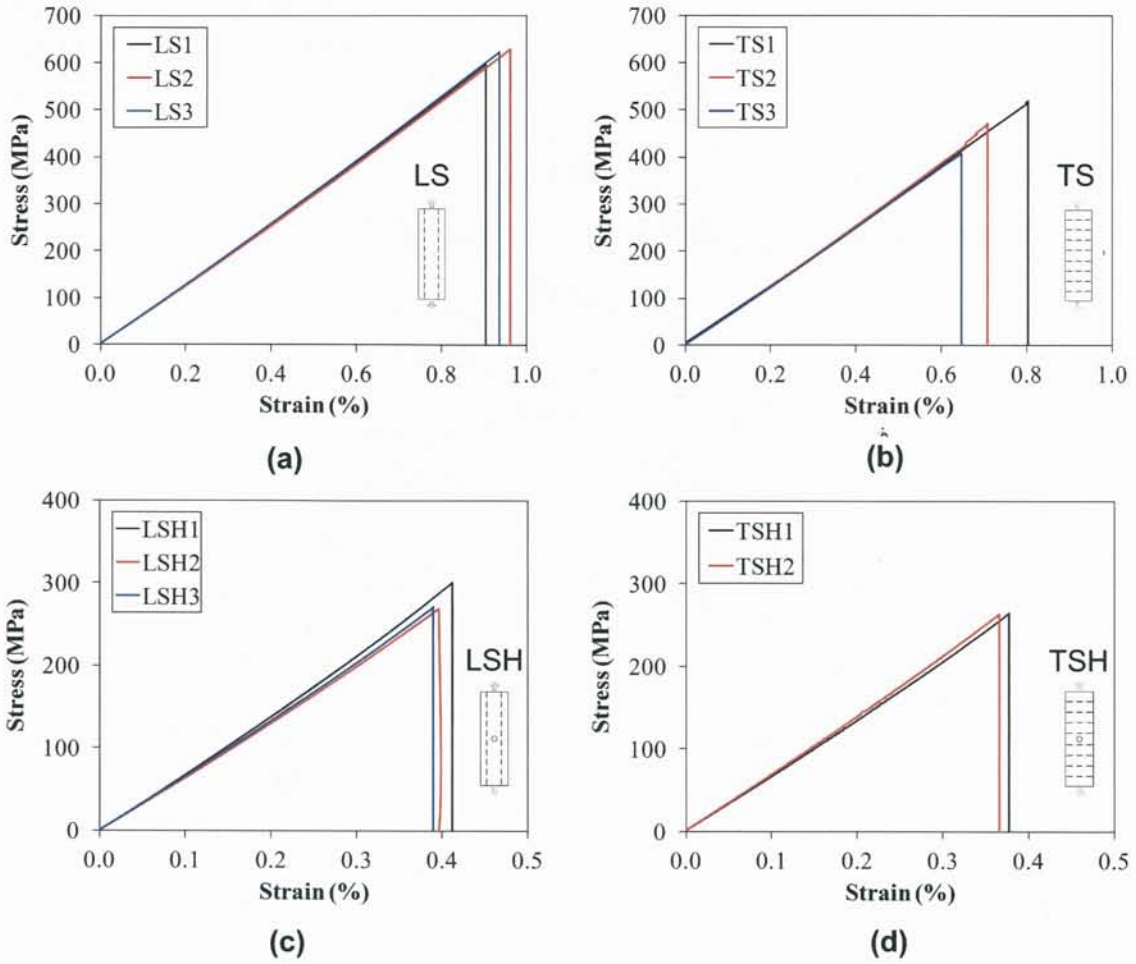

Figure 5.6: Stress-strain curves of (a) LS specimens, (b) TS specimens, (c) LSH specimens, (d) TSH specimens

to stitch debonding. Tensile modulus of LS specimens is 63.5 GPa, while of TS specimens is 62.6 GPa. The stiffness difference of merely 1.4% indicates that the stitch orientation does not affect the response of plain weave to elongate longitudinally under static condition. Tensile modulus is not affected by fiber waviness, which is localized around stitch region only. Poisson's ratio of LS specimens is 0.047, whilst that of TS specimens is 0.055. There is 14.8% difference of Poisson's ratio between LS and TS specimens.

It is shown in Table 5.3 that σ_{OHT} of LSH specimen is 285 MPa, whilst that of TSH specimen is 264 MPa. Strength reduction of 7.3% is experienced by carbon/epoxy when transverse stitching is used for OHT specimens. Failure strain of TSH specimen, which is 0.37%, is 8.1% lower than that of LSH specimen ($\varepsilon_f = 0.40\%$). The reduction of strength and failure strain in open hole specimens can be considered small in this case, and it suggests that the failure may not be greatly controlled by the stitch threads. As later shown, the failure in open hole specimens of LSH and TSH, regardless the stitch orientation, is determined by the stress concentration at the hole rim rather than the stitch debonding.

It is important to note that OHT test is not usually carried out to obtain tensile modulus

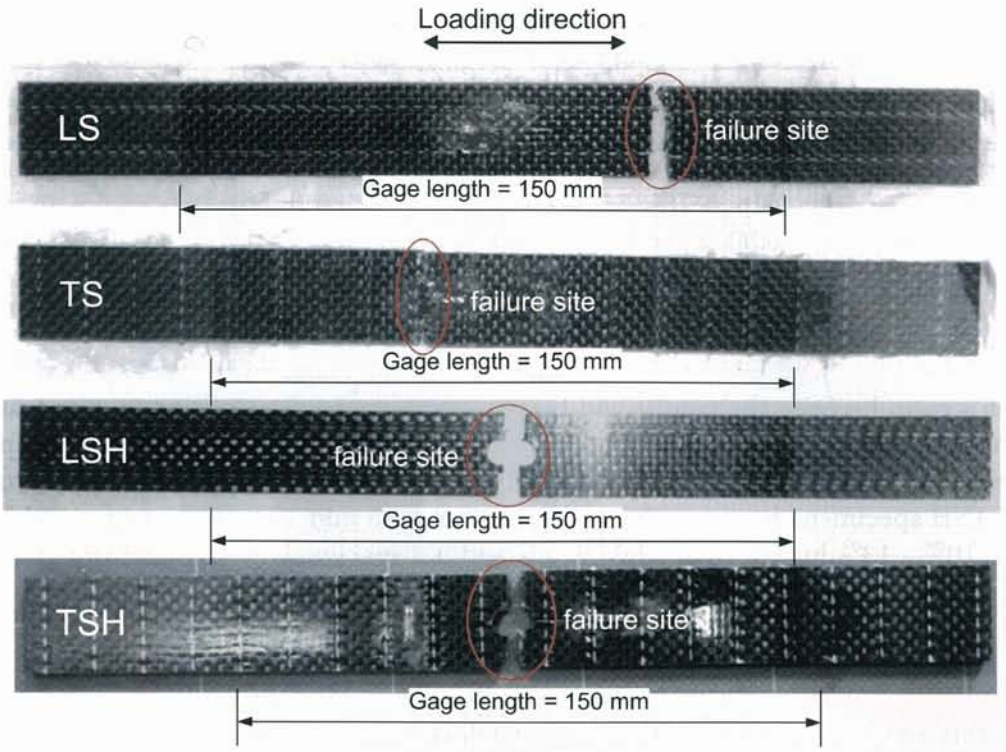

Figure 5.7: Failure mode of LS, TS, LSH and TSH specimens

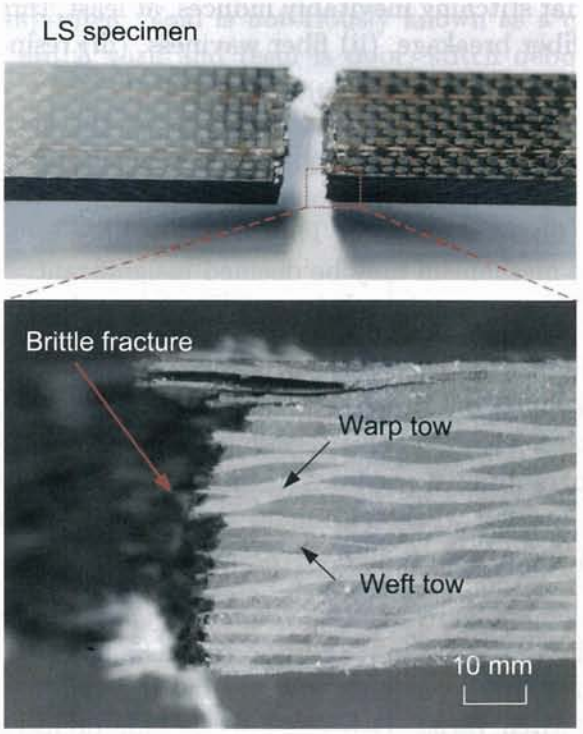

Figure 5.8: Brittle fracture of LS specimen

Table 5.3: Tensile and OHT properties of Kevlar-stitched carbon/epoxy composites

Parameter	Unit	Longitudinal stitch		Transverse stitch	
		Tension	OHT	Tension	OHT
Code	-	LS	LSH	TS	TSH
σ_{ut} or σ_{OHT}	MPa	616 ± 18	285 ± 22	465 ± 56	264 ± 1
ε_f	%	0.93 ± 0.03	0.40 ± 0.01	0.72 ± 0.08	0.37 ± 0.01
E_x	GPa	63.5 ± 0.6	69.9 ± 2.9	62.6 ± 1.0	70.6 ± 1.1
ν_{xy}	-	0.047 ± 0.011	0.050 ± 0.036	0.055 ± 0.012	0.025 ± 0.003

or Poisson's ratio because the results can be very sensitive to the positioning of strain gages in the specimen containing circular holes. In this case, 'stiffening' effect was experienced by OHT specimens, in which higher tensile moduli for LSH and TSH specimens were produced. LSH and TSH specimens have tensile moduli of 69.9 GPa and 70.6 GPa, respectively. These values are 10% - 13% higher than those of LS and TS specimens.

5.3.4 Architectural changes induced by stitching

The implication of having through-thickness stitch threads with regard to the architecture of plain weave composites is given in this section. Fig. 5.9 shows the optical microscopy image and corresponding schematic of architectural changes due to stitching in present plain weave composites. It is shown that stitching inevitably induces, at least, three architectural changes in fabric composites: (i) fiber breakage, (ii) fiber waviness, (iii) resin-rich region.

1. Fiber breakage, which appears as trimmed fibers at the cleavage of stitch penetration hole, is a result of a puncture by the stitch needles and a friction between stitch threads and fiber tows. However, portion of fiber breakage within a fiber tow is usually below 0.5% of total fiber volume [83]. Thus, effect of fiber breakage on the mechanical properties or failure mechanism may be deemed insignificant.

2. Fiber waviness exists in almost all fibrous composite systems. It is characterized by the local deviation of fibers from their respective tow orientation. In this case, plain weave already exhibits waviness due to its inherent architecture. Stitching further induces waviness when stitch needles and their ensuing thread perforate the wavy fiber tows of plain weave. The magnitude of waviness, usually indicated by waviness amplitude and angle, is adversely affected when tensioning force by the stitch yarns is high, and by the diameter of stitch yarns as well.

3. Resin-rich region is generally defined as a volumetric space filled with resin. Coalescence of a number of resin-rich regions may result in resin channel (see Chapter 2). In stitched plain weave, similar to fiber waviness, the size of resin-rich region is partly influenced by the diameter of stitch yarns. Other factors include preform type and manufacturing method. In present experiment, Kevlar stitch thread with linear density of 1500 denier has a diameter of 0.80 mm, which is considered large. When the stitch thread penetrates the fabric, fiber tows of plain weave are consequently misaligned with significant waviness amplitude and angle. A space between stitch yarn and misaligned fibers

is subsequently permeated with the resin during resin infiltration process. Therefore, resin-rich region in plain weave may be large enough to cause early cracking around stitch thread.

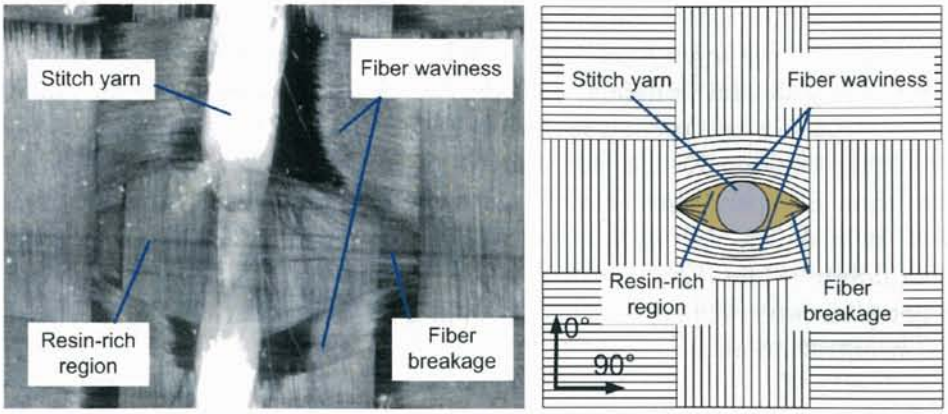

Figure 5.9: Architectural changes and defects due to stitching, namely fiber waviness, resin-rich region, fiber breakage: (a) photomicrograph, (b) illustration

Formation of resin-rich region may give rise to the initiation of cracks because of two reasons. Firstly, resin-rich region may statistically contain relatively a higher number of voids than any other constituents of composites. Void is notoriously known as a crack initiator. Secondly, if the cohesion between stitch yarn and resin is poor, stitch debonding may easily occur. The location with highest possibility to have stitch debonding is resin-rich region, where the volume of resin is high. Upon loading, stitch debonding would grow or interact with other damages. The progression of damage would adversely affect the performance of stitched composites, and cause premature failure.

5.3.5 Premature failure in TS specimens

It is shown in Section 5.3.3 that TS specimens have lower tensile strength in comparison to LS specimens. As mentioned, 24.4% reduction of tensile strength is observed when transverse stitching is introduced into carbon/epoxy. Despite the fact that both LS and TS specimens exhibit similar brittle fracture, further observation shows that strength reduction in TS specimen is mainly attributed to the debonding between stitch thread and surrounding matrix. The so-called stitch debonding is caused by (i) difference of coefficient of thermal expansion (CTE) between Kevlar and epoxy, (ii) poor bonding between Kevlar and epoxy. The first reason is rather apparent as the residual stresses would be high when the difference of thermal expansion coefficient is also high. Upon curing after RTM process, the residual stress would induce the formation of initial cracks between Kevlar stitch thread and epoxy. Another factor is the surface area of stitch thread: because the linear density of Kevlar is 1500 denier, i.e. surface area exposed to resin phase is relatively large, the possibility to have pre-test crack in the resin is also high. As for the second reason (poor bonding between Kevlar and epoxy), it may be due to the absence of surface treatment (e.g. etching) prior to RTM process. Etching

the Kevlar fiber by optimizing the surface roughness is deemed necessary to improve the bonding between Kevlar and epoxy. In this case, etching process is likely absent, and as a result, stitch debonding occurs in stitched carbon/epoxy prior to tensile test. Even when stitch debonding were to develop independently in the individual stitch hole during static test, it may induce formation of resin cracking around resin-rich region. This resin cracking may develop into splitting upon loading. In addition, when fiber splitting in one stitch yarn interact with the neighboring splitting, and form some contiguous cracks in transverse direction, it may eventually create premature failure in TS specimens. Thus, because of the weak interfacial bonding between Kevlar and epoxy, TS specimens would have higher possibility to fail earlier than LS specimens. Fig. 5.10 shows the X-ray image of fracture location in TS specimen. It is shown that a high number of resin cracking have occurred in all stitch holes prior to failure. The direction of cracking is perpendicular to the loading direction. Interaction between two crackings originated from two different stitch holes is possible do to high stress concentration at the crack tip.

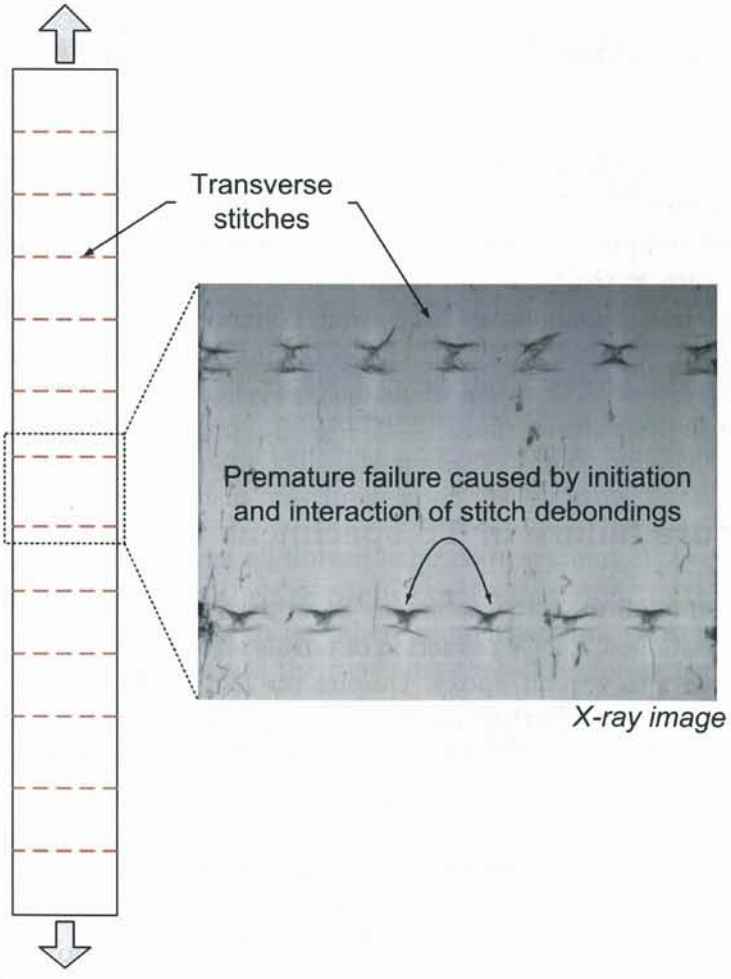

Figure 5.10: X-ray image of TS specimen after failure

5.3.6 Damage mechanisms

Damage initiation and progression in LS and TS specimens

Upon loading, damage origin (initiation) for LS and TS specimens is similar, which is resin-rich region around stitch penetration holes. This damage origin is indicated in Fig. 5.11a. This damage origin, as described earlier, is a result of poor cohesion between Kevlar thread and surrounding epoxy. Crack would become longer upon further loading. However, LS and TS specimens exhibit slightly different damage progression. In LS specimen, crack growing from the stitch thread is in-line with the loading direction, while that in TS specimen is perpendicular to the loading direction. Afterwards, in LS specimens, before the interaction between two cracks around stitch holes occurs, the damage would rapidly grow along the weft tows (perpendicular to the loading direction) towards the specimen edges without necessarily passed through the other stitch holes. In contrast, damage in TS specimen would transversely grow along adjacent stitch holes as a result of interaction between two cracks at the stitch holes (see Fig. 5.10). In this regard, stress concentration at the crack tip of stitch debonding in TS specimen determines the overall failure of TS specimens.

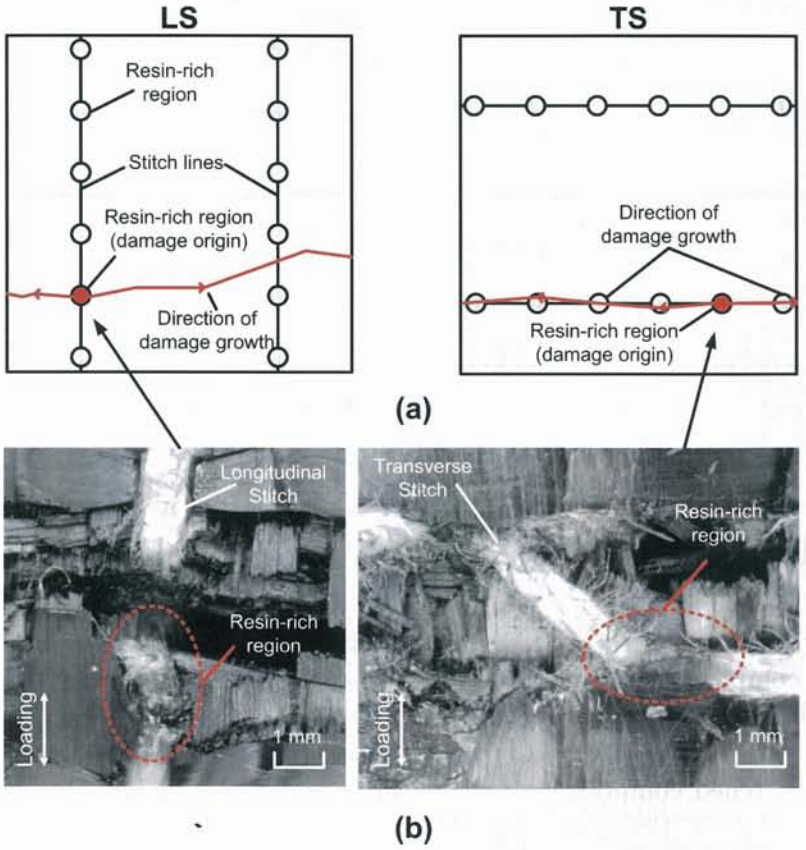

Figure 5.11: Mechanism of damage progression in LS and TS specimens (a) schematic, (b) photomicrograph

Failure characteristics of LS and TS specimens also show that the fracture line always passed through one of the stitch penetration holes. However, the failure in LS specimen is always

characterized by complete breakage of specimen and stitch yarns, while that in TS specimen is characterized by the 'bridging' of two fractured parts provided by the stitches (see Fig. 5.11b). In TS specimen, it is observed that two fractured parts are often still intact because the cracks apparently propagate at the interface between stitch threads and weft tows.

Damage initiation and progression in LSH and TSH specimens

Damage progression in LSH and TSH specimens is markedly different from that of LS or TS specimens. Damage in LSH and TSH specimens as illustrated in Fig. 5.12 always initiates at the hole, and propagate towards the ligament and the specimen edges. The damage in LSH and TSH specimens is greatly controlled by the stress concentration at the hole rim. The failure of LSH and TSH specimens is thus characterized by the fracture of ligaments that does not necessarily pass through the stitch penetration holes. In general, present finding suggests that regardless the stitch orientation, when stitched specimen possesses a hole, its failure would be determined by the stress concentration at the hole rim rather than the damage around the stitches.

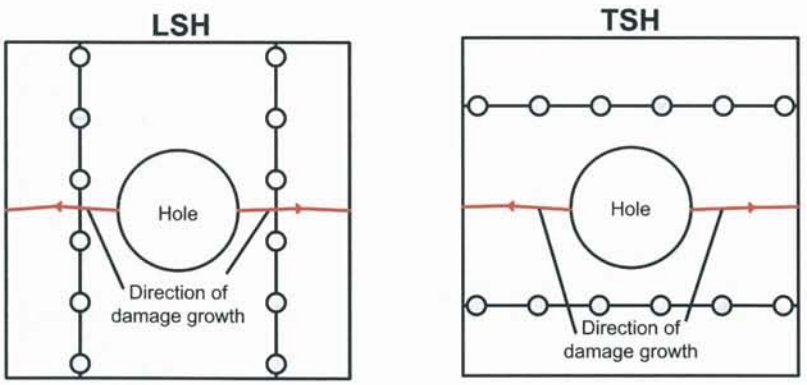

Figure 5.12: Mechanism of damage progression in LSH and TSH specimens

5.4 Analytical Study

Predicting failure strength of stitched composite with hole is important if holes are to be created in stitched composites for practical reason, e.g. joining. OHT strength criterion applicable for unstitched composites widely known as *Average Stress Criterion* (ASC) is presently evaluated. ASC proposed by Whitney and Nuismer in 1974 [116] is employed herein to predict σ_{OHT} of stitched composites. Another criterion proposed by Whitney and Nuismer is *Point Stress Criterion* (PSC). Since both criteria generally yield similar results, only one criterion is discussed herein. ASC requires several parameters, namely tensile strength of specimen without holes (σ_{ut}), normal stress distribution at the ligament (σ_y) and characteristic length (a_0). Tensile strength of stitched composites without hole (LS and TS specimens) is obtained from Table 5.3, while normal stress distribution is measured during experiment. The characteristic length (a_0) for plain weave T300/epoxy plain weave is obtained from Ref. [89].

5.4.1 Normal stress distribution

Normal stress distribution can be estimated by considering an infinite plate with a centrally located circular hole with radius (r) under remote stress (σ_∞) as shown in Fig. 5.13. The exact solution for the normal stress distribution (σ_y) is given by Lekhnitskii [74], and it is expressed as follows

$$\sigma_y = \frac{\sigma_\infty}{2}\left\{2 + \left(\frac{r}{x}\right)^2 + 3\left(\frac{r}{x}\right)^4 - (K_T - 3)\left[5\left(\frac{r}{x}\right)^6 - 7\left(\frac{r}{x}\right)^8\right]\right\} \tag{5.1}$$

K_T (stress concentration factor) can be obtained by the following equation:

$$K_T = 1 + \sqrt{2\left(\frac{E_x}{E_y} - \nu_{xy}\right) + \frac{E_y}{G_{xy}}} \tag{5.2}$$

where E_x, E_y, G_{xy} and ν_{xy} are tensile modulus (longitudinal), tensile modulus (transverse), in-plane shear modulus, and Poisson's ratio, respectively. Mechanical properties in Table 5.3 are used to calculate K_T and normal stress distribution, whereby $E_x = 63.5$ GPa, $E_y = 62.6$ GPa and $\nu_{xy} = 0.047$. As for G_{xy} of 3.8 GPa, it is obtained from Ref. [89].

σ_y can also be obtained by experiment, and following equation can be used:

$$\sigma_y = \frac{E_x\varepsilon_x + \nu_{xy}E_y\varepsilon_y}{1 - \nu_{xy}^2(E_x/E_y)} \tag{5.3}$$

Longitudinal strain ε_x is obtained from the strain gages installed in the x-axis next to the hole, namely SG1, SG2 and SG3. Transverse strain ε_y is obtained from SG5.

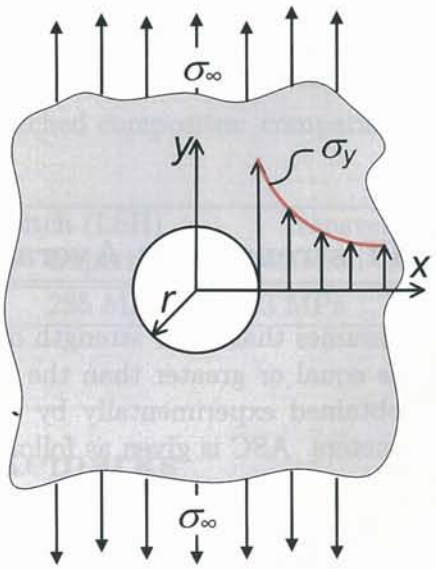

Figure 5.13: Infinite plate with hole under remote stress

Figs. 5.14a and 5.14b show the normal stress distribution along x-axis for LSH and TSH specimens, respectively. Normal stress is normalized with the remote stress. Fig. 5.14 shows that, in general, σ_y obtained by Eq. (5.1) is in a good agreement with experimental result. Thus, it can be concluded that σ_y is insensitive to the stitch orientation. In this case, effect of stitch orientation is outperformed by the effect of hole. Because σ_y is not influenced by the stitch orientation, ASC could therefore be employed to estimate open hole tension strength of stitched composites containing circular holes. ASC is a formula derived from Lekhnitskii theory. Effect of stitch orientation on normal stress distribution could be more profound when the stitch lines are encircling the hole, like in the work of Han et al. [50]. Effect of stitch on normal stress distribution could also be significant when the stitch lines are very close to the holes. If the distance between stitch lines and hole is narrow, the interaction between stress concentration around the hole and the local stress around the stitch may generate further stress amplification. These cases remain to be investigated.

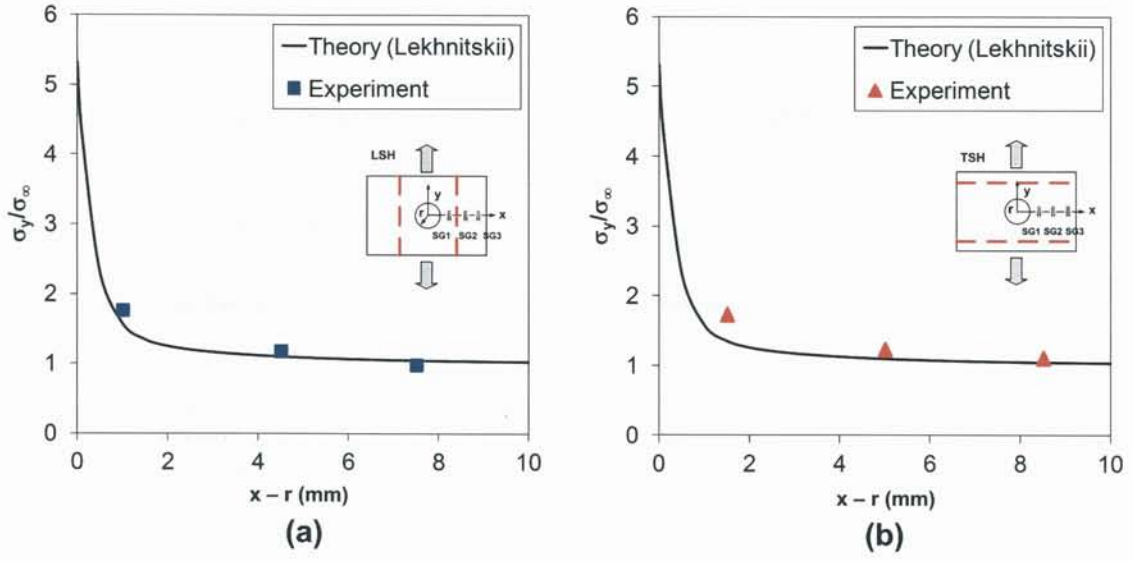

Figure 5.14: Normal stress distribution in x-axis of (a) LSH specimen, (b) TSH specimen

5.4.2 Prediction of OHT strength by Average Stress Criterion

As illustrated in Fig. 5.15, ASC assumes that OHT strength of composites is attained when σ_y at a distance of a_0 in x-axis is equal or greater than the tensile strength of composites without hole (σ_{ut}). a_0 can be obtained experimentally by conducting tensile strength of composites with various hole diameters. ASC is given as follows:

$$\frac{1}{a_0}\int_{r}^{r+a_0} \sigma_{\mathrm{y}}(x)\,\mathrm{d}x \geq \sigma_{ut} \tag{5.4}$$

Substituting Eq. (5.1) into Eq. (5.4) yields the normalized OHT strength:

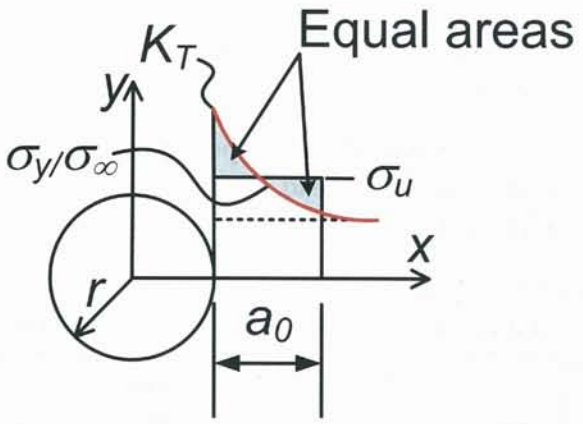

Figure 5.15: Parameters used in Average Stress Criterion

$$\frac{\sigma_{OHT}}{\sigma_{ut}} = \frac{2(1-\xi_1)}{2-\xi_1^2-\xi_1^4+(K_T-3)(\xi_1^6-\xi_1^8)} \tag{5.5}$$

where $\xi_1 = \frac{r}{r+a_0}$. In this case, a_0 of 1.85 is used, and it is obtained from the Ref. [89] for T300/epoxy plain weave.

Table 5.4 shows the comparison between the predicted OHT strength and experimental results. For LSH specimens, σ_{OHT} obtained by ASC is 307 MPa, whilst that obtained by experiment is 285 MPa. For TSH specimens, σ_{OHT} obtained by ASC is 283 MPa, whilst that obtained by experiment is 264 MPa. The difference between experiment and prediction is 7.7% for LSH specimen and 7.2% for TSH specimen. In this regard, ASC can predict σ_{OHT} of stitched composites containing circular holes with reasonable accuracy. However, it should be noted that σ_{OHT} predicted by ASC greatly depends on the characteristic length a_0. To give better accuracy, it is advisable to perform open hole tension test, particularly for stitched composites, with various hole diameters (at least three hole diameters are prescribed).

Table 5.4: OHT strength of stitched composites: comparison between prediction and experiment

Longitudinal stitch (LSH)		Transverse stitch (TSH)	
Prediction (ASC)	Experiment	Prediction (ASC)	Experiment
307 MPa	285 MPa	283 MPa	264 MPa

5.5 Concluding Remarks

Experimental and theoretical investigation of tensile and open hole tension properties of Kevlar-stitched carbon/epoxy composites with longitudinal and transverse stitches have been performed. Several conclusions could be drawn from the studies:

- Stitch orientation affects tensile strength of stitched carbon/epoxy composites without holes. Stitched composites with transverse stitching exhibit around 24% lower strength than that with longitudinal stitching.
- The lower strength of transverse stitched specimens is attributed to the interfacial debonding between Kevlar stitch thread and epoxy resin, which is caused by poor adhesion between Kevlar and epoxy, and the interaction amongst stitch debondings.
- Resin-rich region, specifically at the stitch penetration holes, is found to be the damage initiation site for both longitudinal and transverse stitch specimens.
- Tensile modulus of stitched carbon/epoxy plain weave is insensitive to the stitch orientation. This is because the longitudinal deformation is not affected by the stitch orientation nor the collective fiber waviness due to stitching.
- Failure of stitched carbon/epoxy plain weave is characterized by brittle failure regardless the stitch orientation.
- OHT tests show that the strength of stitched carbon/epoxy composites with holes (i.e. open hole strength) is independent of stitch orientation. OHT strength depends strongly on normal stress distribution and stress concentration generated around the hole rims.
- Because normal stress distribution in stitched composites with holes is independent of stitch orientation, it can therefore be estimated by Lekhnitskii theory. Hence, OHT strength of stitched composites can be estimated by Average Stress Criterion, which is based on Lekhnitskii theory, with reasonable accuracy.

Chapter 6

Kevlar-stitched carbon/epoxy composites with holes under fatigue

6.1 Overview

This chapter discusses experimental investigation of fatigue characteristics and damage mechanisms of Kevlar-stitched carbon/epoxy composites with circular holes. Effect of stitch pattern, namely round stitch and parallel stitch, on fatigue life and fatigue damage mechanisms of Kevlar-stitched composites with holes are evaluated. Fatigue cycle is carried out at constant amplitude with the frequency of 5 Hz. Three cases are studied in this chapter: (i) round stitched composites under tension-tension (T-T) fatigue; (ii) parallel stitched composites under T-T fatigue; (iii) parallel stitched composites under compression-compression (C-C) fatigue. Maximum stress levels applied during fatigue test are defined between 50% and 90% relative to the open hole strength of respective case. Fatigue damage growth is observed and quantified by conducting interrupted test at different cycles coupled with ultrasonic C-scan. Quantification of damage is performed by measuring damage area.

6.2 Experimental Details

6.2.1 Materials

Two types of carbon/epoxy composite are used in this experiment, namely T300/EP828 and T300/PR500. Carbon fiber is T300-3K (CO6303L), which is made by Toray Industries Inc., and available in the form of bi-directional (0/90) fabric or plain weave. The resin of EP-828 (Epikote 828) is a bisphenol type-A epoxy produced by Yuka Shell Epoxy Co. Ltd. PR500 is a high performance epoxy produced by 3M, Co. Stitch thread used to bind the plain weave preforms is Kevlar-29 aramid yarn (DuPont) with linear density of 1000 denier (111 tex). Mechanical properties of carbon T300-3K [6], stitch yarn Kevlar-29 [5, 118], EP828 [91] and PR500 [73, 124] are given in Table 6.1.

To manufacture stitched carbon/epoxy composites, twenty plain weave layers are first stacked

Table 6.1: Mechanical properties of fiber, resin and stitch yarn

Property	Unit	Fiber	Resin		Stitch yarn
		T300-3K	EP828	PR500	Kevlar-29
E_L	GPa	234.6	3.4	3.6	70.5
E_T	GPa	6.03	3.4	3.6	2.59
G_{LT}	GPa	18.2	1.26	2.1	2.17
G_{TT}	GPa	6.6	1.26	2.1	n/a
ν_{LT}	-	0.2	0.35	0.37	0.36
ν_{TT}	-	0.4	0.35	0.37	n/a
σ_{ut}	MPa	3530	85	56.6	2920
ε_f	%	1.5	n/a	1.9	3.6
d_f	μm	7	-	-	15.9
ρ	g/cm^3	1.76	1.54	1.26	1.44
α_L	10^{-6}/K	-0.41	n/a	n/a	-1.1
α_T	10^{-6}/K	5.60	n/a	n/a	5.00

with specified stacking sequence. In present experiment, two stacking sequences are prepared: cross-ply of $[(0/90)]_20$ and quasi-isotropic of $[(\pm45)(0/90)_2(\pm45)_2(0/90)_2(\pm45)_2(0/90)]_S$. Fabrics are then stitched using Kevlar-29 yarn. The stitch type used to insert Kevlar-29 yarn into the fabrics is lock-stitch. After stitching process, resin transfer moulding (RTM) is employed to infuse resin into stitched fabrics. Resin is flowing in radial direction, and curing process during RTM is performed in the mould. Curing temperature and pressure of epoxy are set at around 393 K (120 °C) and 0.60 MPa, respectively. The curing process is performed for about 2 hrs. The cured plate has dimensions of 500 mm in length and 500 mm in width. Nominal thickness of cured plate is 4.5 mm with standard deviation of 0.1 mm. Fiber volume fraction (V_f) of plate without stitch is 51.4±0.8%, whilst that with stitch is 52.1±1.4%. Fig. 6.1 shows optical microscopy images of cross-ply and quasi-isotropic composites, particularly at the edges, region without stitches and region with stitches.

6.2.2 Open hole test specimens

Test specimens were prepared based on the case number. As mentioned, three cases were investigated, and all specimens are composites containing circular holes. In Case 1, specimen with round stitch is studied, and fatigue load is tension-tension (T-T) fatigue ($R = \sigma_{min}$ $/\sigma_{max} = 0.1$). In Case 2, specimen with parallel stitch is studied, and fatigue load is also T-T fatigue ($R = 0.1$). In Case 3, specimen with parallel stitch is studied, and fatigue load is compression-compression (C-C) fatigue ($R = 10$). Table 6.2 summarizes the case studies and corresponding material system, types of specimen, stitch configuration, content of stitch yarn, specimen codes as well as number of specimen used in present investigation.

Holes in the specimen were created using single-angle diamond-coated drill bit with a nominal diameter of 5.70 mm. Fig. 6.2 shows post-drilling condition obtained by optical microscopy and X-ray radiography. It is confirmed that there is no surface ply splintering nor delamination at the hole rim, which indicates that the drilling process was properly conducted.

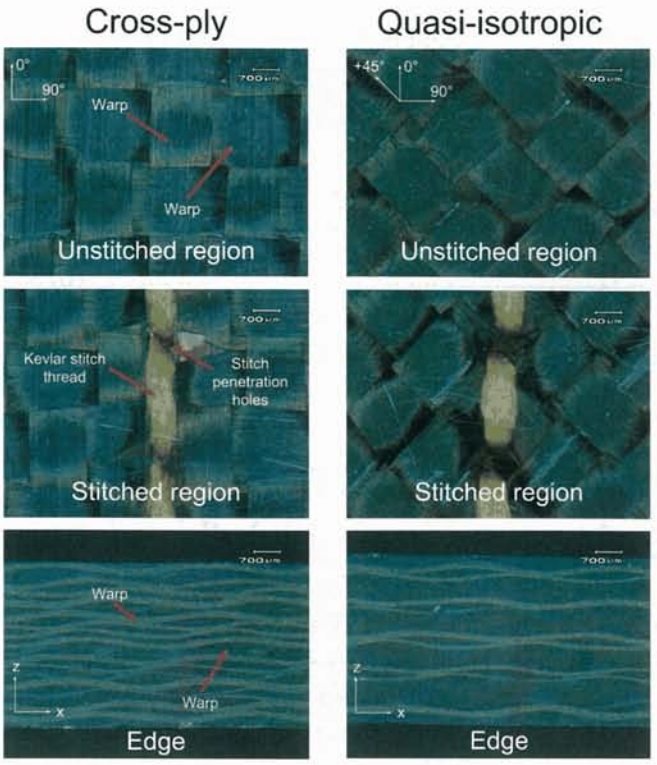

Figure 6.1: Optical microscopy images of cross-ply and quasi-isotropic composites

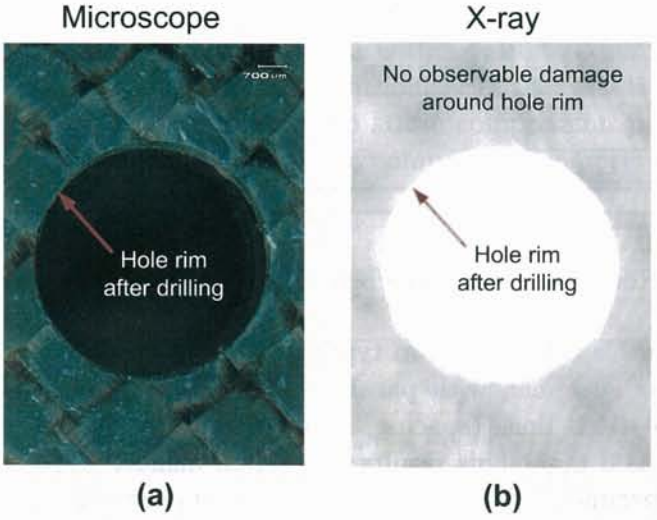

Figure 6.2: Hole condition after drilling process (a) optical microscopy result, (b) X-ray image

The specimens used in Case 1 are of two types: with and without round stitch. Fig. 6.3 shows the schematic of specimen with round stitch, whereby stitch line encircles the hole with diameter of 7 mm. The specimen dimension is 190 mm in length and 25 mm in width. Thickness of specimen is 4.5 mm. Glass/epoxy tabs are glued on the specimen allowing 90 mm gage length. Thickness of tab is 3.5 mm, and length of tab is 50 mm. The distance between hole edge rim and round stitch line is approximately 0.65 mm. Twenty specimens

Table 6.2: Material system, specimen and codes for three cases

Parameter	Case 1 Round stitch (C-C fatigue)	Case 2 Parallel stitch (T-T fatigue)	Case 3 Parallel stitch (T-T fatigue)
Composite system	T300-3K/EP828	T300-3K/PR500	T300-3K/PR500
Tow orientation	$[(0/90)]_{20}$	$[(0/90)]_{20}$	$[(\pm45)(0/90)_2(\pm45)_2$ $(0/90)_2(\pm45)_2(0/90)]_S$
Load ratio, R	0.1	0.1	10
Codes	RTN (unstitched) RTS (stitched)	PTN (unstitched) PTS (stitched)	PCN (unstitched) PCS (stitched)
Static test qty.	2 (unstitched) 2 (stitched)	2 (unstitched) 2 (stitched)	2 (unstitched) 2 (stitched)
Fatigue test qty.	8 (unstitched) 8 (stitched)	4 (unstitched) 4 (stitched)	8 (unstitched) 8 (stitched)

are prepared for Case 1: ten specimens without stitch (code: RTN); ten specimens with stitch (code: RTS). Specimen without stitch serves as a baseline for the stitched one. For each specimen code, two specimens are tested under tension to obtain open hole tension (OHT) strength σ_{OHT}, while eight specimens are subjected to tension-tension fatigue test.

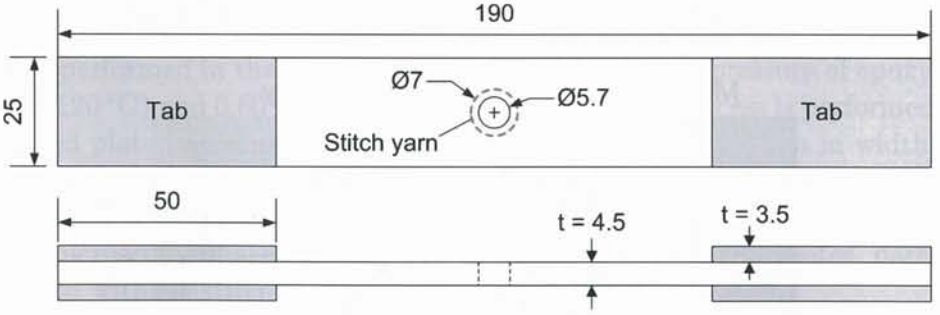

Figure 6.3: Round stitched specimen for T-T fatigue (dimension in mm)

The specimens used in Case 2 are of two types: with and without parallel stitch. Fig. 6.4 shows the schematic of specimen with parallel stitch. In parallel stitch configuration, the distance between two stitch lines (spacing, s) is 15 mm, while the distance between two stitch holes (pitch, p) is 3 mm. This results in a stitch density (SD) of 0.022/mm^2. Stitch content (V_s) for this specimen is 1.06%. The specimen dimension is the same as that in Case 1, which is 190 mm in length and 25 mm in width. Glass/epoxy tabs with thickness of 3.5 mm and length of 50 mm are also used. Twelve specimens are prepared for Case 2: six specimens without stitch (code: PTN); six specimens with stitch (code: PTS). Likewise, specimen without stitch serves as a baseline. For each specimen code, two specimens are tested under tension to obtain σ_{OHT}, while the other four specimens are subjected to tension-tension fatigue test.

Same with Cases 1 and 2, specimens used in Case 3 are of two types: with and without parallel stitch, except that the dimension of specimen for Case 3 is different. The length of specimen is 118 mm, while the width is 38 mm. Using this specimen, open hole compression

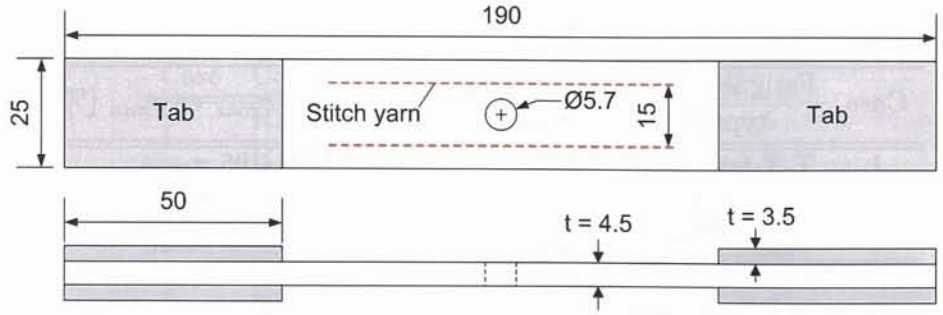

Figure 6.4: Parallel stitched specimen for T-T fatigue (dimension in mm)

(OHC) and C-C fatigue tests are carried out using NAL-III fixture, which is developed by Japan Aerospace Exploration Agency [63]. NAL-III is a small supporting fixture with rounded-corner rectangular windows. The fixture is employed to prevent global buckling during compression test. The fixture has windows with the dimension of 25.4 mm in length and 16.4 mm in width to allow out-of-plane deformation before final failure. The details of the fixture can also be reviewed in [101]. Thus, the specimen is called NAL-III specimen. NAL-III specimen is more economical than the specimen defined in SACMA SRM 3R-94 [11], yet the data scatter for open hole compression strength σ_{OHC} is lower for NAL-III specimen. Fig. 6.5 shows the schematic NAL-III specimen with parallel stitch. For the stitched specimens, spacing and pitch are also 15 mm and 3 mm, respectively. SD is 0.022/mm^2 and V_s is 1.07%. By using the width of 38 mm, NAL-III specimen could accommodate four stitch lines. Glass/epoxy tabs with thickness of 3.5 mm and length of 50 mm are also used. Twenty specimens are prepared for Case 3: ten specimens without stitch (code: PCN); ten specimens with stitch (code: PCS). Likewise, specimen without stitch serves as a baseline. For each specimen code, two specimens are subjected to static compression test in order to obtain σ_{OHC}. The other ten specimens are subjected to compression-compression fatigue test.

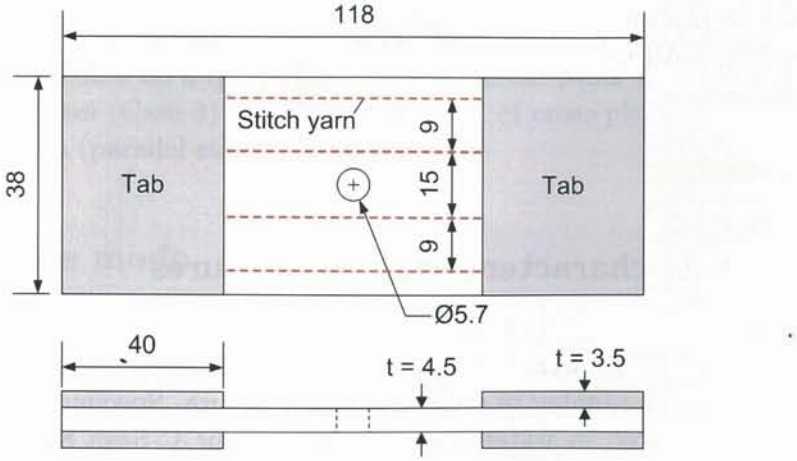

Figure 6.5: Parallel stitched specimen for C-C fatigue (dimension in mm)

Table 6.3: Fatigue test setting for three cases

Case	Fatigue test type	Load ratio $R = \sigma_{min}/\sigma_{max}$	Range of σ_{max} or σ_{min} (%)
1	T-T fatigue	0.1	70 - 95 σ_{OHT}
2	T-T fatigue	0.1	85 - 95 σ_{OHT}
3	C-C fatigue	10	55 - 70 σ_{OHC}

6.2.3 Static test procedures

Prior to fatigue tests, static test was performed to obtain σ_{OHT} or σ_{OHC} depending on the case. In Cases 1 and 2, σ_{OHT} was obtained, while in Case 3, σ_{OHC} was obtained. σ_{OHT} and σ_{OHC} were used to determine σ_{max} or σ_{min} during fatigue tests. Servo hydraulic Instron 8501 was used during static tests. Loading rate during tension test is 1 mm/min, while that during compression test is 0.5 mm/min. No fixture required for OHT test. For OHC test, as mentioned, NAL-III fixture is used. Specimens were tested until they failed, and maximum load (P_{max}) is recorded. σ_{OHT} and σ_{OHC} are calculated by dividing respective P_{max} with gross area (width $\times$ thickness).

6.2.4 Fatigue test procedures

After performing static tests, fatigue tests are carried out. Table 6.3 shows fatigue test setting used in present experiments. T-T fatigue is performed at frequency of 5 Hz in sinusoidal wave pattern. The range of applied maximum stress σ_{max} is defined between 70% and 95% of σ_{OHT}. C-C fatigue test is also conducted at frequency of 5 Hz. The range of σ_{max} is between 55% and 70% of σ_{OHC}. All tests were performed under load control manner.

6.2.5 Damage characterization procedures

To observe the damage growth during fatigue test, interrupted test was carried out by stopping the test at certain number of cycle (N) before failure. Specimen was then removed from the machine, and placed in water chamber. Ultrasonic C-Scan SDS3300R (Krautkramer) probed the surface of the specimen, and image of damage zone was captured. Damage area is assumed as a projected area as seen in C-Scan image. Damage zone was then quantified by measuring the observable damage area from C-scan results. X-ray radiography and optical microscope were also used as post-mortem damage observation tools.

Table 6.4: Open hole strength for Cases 1-3

Case	Code	Open hole strength
1	RTN (unstitched)	$\sigma_{OHT} = 320.0 \pm 3.5$
	RTS (stitched)	$\sigma_{OHT} = 304.7 \pm 2.8$
2	PTN (unstitched)	$\sigma_{OHT} = 301.6 \pm 0.9$
	PTS (stitched)	$\sigma_{OHT} = 301.4 \pm 0.9$
3	PCN (unstitched)	$\sigma_{OHC} = 281.8 \pm 6.7$
	PCS (stitched)	$\sigma_{OHC} = 282.2 \pm 2.6$

6.3 Experimental Results and Discussion

6.3.1 Static test results

Results of open hole static test are given in Table 6.4. Magnitude of σ_{OHT} and σ_{OHC} is an averaged value of two test samples. For Case 1, σ_{OHT} of RTN specimen is 320 MPa, whilst that of RTS specimen is 304.7 MPa. The difference of open hole tension strength between unstitched and round-stitched specimen is around 4.8%. This loss of OHT strength is negligible. For Case 2, σ_{OHT} of PTN specimen is 301.6 MPa, while that of PTS specimen is 301.4 MPa. Similar with Case 1, the difference of σ_{OHT} is also negligible. It is found that, in general, parallel stitch does not impart significant effect on the open hole tensile strength of carbon/epoxy composites. As a reference, tensile strength of typical plain weave carbon/epoxy composites is 536 $\pm$ 80 MPa. Hole of 5.7 mm diameter reduces the strength by around 40%. Presence of hole dismisses the sensitivity of plain weave carbon/epoxy composites to the stitches because failure in open hole specimen is greatly determined by high stress concentration at the hole rim rather the stresses around the stitches. This observation is of similar case with the ones described in Chapter 5. It is postulated here that the normal stresses around the stitches could be lower than that in the hole rim. For Case 3, σ_{OHC} of PCN specimen is 281.8 MPa, whilst that of PCS specimen is 282.2 MPa. Similar to tension test results, it is shown that parallel stitch does not affect σ_{OHC} of carbon/epoxy composites. Tensile modulus of cross-ply plain weave composites used in Cases 1 and 2 are 48.1 GPa (unstitched) and 51.8 GPa (parallel stitched). On the other hand, tensile modulus of quasi-isotropic composites (Case 3) are lower than that of cross-ply composites: 36 GPa (unstitched) and 40.8 GPa (parallel stitched).

6.3.2 Static failure mode

Fig. 6.6 shows some examples for typical static failure of specimens without and with stitch. No significant difference is found between unstitched (Fig. 6.6a) and stitched specimens (Fig. 6.6b). Both specimens generally exhibit brittle fracture. Damage was found to be initiated from the hole rim, and aggressively propagated towards the specimen edges causing catastrophic rupture of all fiber tows in the ligaments.

Fig. 6.7 shows typical static failure of unstitched specimen under compression. Similar to tension case, failure in unstitched specimen under compression is also characterized by brittle

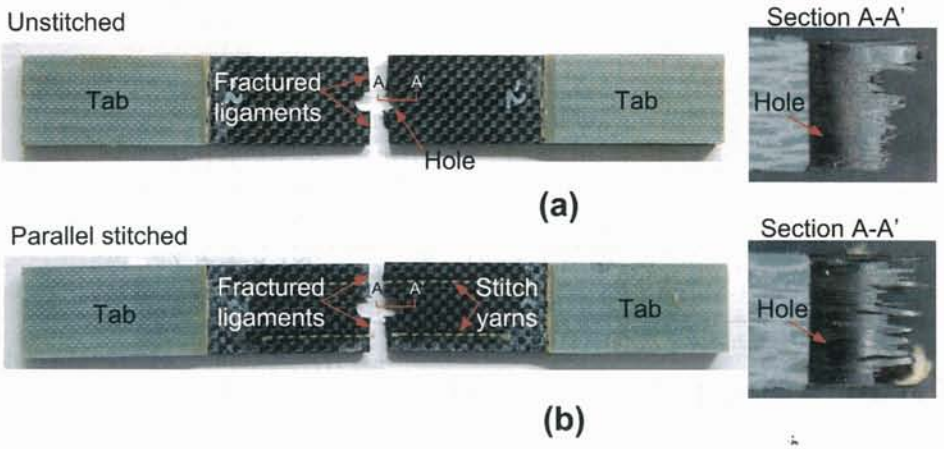

Figure 6.6: Static failure of open hole specimen under tension (a) unstitched specimen (PTN), (b) parallel stitched specimen (PTS)

fracture, in which fractured ligaments are apparent. Optical microscopy on the specimen edge shows that the failure is characterized by shear fracture and delamination. The delamination extends across the gage length and width. In the hole rim, shear fracture and delamination are also evident. Both failure modes characterize the internal part of fractured ligaments.

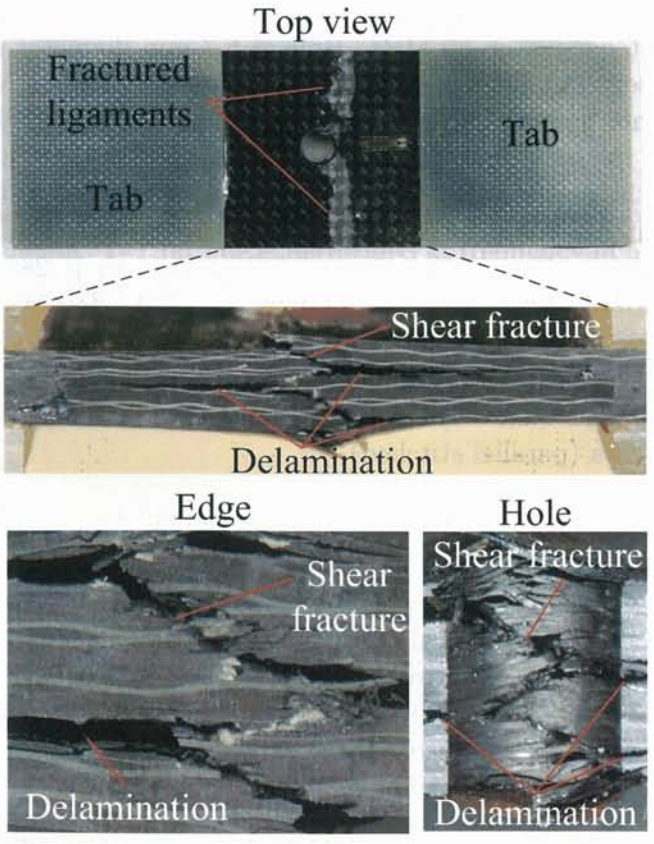

Figure 6.7: Static failure of unstitched specimen with hole (PCN) under compression

Fig. 6.8 shows static failure of stitched specimen under compression, which is also brittle fracture. Shear fracture is dominant in this case. Delamination in stitched specimens is not as dominant as in unstitched specimen. This may indicate that stitches may impede the growth of delamination after fracture. The role of stitches in inhibiting the growth of delamination can be observed in Fig. 6.9. Fig. 6.9 is obtained by cross-sectioning PCS specimen along a stitch line. The stitches provide bridging traction that reduces the extent of delamination.

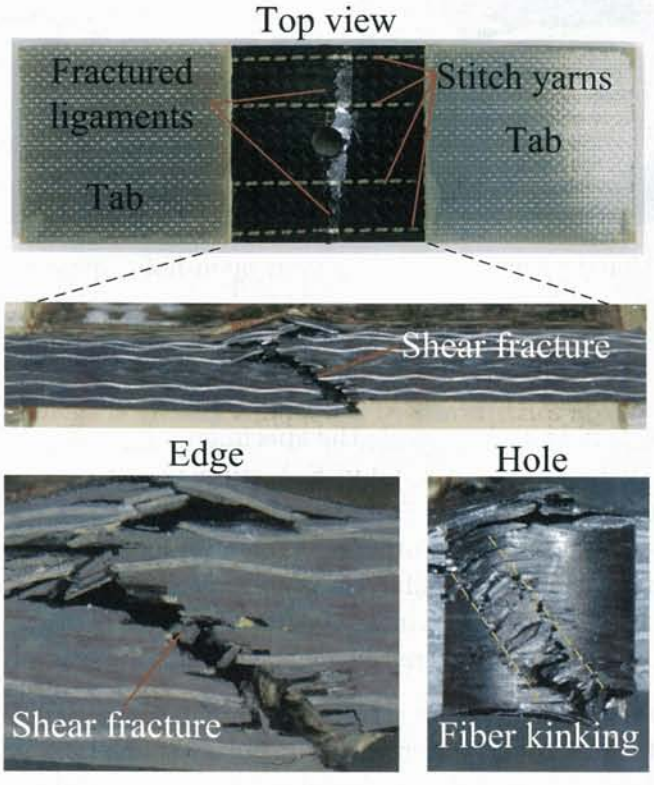

Figure 6.8: Static failure of parallel stitched specimen with hole (PCS) under compression

6.3.3 Fatigue of round stitched composites under T-T loads

Fatigue life

Fatigue life curves for Case 1 of round-stitched (code: RTS) and unstitched (code: RTN) specimens are presented in Fig. 6.10. The curve is established based on the relationship between σ_{max} and fatigue cycle (N), whereby N is plotted in logarithmic scale. It is noteworthy that, same with Chapter 4, a specimen is categorized as 'Run-out' when it is able to withstand fatigue cycle of $N = 10^6$ and beyond. It is found that fatigue life of RTN specimens is better than that of RTS specimens as indicated by the longer cycle-to-failure at similar σ_{max}. For instance, subjected to $\sigma_{max} = 270$ MPa, RTN specimen could survive 5×10^6 cycles, while RTS specimens fail earlier, which is around 1800 cycles. RTS specimen is able to reach 5×10^6 cycles when σ_{max} is reduced to 223 MPa (approximately 73% of σ_{OHT}).

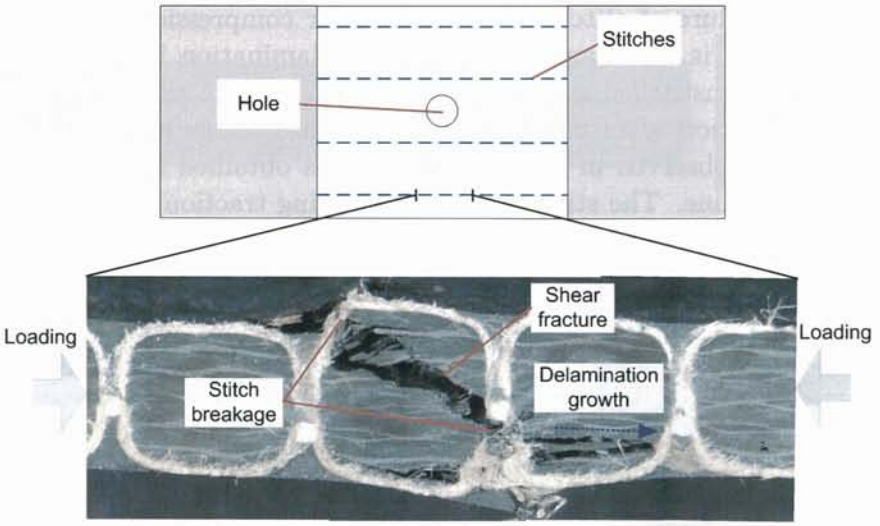

Figure 6.9: Cross-sectional view of stitch region in open hole specimen under compression

This finding suggests that round stitch reduces fatigue limit of carbon/epoxy composites. As will be shown later, round stitch aggravates the damage emanating from the hole rim, and accelerates the damage growth towards the specimen edges. Fig. 6.10 also shows that a large scatter at relatively high σ_{max} is found in S-N curve of round-stitched specimen (RTS), specifically between 40 and 300 cycles. For example, under $\sigma_{max} = 255$ MPa, one specimen prematurely fails at $N = 55$, while the other specimen under the same σ_{max} fails at around $N = 10^6$. This suggests that cycle-to-failure of round-stitched specimens is rather uncertain as compared to that of unstitched specimens, particularly at high σ_{max}. This uncertainty could be due to stitch debonding triggered by poor adhesion between Kevlar and resin.

It is also important to mention that the gradient of S-N curve (m_f) of unstitched specimen is -5.75±2.65, whilst that of round-stitched specimen is -10.4±2.3. There is an increase of slope of about 81%. This could be influenced by different fatigue damage mechanism between unstitched and round-stitched specimens.

Fatigue damage mechanisms

Fig. 6.11 shows ultrasonic C-scan images of RTN (unstitched) and RTS (round stitched) specimens under T-T fatigue. RTN and RTS specimens are subjected to $\sigma_{max} = 266$ MPa and 254 MPa, respectively, which are equivalent to 83% of average σ_{OHT} of the respective specimen types (σ_{OHT} of RTN is 320 MPa; σ_{OHT} of RTS is 304.7 MPa). After $N = 1.28 \times 10^6$, RTN and RTS specimens show slightly different fatigue damage characteristics. Damage in RTN specimen is characterized by axial splitting in 0 ° tows, delamination and transverse cracking in 90 ° tows that initiate from the hole rim. Damage in RTS specimen is similar with RTN specimen that it is also characterized by axial splitting and delamination. However, the damage zone created by transverse cracking in RTS specimen is considerably larger than that in RTN specimen, i.e. damage zone covers the specimen's ligaments. The other difference of damage characteristic between RTN and RTS specimens is that the length of axial splitting in RTS specimen is somewhat shorter than that in RTN specimen. The distinct characteristic

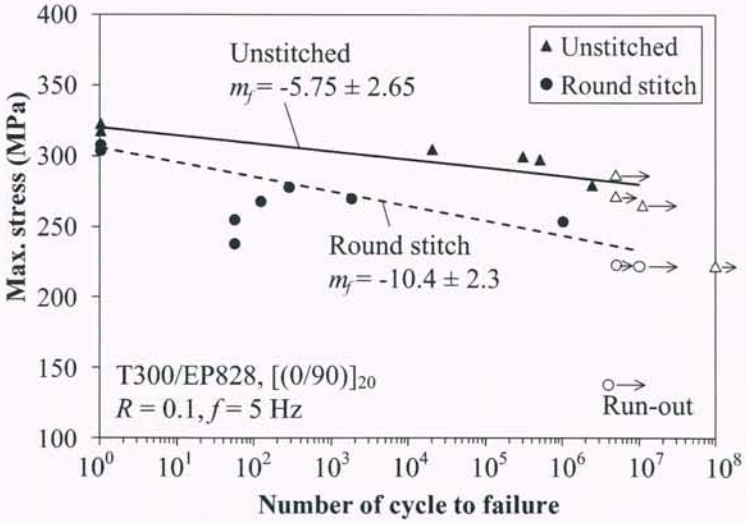

Figure 6.10: Fatigue life of open hole specimens: comparison between RTN (unstitched) and RTS (round stitched) under T-T fatigue

of damage in RTS specimens is greatly influenced by the stitches around the hole rim. In this regard, round stitching is considered too close to the hole rim that it creates local defects once the stitch debonding interacts with the damage emanating from the hole rim. This interaction of damage accelerates the growth of overall damage zone, and results in a premature failure of RTS specimen at high stress level. Fig. 6.11 also shows that when fatigue cycle is continued up to 9×10^6 cycles the only specimen able to withstand such a high number of cycles is RTN specimen. RTS specimen, on the other hand, fails soon after the fatigue cycle is continued. It is observed that RTN specimen experiences a very wide damage zone extending towards the specimen edges. Nevertheless, when the fatigue cycle is continued again, RTN specimen apparently does not fail at 10^7 cycles. Thereafter, the test is discontinued, and this particular specimen is considered 'Run-out'.

Damage area in all RTN and RTS specimens is then quantified. The damage is not decomposed into several types like the one described in Chapter 2 or Chapter 4. Instead, damage area that includes all axial splittings, transverse cracks and delamination is assumed. Damage area is a projected area that includes all damages in the tows and interfaces of the composite. Hence, measurement of damage area is not ply-by-ply basis. This quantification of damage area, which is plotted against number of cycle, aims at studying the general trend of fatigue damage growth.

Fig. 6.12 shows damage growth of RTN and RTS specimens between 4×10^4 and 5×10^6 cycles. RTN-3 and RTS-9 specimens are subjected to σ_{max} = 223 MPa. Despite the fact that the damage growth in both RTN-3 and RTS-9 is linear, and thus considered stable, the damage in RTS-9 specimen is slightly larger than that in RTN-3 specimen. For instance, at similar cycle of $N = 10^6$, damage area in RTS-9 specimen is approximately 75 mm^2, while that in RTN-3 specimen is approximately 59 mm^2. Larger damage size exhibited by RTS specimen seems to be partly influenced by the ratio between σ_{max} and σ_{OHT}. Although both specimens are subjected to the same σ_{max}, which is 223 MPa, but $\sigma_{max}/\sigma_{OHT}$ for RTN-3 is 69%, while that for RTS-9 is 73%. In addition, the larger damage area in RTS-9 specimen may

also be influenced by the application of stitching that encircles the hole. As already shown in Fig. 6.11, round stitch can cause rapid damage growth that may eventually increase the damage size.

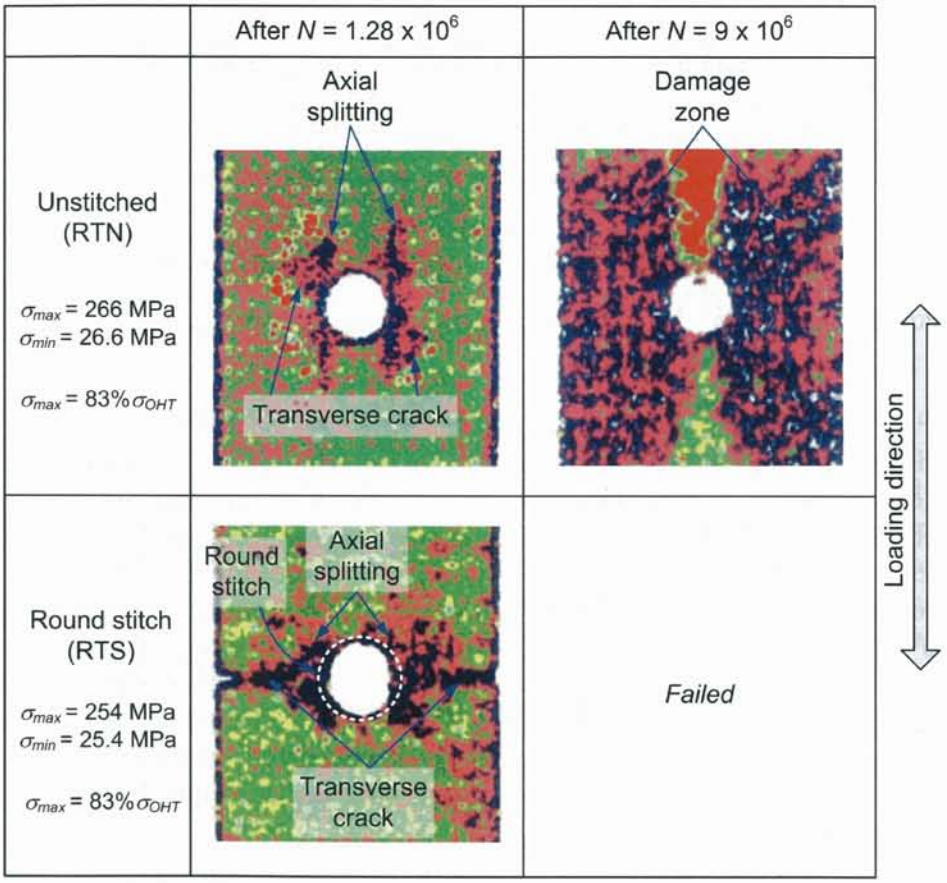

Figure 6.11: Ultrasonic C-scan results of RTN and RTS specimens under T-T fatigue

Fig. 6.13 shows the comparison between RTN and RTS specimens when σ_{max} is increased to 83% of their respective σ_{OHT}. RTN-9 specimen is subjected to σ_{max} = 266 MPa, while RTS-4 specimen is subjected to slightly lower stress, which is σ_{max} = 254 MPa. Damage growth exhibited by RTN-9 and RTS-4 is no longer linear and steady. Damage area in RTN-9 specimen grows rapidly from approximately 25 mm^2 at $N = 10^4$ to 105 mm^2 at $N = 2.5 \times 10^6$. Damage area in RTS-4 specimen also increases sharply from 50 mm^2 at $N = 8 \times 10^4$ to 105 mm^2 at $N = 6 \times 10^5$. However, damage growth rate between RTN-9 and RTS-4 is somewhat different. Below $N = 10^4$, damage size of both specimens is initially similar. As both specimens are cycled above $N = 10^5$, the damage size begins to divert, in which RTS-4 specimen demonstrates a more rapid damage growth than RTN-9. A rapid increase of damage in RTS-4 specimen is due to damage created by round stitching.

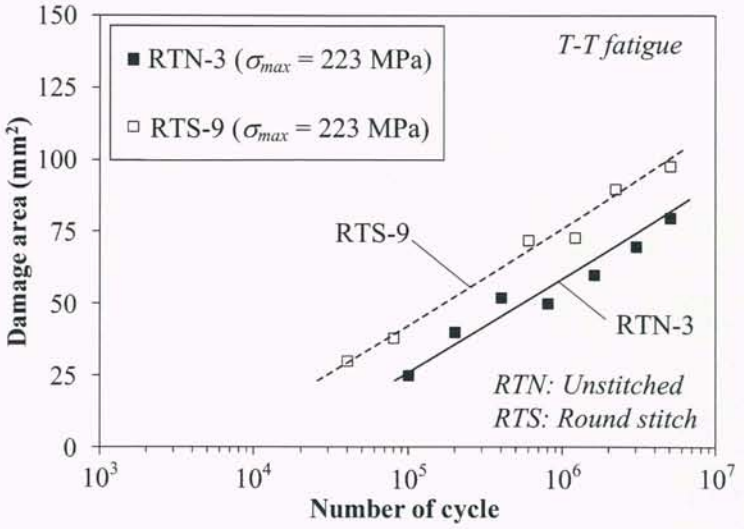

Figure 6.12: Damage growth in RTN and RTS specimens under σ_{max} = 223 MPa

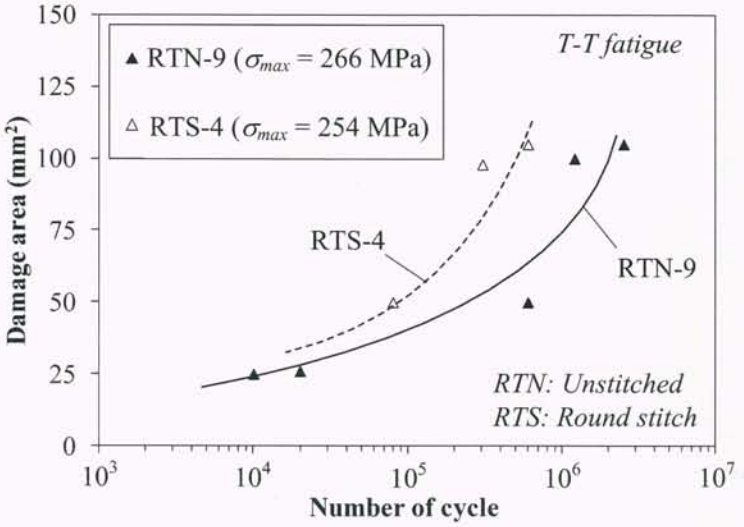

Figure 6.13: Damage growth in RTN and RTS specimens under σ_{max} = 83% of σ_{OHT} (RTN-9, σ_{max} = 266 MPa; RTS-4, σ_{max} = 254 MPa)

6.3.4 Fatigue of parallel stitched composites under T-T loads

Fatigue life

Fig. 6.14 shows the comparison of SN curves between PTN (unstitched) and PTS (parallel stitched) specimens. Both specimens show similar SN curves in terms of magnitude and gradient m_f. m_f of PTN is -5.2±1.9, while that of PTS is -5.35±0.75. It indicates that parallel stitch does not affect the fatigue life of plain weave carbon/epoxy composites. It should be noted that the distance between the stitch lines and the hole is around 4.65 mm, which is rather distant to cause some damage around the hole rim during stitching process.

However, as indicated by run-outs in Fig. 6.14, some of PTN specimens could actually survive $N = 10^7$ when they are subjected to σ_{max} between 255 and 275 MPa, while two PTS specimens fail earlier at similar stress level (one specimen fails at $N = 6 \times 10^6$, and the other specimen fails at $N = 9 \times 10^6$. This fact may imply that there are some differences between unstitched and parallel-stitched specimens in terms of damage behavior, specifically at high-cycle fatigue (above 10^6 cycles).

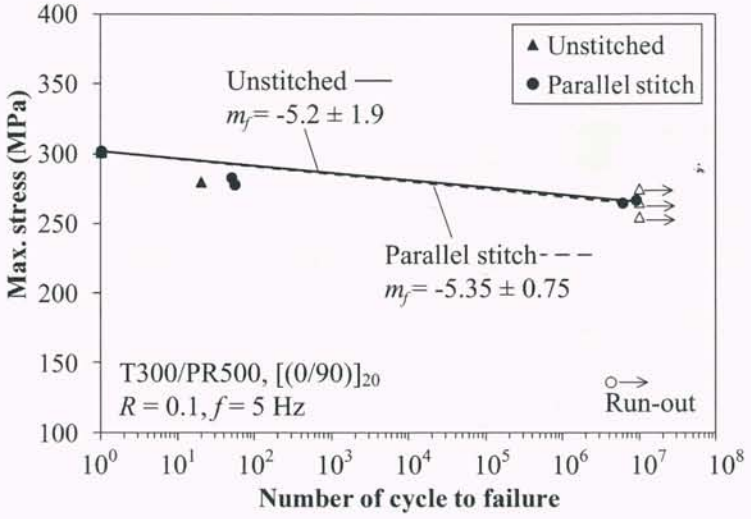

Figure 6.14: Fatigue life of open hole specimens: comparison between PTN (unstitched) and PTS (parallel stitched) under T-T fatigue

Fatigue damage mechanisms

Fig. 6.15 shows C-scan images of PTN and PTS specimens taken at 2×10^6 and 4×10^6 cycles. For PTN specimen, σ_{max} is 286 MPa, which corresponds to 95% of σ_{OHT}. For PTS specimen, σ_{max} is 292 MPa, which corresponds to 97% of σ_{OHT}. It is noteworthy that the location of stitch lines in PTS specimen is indicated by verctical, dashed lines in Figs. 6.15b and 6.15d.

It is depicted in Figs. 6.15a and 6.15b that after 2×10^6 cycles PTN and PTS specimens display similar damage pattern. Axial splitting, transverse cracks and delamination emanating from the hole rim are observed in PTN and PTS. The damages grow towards the edges of the specimen. However, a slight different of damage pattern is observed in PTS specimen (see Fig. 6.15b) as compared to PTN specimen. The other damage type occurs in PTS specimen, namely stitch debonding. Stitch debonding is induced by matrix crackings around stitch penetration holes, specifically in resin-rich regions. After PTN and PTS specimens reach 4×10^6 cycles, as shown in Figs. 6.15c and 6.15d, axial splitting grows longer, and interaction between delamination at the hole and edge delamination becomes pronounce.

As mentioned, stitch debonding occurs in PTS specimen, which is characterized by matrix cracking around stitch holes. Stitch debonding is caused by poor adhesion between Kevlar and resin. Fig. 6.16 shows the X-ray image of stitch debonding found around a number of

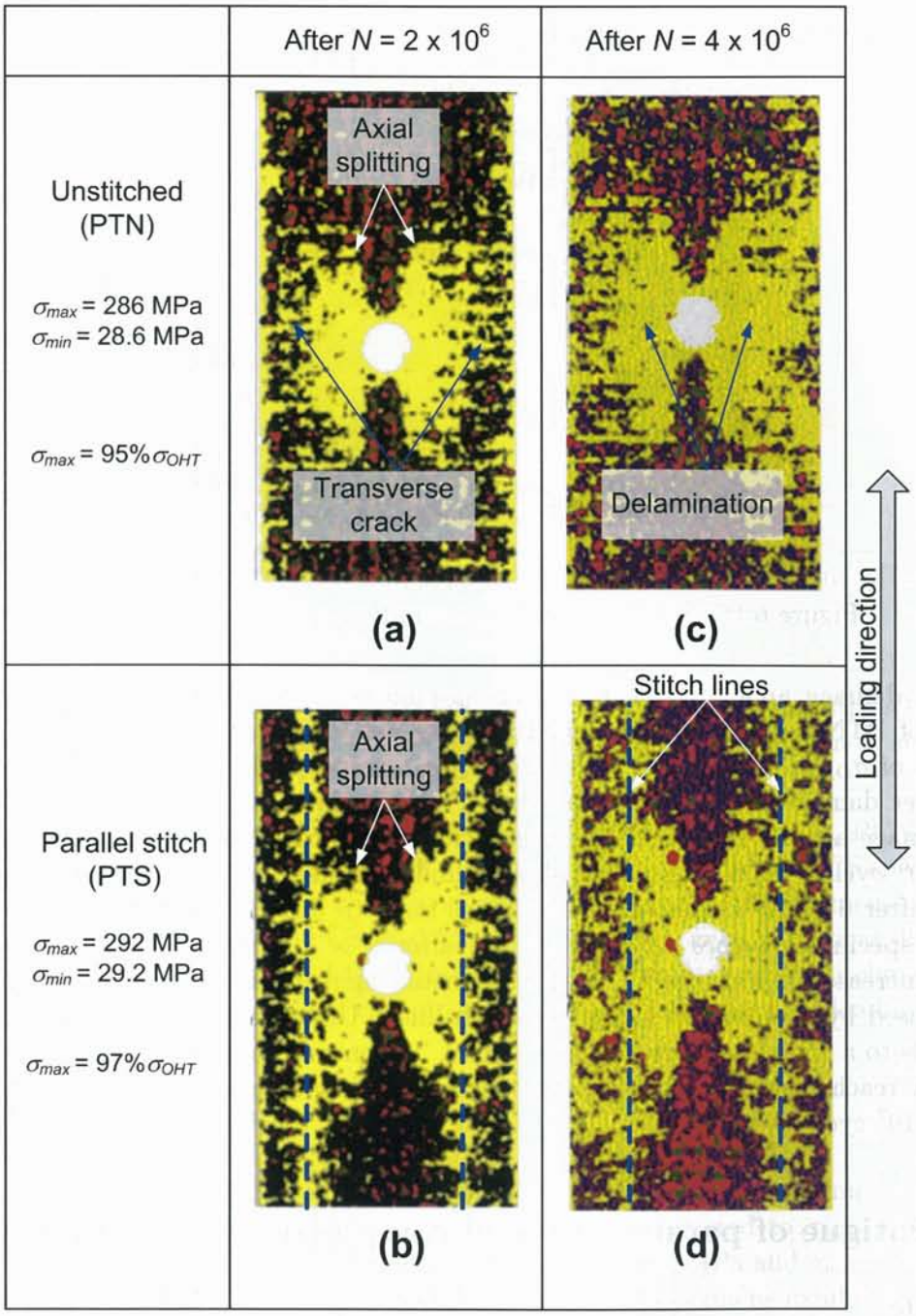

Figure 6.15: Ultrasonic C-scan results of PTN and PTS specimens under T-T fatigue (a) PTN, after $N = 2 \times 10^6$; (b) PTS, after $N = 2 \times 10^6$; (c) PTN, after $N = 4 \times 10^6$; (d) PTS, after $N = 4 \times 10^6$

stitch penetration holes. Stitch debondings would grow, and one stitch debonding would be interconnected with the adjacent stitch debonding. Coalescence of stitch debondings along the stitch lines is recognized as a continuous damage (indicated by the damage along dashed lines in Figs. 6.15b and 6.15d). Such continuous damage along the stitch lines contributes to

a larger damage zone measured in PTS specimen.

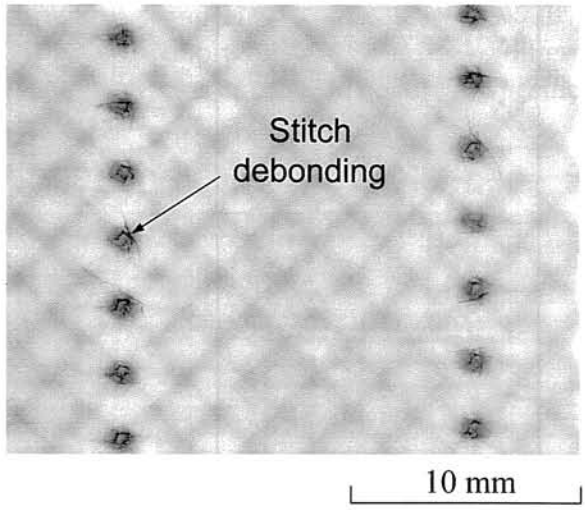

Figure 6.16: Stitch debonding around stitch penetration holes

Growth of damage area in PTN and PTS specimens is shown in Fig. 6.17. Unstitched specimen of PTN-6 and parallel-stitched specimen of PTS-6 are subjected to σ_{max} of 268 MPa (88% of σ_{OHT}) and 265 MPa (89% of σ_{OHT}), respectively. At 2×10^6 cycles, PTS-6 shows larger damage area of 650 mm^2 than PTN-6, which has damage area of 470 mm^2. Larger damage area in PTS-6 specimen is attributed to the damage along the stitch lines. At 4×10^6 cycles, PTS-6 specimen shows similar damage area as compared to PTN-6. However, after 6×10^6 cycles, both specimens start to display a different trend. Damage in PTN-6 specimen reaches saturation stage after 8×10^6 cycles, whilst that in PTS-6 specimen increases exponentially. This exponential increase indicates an unstable damage growth caused by the damage along the stitch lines. Unstable damage in PTS-6 specimen finally leads to a complete fracture at 10^7 cycles. In contrast, because the damage in PTN-6 has already reached saturation stage, the specimen is then able to withstand fatigue loading even after 10^7 cycles.

6.3.5 Fatigue of parallel stitched composites under C-C loads

Fatigue life

For Case 3, as listed in Table 6.3, the range of minimum stress for C-C fatigue test is selected between 55% and 70% of σ_{OHC}. The reason for selecting lower range of applied stress is that distinctive characteristics may be captured at lower stress level rather than at higher stress level. As already shown in Case 2, behavior of PTN and PTS specimens is similar at high applied stress (low-cycle fatigue) indicating that when the strength of two specimen types is similar, their behavior at low-cycle fatigue is also similar. In Case 3, σ_{OHC} of PCN specimen is 281.8 MPa, while that of PCS specimen is 282.2 MPa. Since σ_{OHC} of both specimens is similar, the distinctive characteristics at higher stress level may not be apparent. Particular attention is then to study the fatigue limit and damage behavior at high-cycle fatigue (lower

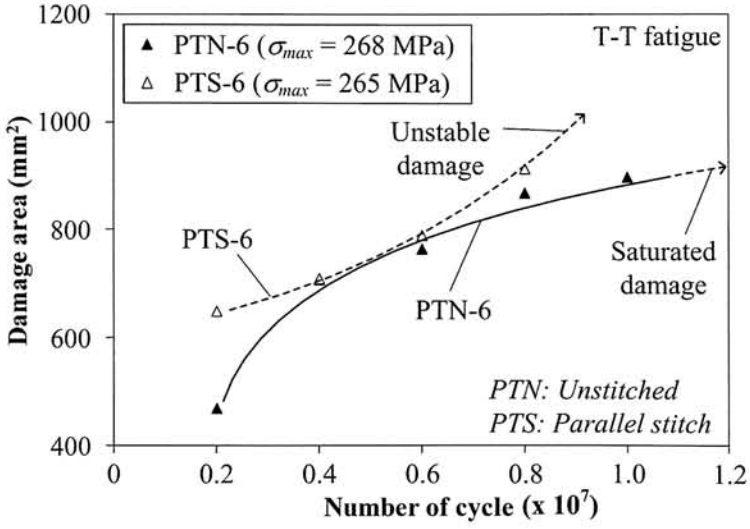

Figure 6.17: Damage growth in PTN and PTS specimens under σ_{max} = 268 MPa (PTN-6) and σ_{max} = 265 MPa (PTS-6)

applied stress). This is done by performing fatigue test at lower maximum stresses. Because high-cycle fatigue behavior is of interest, observation of damage development is also done at larger cyclic interval.

As shown in Fig. 6.18, subjected to σ_{min} between 55% and 70% of σ_{OHC}, PCN and PCS specimens fail between $N = 10^5$ and $N = 10^7$. C-C fatigue life of PCN and PCS specimens are similar although slight difference of S-N curve gradient between both specimens is observed (m_f of PCN is -18.5±2.1; m_f of PCS is -17.2±1.5). However, such statistical difference is negligible, and it may be suggested that, based on S-N curves, parallel stitching does not influence the open hole fatigue life of carbon/epoxy composites under C-C loading.

Fatigue damage mechanisms

To study fatigue damage mechanisms, ultrasonic C-scanning is also performed. The specimens are subjected to σ_{min} of 70% σ_{OHC} (PCN specimen subjected to σ_{max} = -19.7 MPa and σ_{min} = -197 MPa; PCS specimen subjected to σ_{max} = -19.3 MPa and σ_{min} = -193 MPa). As presented in Figs. 6.19a and 6.19b, both PCN and PCS specimens exhibit damage that is emanating transversely from the hole rim at 1.28 × 10^6 cycles. The extent of damage growing from the hole rims could reach approximately 5 mm. However, in conjunction with the growth of damage from the hole, PCS specimen also displays a continuous damage along its parallel stitch lines. When compression fatigue cycle is then continued up to 2.56 × 10^6 cycles, the damage length in PCN specimen is extended up to approximately 10 mm (see Fig. 6.19c). In contrast, the damage length in PCS specimen is somewhat impeded by the stitch lines (see Fig. 6.19d). When fatigue cycle is continued again, PCN specimen shortly fails at 2.97 × 10^6 cycles. On the other hand, PCS specimen is able to withstand compression fatigue up to around 5.3 × 10^6 cycles, which is almost double than that of PCN specimen. It suggests that parallel stitching may offer some advantages when specimen with hole is

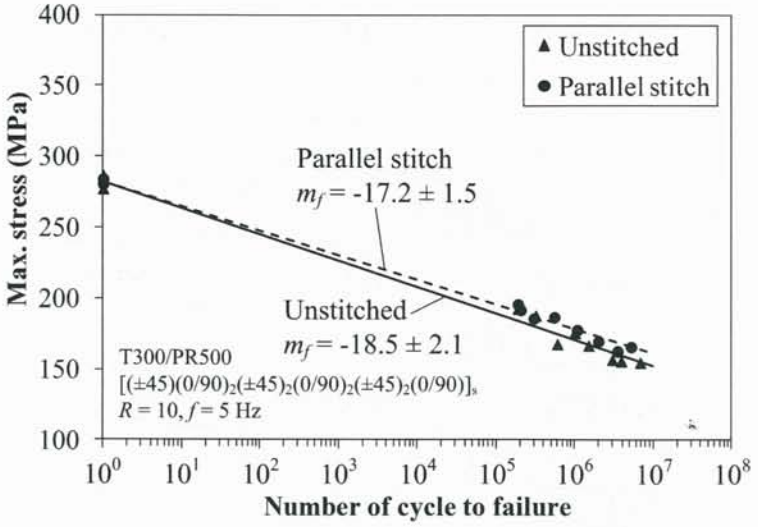

Figure 6.18: Fatigue life of open hole specimens: comparison between PCN (unstitched) and PCS (parallel stitched) under C-C fatigue

subjected to C-C loading. However, this may not be apparent from the S-N curves.

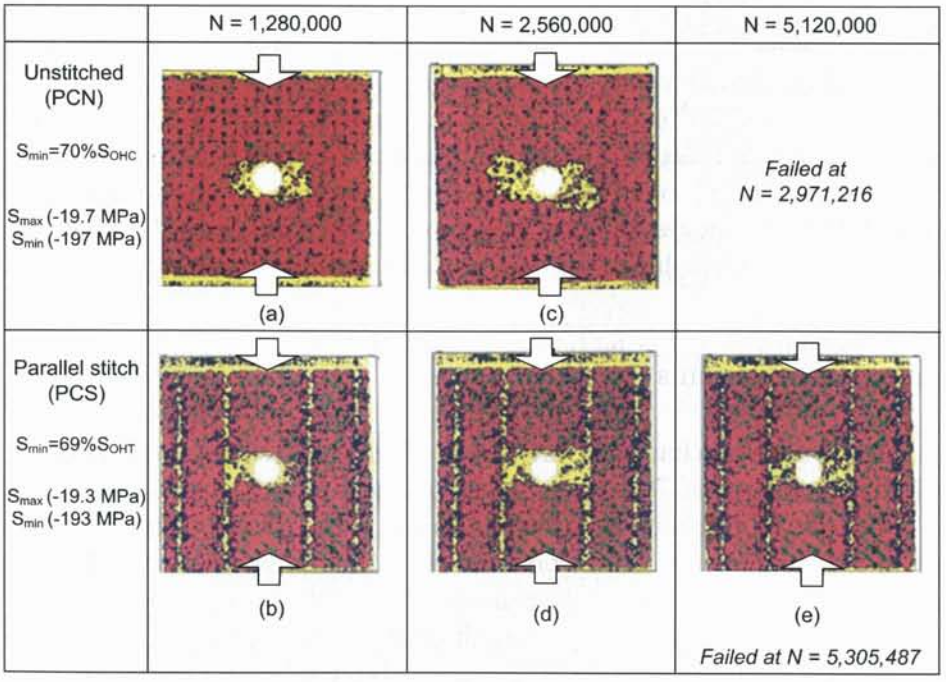

Figure 6.19: Ultrasonic C-scan results of PCN and PCS specimens under C-C fatigue (a) PCN, after $N = 1.28 \times 10^6$; (b) PCS, after $N = 1.28 \times 10^6$; (c) PCN, after $N = 2.56 \times 10^6$; (d) PCS, after $N = 2.56 \times 10^6$, (e) PCS, after $N = 5.12 \times 10^6$

Damage growth in PCN and PCS specimens is quantified for various σ_{min} (in the range of 55-70% of σ_{OHC}) and plotted against number of cycle. As shown in Fig. 6.20, both PCN and PCS specimens display gradual increase of damage area. However, damage growth rate

in PCS specimens is higher than that in PCN specimens. At similar number of cycle, this results in larger damage area in PCS specimens as compared to that in PCN specimen. As already shown in Fig. 6.19, damage growing from the hole rims of PCS specimens is somewhat impeded by the stitch lines, and it develops aggressively along the stitch lines. Meanwhile the damage at the hole rim progresses in a slower rate as compared to that along the stitch lines. Because the measured damage also includes the damage along four stitch lines, the overall damage size measured in PCS specimens is by no means larger than that in PCN specimens. For that reason, larger damage in open hole specimens under compression shown in C-scan images may not always correlate with the reduction of fatigue life. Instead, PCS specimens exhibiting larger damage area show similar performance with PCN specimens.

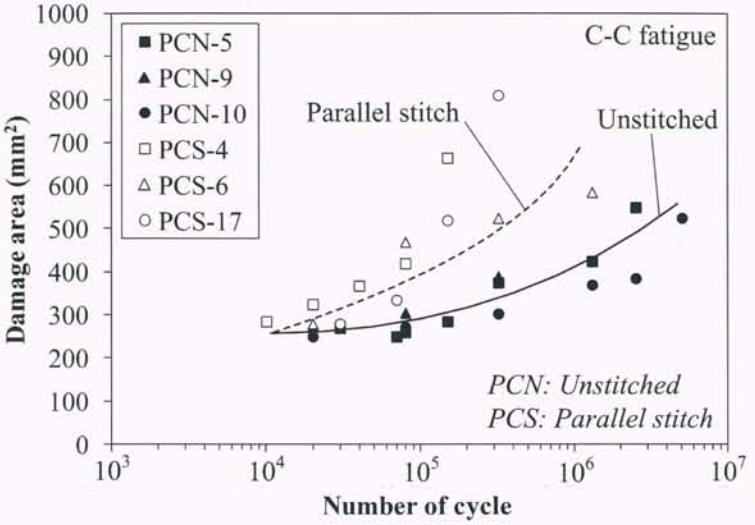

Figure 6.20: Damage growth in PCN and PCS specimens under various σ_{min}

6.4 Concluding Remarks

Experimental investigation of open hole fatigue characteristics of plain weave carbon/epoxy composites has been performed. Fatigue life and damage growth of stitched and unstitched composites under T-T and C-C fatigue are investigated. Several conclusions can be drawn from the investigation:

- Round stitch is found to reduce fatigue limit of carbon/epoxy composites under tensiontension fatigue loading. Round stitch accelerates damage growth emanating from the hole rim, and directs the damage towards the edge of specimen. This damage is relatively unstable when the specimen is subjected to σ_{max} above 83% of σ_{OHT}.
- Under T-T fatigue, parallel stitch generally does not affect SN curve of carbon/epoxy composites. However, stitching apparently makes the growth of damage unstable after 8 $\times 10^6$ cycles. As a result, stitched specimens are completely fractured before 10^7 cycles, while unstitched specimens are able to withstand cyclic loading up to 10^7 cycles.

- Similar to T-T fatigue, parallel stitched composites under C-C fatigue show similar fatigue life as compared to unstitched composites. But, parallel stitch may impart some advantages in impeding damage growth emanating from the hole rim at high cycle. As a result, parallel stitched specimen could withstand C-C fatigue beyond 5.3 $\times$ 10^6 cycles, while unstitched specimen fails earlier, which is at 2.97 $\times$ 10^6 cycles.
- Should geometrical changes (holes) be required in stitched composites for particular application, it is advisable to provide sufficient clearance in order to avoid initial defects around the holes. Round stitching is not recommended in this regard.

Chapter 7

Conclusions and recommendations

7.1 Conclusions

Effect of stitch parameters on the in-plane mechanical properties and damage mechanisms of stitched carbon/epoxy composites subjected to static and fatigue loads has been investigated experimentally and analytically. Stitch parameters are stitch density, stitch thread thickness, stitch pattern and stitch orientation. Stitch materials under investigation are Kevlar-29 and Vectran. Detailed damage mechanisms in carbon/epoxy are also revealed, and effect of stitch parameters on the mechanisms is clarified. Architectural changes induced by stitching are fully characterized, and their effect on properties and failure is clarified.

Experimental investigation of Vectran-stitched carbon/epoxy composites shows that stitch density (SD) of 0.111/mm^2 (densely stitched composite, or stitched 3×3) is able to modestly increase tensile strength and failure strain of carbon/epoxy of around 10%. The reason is that stitched 3×3 is effective in impeding the delamination growth emanating from the edges during static test. Tensile modulus of carbon/epoxy is slightly reduced with Vectran stitches, and this is strongly correlated with fiber waviness (combined out-of-plane and in-plane waviness) induced by stitch threads and manufacturing method. In contrast, compression modulus is not sensitive to the stitch density and stitch thread thickness; some increase of stiffness is noted during compression of stitched composites, but this is mainly due to fiber volume fraction and geometrical factor, not the stitch parameters. However, stitching generally reduces compressive strength of carbon/epoxy composites regardless stitch density or stitch thread thickness. The reduction of compressive strength of up to around 14% (with the largest reduction exhibited by stitched 6×6 200 denier) is strongly correlated with fiber waviness due to stitching, and early cracking in resin-rich region. This early cracking induces fiber splitting and fiber kinking at relatively lower load. In accordance with the finding during static tension test, stitched 3×3 is also effective in improving fatigue life of carbon/epoxy due to effective impediment of delamination. Stitched 3×3 experiences higher stiffness degradation under fatigue. The stiffness degradation is triggered by a vast amount of off-axis cracks that induce the initiation of delamination. Despite its effectiveness in delaying the growth of delamination, however, stitching causes higher amount of transverse and oblique cracks. This behavior is attributed to fiber compaction mechanism occurred in off-axis tows, which results in an increased of local fiber volume fraction. Subjected to transverse loading, fiber

tows with higher local fiber volume fraction experience high stress concentration between fibers, and easy to have fiber/matrix debonding. Quantification of compaction mechanism by burn-off test and optical microscopy successfully reveals that stitching indeed causes some increase of local fiber volume fraction.

Experimental investigation of Kevlar-stitched carbon/epoxy composites with and without holes reveals that Kevlar-stitched composites without holes is sensitive to the stitch orientation, in which transverse stitching causes significant tensile strength reduction as compared to longitudinal stitching. The reduction can reach 24%. Lower strength exhibited by transverse stitched composites is attributed to the interfacial debonding between Kevlar stitches and epoxy and the subsequent interaction amongst debondings. Interfacial debonding is mainly due to the poor adhesion between Kevlar stitch and surrounding matrix. It is also partly caused by fiber waviness of load-bearing tows (0° tows). Kevlar-stitched composites with holes, in contrast, is more or less independent of the stitch orientation. The failure of stitched composites with holes depends strongly on stress concentration generated at the hole regardless stress orientation. Kevlar-stitched composites with holes is also sensitive to stitch pattern, in which round stitching (stitches encircling the holes) significantly degrades the fatigue life. The reason is because round stitching accelerates damage growth emanating from the hole rim, and directs the damage towards the edge of specimen. The damage is also initiated by poor adhesion between Kevlar and resin, which appears as stitch debonding. The damage around the holes eventually causes an unstable damage growth and early failure, especially when the specimen with round stitch is subjected to relatively high maximum stress. Fatigue life of Kevlar-stitched composites with holes is not sensitive to the parallel stitching since this stitch pattern does not significantly change the fatigue damage behavior.

The first analytical studies show that homogenization method with asymptotic expansion series is reasonably accurate and efficient in predicting 3-D thermo-elastic constants of stitched composites. Good agreement was found when tensile modulus of homogenization method was compared with the experimental result. Further adjustment with refined models, i.e. by including fiber waviness, will be made in the near future. The second analytical studies on the validation of Average Stress Criterion (ASC), a formula based on Lekhnitskii theory, shows that ASC is applicable to estimate open hole tension strength of stitched composites with different stitch orientation.

Based on the above findings, it can therefore be stated herein that stitching is effective in maintaining or improving in-plane mechanical properties of carbon/epoxy composites under static and fatigue loads if following conditions are met:

- Stitching must be able to impede delamination
- Stitching should minimize waviness in both in-plane and out-of-plane directions
- Stitching should not cause stitch debonding; this can be done by surface treatment of stitch thread
- Fiber compaction due to stitching is minimized (or optimized)
- Resin-rich region should be minimized; this can be done by employing thinner yet stronger thread, e.g. Vectran

- Voids should be minimized; VaRTM process can be opted
- Thinner 90 ° tows should be used to improve transverse crack onset
- Hole made in stitched composites should not interact with stitch threads
- Direction of stitching is in-line with loading direction (this is applicable for lock-stitch configuration)

At present, in order to enhance both in-plane and out-of-plane mechanical properties, stitched 3×3 using Vectran is a feasible choice for carbon/epoxy composites. However, as already mentioned, future design of stitched composites must (i) ensure the straightness of fiber tows by optimizing the binding forces during stitching process (manufacture-related issues), (ii) optimize the thickness of off-axis plies (particularly 90 ° tows) so as to increase crack onset, (iii) use lower denier of stitch thread as strong and stiff as Vectran to minimize resin-rich region, (iv) use resin infiltration method that significantly reduces void content. In terms of the structural design using stitched composites, it is not advisable to create holes in stitched composites. Should lock-stitch is opted as stitch type, the direction of loading should be in-line with the stitch orientation.

Finally, understanding of basic mechanical characteristics of stitched carbon/epoxy composites endorses that stitching using Vectran is a viable reinforcement technique for composite materials employed in the next generation aircraft.

7.2 Recommendations

Future works potentially performed by present author as well as the recommendations for other researchers are given here:

- Waviness or undulation of fiber tows in finite element model (mesomechanics model) using homogenization method can be investigated (currently, it is the work in progress)
- Effect of stitch thread thickness on tensile and T-T fatigue properties as well as damage mechanism can be studied (work in progress)
- Investigation of C-C performance of Vectran-stitched composites, especially when it is combined with environmental effects (hot/wet, hot/dry), can be investigated.
- Robust numerical model to predict the damage progression and failure of stitched composites under tension, compression and fatigue is still not available. It is therefore important to pursue the research in this direction by employing the homogenization method that already predicts the thermo-elastic constants with high accuracy.
- Fire properties of stitched composites have not been found in open literatures. In fact, fire properties may have practical importance in the design of aircraft structures. It is therefore advisable to investigate the fire characteristics and residual strength of stitched composites after fire.

Bibliography

[1] D.O. Adams and S.J. Bell. Compression strength reduction in composite laminates due to multiple-layer waviness. *Compos Sci Technol*, 53(2):207–212, 1995.

[2] S. Adanur and S.R. Gongalareddy. Compressive properties of stitched woven fiberglass fabric reinforced composite sections for civil engineering applications. In *Proceeding of 3rd Int Conf Compos Engng (ICCE-3)*, 1996. New Orleans, USA, 21-26 July.

[3] S. Adden and P. Horst. Stiffness degradation under fatigue in multiaxially loaded non-crimp-fabrics. *Int J Fatigue*, 32:108–122, 2010.

[4] Anon. Denatite XNR6813/XNH6813, Technical Information Sheet.

[5] Anon. Kevlar, Aramid Fiber, Technical Guide.

[6] Anon. T300, Data Sheet, No. CFA-001.

[7] Anon. T800S, Data Sheet, No. CFA-019.

[8] Anon. Vectran Technical Data Sheet.

[9] Anon. *Testing Methods for Fibre Content and Void Content of Carbon Fiber Reinforced Plastics, JIS K 7075.* Japan Standard Association, 1991. (in Japanese).

[10] Anon. *SACMA Recommended Test Method for Compressive Properties of Oriented Fiber-Resin Composites, SRM 1R-94.* Suppliers of Advanced Composite Materials Association (SACMA) , 1994.

[11] Anon. *SACMA Recommended Test Method for Open-Hole Compression Properties of Oriented Fiber-Resin Composites, SRM 3R-94.* Suppliers of Advanced Composite Materials Association (SACMA) , 1994.

[12] Anon. *SACMA Recommended Test Method for Tensile Properties of Oriented Fiber-Resin Composites, SRM 4R-94.* Suppliers of Advanced Composite Materials Association (SACMA) , 1994.

[13] Anon. The advanced stitching machine: making composite wing structures of the future. Technical Report FS-1997-08-31-LaRC, NASA, 1997.

[14] Anon. *Standard Test Method for Open Hole Tensile Strength of Polymer Matrix Composite Composites, ASTM D 5766/D 5766M.* American Society for Testing and Materials, 2003.

[15] Anon. Loctite 3631TM, Technical Data Sheet, 2006.

[16] Anon. Status of FAA's actions to oversee the safety of composite airplanes. Technical report, US Government Accountability Office, 2011.

[17] Y. Aono, K. Hirota, S.H. Lee, T. Kuroiwa, and K. Takita. Fatigue damage of GFRP laminates consisting of stitched unit layers. *Int J Fatigue*, 30:1720–1728, 2008.

[18] Y. Aono, H. Noguchi, S.H. Lee, T. Kuroiwa, and K. Takita. Fatigue strength of double-bias mat composites composed of stitched unit layers. *Int J Fatigue*, 28:1375–1381, 2006.

[19] F. Aymerich, R. Onnis, and P. Priolo. Analysis of the fracture behaviour of a stitched single-lap joint. *Compos Part A*, 36(5):603–614, 2005.

[20] F. Aymerich and P. Priolo. Characterization of fracture modes in stitched and unstitched cross-ply laminates subjected to low-velocity impact and compression after impact loading. *Int J Impact Engng*, 35(7):591–608, 2008.

[21] F. Aymerich, P. Priolo, and C.T. Sun. Static and fatigue behaviour of stitched graphite/epoxy composite laminates. *Compos Sci Technol*, 63(6):907–917, 2003.

[22] A. Baker, S. Dutton, and D. Kelly. *Composite materials for aircraft structures*. AIAA, second edition, 2004.

[23] S. Behzadi, P.T. Curtis, and F.R. Jones. Improving the prediction of tensile failure in unidirectional fibre composites by introducing matrix shear yielding. *Compos Sci Technol*, 69(14):2421–2427, 2009.

[24] U. Beier, F. Wolff-Fabris, F. Fischer, J.K.W. Sandler, V. Alstädt, G. Hülder, E. Schmachtenberg, H Spanner, C. Weimer, T. Roser, and W. Buchs. Mechanical performance of carbon fibre-reinforced composite based on preforms stitched with innovative low-melting temperature and matrix soluble thermoplastic yarns. *Compos Part A*, 39(9):1572–1581, 2008.

[25] B. Béral. Airbus composite innovation: current and future perspectives. In *Proceeding of 8th Asia-Australasia Conf on Compos Mater (ACCM-8)*, 2012. Kuala Lumpur, Malaysia, 6-8 November.

[26] S. Black. An elegant solution for a big composite part. *High Performance Composites*, May, 2003.

[27] B. Budiansky and N.A. Fleck. Compressive kinking of fiber composites: A topical review. *Appl Mech Rev*, 47 (Part 2)(6):S426–S250, 1994.

[28] R.J. Cano and M.B. Dow. Properties of five toughened matrix composite materials. Technical Report 3254, NASA, 1992.

[29] V. Carvelli, V.N. Tomaselli, S.V. Lomov, I. Verpoest, V. Witzel, and B. Van den Broucke. Fatigue and post-fatigue tensile behaviour of non-crimp stitched and unstitched carbon/epoxy composites. *Compos Sci Technol*, 70(15):2216–2224, 2010.

[30] G. Chen, X. Cheng, Z. Li, and C. Kou. The effect of environment on tensile properties of stitched and unstitched laminates (with a hole). *J Reinf Plast Compos*, 24(17):1883–1889, 2005.

[31] M.T. Cholakara, B.Z. Jang, and C.Z. Wang. Deformation and failure mechanisms in 3d composites. In *Proceeding of 34th Int SAMPE Sympos*, 1989. Nevada, USA, 8-11 May.

[32] T.-W. Chou. *Microstructural design of fiber composites.* Cambridge University Press, 1992.

[33] H.J. Chun, H.W. Kim, and J.H. Byun. Effects of through-the-thickness stitches on the elastic behavior of multi-axial warp knit fabric composites. *Compos Struct*, 74(4):484–494, 2006.

[34] B.N. Cox and G. Flanagan. Handbook of analytical methods for textile composites. Technical Report 4750, NASA, 1997.

[35] L.C. Dickinson. A designed experiment in stitched/RTM composites. Technical Report N95-92046, NASA, 1995.

[36] L.C. Dickinson, G.L. Farley, and M.K. Hinders. Prediction of effective three-dimensional elastic constants of translaminar reinforced composites. *J Compos Mater*, 33(11):1002–1029, 1999.

[37] M.B. Dow and D.L. Smith. Damage-tolerant composite materials produced by stitching carbon fabrics. In *Proceeding of 21st Int SAMPE Technical Conf*, 1989. New Jersey, USA, 25-28 September.

[38] K.A. Dransfield, L.K. Jain, and Y.-W. Mai. On the effects of stitching in CFRPs - I. Mode I delamination toughness. *Compos Sci Technol*, 58(6):815–827, 1998.

[39] X. Du, F. Xue, and Z. Gu. Experimental study of the effect of stitching on strength of a composite laminate. In *Proceeding of Int Sympos on Compos Mater and Struc*, 1986. Beijing, PR China, 10 13 June 1986.

[40] F. Edgren, L.E. Asp, and R. Joffe. Failure of NCF composites subjected to combined compression and shear loading. *Compos Sci Technol*, 66(15):2865–2877, 2006.

[41] F. Edgren, D. Mattsson, L.E. Asp, and J. Varna. Formation of damage and its effects on non-crimp fabric reinforced composites loaded in tension. *Compos Sci Technol*, 64(5):675–692, 2004.

[42] G.L. Farley. A mechanism responsible for reducing compression strength of through-the-thickness reinforced composite materials. *J Compos Mater*, 26(12):1784–1795, 1992.

[43] N.A. Fleck. Compressive failure of fiber composites. *Adv Appl Mech*, 33:43–119, 1997.

[44] A. Gagel, B. Fiedler, and K. Schulte. On modelling the mechanical degradation of fatigue loaded glass-fibre non-crimp fabric reinforced epoxy laminates. *Compos Sci Technol*, 66(5):657–664, 2006.

[45] R.F. Gibson. *Principles of composite material mechanics.* McGraw-Hill, 1994.

[46] A. Gonzáles, E. Graciani, and F. París. Prediction of in-plane stiffness properties of non-crimp fabric laminates by means of 3D finite element analysis. *Compos Sci Technol*, 68(1):121–131, 2008.

[47] M. Grassi, X. Zhang, and M. Meo. Prediction of stiffness and stresses in z-fibre reinforced composite laminates. *Compos Part A*, 33(12):1653–1664, 2002.

[48] J.M. Guedes and N. Kikuchi. A homogenization method for pre and post processings of finite element analysis. *Computer Meth Appl Mech Engng*, 83:143–198, 1990.

[49] A.J. Gunnion, M.L. Scott, R.S. Thomson, and D. Hachenberg. Thickness effect on the compressive stiffness and strength of stitched composite laminates. *Compos Struct*, 66(1-4):479–486, 2004.

[50] X.P. Han, L.X. Li, X.P. Zhu, and Z.F. Yue. Experimental study on the stitching reinforcement of composite laminates with a circular hole. *Compos Sci Technol*, 68(7-8):1649–1653, 2008.

[51] B. Harris, editor. *Fatigue in composites.* Woodhead Publishing, 2003.

[52] H. Harris, N. Schinske, R. Krueger, and B. Swanson. Multiaxial stitched preform reinforcement for RTM fabrication. In *Proceeding of 36th Int SAMPE Sympos*, 1991. California, USA, 15-18 April.

[53] J.W.S. Hearle, editor. *High-performance fibres*, chapter Other high modulus-high tenacity (HM-HT) fibres from linear polymers. Woodhead Publishing, 2001.

[54] I. Herszberg and M.K. Bannister. Compression and compression-after-impact properties of thin stitched carbon/epoxy composites. In *Proceeding of 5th Australia Aeronautical Conf*, 1993. Melbourne, Australia, September 13-15.

[55] I. Herszberg, A. Loh, M.K. Bannister, and H.G.S.J. Thuis. Open hole fatigue of stitched and unstitched carbon/epoxy laminates. In *Proceeding of 11th Int Conf Compos Mater (ICCM-11)*, 1997.

[56] H. Hesz and N. Himmel. Structurally stitched NCF CFRP laminates. Part 1: Experimental characterization of in-plane and out-of-plane properties. *Compos Sci Technol*, 71(5):549–568, 2011.

[57] H. Hesz, Y.C. Roth, and N. Himmel. Elastic constants estimation of stitched NCF CFRP laminates based on a finite element unit-cell model. *Compos Sci Technol*, 67(6):1081–1095, 2007.

[58] T. Hobbiebrunken, M. Hojo, K.K. Jin, and S.K. Ha. Influence of non-uniform fiber arrangement on microscopic stress and failure initiation in thermally and transversely loaded CF/epoxy laminated composites. *Compos Sci Technol*, 68(15-16):3107–3113, 2008.

[59] J.M. Hodgkinson, editor. *Mechanical testing of advanced fibre composites*, chapter Tension. Woodhead Publishing, 2000.

[60] A. Hosoi, N. Sato, Y. Kusumoto, K. Fujiwara, and H. Kawada. High-cycle fatigue characteristics of quasi-isotropic CFRP laminates over 10^8 cycles (Initiation and propagation of delamination considering interaction with transverse cracks). *IJ Fatigue*, 32:29–36, 2010.

[61] M.V. Hosur, M.R. Karim, and S. Jeelani. Experimental investigations on the response of stitched/unstitched woven S2-glass/SC15 epoxy composites under single and repeated low velocity impact loading. *Compos Struct*, 61(1-2):89–102, 2003.

[62] A.B. Hulcher, S.N. Tiwari, and J.M. Marcello. Fabrication of thermoplastic composite laminates having film interleaves by automated fiber placement. Technical Report NCC1-227, NASA, 2001.

[63] T. Ishikawa. Status and summary of test method standardization of advanced composites in japan. In *Proceeding of 24th Int Council Aeronautical Sci (ICAS-24)*, 2004. Yokohama, Japan, Aug 29 - Sep 3.

[64] L.K. Jain, K.A. Dransfield, and Y.-W. Mai. On the effects of stitching in CFRPs - II. Mode II delamination toughness. *Compos Sci Technol*, 58(6):829–837, 1998.

[65] L.K. Jain and Y.-W. Mai. On the effect of stitching on mode I delamination toughness of laminated composites. *Compos Sci Technol*, 51(3):331–345, 1994.

[66] D.C. Jegley. Experimental behavior of fatigued single stiffener PRSEUS specimens. Technical Report TM-2009-215955, NASA, 2009.

[67] R. Kamiya and T.-W. Chou. Strength and failure behavior of stitched carbon/epoxy composites. *Metal and Mater Trans A*, 31A:899–909, 2000.

[68] M. Kawai and T. Taniguchi. Off-axis fatigue behavior of plain weave carbon/epoxy fabric composites at room and high temperatures and its mechanical modeling. *Compos Part A*, 37(2):243–256, 2006.

[69] V. Koissin, J. Kustermans, S.V. Lomov, I. Verpoest, B. Van Den Broucke, and V. Witzel. Structurally stitched NCF preforms: quasi-static response. *Compos Sci Technol*, 69(15-16):2701–2710, 2009.

[70] R. Krueger. Modeling of unit-cells with Z-pins using FLASH: pre-processing and post-processing. Technical Report CR-2005-213905, NASA, 2005.

[71] D. Kugler and T.J. Moon. Indentification of the most significant processing parameters on the development of fiber waviness in thin laminates. *J Compos Mater*, 36:1451–1479, 2002.

[72] F. Larsson. Damage tolerance of a stitched carbon/epoxy laminate. *Compos Part A*, 28A(11):923–934, 1997.

[73] C.L. Lee, J.C. Ho, and K.H. Wei. Resin transfer molding (RTM) process of a high performance epoxy resin. I: Kinetic studies of cure reaction. *Polym Engng Sci*, 40(4):929–934, 2000.

[74] S.G. Lekhnitskii. *Anisotropic plates*. Gordon and Breach Science Publishers, 1968.

[75] S.V. Lomov, D.S. Ivanov, T.C. Truong, I. Verpoest, F. Baudry, K. Van den Bosche, and H. Xie. Experimental methodology of study of damage initiation and development in textile composites in uniaxial tensile test. *Compos Sci Technol*, 68(12):2340–2349, 2008.

[76] Y. Mahadik and S.R. Hallett. Effect of fabric compaction and yarn waviness on 3D woven composite compressive properties. *Compos Part A*, 42(11):1592–1600, 2011.

[77] P. Mattheij, K. Gliesche, and D. Feltin. 3D reinforced stitched carbon/epoxy composites made by tailored fibre placement. *Compos Part A*, 31(6):571–581, 2000.

[78] V.R. Mehta and S. Kumar. Temperature dependent torsional properties of high performance fibres and their relevance to compressive strength. *J Mater Sci*, 29(14):3658–3664, 1997.

[79] A. Miravete, editor. *3-D textile reinforcements in composite materials*, chapter Why are 3-D textile technologies applied to composite materials. Woodhead Publishing, 1999.

[80] A.P. Mouritz. Ballistic impact and explosive blast resistance of stitched composites. *Compos Part B*, 32(5):431–439, 2001.

[81] A.P. Mouritz. Tensile fatigue properties of 3D composites with through-thickness reinforcement. *Compos Sci Technol*, 68(12):2503–2510, 2008.

[82] A.P. Mouritz and B.N. Cox. A mechanistic approach to the properties of stitched laminates. *Compos Part A*, 31(1):1–27, 2000.

[83] A.P. Mouritz and B.N. Cox. A mechanistic interpretation of the comparative in-plane mechanical properties of 3D woven, stitched and pinned composites. *Compos Part A*, 41(6):709–728, 2010.

[84] A.P. Mouritz, K.H. Leong, and I. Herszberg. A review of the effect of stitching on the in-plane mechanical properties of fibre-reinforced polymer composites. *Compos Part A*, 28A(12):979–991, 1997.

[85] J. Nie, Y. Xu, L. Zhang, X. Yin, L. Cheng, and J. Ma. Effect of stitch spacing on mechanical properties of carbon/silicon carbide composites. *Compos Sci Technol*, 68(12):2425–2432, 2009.

[86] M.C.Y. Niu. *Composite airframe structures: Practical design information and data*. Conlimit Press, 1992.

[87] T. Ogasawara and T. Ishikawa. Evaluation of standard compressive strengths of graphite/epoxy composite laminates Part II. In *Proceedings of 46th JSASS/JSME Struc Conf*, 2004. Hachinohe, Japan (in Japanese).

[88] T. Ogasawara and T. Ishikawa. Evaluation of standard compressive test methods for carbon fiber composites and proposal of a simple test method (NAL-II). Technical Report JAXA-RM-08-010, JAXA, 2009. (in Japanese).

[89] S.D. Pandita, K. Nishiyabu, and I. Verpoest. Strain concentrations in woven fabric composites with holes. *Compos Struct*, 59(3):361–368, 2003.

[90] F. Pang, C.H. Wang, and R.G. Bathgate. Creep response of woven-fibre composites and the effect of stitching. *Compos Sci Technol*, 57(1):91–98, 1997.

[91] J. Parthenios, D.G. Katerelos, G.C. Psarras, and C. Galiotis. Aramid fibers; a multi-functional sensor for monitoring stress/strain fields and damage development in composite materials. *Engng Fract Mech*, 69(9):1067–1087, 2002.

[92] A. Pegoretti, A. Zanolli, and C. Migliaresi. Preparation and tensile mechanical properties of unidirectional liquid crystalline single-polymer composites. *Compos Sci Technol*, 66(13):1970–1979, 2006.

[93] M.A. Portanova, Jr. C.C. Poe, and J.D. Whitcomb. Open hole and post-impact compression fatigue of stitched and unstitched carbon/epoxy composites. Technical Report TM-102676, NASA, 1990.

[94] J.N. Reddy and A.V. Khrisna Murty, editors. *Composite Structures: Testing, Analysis and Design*, chapter On delamination failures in composite laminates. Narosa Publishing House, 1992.

[95] J.R. Reeder. Comparison of the compressive strengths for stitched and toughened composite systems. Technical Report TM-109108, NASA, 1994.

[96] A. Riccio, M. Zarelli, and N. Tessitore. A numerical model for delamination growth simulation in non-crimp fabric composites. *Compos Sci Technol*, 67(15-16):3345–3359, 2007.

[97] H. Seibert. Applications for PMI foams in aerospace sandwich structures. *Reinforced Plastics*, 2006.

[98] M.Z. Shah Khan and A.P. Mouritz. Fatigue behaviour of stitched GRP laminates. *Compos Sci Technol*, 56(6):695–701, 1996.

[99] S. Sridharan, editor. *Delamination behaviour of composites*, chapter Delamination in the context of composite structural design. Woodhead Publishing, 2008.

[100] C.A. Steeves and N.A. Fleck. In-plane properties of composite laminates with through-thickness pin reinforcement. *IJ Sol Struct*, 43(10):3197–3212, 2006.

[101] H. Suemasu, H. Takahashi, and T. Ishikawa. On failure mechanisms of composite laminates with an open hole subjected to compressive load. *Compos Sci Technol*, 66(5):634–641, 2006.

[102] K.T. Tan. *Characterization of impact damage tolerance and performance of stitched CFRP laminate.* PhD thesis, Tokyo Metropolitan University, 2011.

[103] K.T. Tan, N. Watanabe, Y. Iwahori, and T. Ishikawa. Understanding effectiveness of stitching in suppression of impact damage: An empirical delamination reduction trend for stitched composites. *Compos Part A*, 43(6):823–832, 2012.

[104] K.T. Tan, N. Watanabe, M. Sano, Y. Iwahori, and H. Hoshi. Interlaminar fracture toughness of Vectran-stitched composites: Experimental and computational analysis. *J Compos Mater*, 44(26):3203–3229, 2010.

[105] P. Theobald, B. Zeqiri, and J. Avison. Couplants and their influence on ae sensor sensitivity. In *Proceeding of 28th European Working Group on Acoustic Emission (EWGAE-28)*, 2008. Krakow, Poland, September 16-19.

[106] H.G.S.J. Thuis and E. Bron. The effect of stitching density and laminate lay-up on the mechanical properties of stitched carbon fabrics. Technical Report CR96126L, Nationaal Lucht- en Ruimtevaartlaboratorium (NLR), The Netherlands, 1996.

[107] L. Tong, A.P. Mouritz, and M.K. Bannister. *3D fibre reinforced polymer composites.* Elsevier, 2002.

[108] T.C. Truong, M. Vettori, S. Lomov, and I. Verpoest. Carbon composites based on multi-axial multi-ply stitched preforms. part 4. mechanical properties of composites and damage observation. *Compos Part A*, 36(9):1207–1221, 2005.

[109] K. Vallons, I. Duque, S.V. Lomov, and I. Verpoest. Loading direction dependence of the tensile stiffness, strength and fatigue life of biaxial carbon/epoxy NCF composites. *Compos Part A*, 42(1):16–21, 2011.

[110] K. Vallons, S.V. Lomov, and I. Verpoest. Fatigue and post-fatigue behaviour of carbon/epoxy non-crimp fabric composites. *Compos Part A*, 40(3):251–259, 2009.

[111] N.E. Vandermey, D.H. Morris, and J.E. Masters. Damage development under compression-compression fatigue loading in a stitched uniwoven graphite/epoxy composite material. Technical Report CCMS-9l-l6, VPI-E-91-14, Virginia Polytechnic Institute and State University, 1991.

[112] A.P. Vassilopoulos and T. Keller, editors. *Fatigue of fiber-reinforced composites.* Springer, 2011.

[113] A. Velicki and D.C. Jegley. PRSEUS development for the hybrid wing body aircraft. In *Proceeding of AIAA Centennial of Naval Aviation Forum*, 2011. Virginia, USA, 21-22 September.

[114] T.J. Vogler and S. Kyriakides. On the initiation and growth of kink bands in fiber composites: Part I. experiments. *IJ Solid Struct*, 38(15):2639–2651, 2001.

[115] C. Weimer and P. Mitschang. Aspects of the stitch formation process on the quality of sewn multi-textile-preforms. *Compos Part A*, 32(10):1477–1484, 2001.

[116] J.M. Whitney and R.J. Nuismer. Stress fracture criteria for laminated composites containing stress concentrations. *J Compos Mater*, 8(3):253–265, 1974.

[117] E. Wu and J. Wang. Behavior of stitched laminates under in-plane tensile and transverse impact loading. *J Compos Mater*, 29:2254–2279, 1995.

[118] Y. Yamashita, S. Kawabata, S. Okada, and A. Tanaka. Mechanical characteristics of pbo single fiber. In *Proceeding of 6th Asian Textile Conf*, 2001. Hong Kong, 22-24 August.

[119] Y. Yasui, F. Hori, M. Amano, and J. Takeuchi. Method and apparatus for production of a three-dimensional fabric. *US Patent 5833802*, 1998.

[120] A. Yoshimura. *Study on damage progression of CFRP laminates with through-the-thickness stitch.* PhD thesis, University of Tokyo, 2006. (in Japanese).

[121] A. Yoshimura, T. Nakao, S. Yashiro, and N. Takeda. Improvement on out-of-plane impact resistance of CFRP laminates due to through-the-thickness stitching. *Compos Part A*, 39(9):1370–1379, 2008.

[122] A. Yoshimura, S. Yashiro, T. Okabe, and N. Takeda. Characterization of tensile damage progress stitched CFRP laminates. *Adv Compos Mater*, 16(3):233–244, 2007.

[123] J. Zhang and Y. Wei. A predictive approach to the in-plane mechanical properties of stitched composite laminates. *Acta Mech Sol Sinica*, 20(2):130–140, 2007.

[124] F.M. Zhao and N. Takeda. Effect of interfacial adhesion and statistical fiber strength on tensile strength of unidirectional glass fiber/epoxy composites. Part I: experiment results. *Compos Part A*, 31(11):1203–1214, 2000.

Publication

(*) *Publication related to this thesis*

A. Peer-reviewed journal papers

1. *__A. Yudhanto__, N. Watanabe, Y. Iwahori, H. Hoshi. (2012) Effect of Stitch Density on Tensile Properties and Damage Mechanisms of Stitched Carbon/Epoxy Composites. *Composites Part B* (Elsevier), Vol. 46, pp. 151-165.

2. *__A. Yudhanto__, Y. Iwahori, N. Watanabe, H. Hoshi. (2012) Open Hole Fatigue Characteristics and Damage Growth of Stitched Plain Weave Carbon/Epoxy Laminates, *International Journal of Fatigue* (Elsevier), Vol. 43, pp. 12-22.

3. *__A. Yudhanto__, N. Watanabe, Y. Iwahori, H. Hoshi. (2012) The Effects of Stitch Orientation on the Tensile and Open Hole Tension Properties of Plain Weave Carbon/Epoxy Laminates, *Materials & Design* (Elsevier), Vol. 35, pp. 563-571.

4. T.E. Tay, G. Liu, **A. Yudhanto**, V.B.C Tan. (2008) A Micro-Macro Approach to Modeling Progressive Damage in Composite Structures, *Int. Journal of Damage Mechanics* (SAGE Pub), Vol. 17, pp. 5 28.

5. **A. Yudhanto**, T.E. Tay, V.B.C. Tan. (2006) Micromechanical Characterization Parameters for A New Failure Theory for Composite Structures, *Key Engineering Materials* (TransTech), Vol. 306-308, pp. 781-786.

B. International conference proceedings

1. *__A. Yudhanto__, N. Watanabe, Y. Iwahori, H. Hoshi. Microcracking and Delamination of Stitched Composites under Static and Fatigue Loads, 8^{th} Asia-Pacific Conference on Composite Materials (ACCM-8), Kuala Lumpur, Malaysia, November 6-8, 2012.

2. *__A. Yudhanto__, N. Watanabe, Y. Iwahori, H. Hoshi. Effect of stitch density on fatigue behavior of Vectran-stitched composites, 15^{th} US-Japan Conference on Composites (ASC-27), Arlington, Texas, USA, October 1-3, 2010.

3. *__A. Yudhanto__, N. Watanabe, Y. Iwahori, H. Hoshi. Static and Fatigue Damage Mechanisms in Stitched Carbon/Epoxy Laminates, 10^{th} China-Japan Joint Conference on Composites (CJJCC-10), Chengdu, PR China, September 8-12, 2012.

4. *__A. Yudhanto__, N. Watanabe, Y. Iwahori, H. Hoshi. Damage Characterization in Stitched Carbon/Epoxy Laminates subjected to Monotonic and Cyclic Loadings, 15^{th} European Conference on Composite Materials (ECCM-15), Venice, Italy, June 24-28, 2012.

5. *__A. Yudhanto__, N. Watanabe, Y. Iwahori, H. Hoshi. Damage Characterization in Stitched Carbon/Epoxy Composites under Static and Fatigue Loadings, 4^{th} AUN/SEED-Net Reg. Conf. Mechanical and Aerospace Technology (RCMeAe-4), Ho Chi Minh City, Vietnam, January 10-11, 2012.

6. *__A. Yudhanto__, N. Watanabe, Y. Iwahori, H. Hoshi. Mechanical Properties of Vectran-Stitched Laminates under Static and Fatigue Loadings, 6^{th} International Conference on Fracture of Polymers, Composites and Adhesives, Les Diablerets, Switzerland, September 11-15, 2011.

7. *__A. Yudhanto__, N. Watanabe, Y. Iwahori, H. Hoshi. Mechanical Properties of Vectran-Stitched Composites: Numerical Simulation and Experimental Validation. 18^{th} International Conference of Composite Materials (ICCM-18), Jeju Island, South Korea, August 21-26, 2011.

8. *__A. Yudhanto__, N. Watanabe, Y. Iwahori, H. Hoshi. In-plane Mechanical Properties of Vectran-Stitched Composites by Homogenization Method, 16^{th} International Conference on Composite Structures (ICCS-16), University of Porto, Portugal, June 28-30, 2011.

9. *__A. Yudhanto__, N. Watanabe, Y. Iwahori, H. Hoshi. Tensile Fatigue Properties of Vectran-Stitched Composites Containing Hole, 3^{rd} Regional Conference on Mechanical & Aerospace Technology (RCMeAe-3), Manila, Philippines, March 4-5, 2011.

10. *__A. Yudhanto__, N. Watanabe, Y. Iwahori, H. Hoshi. Damage Progression in Stitched Composites containing Circular Hole under Fatigue Loads, 14^{th} US-Japan Conference on Composites (ASC-26), Dayton, Ohio, USA, September 20-23, 2010.

11. *__A. Yudhanto__, N. Watanabe, H. Hoshi, Y. Iwahori. In-Plane Mechanical Characteristics of Stitched Fabrics with and without Circular Hole, 14^{th} European Conference on Composite Materials (ECCM-14), Budapest, Hungary, June 7-10, 2010.

12. __A. Yudhanto__, E.T. Ong, E.H. Ong. Effects of Element Formulations of 8-noded Hexahedron on HDD Dynamics under Shock, 6^{th} Asia-Pacific Conference on Shock and Impact on Structures, Beijing, China, 2007.

13. K.T. Chua, __A. Yudhanto__, J.Q. Mou, E.H. Ong. Investigation of Soft-Failure of Small-Form Factor HDD under Forced Vibration, Asia-Pacific Magnetic Recording Conference, Singapore, November 2006.

14. __A. Yudhanto__, T.E. Tay, V.B.C Tan. Micromechanical Characterization Parameters for A New Failure Theory for Composite Structures, 6^{th} International Conference on Fracture and Strength of Solids (FEOFS 2005), Bali, Indonesia, April 4-6, 2005.

15. B.K. Hadi, __A. Yudhanto__. Wrinkling of Sandwich Panels by 3D Finite Element Analysis, 4^{th} Indonesian-Taiwan Workshop on Aeronautical Science, Technology and Industry (RC-ASTI), Bandung, May 18-19, 2004. pp. 25-32.

16. B.K. Hadi, __A. Yudhanto__. Buckling of Sandwich Panels by 3D Finite Element Analysis, 4^{th} Indonesian-Taiwan Workshop on Aeronautical Science, Technology and Industry (RC-ASTI), Bandung, May 18-19, 2004. pp. 111-122.

17. **A. Yudhanto**, B.K. Hadi. Sandwich Panels Stability under Constant Displacement, 3^{rd} International Conference on Numerical Analysis in Engineering, Batam, Indonesia, March 13-15, 2003.

C. Domestic conference proceedings

1. *__A. Yudhanto__, N. Watanabe, Y. Iwahori, H. Hoshi. Compressive characteristics and damage mechanisms of stitched composites, 4^{th} Japan Society of Composite Materials Conference (JCCM4), Tokyo, March 7-9, 2013.

2. *__A. Yudhanto__, N. Watanabe. Effect of Compaction Mechanism on Damage Development in Stitched Composites, 54^{th} Conference on Structural Strength (JSASS), Kumamoto, August 1-3, 2012.

3. *__A. Yudhanto__, N. Watanabe, Y. Iwahori, H. Hoshi. Effects of Stitching on the Fatigue Behavior of Stitched Carbon/Epoxy Laminates, 3^{rd} Joint Symposium on Composite Materials (JCOM41/JCCM3), Kyoto, March 7-9, 2012.

4. *__A. Yudhanto__, N. Watanabe, Y. Iwahori, H. Hoshi. Numerical and Experimental Studies of the Mechanical Properties of Stitched Composites, Annual Meeting of Science and Technology Studies (AMSTECS 2011), Campuses of GRIPS & Tokyo Institute of Technology, Tokyo, June 11-12, 2011. (*Best Presenter*)

5. *__A. Yudhanto__, N. Watanabe, Y. Iwahori, H. Hoshi. Prediction of Mechanical Properties of Vectran-Stitched Composites by Homogenization Method, 2^{nd} Japan Society of Composites Materials Conference (JCCM2), University of Tokyo, Tokyo, March 16-18, 2011.

6. *__A. Yudhanto__, N. Watanabe, Y. Iwahori, H. Hoshi. Open Hole Tension Characteristics of Plain-Woven and Non-Crimp Fabrics with Stitches, 52^{nd} Conference on Structural Strength (JSASS), Tottori, July 21-23, 2010.

Acknowledgments

Praise be to Allah the most compassionate and merciful without whom I would not have come thus far. Many people have directly and indirectly contributed to the completion of this work. I would like to extend a sincere gratitude to my PhD advisor, Prof Naoyuki Watanabe, for his excellent supervision and academic supports during my studies at Tokyo Metropolitan University (TMU). His sharpness in identifying challenging topics and methods has configured my scientific journey. This study would not be possible without generous funding from Tokyo Metropolitan Government under the project of Asian Network of Major Cities 21 (ANMC-21). Scholarship from Asian Human Resources Fund is greatly appreciated. Gratitude also goes to Dr Yutaka Iwahori and Dr Hikaru Hoshi of Advanced Composites Technology Center, Japan Aerospace Exploration Agency (JAXA), who shared their knowledge and skills during my research in JAXA. I am deeply indebted to Prof Masahito Asai, Dean of Graduate School of System Design cum project leader, who has been a wonderful host at TMU. This thesis also receives critics, comments and thorough review from PhD thesis committee members: Prof Hiroshi Suemasu (Sophia University), Prof Koichi Kitazono (TMU) and Prof Satoshi Kobayashi (TMU), Prof Masahito Asai (TMU). Experimental assistance and JAXA-TMU research liaison provided by Dr Shin-ichi Takeda (JAXA) and Dr Atsushi Kondo (MSC Japan), respectively, are greatly appreciated. Thanks to Mr Kenji Sekido (Kitazono Laboratory) and Dr Sugeng Supriadi (formerly Manabe Laboratory) for optical microscopy. Thanks to my resident advisor Dr Ayumu Inasawa, who selflessly helped me out since day one, and staff of International House (Ms Sekiguchi, Ms Yamada) and Hino Campus (Ms Shimazaki). My academic endeavour to Japan was due to Prof TE Tay (National University of Singapore) and Prof Takashi Ishikawa (Nagoya University; formerly JAXA) whom I'd like to thank for their kindness. Academic assistance from current and former members of Watanabe Laboratory is greatly acknowledged, especially Dr Shumpei Ozawa (Chiba Tech), my tutor Mr Satoshi Takahashi (Toyota), Dr Tan Kwek-Tze (IMRE-A*STAR), Mr Yousuke Oishi and Mr Yoshiaki Tabuchi (Kobe Steel). Heartfelt companionship with Indonesian friends in TMU and Hino is always remembered (Mr Dady, Mr Ridlo, Ms Ressa, Dr Triwanto Simanjuntak, Mr Banung, Mr Agus, Ms Ninien, Mr Jonny, Mr Yusuf, Mr Hamdan, Mr Aep et al.). Prayers from my mother, sister, brother and in-laws in Jakarta are deeply appreciated. Living in Hino City wouldn't have been easier without the help from Mrs Eri Kasai and her family for whom I extend my gratitude. Thanks to Prof B.K. Hadi (Bandung Institute of Technology) who had introduced composite mechanics 13 years ago. Finally yet importantly, I would like to sincerely thank my wife Tuti for her patience, encouragement and love (also, for helping me counting crack density), and our son Ezra for his bubbly nature and endless curiosity. This work is dedicated to my father Dr Goenawan Nambar (1947-2012) who had exemplified values to become a fine human being, and shown the meaning of life: to be useful to others.

Vita

Author was born in Bondowoso in 1978, and raised in various cities of East Java, Indonesia. He enrolled to the Department of Aeronautics and Astronautics, Bandung Institute of Technology (ITB), in 1997 and received B.Eng (*Sarjana Teknik*) degree in July 2002. After graduation, he worked at the Lightweight Structures and Aerodynamics Laboratory, Inter-University Research Center of ITB (2002-2003). In July 2003, he enrolled to master program at the Department of Mechanical Engineering, National University of Singapore (NUS), under AUN-SEED/Net scholarship. After submitting his thesis in August 2005, he returned to ITB to briefly work in an aircraft project. He received his M.Eng degree in March 2006 while he was working as a Research Engineer at the Data Storage Institute, Agency for Science Technology and Research (A*STAR) Singapore (2006-2007). He then joined Hitachi Global Storage Technologies (HGST) Singapore as Product Engineer in October 2007. In October 2009, he pursued his PhD research at the Aerospace Engineering Division, Graduate School of System Design, Tokyo Metropolitan University, Japan, under Asian Human Resources Fund.


NIHON
Bunkyo